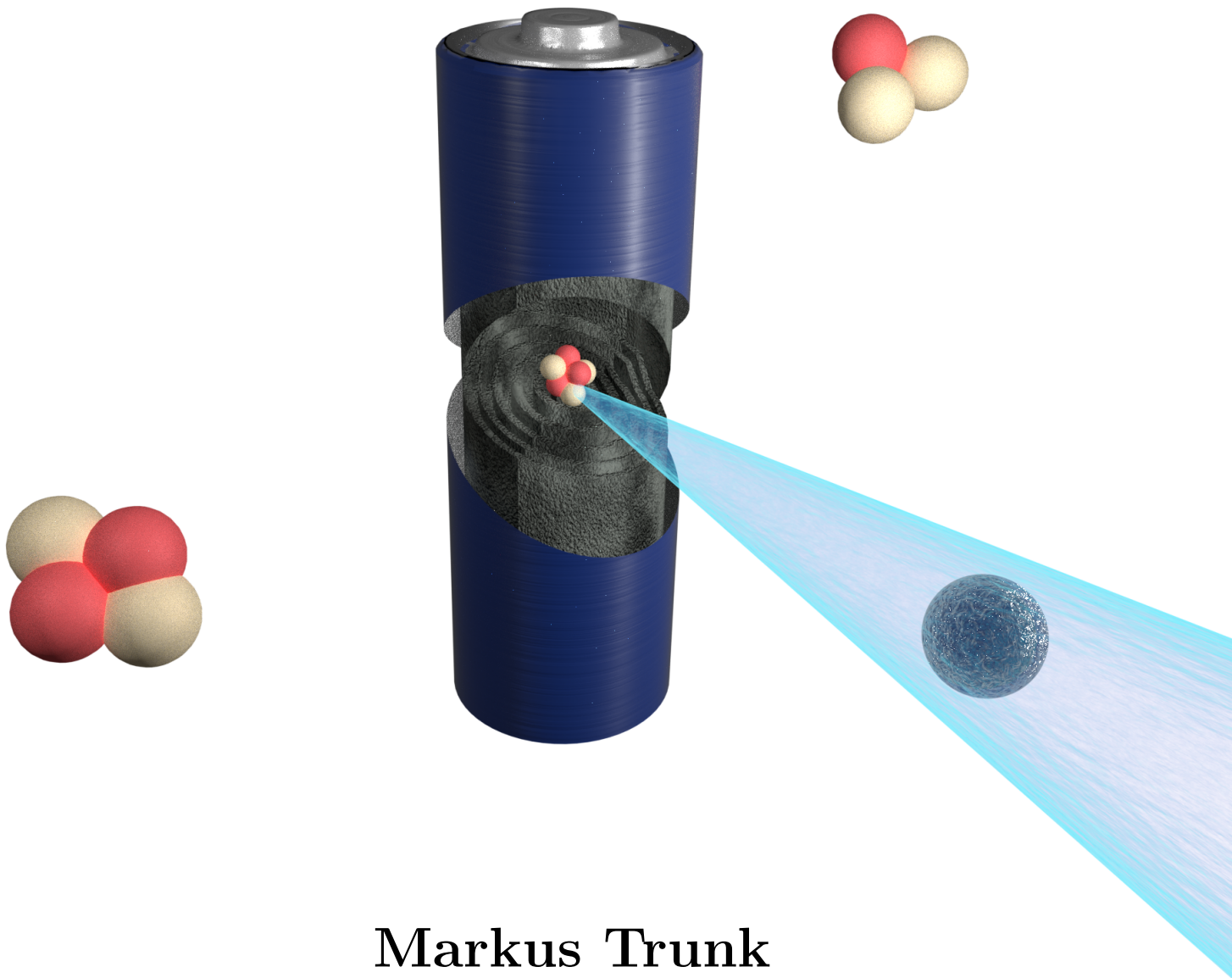


Determination of Isotope Concentration Profiles in Materials Science Applications Using Cold Neutrons



Markus Trunk

Dissertation

TECHNISCHE UNIVERSITÄT MÜNCHEN

Physik-Department
Elementarteilchenphysik bei niedrigen Energien

Determination of Isotope Concentration Profiles in Materials Science Applications Using Cold Neutrons

Markus Trunk

Vollständiger Abdruck der von der Fakultät für Physik der Technischen Universität München zur Erlangung des akademischen Grades eines

Doktors der Naturwissenschaften (Dr. rer. nat.)

genehmigten Dissertation.

Vorsitzender: Prof. Dr. Martin Zacharias

Prüfer der Dissertation: 1. Prof. Dr. Bastian Märkisch

2. Prof. Dr. Winfried Petry

Die Dissertation wurde am 20.01.2021 bei der Technischen Universität München eingereicht und durch die Fakultät für Physik am 13.04.2021 angenommen.

Zusammenfassung

Die Neutronen-Tiefenprofilanalyse (engl.: *Neutron Depth Profiling*; kurz: NDP) ist eine zerstörungsfreie Methode, mit der selbst kleinste Mengen oberflächennaher Isotopenkonzentrationen mit hoher Tiefenauflösung quantifiziert werden können. Durch seinen hohen Einfangsquerschnitt und einer großen Zerfallsenergie ist die ${}^6\text{Li}(n,\alpha){}^3\text{H}$ Reaktion ideal für die NDP geeignet. Hierbei kann aus einem Energiespektrum ein Isotopen-Konzentrationsprofil bis zu einer Tiefe von mehreren zehn Mikrometern zerstörungsfrei gemessen werden. Da Lithium-Ionen-Batterien aktuell eine der am stärksten wachsenden Technologien in der mobilen Energiespeicherung sind und das ${}^6\text{Li}$ Isotop mit seiner natürlichen Häufigkeit von $\approx 7.6\%$ in jeder dieser Zellen eingesetzt wird, bietet die NDP ideale Bedingungen um die chemischen und physikalischen Vorgänge in den Elektroden und im Elektrolyten auch während des Betriebs zu beobachten.

Im Rahmen dieser Arbeit wurden entscheidende Beiträge bei der Entwicklung des neuartigen NDP-Instruments “N4DP” geleistet, um am Heinz Maier-Leibnitz Zentrum (MLZ) in Garching b. München eine orts- und zeitaufgelöste Tiefenprofil-Analyse zu etablieren und somit einen wesentlichen Beitrag in der Batterieforschung zu liefern. Das entwickelte N4DP Instrument weist ein hohes Signal-zu-Untergrund Verhältnis auf und der ausgewählte Strahlplatz der prompten Gamma-Aktivierungsanalyse bietet den höchsten Fluss kalter Neutronen, der weltweit für die NDP Methode verwendet wird, was Messungen mit maximaler zeitlicher Auflösung erlaubt. Zudem ermöglichen siliziumbasierte Oberflächensperrschichtdetektoren mit höchster Energieauflösung eine Tiefengenauigkeit nahe der physikalisch möglichen Grenze.

Im Rahmen dieser Arbeit konnten mittels NDP Lithiumeinlagerungen in einem breiten Spektrum von Batterieanoden systematisch quantifiziert werden. Es wurden (ir-)reversible Lithiumeinlagerungen sowohl in Graphit-basierten Anoden, ähnlich wie sie heutzutage in kommerziellen Systemen Anwendung finden, als auch in neuartigen, Silizium-Graphit-basierten, Anoden *ex situ* untersucht und mit elektrochemischen Methoden verglichen. Um möglichen Verlust von Lithium beim Ausbau der Anoden zu vermeiden, wurden zudem *operando* Messungen an Graphit-basierten Anoden durchgeführt. Hierzu wurde ein neuartiges Batteriedesign entwickelt, um eine Messung der oberflächennahen NDP Methode zu ermöglichen und ein Sieden des flüssigen Elektrolyten bei niedrigem Umgebungsdruck zu verhindern. Es konnten sowohl die gleichmäßige Einlagerung von Lithium während des ersten Lade- Entladezyklus bei langsamen (Ent-)Ladevorgang, als auch die Bildung von metallischem Lithium auf der Anode bei schnellem Laden beobachtet werden.

Abstract

Neutron Depth Profiling (NDP) is a non-destructive method to quantify even smallest amounts of near-surface isotope concentrations with high depth resolution. Due to its high capture cross section and a large decay energy, the ${}^6\text{Li}(n,\alpha){}^3\text{H}$ reaction is ideally suited for the NDP. Here, an isotope concentration profile can be measured non-destructively from an energy spectrum down to a depth of several tens of micrometers. Since lithium-ion batteries are currently one of the fastest growing technologies in mobile energy storage and the ${}^6\text{Li}$ isotope with its natural abundance of $\approx 7.6\%$ is used in each of these cells, the NDP offers ideal conditions to observe the chemical and physical processes in the electrodes and electrolyte during operation.

In the frame of this thesis, essential contributions to the development of the new instrument “N4DP” were conducted, in order to establish a spatially and time-resolved depth profile analysis at the Heinz Maier-Leibnitz Center (MLZ) in Garching b. Munich to significantly contribute to battery research. The developed N4DP instrument offers a high signal-to-background ratio and the selected facility of the prompt-gamma-activation analysis provides the highest flux of cold neutrons used worldwide for the NDP method, which allows measurements with maximum temporal resolution. In addition, silicon-based surface barrier detectors with highest energy resolution allow depth accuracy close to the physically possible limit.

In the framework of this thesis, NDP was used to systematically quantify lithium accumulations in a broad set of battery anodes. Here, (ir-)reversible lithium accumulations in graphite-based anodes, similar to those used in commercial systems today, as well as in novel, silicon-graphite-based, anodes could be quantified *ex situ* and compared to electrochemical studies. To avoid possible loss of lithium during removal of the anodes, *operando* measurements were also performed on graphite-based anodes. For this purpose, a novel battery design was developed to enable measurement of the near-surface NDP method and to prevent boiling of the liquid electrolyte at low ambient pressure. This allowed to study the homogeneous lithium accumulation occurring at low (dis-)charging rates during the first (dis-)charge cycle and to observe the formation of metallic lithium on the anode during fast charging.

Table of Contents

Zusammenfassung	i
Abstract	ii
List of abbreviations	ix
1 Introduction	1
1.1 Emission of Greenhouse Gases	1
1.2 Energy Transition in Germany	3
1.3 Lithium-Ion Batteries	5
1.4 Neutron-Based Lithium-Ion Battery Characterization	5
1.5 Structure of This Work	7
2 Fundamentals of Neutron Depth Profiling	9
2.1 Neutrons as a Probe	9
2.2 Neutron Capture	10
2.2.1 γ Emission	12
2.2.2 Charged-Particle Emission	12
2.3 Energy Loss of Charged Particles in Matter	14
2.4 Depth Analysis	17
3 Experimental Setup	19
3.1 The N4DP Setup at the MLZ	19
3.1.1 The Research Neutron Source FRMII	19
3.1.2 The NL4b Beam Line	21
3.1.3 The N4DP Experimental Setup	23
3.2 Additional NDP Setups	29
3.2.1 The N4DP Demonstrator Setup	29
3.2.2 The Cold Neutron Depth Profiling Instrument at the NCNR	31
4 Data Analysis of Neutron Depth Profiling	35
4.1 Calibration	35
4.1.1 Energy Calibration	35
4.1.2 Normalization of Concentrations	36

4.2	Particle Energy Spectra and Concentration Profiles	39
4.3	Signal Broadening and Depth Mapping	41
4.4	Experimental Verification	43
5	Battery Research Using Neutron Depth Profiling	47
5.1	Working Principle of Lithium-Ion Batteries	47
5.2	NDP on Anodes for Lithium-Ion Batteries	51
5.2.1	<i>Ex situ</i> NDP Measurements	51
5.2.2	<i>Operando</i> NDP Experiments	52
5.3	Coin Cell Battery Development for <i>operando</i> NDP	52
5.3.1	NDP Battery Cell Concept	53
5.3.2	Charged-Particle Window	53
5.3.3	Graphite Anode	54
5.3.4	Coin Cell Assembly	57
5.3.5	Optical Performance of the <i>Operando</i> Coin Cell	59
5.3.6	Influence of the Coin Cell Design on the NDP Signal	60
6	Passivated Lithium Accumulations in Graphite Anodes	61
6.1	Electrode Lamination in Li-Ion Batteries	61
6.2	Sample Preparation	62
6.3	Characterization of Immobilized Lithium in Graphite Anodes	64
6.3.1	XRD Measurements	64
6.3.2	NDP Measurements	66
6.4	Conclusion	72
7	Silicon-Graphite Anodes for Li-Ion Batteries	75
7.1	Lithium Accumulation During the First (Dis-)Charge Cycle	75
7.2	Lithium Immobilization During Extended Cycling	80
7.3	Conclusion	85
8	Operando Investigation of Lithium Transport in Graphite Anodes	87
8.1	<i>Operando</i> Lithium Intercalation During Formation	87
8.2	Lithium Transport Process During Fast Charging	93
8.3	Conclusion	100
9	Conclusion and Outlook	103
9.1	Conclusion	103
9.2	Outlook	105
9.2.1	Technical Developments	105
9.2.2	Future Applications	107

Appendix A Complementary Characterization Methods	109
A.1 X-Ray Diffraction	109
A.2 Optical Microscopy	110
A.3 Atomic Force Microscopy	111
Appendix B Beam Profile Images	113
Appendix C Ex Situ Graphite Anode Spectra	115
Bibliography	122
List of Publications	147
Acknowledgment	151

List of abbreviations

ADC	Analog-to-Digital Converter
AFM	Atomic Force Microscopy
CC	Constant Current
CCD	Charge-Coupled Device
CNDP	Cold Neutron Depth Profiling
CV	Constant Voltage
DOD	Depth of Discharge
DSSD	Double-Sided Silicon Strip Detector
ENC	Equivalent Noise Charge
FRM II	Forschungsreaktor (engl.: <i>research reactor</i>) München II
HV	High Voltage
MLZ	Heinz Maier-Leibnitz Zentrum
N4DP	NDP instrument at the PGAA facility of MLZ
NCNR	NIST Center for Neutron Research
NDP	Neutron Depth Profiling
NIST	National Institute of Standards and Technology
NL4b	Neutronenleiter (engl.: <i>neutron guide</i>) 4b at FRM II
OCV	Open-Circuit Voltage
PGAA	Prompt Gamma Activation Analysis
PHD	Pulse-Height Defect
SDD	Sample-to-Detector Distance
SEI	Solid-Electrolyte-Interphase
SEM	Scanning Electron Microscopy

SOC	State of Charge
SR1	Strahlrohr (engl.: <i>beam tube</i>) 1 at FRM II
SSD	Silicon Surface-Barrier Detector
UCN	Ultra-Cold Neutron
XRD	X-Ray Diffraction

This work focuses on Neutron Depth Profiling (NDP) and mainly on its application on electrodes for lithium-ion batteries. In this chapter, first the need for the reduction of greenhouse gases is discussed and the greenhouse gas emissions for different primary energy sources are compared to each other. Afterwards, the energy transition in Germany is outlined and the impact of the transformation of combustion engines to fuel-cell and all-electric vehicles on the emission of greenhouse gases is discussed. In Sec. 1.3 lithium-ion batteries are shortly introduced. In Sec. 1.4 neutron-based characterization techniques on lithium-ion batteries are discussed with a focus on NDP. The N4DP instrument is shortly introduced and the beam flux density at the measurement site is compared to other NDP facilities worldwide. An overview of the further structure of this thesis is given in Sec. 1.5.

1.1 Emission of Greenhouse Gases

The global control of the climate change is an essential step for many of the 17 Sustainable Development Goals decided by the United Nations to be achieved until 2030 [1]. While in 1998, the United Nations agreed on the reduction of overall gas emissions in the Kyoto Protocol, they deduced in 2015 during the Paris Agreement a global maximum temperature increase of 2 °C compared to that of the pre-industrial times [2–4]. However, in 2018 a report commissioned by the Intergovernmental Panel on Climate Change (IPCC) illustrated the importance of a temperature increase not greater than 1.5 °C in order to reduce impacts on environment, economy, as well as social inequality including global poverty [5]. Among other parameters, the authors highlight the importance of the greenhouse gas emission to achieve the 1.5 °C temperature limit and so they propose a reduction of the CO₂ emission to 45 % of the level in 2010 until 2030, further reducing to zero net emission around 2050 [5]. CO₂, together with H₂O vapor, O₃, N₂O, CH₄ and fluorinated greenhouse gases is one of the main gases promoting the greenhouse effect [6–8]. On the other hand, in order to achieve the 2 °C goal suggested in the Paris Agreement, a CO₂ reduction of 25 % until 2030 and zero net emission until 2070 would be necessary [5]. In order to reduce the anthropogenic CO₂ emission as well as other greenhouse gases, the development of carbon-capture and carbon-storage systems together with low-to-zero carbon power generation technologies is of utmost importance [9].

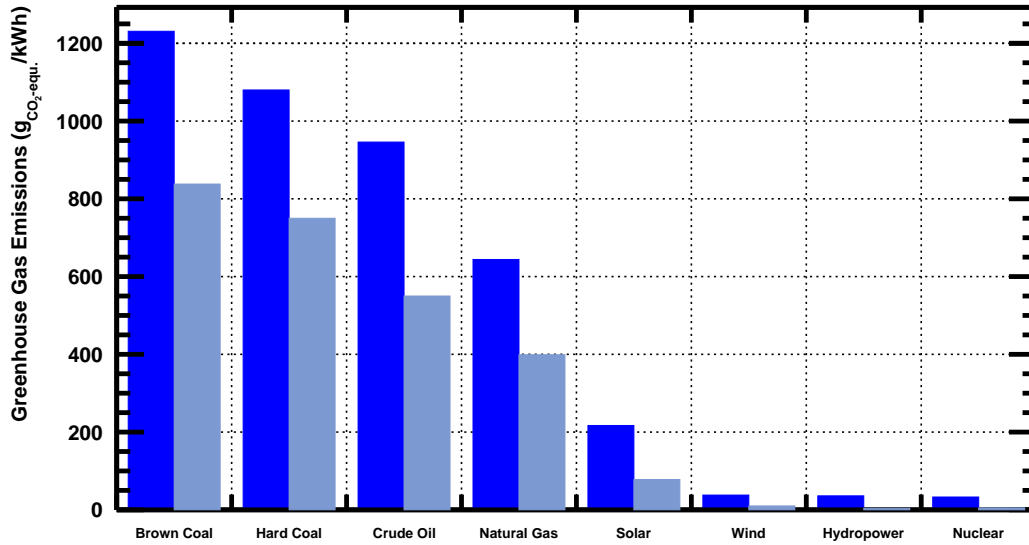


Figure 1.1: Maximum (dark blue) and minimum (light blue) reported emissions of greenhouse gases for different primary energy sources given in CO₂-equivalent g per kWh with respect to their life cycle, i.e. also including emissions during construction and dismantling of the facilities. While fossil-fuel-based energy sources (brown coal, hard coal, crude oil and natural gas) induce the highest CO₂-equivalent emissions, renewable energy sources together with nuclear power show significantly lower emissions. Data obtained from [10].

An overview of the CO₂-equivalent emissions for one kWh of the most common energy sources is shown in Fig. 1.1 with respect to their life cycles, i.e. taking also into account emissions during construction and dismantling of the individual power stations [10]. Fossil-fuel-based power generation utilizing brown coal, hard coal, crude oil and natural gas induce the highest CO₂-equivalent emissions in the range exceeding 1000 down to ≈ 400 g_{CO₂}/kWh, respectively. The use of solar power induces significantly less greenhouse gases in the range of (78–217) g_{CO₂}/kWh. The lowest CO₂-equivalent emissions are induced by power generation using wind (10–38) g_{CO₂}/kWh, hydropower (4–36) g_{CO₂}/kWh and nuclear power (5–33) g_{CO₂}/kWh.

In 2018, $\approx 87\%$ of the global energy consumption was generated using fossil fuels and only $\approx 4\%$ and $\approx 2\%$ were generated using renewable energies and nuclear power, respectively [11]. In order to reduce the carbonization of the atmosphere and the ocean, environment degradation, acid rain and global warming induced by the emission of greenhouse gases, fossil-fuel-based primary energy sources have to be replaced with energy sources emitting a low amount of CO₂ [5, 12]. While nuclear power is suitable for the use of a constant energy baseload, renewable energy sources are volatile to natural fluctuations. In order to maintain a robust power grid and to mitigate power fluctuations, electrical energy obtained in periods of surplus power generation needs to be stored for times with a shortage of electrical energy [13]. Energy can be stored chemically using hydrogen storage, electrochemically using various types of batteries,

mechanically using flywheels, hydraulic or compressed air systems, thermally by heating or cooling systems or electromagnetically using superconducting magnetic energy storages or superconductors [14–16]. Recently, a highly efficient superconductor with an energy density up to 73 Wh/kg and high durability of 10000 (dis-)charge cycles while maintaining 90 % of its capacity was developed at TUM via attaching functionalized metal-organic frameworks on functionalized graphene [17]. In the case of hydrogen storage using e.g. compressed, liquefied or metal hydride systems, hydrogen can be converted to electrical energy using fuel cells when the energy demand exceeds the available energy capacity [14]. It can be used as fuel for fuel-cell-based electric cars, aviation fuel or can be further processed with methane to fuel for engine applications [14, 18, 19].

1.2 Energy Transition in Germany

The energy transition in Germany has heavily been influenced by the Renewable Energy Sources Act (German: *Erneuerbare Energien Gesetz*; EEG), which replaced in 2000 the previous Electricity Feed-in Act from 1991 [20, 21]. It has continuously been and is still being reworked since then and it mainly regulates the development of and the financial support for produced electricity from renewable energy sources. While this promotes the growth of renewable energy sources, the costs are passed to the population. In 2020 the EEG reallocation charge was ≈ 6.8 ct/kWh, which is one of the reasons that in Germany the residential electricity prices were with ≈ 31 ct/kWh in 2019 one of the highest in Europe [22, 23]. In 2020 the COVID-19 pandemic led to a significant reduction of the electricity consumption in Germany and consequently the EEG reallocation charge would rise sharply in the following year but it was limited by the government to 6.5 ct/kWh in 2021 using an economic stimulus package [24].

The Climate Protection Plan 2050 decided by the German government in 2010, which was later continuously expanded, calls among other things a reduction of the greenhouse gas emissions of 80 % compared to that of 1990, a reduction of energy usage of 50 % compared to that of 2008 and an usage of at least 80 % renewable energies of the total electricity consumption for 2050 [25–27]. The energy transition in Germany has progressed so far that the net energy production which consisted of ≈ 60 % from fossil-fuel-based energy sources and only of ≈ 7 % from renewable energy sources in the year 2000 changed to ≈ 49 % fossil-fuel-based energy sources and ≈ 36 % renewable energy sources in 2018 [28]. However, on 11 March 2011 as a result of an earthquake with a magnitude of 9.0 and a subsequent tsunami with over 13 m height the nuclear accident in Fukushima took place [29, 30]. Due to the major release of radioactive material in the atmosphere it was later rated with the highest level 7 (major accident) rank on the International Nuclear and Radiological Event Scale (INES) [31, 32]. In response to this accident and to the public reaction on it, Germany passed a law for its nuclear phase-out, where eight power plants were immediately shut down in August 2011 followed by an incremental dismantling of the remaining nine power plants until end of 2022 [33]. Therefore, the contribution from nuclear power generation to the net energy production was simultaneously to the expansion of

renewable energies reduced from originally $\approx 30\%$ in the year 2000 to $\approx 12\%$ in 2018 and is planned to be zero in 2023 [28, 33]. A part of the increased renewable energy production has to be used for compensating the reduced contribution from the nuclear power sector [34]. As a consequence, this fraction is no longer available for replacing fossil-fuel-based power generation exhibiting a much higher CO_2 footprint than nuclear power (c.f. Fig. 1.1) slowing down the energy transition process towards low greenhouse gas emissions. Between 2002 and 2018 the power generated from renewable energies increased by ≈ 180 TWh but only ≈ 44 TWh of it were used to replace fossil-fuel-based power generation and ≈ 85 TWh had to be used to compensate the reduction in nuclear power [34]. The remaining ≈ 52 TWh are in the same range as the increase of the net export between 2002 and 2018 and a correlation between the fluctuating power generation from photovoltaic power generation and the energy export can be found [34]. Due to insufficient available storage systems and to maintain the energy baseload, the fluctuating power from renewable energies were balanced in Germany via regulating fossil-fuel-based power plants using curtailment and redispatch [34]. A permanent operation of fossil-fuel-based power plants originally intended as reserve might be necessary in the future thus possibly compromising the security of the energy supply [34]. In 2019 the resulting energy mix in Germany produced CO_2 -equivalent greenhouse gases of $\approx 401 \text{ g}_{\text{CO}_2}/\text{kWh}$ according to recent estimations, which was below the average of $\approx 449 \text{ g}_{\text{CO}_2}/\text{kWh}$ of the G20 states being an international cooperation between 20 countries with the most advanced or emerging economies to govern the global economy [35, 36]. For comparison, the energy mix in France was generated in 2019 to $\approx 72\%$ from nuclear power and to $\approx 19\%$ from renewable energy sources, which resulted in a CO_2 -equivalent greenhouse emission of only $49 \text{ g}_{\text{CO}_2\text{e.q.}}/\text{kWh}$ [36, 37]. This comparison clearly illustrates why the International Energy Agency (IEA) emphasizes the key role of nuclear power generation alongside the development of renewable energy sources during the energy transition [34, 38].

Apart from energy industry ($\approx 30\%$) and energy and process-related emissions in industry ($\approx 23\%$), the transport sector was with $\approx 20\%$ one of the main contributors to the emission of greenhouse gases in Germany in 2019 [39]. In order to reduce the impact of automotive applications on the emission of greenhouse gases, efforts are made to replace fossil-fuel-based combustion engines with fuel-cell vehicles or all-electric vehicles. If a large amount of the generated energy would be stored using hydrogen, an allocation of the transport sector to fuel-cell cars and all-electric cars seems to be a promising approach for the future [34]. For all-electric vehicles the electric energy is typically stored using lithium-ion batteries, which are shortly outlined in Sec. 1.3 and discussed in more detail in Chap. 5. Since the electricity originates from the power grid, the CO_2 emission of full-electric vehicles strongly depends on the country-specific energy mix. Assuming an average electricity consumption of $\approx 0.2 \text{ kWh}/\text{km}$ for a passenger car, the CO_2 -equivalent emission for all-electric passenger cars can be estimated to be $\approx 80 \text{ g}_{\text{CO}_2}/\text{km}$ in Germany for 2019 [40]. This value is already smaller than $\approx 120 \text{ g}_{\text{CO}_2}/\text{km}$ being the average emission of passenger cars using combustion engines in 2018 and it is also below the EU target of $95 \text{ g}_{\text{CO}_2}/\text{km}$ proposed for all new passenger cars at the end of 2020 [41]. For comparison, the CO_2 -equivalent greenhouse gas emission of an all-electric vehicle can be estimated in the same

manner to $\approx 10 \text{ g}_{\text{CO}_2}/\text{km}$ using the French energy mix of 2018. This shows that there can be a large impact of greenhouse gas reduction of all-electric vehicles compared to passenger cars using combustion engines but it also strongly depends on the country-specific primary energy generation.

1.3 Lithium-Ion Batteries

Lithium-ion batteries have rapidly evolved in recent years since their commercialization in 1991 and are nowadays ubiquitous [42]. Due to their high energy density and low weight, they are favorable especially for mobile applications like sensors, internet-of-things, mobile phones, handheld applications, medical applications, power tools (e.g. remote control, battery screwdrivers) and aerospace applications [43–45]. They are also increasingly used to supply energy in hybrid and all electric plug-in automotive applications, where combustion engines are replaced and the emission of greenhouse gases is significantly reduced depending on the energy mix of the country, as discussed above [43, 46, 47].

The range limitation of electric vehicles and high costs of the batteries currently limits the transition from fossil-fuel-based to electric mobility. Lithium-ion batteries need to be optimized for sustainability, high capacity, light weight and peak power performance [15]. In order to increase their energy density, novel electrode materials are studied, e.g. pure lithium anodes with specific capacities of 3860 mAh/g or silicon-based anode compositions with specific capacities exceeding 4000 mAh/g substituting conventional graphite anodes with specific capacity of 372 mAh/g [48]. However, these systems respectively suffer from dendrite formation or fast degradation and only small improvements of the optimized lithium-ion batteries with specific energies of $\approx 200 \text{ Wh/kg}$ are expected in the near future [49]. Furthermore, irreversible processes and limited diffusion rates reduce the lifetime and charging speed of lithium-ion batteries [50, 51]. In the framework of this thesis, aging processes in graphite- and novel silicon-graphite-based anodes are studied *ex situ* using Neutron Depth Profiling. Furthermore, the lithium transport at low and high cycling rates in commercially relevant graphite anodes is measured *operando* for the first time.

1.4 Neutron-Based Lithium-Ion Battery Characterization

Due to their high penetration, non-destructive properties and high nuclide sensitivity, neutrons offer unique possibilities for sample characterization thus complementing techniques like X-ray-based methods (XPS, XRD, GISAXS), secondary ion mass spectroscopy (SIMS), or scanning electron microscopy (SEM). Especially when measuring light nuclides like ${}^6\text{Li}$ in a matrix of heavy nuclei like transition metals, as they are used in lithium-ion batteries (c.f. Chap. 5), neutrons offer unique characterization possibilities without harming or influencing the battery component or even the operating cell [52].

Neutron Powder Diffraction (NPD) techniques are used to reveal *in situ* and *operando* structural changes of electrodes used for lithium-ion batteries in the range of the atomic order [53–55].

Morphological changes occurring in electrodes can be followed using Small-Angle Neutron Scattering (SANS) [56]. Neutron Reflection allows to probe *operando* kinetics and structures near interfaces [57, 58]. Neutron Radiography and Neutron Tomography are used to visualize *in situ* the electrolyte filling process in lithium-ion batteries [59, 60]. Neutron Depth Profiling (NDP) allows to probe *in situ* and *operando* the kinetics and transport dynamics in lithium-ion battery components by measuring lithium concentrations with respect to depth [61, 62].

NDP, first applied conceptually around 1972 by Ziegler *et al.*, is based on the residual energy measurement of charged particles emitted by some isotopes after neutron capture [63, 64]. The energy loss these charged particles experience on their way through the sample allows to determine the depth of their origin with depth resolutions up to a few tens of nanometers [65]. NDP allows to directly probe the lithium accumulation in the cell, thus complementing electrochemical insights on the performance of the whole battery.

In the framework of this thesis, essential contributions to the Neutron Depth Profiling instrument “N4DP” at the Heinz Maier-Leibnitz Zentrum (MLZ) in Garching, Germany, were performed, which was developed together with L. Werner and several samples for materials science applications like electrodes for lithium-ion batteries were characterized [66]. As listed in Tab. 1.1, the N4DP instrument utilizes with $2 \times 10^9 \text{ cm}^{-2}\text{s}^{-1}$ one of the highest cold neutron flux densities worldwide available at an NDP experiment site, allowing to follow even fast kinematics with high statistical significance. As discussed later (c.f. Chap. 3 and Sec. 9.2.1), it is planned to utilize in the near future a focusing guide for NDP exceeding a neutron flux of $10^{10} \text{ cm}^{-2}\text{s}^{-1}$, similar to that currently used for Prompt-Gamma-Activation techniques providing a flux of $5 \times 10^{10} \text{ cm}^{-2}\text{s}^{-1}$ at its focal point.

Institution	Location	Neutron Flux Density $\left(\frac{1}{\text{cm}^2\text{s}}\right)$	Ref.
N4DP, TUM, MLZ	Garching, Germany	2×10^9 (5×10^{10})	[67]
NIST NCNR	Gaithersburg, USA	1.22×10^9	[65, 68]
Maria, JCNS, MLZ	Garching, Germany	0.7×10^9	[69]
CARR	Beijing, China	4.8×10^8	[70]
CMRR	Mianyang, China	2.1×10^8	[71]
HANARO	Daejeon, Republic of Korea	1.8×10^8	[72]
PSBR	Pennsylvania, USA	3×10^7	[73]
NARS, Ohio State	Columbus, Ohio, USA	1.27×10^7	[74]
ÚJF NPI	Řež, Czech Republic	1×10^7	[75]
RID	Delft, Netherlands	$\approx 10^7$	[62]

Table 1.1: List of various NDP facilities operating worldwide, listed by the neutron flux density available at the experiment site. The institutions are given together with their location and respective references. Adapted, updated and extended from [66, 76, 77].

1.5 Structure of This Work

In the framework of this thesis, major developments of the new N4DP instrument were performed and a wide range of samples were characterized to gain novel insights into materials used for lithium-ion batteries.

In Chap. 2 the theoretical background of neutron-based characterization methods is discussed with a focus on Neutron Depth Profiling. In Chap. 3, the experimental setups of the neutron-based methods used in this work are presented. While the focus is on the N4DP experiment, two further NDP setups are discussed. NDP calibration procedures and data analysis are presented in Chap. 4 on the basis of different reference measurements. Specifications, limitations, and developments of lithium-ion batteries for NDP measurements are discussed in Chap. 5. Here, a special cell design was developed which makes it possible to use the NDP method in real time during battery operation. Applications of NDP on anodes for lithium-ion batteries are presented in the three subsequent chapters. Here, different setups are studied and discussed in order of increasing complexity: first in Chap. 6, *ex situ* NDP measurements on graphite anodes are presented. Today, graphite-based anodes are used most frequently for lithium-ion batteries in industry. In Chap. 7, results on *ex situ* NDP measurements on novel silicon-graphite-based anodes are discussed. Silicon provides a high theoretical capacity but undergoes strong irreversible processes upon operation which induce a significant change in composition [48]. A forward-mapping method is also presented which can be used for the separation of different signals. It enables to follow the irreversible anode mass swelling at different aging stages. In Chap. 8, first *operando* NDP measurements on commercially relevant graphite-based anodes for lithium-ion batteries are presented. Here, the focus is on the lithium accumulation during the first (dis-)charge process and upon fast charging. A conclusion and an outlook are given in Chap. 9.

Fundamentals of Neutron Depth Profiling

CHAPTER 2

In this chapter, the fundamentals of Neutron Depth Profiling (NDP) are discussed and brought into a greater context. First, the application of neutrons as characterization probe is discussed in Sec. 2.1. Then, in Sec. 2.2, the capture of neutrons is presented focusing on two possible capture reactions: γ and charged-particle emission. The energy loss of these particles in matter is examined in Sec. 2.3. Eventually, the relation between energy loss and the depth of origin is discussed in Sec. 2.4.

2.1 Neutrons as a Probe

Free neutrons are a suitable probe to non-destructively study materials using absorption, transmission or scattering techniques [78]. They are used for a wide range of applications in physics, chemistry material sciences, biology and medicine [79–83]. Their non-destructive nature is of special interest for delicate applications like archaeometry, studies of solar cells and lithium-ion batteries [52, 78, 84–86].

Neutrons are baryons and they consist of one **u** and two **d** valence quarks. They exhibit particle properties including a rest mass of $m_N \approx 1.67 \times 10^{-27}$ kg and a confinement radius of $R \approx 0.7$ fm [78]. They exhibit no electric properties, i.e. no (measurable) electric charge or electric dipole momentum, which results in a good penetration depth [78]. In order to use neutrons as a probe, they are typically extracted from atomic nuclei using nuclear fission or spallation [78]. In contrast to stable neutrons bound in atomic nuclei, free neutrons undergo β^- decay:



with a mean lifetime of (879.4 ± 0.6) s [87]. Apart from their particle nature, free neutrons can also be treated as waves with a corresponding de Broglie wavelength λ which is adjustable using thermal heating or cooling [88]. Due to their high scattering cross section, neutrons are especially sensitive to hydrogen [59, 89]. Furthermore, their magnetic moment $\mu_N \approx 9.662 \times 10^{-27}$ J/T and spin $I_Z = -\frac{1}{2}$ allow to probe local distributions of magnetic atoms and their spin orientation [78,

87, 90–93]. For example, in 2009, lattices of skyrmions, which are quasi particles associated with topologically stable field configurations, could be experimentally observed using neutrons for the first time in a magnetic MnSi lattice [94].

2.2 Neutron Capture

If the investigated nuclides exhibit an energy level close to (above) the vacuum level E_{vac} , which is excitable by neutron capture, thermal or cold (hot) neutrons may be captured thus forming a highly excited $^{A+1}Z^*$ compound nucleus. It then either de-excites by the emission of prompt γ cascades, charged particles or a combination of both. As shown in Fig 2.1, especially light elements like lithium and boron contain several nuclides (natural abundances) with extremely high thermal neutron capture cross section σ_{th} and thus even small concentrations can be detected in a matrix of heavy nuclei [95, 96]. For thermal and cold neutrons at an energy range close to the vacuum level and outside of high-energetic resonances, the neutron capture cross section σ can be described as a function of energy [78, 97]:

$$\sigma = \sigma_{\text{th}} \sqrt{\frac{E_{\text{th}}}{E}} = \sigma_{\text{th}} \frac{\lambda}{\lambda_{\text{th}}} \quad , \quad (2.2)$$

where $E_{\text{th}} = 25 \text{ meV}$ and $\lambda_{\text{th}} = 1.8 \text{ \AA}$ are the mean kinetic energy and wavelength of thermal neutrons, respectively. In this work a polychromatic neutron beam with a mean energy of $\bar{E} = 1.83 \text{ meV}$ ($\bar{\lambda} = 6.7 \text{ \AA}$) is utilized [67]. Following Eq. (2.2), this cold ($E < E_{\text{th}}$) neutron beam induces a 3.7 times higher capture cross section compared to a thermal one.

The non-destructive property of neutron-based methods, which states that the sample is not altered in functionality or shape, can be understood using the principle of neutron capture. The Beer-Lambert law describes the attenuation of a pristine neutron flux Φ_0 of a single wavelength after penetrating through a depth d of a material with individual nuclide densities n_i and capture cross sections σ_a^i [52]:

$$\Phi(d) = \Phi_0 \exp\left(-d \sum_i \sigma_a^i n_i\right) \quad . \quad (2.3)$$

In the following an upper limit on the influence of neutron capture on the investigated lithium-ion batteries in the experimental setup will be estimated based on Eq. (2.3). Here, an electrode (typical thickness $d \approx 50 \mu\text{m}$) is substituted with a sheet just as thick but composed of natural lithium, which is the dominant origin of neutron capture in these devices. Based on Eq. (2.3), a thermal neutron flux Φ would be reduced by $\approx 1.6\%$ of its pristine value Φ_0 . Using a thermal equivalent neutron flux of $2 \times 10^9 \text{ cm}^{-2}\text{s}^{-1}$ and a beam spot size of 0.126 cm^2 at the experimental facility, as described in Sec. 3.1.3, this translates to a lithium loss of $4 \times 10^6 \text{ }^6\text{Li/s}$, which is negligible compared to the pristine number of lithium atoms ($3 \times 10^{19} \text{ natLi}$) in the illuminated sample volume. During *operando* battery applications, this lithium loss would result in an electric current of $\approx 1.9 \text{ pA}$ assuming that all produced particles leave the sample leading to a release of $3e^-$ per lithium atom, which is an overestimation due to the short range of the

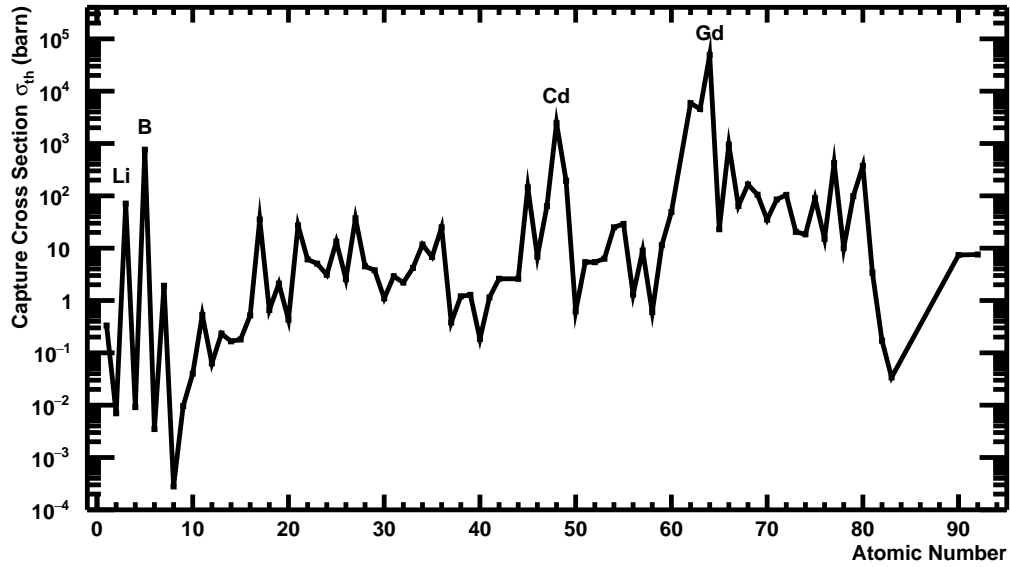


Figure 2.1: Capture cross sections of stable elements for thermal neutrons ($\lambda_{\text{th}} = 1.8 \text{ \AA}$). The capture cross section changes with the neutron wavelength by $\sigma \propto \lambda$, as shown in Eq. (2.2). The cross sections are weighted by the natural abundance of the individual isotopes. Lithium (Li), boron (B), cadmium (Cd) and gadolinium (Gd) are highlighted due to their high thermal neutron-capture cross sections. Data obtained from [98].

charged particles. This value is negligible when compared to the typical operation current in the μA range.

Apart from absorption, neutrons also can coherently (σ_{coh}) and incoherently (σ_{inc}) be scattered resulting in a combined thermal neutron scattering cross section $\sigma_s = \sigma_{\text{coh}} + \sigma_{\text{inc}}$ [95, 99, 100]. Thermal neutron scattering cross sections are listed in Tab. 2.1 for all stable nuclides detectable using NDP [77, 95]. For ${}^6\text{Li}$ and ${}^{10}\text{B}$ nuclides, being the two nuclides this work focuses on, the combined scattering cross sections σ_s are negligibly small compared to the absorption cross sections inducing charged-particle emission (c.f. Tab. 2.2).

Nuclide	σ_{coh} (barns)	σ_{inc} (barns)	σ_s (barns)
${}^3\text{He}$	(4.42 ± 0.10)	(1.6 ± 0.4)	(6.0 ± 0.4)
${}^6\text{Li}$	(0.51 ± 0.05)	(0.46 ± 0.05)	(0.97 ± 0.07)
${}^{10}\text{B}$	(0.144 ± 0.008)	(3.0 ± 0.4)	(3.1 ± 0.4)
${}^{14}\text{N}$	(11.03 ± 0.05)	(0.5 ± 0.1)	(11.53 ± 0.11)
${}^{17}\text{O}$	(4.20 ± 0.22)	(0.004 ± 0.003)	(4.20 ± 0.22)
${}^{33}\text{S}$	(2.8 ± 0.2)	(0.3 ± 0.6)	(3.1 ± 0.6)
${}^{35}\text{Cl}$	(17.06 ± 0.06)	(4.7 ± 0.6)	(21.8 ± 0.6)

Table 2.1: List of coherent, incoherent and total thermal neutron scattering cross sections of stable nuclides detectable using NDP (c.f. Tab. 2.2). Data obtained from [95].

2.2.1 γ Emission

Prompt γ cascades emitted from radiative ${}^AZ(n,\gamma){}^{A+1}Z$ reactions are characteristic [97]. This is used in the Prompt Gamma Activation Analysis (PGAA) method to determine the number n of atoms of certain nuclides by measuring the count rate R_γ^0 using

$$R_\gamma^0 = n \cdot \Phi \cdot \sigma_\gamma \cdot \varepsilon(E_\gamma) \quad (2.4)$$

for thin samples [97]. Here, Φ is the thermal equivalent neutron flux, σ_γ describes the thermal capture cross-section for the ${}^AZ(n,\gamma){}^{A+1}Z$ reaction and $\varepsilon(E_\gamma)$ is the energy-dependent detection efficiency. For thick samples, corrections for neutron self-absorption need to be taken into account [99]. Due to the high penetration depth of γ radiation, only a small correction is needed especially for low energies and heavy target material. PGAA is a bulk technique and probes the mean composition in the irradiated volume.

2.2.2 Charged-Particle Emission

A few stable and mainly light nuclides, as listed in Tab. 2.2, emit charged p (i.e. ${}^1\text{H}$) or α (i.e. ${}^4\text{He}$) particles and a residual charged particle upon neutron capture. Neutron Depth Profiling (NDP) is based on the detection of these particles. It was first utilized in 1972 by Ziegler *et al.* for determining boron distributions in ion-implanted silicon and other substrates [63, 64].

The charged particle emission will be discussed with focus on lithium and boron, since they are the two prominent elements detected in this work. When a low-energetic (cold, thermal) neutron close to the vacuum level E_{vac} is captured by a AZ (${}^6\text{Li}$; ${}^{10}\text{B}$) nucleus, a highly excited ${}^{A+1}Z^*$ ($E({}^7\text{Li}^*) = 7.25$ MeV; $E({}^{11}\text{B}^*) = 11.46$ MeV) compound nucleus is formed [96, 101]. This excitation energy originates from the difference in binding energies $\Delta\text{BE} = \text{BE}({}^{A+1}Z) - \text{BE}({}^AZ)$.

Nuclide	Natural Abundance (%)	Reaction	Thermal Neutron Capture Cross Section (barns)	Energies of Emitted Particles (keV)	
				Particle 1	Particle 2
${}^3\text{He}$	0.000134	${}^3\text{He}(n,p){}^3\text{H}$	5316.00	572.465	191.291
${}^6\text{Li}$	7.59	${}^6\text{Li}(n,\alpha){}^3\text{H}$	938.47	2055.55	2727.92
${}^{10}\text{B}$	19.9	${}^{10}\text{B}(n,\alpha){}^7\text{Li}$	241.31	1776.53	1013.50
		${}^{10}\text{B}(n,\alpha){}^7\text{Li}^*$	3600.48	1472.42	840.012
${}^{14}\text{N}$	99.636	${}^{14}\text{N}(n,p){}^{14}\text{C}$	1.8271	583.850	42.0202
${}^{17}\text{O}$	0.038	${}^{17}\text{O}(n,\alpha){}^{14}\text{C}$	0.235	1413.67	404.075
${}^{33}\text{S}$	0.75	${}^{33}\text{S}(n,\alpha){}^{30}\text{Si}$	0.168621	3081.95	411.554
${}^{35}\text{Cl}$	75.76	${}^{35}\text{Cl}(n,p){}^{35}\text{S}$	0.5	597.795	17.229

Table 2.2: List of stable nuclides detectable using NDP due to charged-particle emission upon neutron capture. A few radioactive isotopes like ${}^7\text{Be}$, ${}^{22}\text{Na}$, ${}^{37}\text{Ar}$, ${}^{40}\text{K}$, ${}^{59}\text{Ni}$, ${}^{65}\text{Zn}$ and ${}^{210}\text{Po}$ can be detected as well. Data obtained from [77].

Together with the rest mass of the compound nucleus $A+1Z$ (${}^7\text{Li}$; ${}^{11}\text{B}$) this energy is split forming an α particle, a residual nucleus (${}^3\text{H}$; ${}^7\text{Li}^{(*)}$) and an excess of energy which is transferred to kinetic motion of both particles. This residual energy is given by the Q-value, which is the difference of the rest mass m_i of the mother ($m_{{}^6\text{Li}}+m_n$; $m_{{}^{10}\text{B}}+m_n$) and m_f of daughter nuclei ($m_\alpha+m_{{}^3\text{H}}$; $m_\alpha+m_{{}^7\text{Li}^{(*)}}$):

$$Q = \left(\sum_i m_i - \sum_f m_f \right) c^2 \quad , \quad (2.5)$$

where $c \approx 2.998 \times 10^8$ m/s is the speed of light in vacuum [102, 103]. The Q-value of the ${}^6\text{Li}(n,\alpha){}^3\text{H}$ reaction is 4.8 MeV, while for the ${}^{10}\text{B}(n,\alpha){}^7\text{Li}^{(*)}$ reaction 2.8 MeV can be transferred to kinetic motion. All nuclides listed in Tab. 2.2 exhibit a Q-value in the keV–MeV range. Here, energy and momentum contribution of the incoming neutron can be considered as negligible being in the meV range (typically thermal (≈ 25 meV) or cold (< 25 meV) neutrons are used for NDP and at the N4DP experiment a mean neutron energy of 1.83 meV is utilized) [67]. The low energy of the neutron beam makes it possible to use a polychromatic neutron beam with its full intensity and no velocity filtering is required, like for many neutron scattering techniques using monochromatic beams [52, 78]. The contribution of thermal kinetics within the sample (≈ 25 meV) is also negligible compared to the Q-values. Thus, the center-of-gravity of the reaction can be considered as static leading to a split of the Q-value to the kinetic motion of both particles following momentum conservation. Due to the two-body kinematics the two charged particles are emitted back-to-back (opening angle of 180°) isotropically with known kinetic energies, which are listed in Tab. 2.2.

Only for the ${}^{10}\text{B}(n,\alpha){}^7\text{Li}^{(*)}$ reaction two decay channels are observed, as shown in Tab. 2.2. Here, the decay directly into the ${}^7\text{Li}$ ground state is suppressed ($\sigma_{\text{th}} = 241$ barn). The excited ${}^{11}\text{B}^*$ compound nucleus preferably ($\sigma_{\text{th}} = 3.6$ kbarn) decays into an α particle and a ${}^7\text{Li}^*$ at a well-defined energy level (478 keV) [101, 104]. It then de-excites with a half life of 73 fs into the ${}^7\text{Li}$ ground state emitting a γ -photon at this energy [101, 104]. Since a fraction of the production energy is used for the γ -photon, the kinetic energies of both charged particles is reduced following energy conservation (c.f. Tab. 2.2). When detecting the γ ray of the ${}^{10}\text{B}(n,\alpha){}^7\text{Li}^*$ reaction using PGAA, a 15.2-keV-broad peak is observed due to the Doppler effect induced by the moving ${}^7\text{Li}^*$ recoil particle [104–107].

Thanks to the long range of neutrons in matter, the neutron flux is nearly constant in the sample. Consequently, the production rate of the charged particles reflects the local concentration of the investigated nuclides. As mentioned for the γ emission, thick layers of materials with high capture cross sections attenuate the neutron beam thus reducing the emission of charged particles (neutron self-absorption) based on Eq. (2.3).

2.3 Energy Loss of Charged Particles in Matter

After production, the charged particles penetrate through the sample until they reach its surface and eventually emanate to the detectors. A particle with velocity $v_1 = \beta c$ can be slowed down due to collisions with the electrons and atoms of the sample matrix inducing ionization, atomic or collective excitation. The property of a material to decelerate a charged particle with kinetic energy E within a certain thickness x is defined by the stopping power $S(E) = -\frac{dE}{dx}$, given in energy loss per unit length (typically in the $\frac{\text{keV}}{\mu\text{m}}$ range). The total stopping power

$$\frac{dE}{dx} = \left. \frac{dE}{dx} \right|_e + \left. \frac{dE}{dx} \right|_n \quad (2.6)$$

consists of the electronic stopping power $\left. \frac{dE}{dx} \right|_e$ induced by inelastic collisions with the electrons and the nuclear stopping power $\left. \frac{dE}{dx} \right|_n$ caused by quasi-elastic collisions with the atoms of the host material. The electronic stopping dominates for particle energies E typically being in the keV range and higher, i.e. high particle velocities v_1 and a low atomic number Z_1 of the charged particle. It gives rise to a series of collisions with small energy losses per collision (typically smaller than 100 eV) and only small path length deflections resulting in a rather straight travel path [108]. The nuclear stopping, dominating at low particle energies E being in the low-to-sub keV range (low velocities v_1) and high Z_1 , gives rise to significant angular deflections of the trajectory of the charged particle induced by large discrete energy losses [103, 109].

At intermediate particle velocities $0.05 < \beta\gamma < 1000$, where $\beta = \frac{v_1}{c}$ describes the velocity of the charged particle and $\gamma = \frac{1}{\sqrt{1-\beta^2}}$ is the Lorentz factor, the mean of the electronic stopping power can empirically be described by the Bethe-Bloch formula [108–111]:

$$-\left. \frac{dE}{dx} \right|_e = \frac{4\pi e^4}{m_e c^2} \cdot n_e \cdot \frac{Z_1^{*2}}{\beta^2} \left[\ln \left(\frac{2m_e c^2 \beta^2}{I(1-\beta^2)} \right) - \beta^2 - \frac{C}{Z_2} - \frac{\delta}{2} \right] \quad , \quad (2.7)$$

where

$$n_e = \frac{N_A \cdot Z_2 \cdot \rho}{A \cdot M_u} \quad (2.8)$$

describes the electron density in the sample material [103, 109, 110]. Here, N_A is the Avogadro number and ρ is the bulk density of the host material. The molar mass M of the sample material is described by $A \cdot M_u$, where A is the relative atomic mass number of the host material and $M_u \approx 1 \text{ g/mol}$ is the molar mass constant defined by the atomic mass of one atom of ^{12}C [112]. The effective mean excitation potential I accounts for the accessible quantum mechanical energy levels in the host material which depends on its atomic structure and is therefore different for the individual host materials [109, 111]. Although the excitation potential shows resonances with Z_2 which can be determined experimentally, it is typically on the order of $I \approx 10 \cdot Z_2$ (eV) with Z_2 being the atomic number of the host material [103, 108]. The shell correction term $\frac{C}{Z_2}$ accounts for the velocity contribution of the electrons in the host material at low particle energies and the density correction $\frac{\delta}{2}$ corrects for the dielectric polarization of the sample at high particle energies when going towards relativistic velocities [111]. At relativistic particle velocities with

$\beta\gamma > 1000$ radiative effects start to dominate, which are Z_1 -dependent [108]. It is to state that the Bethe-Bloch formula given in Eq. (2.7) is only valid for “heavy” charged particles, meaning $m_{\text{particle}} \gg m_e$, which is the case for all charged particles emitted upon neutron capture listed in Tab. 2.2 [111].

Furthermore, Eq. (2.7) shows a quadratic dependence of the energy loss on the effective charge Z_1^* of the particle. At velocities $v_1 > v_0 Z_1^{\frac{2}{3}}$, the charged particle is a bare nucleus (fully stripped, i.e. its total charge equals its atomic number Z_1) and the effective charge is equal to the atomic number of the nucleus ($\frac{Z_1^*}{Z_1} = 1$). Here, the particle velocity v_1 is compared to that of the electrons in the host material being in the order of the Bohr velocity

$$v_0 = \frac{\hbar}{m_e a_0} \approx 2.188 \times 10^6 \frac{\text{m}}{\text{s}} \quad , \quad (2.9)$$

which describes the velocity of an electron in the inner orbit of the hydrogen atom at the Bohr radius

$$a_0 = \frac{\hbar^2}{m_e e^2} \approx 0.5292 \text{ \AA} \quad . \quad (2.10)$$

Hereby, $\hbar \approx 6.582 \times 10^{-16}$ eVs is the reduced Planck constant, $m_e \approx 9.1095 \times 10^{-31}$ kg is the electron rest mass and $e \approx 1.6022 \times 10^{-19}$ C is the electron charge [103]. At reduced kinetic energies, however, an effective particle charge Z_1^* needs to be taken into account, because electrons from the surrounding material can be captured in its electronic shell reducing its effective net charge and consequently the electronic stopping power.

At low particle velocities $\beta < 0.01$, i.e. at particle velocities about the electron velocities in the host material being in the range of the Bohr velocity v_0 , the electronic shells of the particle and the host material might overlap, thus forming a quasi-molecule [103, 109]. During the duration of the collision and the lifetime of the molecule, electrons between the particle and the host material can be exchanged, leading to quasi-classical momentum transfers [109]. When electrons are transferred from the host material to the electron shell of the particle, they need to be accelerated to the particle velocity and the momentum $m_e v_1$ slows the particle down. Electrons transferred from the particle to the host material do not alter the particle energies and therefore only a particle deceleration is induced [103]. The electronic energy loss in this velocity range is observed to be proportional to v_1 and is described by Sugiyama based on the theories of Lindhard and Scharff [113, 114]:

$$-\left. \frac{dE}{dx} \right|_e = \xi_e 8\pi e^2 a_0 N \frac{Z_1^* Z_2^* v_1}{Z_S^* v_0} \quad , \quad (2.11)$$

where $\xi_e \approx Z_1^{1/6}$,

$$N = \frac{N_A \cdot \rho}{A \cdot M_u} \quad (2.12)$$

is the atomic density of the host material and Z_S^* is the effective screening factor being a combination of the screened atomic numbers of the particle Z_{S1} and the host material Z_{S2} [103, 109, 113, 114]. At particle velocities $0.01 < \beta < 0.05$ the electronic stopping power can phenomenologically be described by a fitting interpolation of the two regimes (Bethe stopping and Lindhard-Scharff stopping) [108, 115, 116].

At low particle energies in the low-to-sub keV range, nuclear collisions dominate the particle stopping [103]. They are dominated by quasi-elastic collisions with the atoms of the host material described by classical momentum transfer and are the main cause for particle deflection [103, 109, 114]. It is to note that the experimental setup later presented in Chap. 3 exhibits a trigger threshold in the range of ≈ 200 keV, i.e. only particles with higher energies are detected using NDP. Therefore, electronic stopping is the dominant cause for energy loss in NDP. The nuclear energy loss scales with $(1 + \frac{M_2}{M_1})^{-1}$, while M_1 and M_2 respectively are the masses of the particle and the host material [103, 109, 114]. This further reduces the influence of light particles passing through heavier host materials, as it is the case for most applications investigated using NDP.

In summary, for the light particles produced after neutron capture (c.f. Tab. 2.2), the electronic stopping is the dominant process giving rise to a straight travel path. This is exemplarily visualized in Fig. 2.2 a, where the mean electronic and nuclear energy losses of ^3H and α particles in a silicon matrix are shown in the energy range between 10 keV and 10 GeV. The data were obtained using the SRIM (Stopping and Range of Ions in Matter) software developed by James Ziegler *et al.*, which is based on experimental data of heavy-ion scattering experiments in various materials [111, 117]. While the electronic stopping dominates the nuclear stopping for both particles, the α particle (due to its higher atomic number Z_1) exhibits a much higher electronic energy loss than the ^3H particle, which scales with Z_1^* at lower energies and with Z_1^{*2} at higher energies, as described by Eq. (2.7) and Eq. (2.11). The higher stopping power of the α conse-

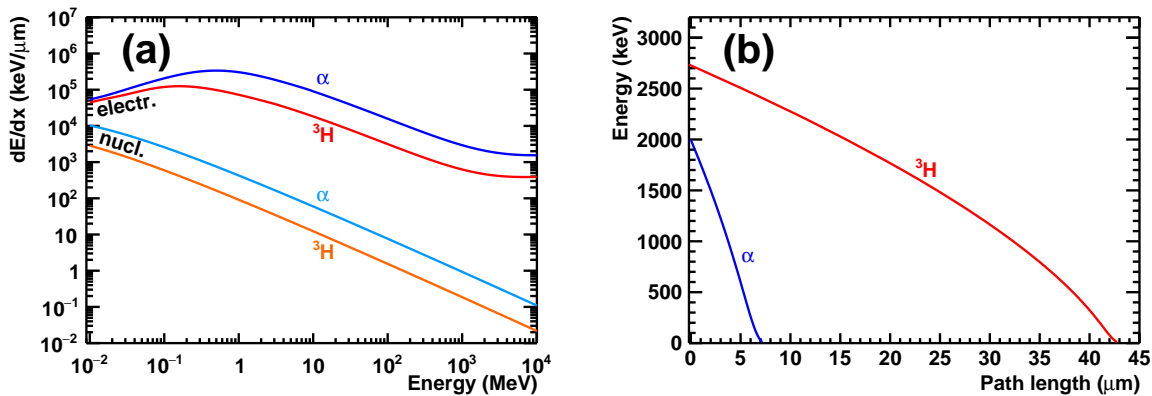


Figure 2.2: (a) Electronic and nuclear energy loss for ^3H and α charged particles in silicon. Due to the light ions passing through a heavy host material, the electronic energy loss dominates in the energy range of 10 keV to 10 GeV. (b) Remaining energies of the ^3H and α charged particles of the $^6\text{Li}(n,\alpha)^3\text{H}$ reaction depending on the travel path in silicon. Due to its lower atomic number, the ^3H particle has an increased penetration range compared to the α particle. All data were obtained using the SRIM software [111].

quently leads to a shorter penetration depth, as shown in Fig. 2.2 b for ${}^3\text{H}$ and α produced at energies of the ${}^6\text{Li}(n,\alpha){}^3\text{H}$ reaction (c.f. Tab. 2.2).

2.4 Depth Analysis

When the depth where the particles are produced is not large enough to stop them within the sample, they will eventually emanate from its surface and their remaining energy can be detected. Since their production energy is well-defined (c.f. Tab. 2.2) the emission depth can be determined from the remaining energy, similarly as shown in Fig. 2.2 b. This is only true when the bulk host material density ρ is well-known, since the stopping power is proportional to it, as shown in Eq. (2.7) and (2.11). Assuming a straight path and a constant (known) density ρ , the distance d from the particle origin to the sample surface is correlated to the stopping power $S(E)$ by:

$$d = \int_{x=0}^{x=d} dx = \int_{E_0}^{E(d)} \frac{dx}{dE} dE = - \int_{E_0}^{E(d)} \frac{1}{S(E)} dE = \int_{E(d)}^{E_0} \frac{1}{S(E)} dE \quad . \quad (2.13)$$

The maximum penetration depth D of a charged particle produced at an energy E_0 is then:

$$D(E_0) = \int_0^{E_0} \frac{1}{S(E)} dE \quad . \quad (2.14)$$

The shorter penetration depth of the α compared to that of the ${}^3\text{H}$ particle results in a steeper energy-to-depth relation shown in Fig. 2.2 b. Since the energies are measured in distinct intervals (ADC channels, c.f. Sec. 3.1.3), this allows to measure near-surface layers with a resolution down to the nm range for the α , while the ${}^3\text{H}$ enables probing a greater penetration depth but with a lower resolution [118]. As discussed in Sec. 2.3, the energy loss induced by collisions with the host material is a statistical process thus reducing the depth resolution. It can be estimated based on the signal broadening induced by energy straggling (σ_{stragg}) and multiple small-angle scattering (σ_{scatt}) taking place upon collisions of the particles with the host material. As shown in Fig. 2.3 for α and ${}^3\text{H}$ particles in a silicon matrix, the resulting broadening $\sigma = \sqrt{\sigma_{\text{stragg}}^2 + \sigma_{\text{scatt}}^2}$ increases up to the μm range for thick samples (low residual energies). This broadening originating from the statistical collisions imposes an upper limit of the depth resolution when using NDP on an ideal sample. It is reduced by signal broadening induced from the experimental setup, as discussed in Chap. 3 and Chap. 4, and by inhomogeneous material distributions (in the μm range) within a sample giving rise to various particle travel paths in the sample (c.f. Chap. 6–8). The bulk density in many material-science applications is often poorly defined and it may also vary locally as a function of depth. For example, anodes for lithium-ion batteries used in this work were prepared via mixing active material particles of grain sizes in the μm range in a liquid ink leading to a porous anode film after drying. While these anode films appear to be homogeneous on the large scale, the charged particles are sensitive to density variations on the μm -level.

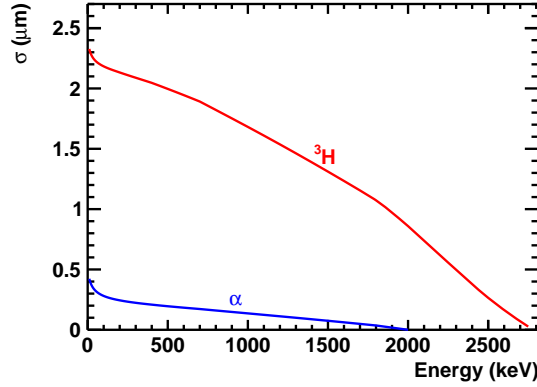


Figure 2.3: Statistical collisions of the particles with the host material give rise to a signal broadening resulting in lower depth resolutions with greater travel path (lower residual energy). Here, the combined signal broadenings σ induced by energy straggling σ_{stragg} and σ_{scatt} multiple small-angle scattering are shown for α and ${}^3\text{H}$ particles from the ${}^6\text{Li}(n,\alpha){}^3\text{H}$ reaction in a silicon matrix. The highest depth resolution is provided by the α particle close to the surface. During measurements, this idealized depth resolution is further reduced by the experimental setup and the sample itself. Data were obtained using the SRIM software [111].

For the energy loss, inelastic collisions with the electrons of the host-material are necessary and thus the charged particles do not lose energy in voids between the collision partners, as it would be the case e.g. in a low-density material or in vacuum. The particles do not probe the depth x itself, but are rather sensitive to the number of inelastic collisions on their travel path. Consequently, a long path x in a material with low bulk density ρ would result in the same energy loss, as a shorter path in the same material but with greater bulk density, e.g. produced via material compression, and so these cases are indistinguishable in NDP [118]. Here, the mass thickness m_A (also referred to as “mass loading”, “surface mass density”, or “areal density”) is commonly used as figure of merit, which accounts for the mass of material along the travel path and defines the number of collisions with effective mean excitation potentials I . The mass thickness m_A is defined as mass per unit area:

$$m_A = \frac{m}{A} = x \cdot \rho \quad . \quad (2.15)$$

Using the relation $dm_A = \rho \cdot dx$, the stopping power can be expressed as a function of mass thickness:

$$-\frac{dE}{dm_A} = -\frac{1}{\rho} \cdot \frac{dE}{dx} \quad , \quad (2.16)$$

which can then be used also for samples with an unknown bulk density. For most cases in this work, the particle energies were translated to mass thickness m_A and thus were translated to depth x only when the uniformity of the bulk density ρ could be reasonably assumed.

The experimental setups of the NDP instruments utilized in the framework of this thesis are presented in this chapter. A special focus will be put on the newly developed “N4DP” instrument at the Prompt Gamma Activation Analysis (PGAA) facility of the Heinz Maier-Leibnitz Zentrum (MLZ). Major developments of it were performed in the framework of this thesis. It was developed together with L. Werner and more information on technical details can be found in [66, 119]. Two additional NDP setups will be presented: a demonstrator setup used for the first NDP measurements which was later upgraded to the final version, and also the cold neutron depth profiling instrument “CNDP” at the NIST Center for Neutron Research, Gaithersburg (USA) where a measurement was performed during the reactor break at FRM II in 2019. Further characterization methods complementary to the neutron-based techniques used within the framework of this thesis are presented in the Appendix A.

3.1 The N4DP Setup at the MLZ

Unique opportunities at the research neutron source Heinz Maier-Leibnitz (FRM II) being part of the Heinz Maier-Leibnitz Zentrum (MLZ) fostered the idea to develop a conceptually new Neutron Depth Profiling (NDP) instrument for time resolved and position sensitive NDP. A short overview of the research neutron source FRM II is given and the N4DP experiment is presented this section, which is situated at the NL4b neutron guide of the FRM II.

3.1.1 The Research Neutron Source FRM II

The research neutron source FRM II is one of the leading facilities for neutron-based research and became first critical in 2004 and is in regular operation since 2005 [120]. It generates free neutrons by the nuclear fission of ^{235}U . Besides typical heavy nuclides like ^{139}Ba and ^{94}Kr , an average of 2.4 neutrons per fission is produced and 1-2 neutrons are available for scientific use [121, 122]. At the nominal power of $P = 20\text{ MW}$ the fuel element produces a maximum thermal neutron flux density of $8 \times 10^{14}\text{ cm}^{-2}\text{s}^{-1}$ in the D_2O moderator. The total operation time of FRM II is typically 240 days per year consisting of 4 cycles with 60 days each (one fuel element per cycle) [120]. A hot graphite source at a temperature of 2300 K and a cold liquid

D₂ source at 18 K act as secondary sources and enable the use of neutrons at different energies and wavelengths [88]. A converter facility provides fast fission neutrons using subcritical fission in a uranium plate [123]. An additional ultra-cold neutron (UCN) secondary source is under construction.

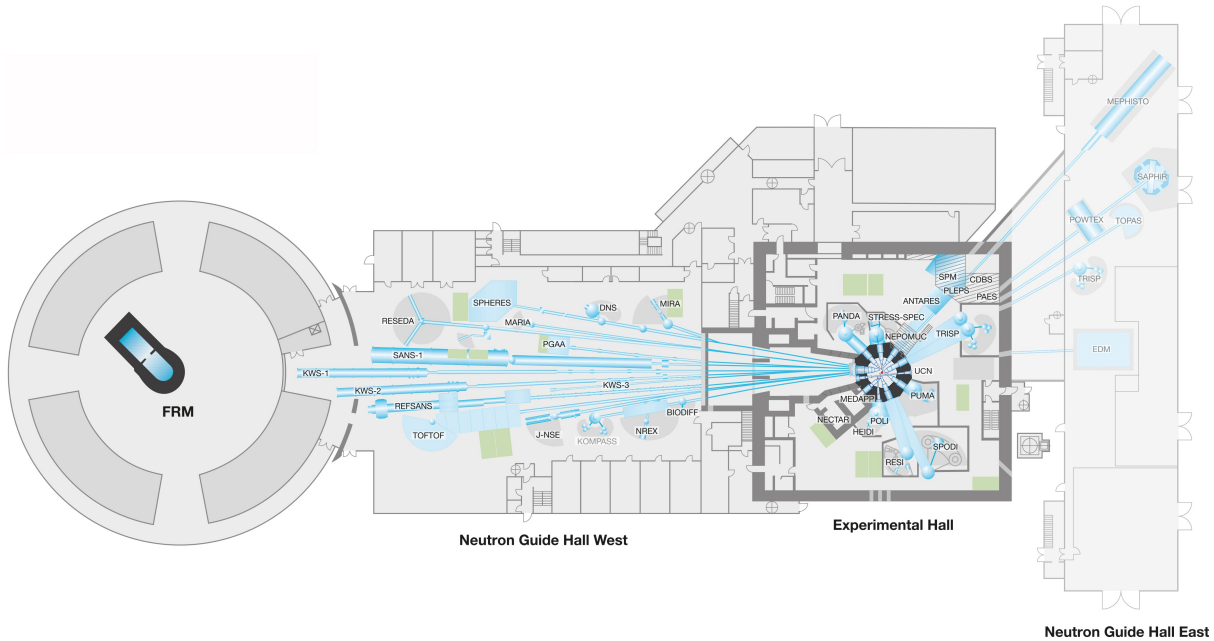


Figure 3.1: Schematic overview of the research neutron source FRM II. 33 experimental facilities are operating or under construction [124]. Neutrons are used at a wide temperature range depending on the individual experimental requirements. Experiments situated in the Experimental Hall are close to the reactor core, while longer neutron guides transport neutrons in the Neutron Guide Hall West. Experiments and neutron guides in the Neutron Guide Hall East are under construction. The Neutron Guide Hall West ends on the left side into the FRM, which was commissioned in 1957 as the first research power reactor in Germany and was operated until 2000 [125]. It is famous for its egg-like structure and is used in the town coat of arms of Garching since 1967 [126]. Taken from [127].

An overview of the FRM II site is shown in Fig. 3.1 a. There are 33 experimental facilities under operation or partly under construction [124]. The ones utilizing hot neutrons e.g. the diffractometers (HEIDI, POLI) are located in the Experimental Hall close to the hot source in order to maximize the neutron flux of fast neutrons [128, 129]. Due to their larger de Broglie wavelength, cold neutrons can be transported efficiently over larger distances through neutron guides via constructive superposition. At FRM II, neutron guides with ^{58}Ni coating exhibiting a high neutron scattering length density, or super-mirror coatings with m values up to 3.0 are being used [123, 130, 131]. For instance, cold neutrons are guided through the SR1 into the Neutron Guide Hall West up to a distance of 70 m (NL5-S neutron guide to RESEDA) [123, 132]. During reactor commissioning in 2004, the neutron guides were characterized by measuring the neutron flux distributions and beam divergences using time-of-flight spectroscopy, gold foil activation and software simulations [131].

Due to a wavelength ($\lambda_{\text{th}} \approx 1.8 \text{ \AA}$) on the order of the atomic structures, thermal neutrons are used for various diffractometers (RESI, SPODI, STRESS-SPEC, POWTEX, SAPHIR) [133–137]. They can be utilized for spectrometry (PUMA, TRISP, TOPAS), neutron radiography, tomography (NECTAR) and for medical treatments (MEDAPP), too [138–142]. For NECTAR and MEDAPP, a uranium-based converter plate can be moved into the thermal neutron beam producing fast neutrons. At FRM II, most experimental facilities utilize cold neutrons, which are due to their longer wavelengths ($\lambda_{\text{cold}} \approx 6 \text{ \AA}$) suited to study mesoscopic distances in e.g. polymers, proteins or macromolecules using the BIODIFF diffractometer [143]. They furthermore exhibit significantly higher capture cross sections compared to thermal or fast neutrons which enables the detection of uniquely low quantities by prompt gamma activation (PGAA) [144]. Cold neutrons are at FRM II also utilized for (very) small angle scattering (KWS-1, KWS-2, KWS-3, SANS-1), radiography and tomography (ANTARES), spectrometers (DNS, J-NSE, KOMPASS, PANDA, RESEDA, SPHERES, TOFTOF), reflectometers (MARIA, NREX, REFSANS), a diffractometer (BIODIFF), magnetic structures (MIRA), or for particle physics (MEPHISTO, under construction) [132, 145–162]. At FRM II, also a thermal-capture-induced positron source is installed for the characterization of solid-state materials, surfaces and fundamental research (NEPOMUC) [163, 164].

3.1.2 The NL4b Beam Line

The PGAA facility is located in the Neutron Guide Hall West and it is connected to the D_2 cold neutron source via the NL4b guide of the SR 1. As shown in the photograph in Fig. 3.2 a, the NL4b neutron guide is curved (radius: 390 m) in order to reduce influences from γ radiation and fast neutrons from the reactor [96, 123, 166]. In this way an average cold neutron energy

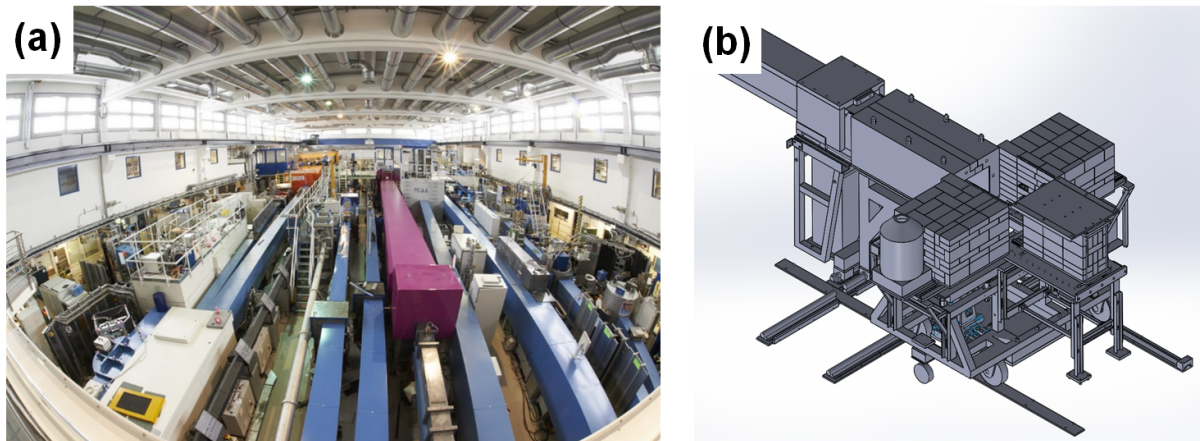


Figure 3.2: (a) Photograph of the NL4b neutron guide transporting cold neutrons to the PGAA facility. The curvature of the NL4b guide ($r = 390 \text{ m}$) reduces contributions of γ radiation and fast neutrons. Taken from [165] (Courtesy of W. Schürmann (TUM)). (b) Sketch of the PGAA facility. The end of the NL4b neutron guide and the sample position are connected by a lead tunnel, in which an interchangeable neutron collimator and a focusing guide are located. Adapted from [144].

of $E = 1.83 \text{ meV}$ ($\lambda = 6.7 \text{ \AA}$) is obtained at the experimental setup [144]. A concrete shelter surrounds the end of the NL4b guide and the PGAA facility in order to (i) reduce neutron-induced radiation exiting the PGAA facility into the Neutron Guide Hall and (ii) minimize the radiative influence from neighboring instruments on the sensitive germanium detectors used for the PGAA.

The guide enters the concrete shelter as shown in Fig. 3.2 a, b and merges after about 55 cm within the shelter into an 1 m-long lead tunnel connecting the guide with the measurement position [144]. It accommodates a 95-cm-long collimator and a 1079-mm-long elliptical focusing guide extension, both can be interchanged pneumatically [144, 166]. When using the collimator consisting of three $20 \text{ mm} \times 20 \text{ mm}$ boron-carbide apertures, a thermal equivalent neutron flux density of $2 \times 10^9 \text{ cm}^{-2} \text{ s}^{-1}$ is obtained [67, 144]. Using a set of three attenuators, the neutron flux can be reduced to 47 %, 16 %, or 5.9 % of its initial intensity [67, 144]. The attenuators can also be combined to further reduce the flux [144]. The focusing extension, which consists of an elliptically tapered guide, increases the neutron flux density to $5 \times 10^{10} \text{ cm}^{-2} \text{ s}^{-1}$ [67]. An asymmetry of the guide tapering gives rise to two different focal points [166]: The horizontal one is located at a distance of 40 mm from the neutron guide exit, whereas the vertical point is situated at $(130 \pm 5) \text{ mm}$ [166]. The position of the highest flux is located between them: At $(75 \pm 3) \text{ mm}$ behind the neutron guide exit [166]. In each direction beam divergence is increased by the focusing, which are 5.4° and 6.2° for the horizontal and vertical directions, respectively [166]. The beam profiles for both the collimated and focused guide at different distances from the exit of the neutron guide was recorded with and without additional beam collimator using a radiation-sensitive film¹ and they are shown in Fig. App. B.1 a–d. In contrast to the focusing geometry resulting in a large divergence, the beam profile shows a low divergence for the collimated geometry. Here, also additional profile maxima evolve at greater distances, which might arise from a combination of inhomogeneities of the supermirror and the curvature of the neutron guide itself [166].

At the end of the tunnel, a combination of boron-containing plastic and lead shielding reduce the background from neutrons and γ radiation produced in the collimation system. The beam opening is $2 \text{ cm} \times 1 \text{ cm}$ and the beam area can be further reduced using a borated collimator. Perpendicular to the neutron path, two high-purity germanium detectors are facing the sample position for the detection of neutron-capture induced γ radiation. Their signals are processed using a NIM-based read-out chain and a digital spectrometer² [144]. Currently three different experimental setups share the neutron beam at the NL4b target point: PGAA, Prompt Gamma-ray Activation Imaging and Neutron Tomography (PGAI-NT), and N4DP. After exiting the measurement chamber, neutrons are absorbed by the beam stop, which consists of boron-carbide plates and lead bricks [144].

¹Gafchromic Film, RTQA2-1010

²DSPEC-50 digital spectrometer, ORTEC

3.1.3 The N4DP Experimental Setup

N4DP experimental setup at the PGAA facility

A top-view scheme of the N4DP (Neutrons **f**or **D**epth **P**rofilin**g**) chamber is shown in Fig. 3.3 a. In this thesis, this arrangement is referred to as “Setup I”. A CAD model of the 48-cm-tall chamber is displayed in Fig. 3.3 b. It consists of two stainless-steel pipes (inner diameter of 35 cm) and an octagonal aluminum section at the height of the neutron guide. Since neutron-capture and -scattering reactions on structural materials may massively contribute to background, material amounts should be reduced close to the neutron beam and the distance of the neutron beam to the walls should be maximized. As indicated in Fig. 3.3 a, the chamber fills the free volume inside the lead shielding completely. In the octagonal centerpiece several CF100 and CF63 flanges are attached. The flanges on the front and backside are equipped with 100- μm -thick aluminum vacuum windows of ≈ 40 mm diameter attached with a special adhesive interface³ acting as entry and exit windows for the neutron beam. Two flanges perpendicular to the neutron beam serve as windows for γ detection using the PGAA detectors. The remaining four larger flanges act as multi-purpose interfaces for electronics, e.g. cabling feed-throughs for the slow control or connections to sample environments requested by the users, mainly given by electric device connections (operating batteries or other electronic samples), temperature tracking, and temperature control. The opening on top of the chamber has two KF40 connections currently used for atmospheric changes, pressure control and pumping. Two feed-throughs on the top enable

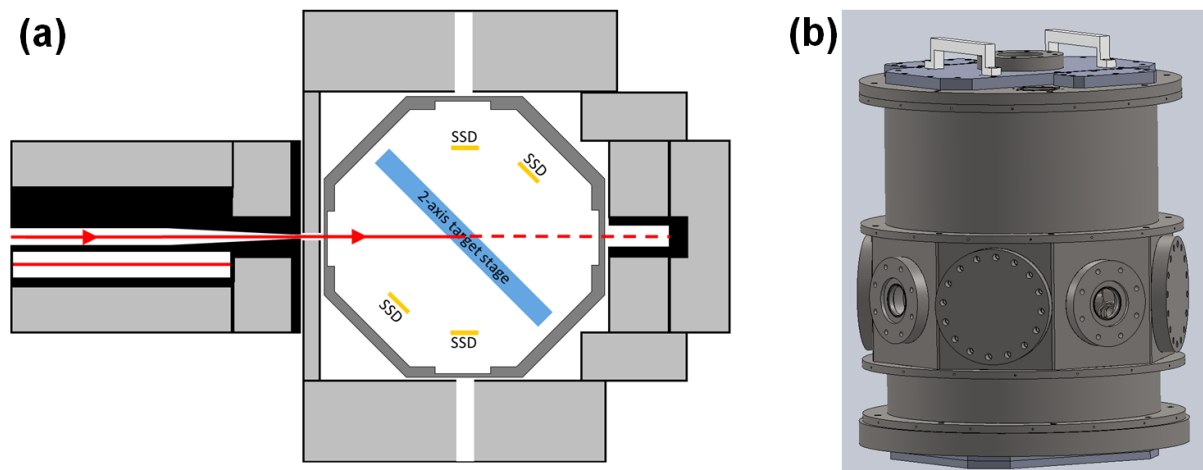


Figure 3.3: (a) Top-view scheme of the N4DP experiment mounted in the center of the PGAA facility⁴ [119]. (b) CAD model of the N4DP measurement chamber. Its center consists of an octagonal aluminum part aligned at the height of the neutron beam.

³2 K Epoxy UHU Endfest

⁴Reprinted from “The new neutron depth profiling instrument N4DP at the Heinz Maier-Leibnitz Zentrum”, L. Werner *et al.*, Nuclear Instruments and Methods in Physics Research Section A, 2018, 911, 30–36, with permission from Elsevier, license no. 4915850880785.

the positioning of the preamplifier and the electric connection to the charged-particle detectors directly on the chamber acting as a Faraday cage. A large 30 cm×15 cm opening on the top also enables a fast and convenient sample change. This opening is closed via an aluminum lid containing a glass window allowing for visual inspection of the targets during evacuation.

Neutron Beam

After leaving the NL4b guide (c.f. Fig. 3.3a), the neutron beam enters the chamber through a 100- μ m-thick aluminum window. A combination of a \approx 5-mm-thick boron-containing rubber and an additional 25-mm-thick lead shielding in front of the chamber reduces neutron and γ radiation emanating from the neutron guide. In the chamber, the neutron beam hits the sample placed at a distance of \approx 26 cm from the exit of the neutron guide mounted on a 2-axis target stage. When using the elliptical guide extension, this sample position is currently behind the position of the highest flux density (7.5 cm) and the vertical focal point (13.0 cm), as discussed in Sec. 3.1.2. A focusing guide optimized for the N4DP geometry is under development. Instead of the divergent beam profile caused by the focusing, as discussed in Sec. 3.1.2, only the highly collimated neutron beam was used for the experiments performed in the framework of this thesis. An additional collimator with a circular bore hole of 4 mm was used as an insert to the lead shielding in front of the chamber to ensure the beam size to be smaller than the sample area, which is typically not smaller than 10 mm×10 mm. Keeping the NDP-active area constant and smaller than the individual sample sizes allows for a direct and precise quantification, since uncertainties arising from the individual sample geometry do not contribute. In Fig. 3.4a, a

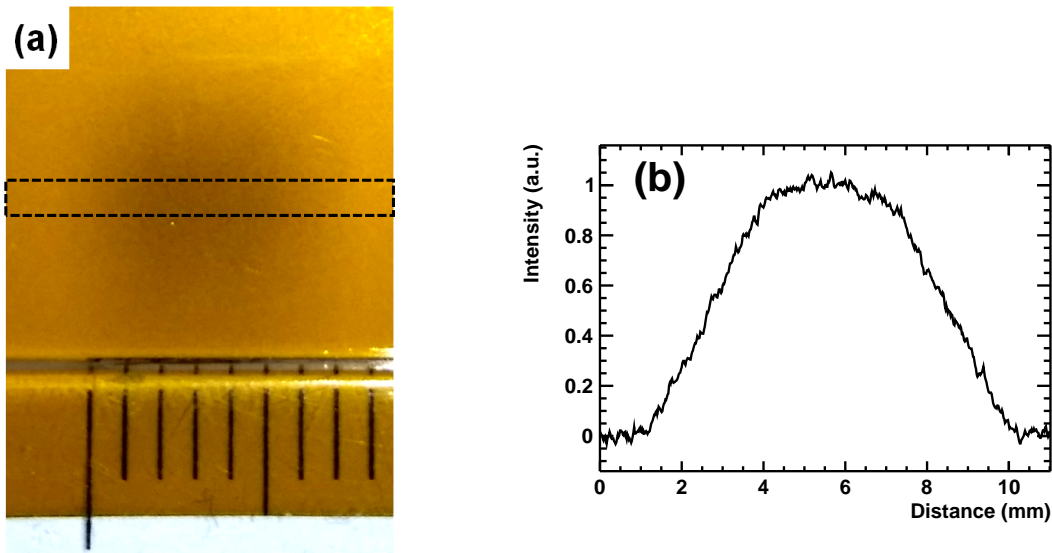


Figure 3.4: (a) Photograph of the collimated neutron beam at the sample position using a radiation-sensitive film with a 1 mm-thick scale for comparison. The beam area is reduced using a boron-containing collimator with a hole of 4 mm diameter. (b) Horizontal beam profile optically measured by the gray scale in the photograph from a horizontal cut (marked as dashed lines). A homogeneous beam profile is observed in the center and it linearly decreases on the edges.

photograph of the beam spot size at sample position is shown, which was recorded using a radiation-sensitive film⁵. In Fig. 3.4 b, the gray scale in the horizontal cut shown in Fig. 3.4 a is used as optical measure of the neutron beam intensity. It shows a rather homogeneous beam profile at the sample position with smeared edges, while most of the intensity is within 4 mm.

Sample positioning

Especially for position sensitive NDP, an accurate and reproducible sample positioning is necessary. Here, a combination of two linear stepper motors⁶ with digital encoder system was chosen as a 2-axis target drive, as presented in the CAD-model of the bottom lid of the chamber shown in Fig. 3.5 a [167]. As indicated in Fig. 3.5 a, this stage can be mounted at distinct angles of 15° , 45° and 75° with respect to the neutron beam axis to vary the footprint of the beam area on the sample and optimize the detector position. In this work it was kept at 45° resulting in a relatively small beam area allowing for accurate illumination of the neutron beam on the sample while the detector, which was placed parallel to the sample surface, had a sufficient distance to the incoming neutron beam thus reducing background signal.

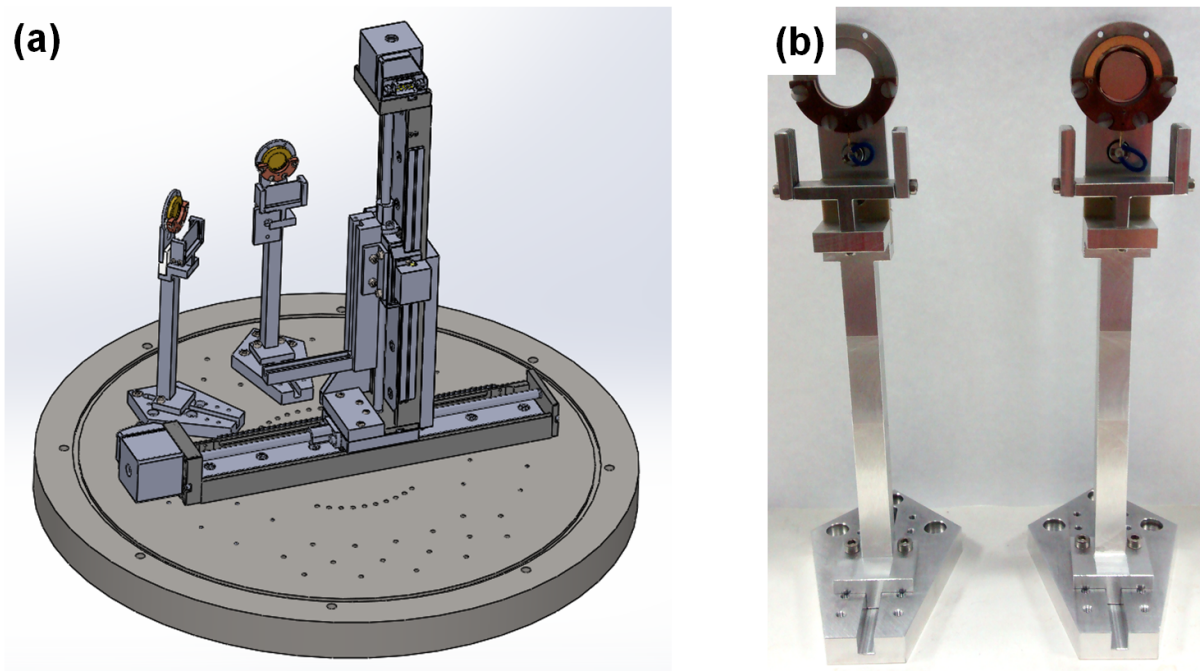


Figure 3.5: (a) CAD model of the inner part of the N4DP chamber. A 2-axis target stage is mounted together with charged-particle detectors on the ground of the measurement chamber. (b) Photograph of the custom-made detector holders. On the right side a charged-particle detector is mounted. The holder in front of the detector can be used to place an aperture or a charged-particle separation foil in front of the detector.

⁵Gafchromic Film, RTQA2-1010

⁶VT-50L, Micronix USA, 200 mm travel range, 50 N max. load capacity, 50 nm resolution, $\pm 3 \mu\text{m}$ accuracy

Furthermore, the sample holder needs to be modular to meet the needs of the individual materials science application. A sample holder mounting system was designed similar to that of a sliding caliper to allow for quick and accurate positioning of the individual sample holder. The three typical sample holders used in the framework of this thesis are shown in Fig. 3.6. Sample holders for (a) up to 30 fragile samples, (b) up to 36 stable samples and (c) simultaneous operation of 4 coin-cell batteries (mounted together with 5 static samples) are shown. Static samples are clamped using 0.60-mm-thick elastic nylon threads⁷. For *operando* (dis-)charging lithium-ion batteries a commercial portable potentiostat⁸ was connected via electric vacuum feed-throughs.

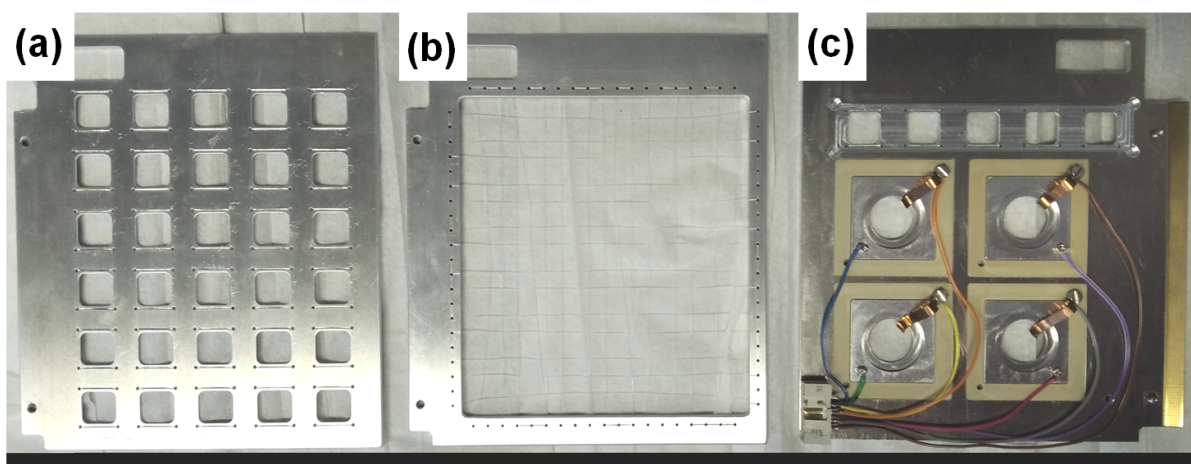


Figure 3.6: N4DP sample holders for various applications: (a) a standard sample holder for 30 static samples. The aluminum frame provides a good stability especially for thin and fragile samples. (b) Up to 36 mechanically stable samples could be mounted by a grid of strings, which reduces the background compared to the massive aluminum holder. (c) A sample holder for *operando* measuring coin-cell shaped lithium-ion batteries. Up to four lithium-ion batteries could be mounted and individually connected. On the top up to five reference samples can be placed.

Gas Environment

For experiments using solid samples, the chamber was typically evacuated to 10^{-5} mbar in order to minimize additional energy loss of the detected charged particles on their way from the sample to the detector. At 10^{-5} mbar the energy loss of the charged particles (^3H , α , ^7Li) in the rest gas is estimated to be in the sub-eV range [168]. This is negligible compared to both the energy of the charged particles and the detector resolution being in the keV range. An oil-free combination of a roughing pump⁹ and a molecular pump¹⁰ was used in order to avoid the accumulation of thin hydro-carbon layers in the chamber.

⁷Rico Design GmbH, No. 7092.07.81

⁸Bio-Logic, SP-300

⁹ECODRY plus, Leybold

¹⁰Turbovac 350i, Oerlikon Leybold Vacuum

When measuring liquid-electrolyte-based lithium-ion batteries, a typically small outer gas pressure is necessary to prevent the liquid electrolyte within the cell from vaporization. A constant gas pressure in the N4DP chamber was chosen to be above the vapor pressure of $p_{\text{vap}} < 100$ mbar at 25° C of typically used liquid electrolyte components like ethylene carbonate (EC), dimethyl carbonate (DMC), and ethylmethyl carbonate (EMC) [169]. When measuring a liquid-electrolyte-based lithium-ion battery, the air in the chamber was replaced with a helium atmosphere in order to (i) avoid signals induced by neutron capture of nitrogen (c.f. table 2.2) and to (ii) minimize the energy loss of the charged particles. Due to the lower stopping power the energy loss in helium is about ≈ 6 -times smaller compared to that in air in the energy range of particles of interest for NDP. In order to exchange the atmosphere after the battery was placed inside the chamber, it was flushed ten times from 900 mbar to 300 mbar before the final helium pressure was set (typically in the range between 150 mbar and 900 mbar). Using this flushing method a helium atmosphere with air impurities $< 10^{-4}$ could be established within the chamber.

Already a 150 mbar helium atmosphere stops all charged particles with an atomic number of $Z > 3$ produced by neutron-capture reactions (c.f. table 2.2) [168]. However, α and ^3H particles from the $^6\text{Li}(n,\alpha)^3\text{H}$ reaction and the ^7Li from the $^{10}\text{B}(n,\alpha)^7\text{Li}$ reaction respectively lose ≈ 0.5 MeV, ≈ 0.1 MeV and ≈ 0.7 MeV of its production energy before reaching the detector [168]. Furthermore, thin foils were used to avoid leakage of the liquid electrolyte. As discussed in Chap. 5, a nominally 7.5- μm -thick Kapton[®] foil was used, in which α and ^3H charged particles lose about 2 MeV and 301 keV, respectively [168, 170]. The use of this foil (so-called “separation foil”) alone is sufficient to block the α particles with production energies of 2055.55 keV (c.f. Tab. 2.2) and therefore only the ^3H particles are used for these measurements.

Detectors

For the detection of the charged particles, silicon surface-barrier detectors¹¹ (SSD) were used. A thin (manufacturer specification: 80 nm silicon equivalent) entry window minimizes the charged-particle energy loss and energy straggling when entering the detector. Conceptually the detector thickness has to be optimized for three different parameters. For the energy measurement the detector has to be thick enough to stop all particles of interest. A thicker detector would provide a lower capacity reducing the electric noise signal that can be achieved. However, thicker detectors would also increase the active volume and therefore increase the background from γ interactions and the average energy deposit from β particles. We have chosen a (totally depleted) thickness of 100 μm , which is thick enough to stop light particles with energies of up to $E(\text{p}) \approx 3.2$ MeV, $E(^3\text{H}) \approx 4.8$ MeV, $E(\alpha) \approx 13$ MeV and $E(^7\text{Li}) \approx 25$ MeV [168]. This is sufficient for the detection of charged particles of interest, which carry production energies of $E(\text{p}) \approx 0.6$ MeV, $E(^3\text{H}) \approx 2.7$ MeV, $E(\alpha) \approx 3.1$ MeV and $E(^7\text{Li}) \approx 1$ MeV (c.f. Tab. 2.2). Since

¹¹ORTEC AMETEC, Model no. AD-025-150-100, with an active area of 150 mm²

the particles produced upon neutron capture (c.f. Tab. 2.2) are completely stopped within the detector, the intrinsic detector efficiency is close to unity, independent of the particle energy [171]. Furthermore, a rather large active area of 150 mm^2 was chosen. A large active area increases the detector capacity thus worsening the electronic noise but allows due to its larger geometrical acceptance for measuring even small nuclide amounts in the sample.

As shown in Fig. 3.5 a and b, the SSDs were mounted in custom-made holders which could be placed at angles between 0° and 90° with 15° intervals with respect to the neutron beam both in front and back of the target stage. If not stated otherwise, the detector used was placed at 45° to the neutron beam, i.e. parallel to the target stage surface. As shown in the photograph in Fig. 3.5 b, a sliding grid in front of the detector allows for the positioning of different separation foils or pinhole apertures in front of the detector. In this work, a nominal $7.5\text{-}\mu\text{m}$ -thick Kapton[®] foil was positioned for some measurements on it. The detectors are positioned on custom-made bottom pieces, which allow not only the angular adjustment but also an adjustment of the sample-to-detector distance (SDD). Here, SDDs between 87.1 mm and 141.1 mm in 9 mm intervals could be selected. Typically, the detector was placed at a distance of 96.1 mm from the sample holder. From this experimental arrangement an upper limit of the geometrical acceptance angle of the charged particles can be estimated. Assuming a maximum diameter ($d = 5.66\text{ mm}$) of the illuminated sample area, $\text{SDD} = 96.1\text{ mm}$ and the detector active diameter $D = 13.8\text{ mm}$, the maximum acceptance for the straight particle travel path can be estimated to $\approx 5.8^\circ$. This angle results in a maximum elongation of $\approx 0.5\%$ compared to the particle path length perpendicular to the sample surface, which is small compared to the signal broadenings caused by the statistical energy losses observed in Chap. 6–8 and so a straight particle travel path can reasonably be assumed.

Data Acquisition

Energies of charged particles are measured using conventional VME (Versa Module Europa bus) and NIM (Nuclear Instrumentation Module standard) based modular crate electronics and data-acquisition system. A NIM-based high-voltage (HV) supply¹² was used to operate the detectors at 130 V . The detector signal is subsequently amplified using a charge-sensitive preamplifier module¹³ and a shaping amplifier¹⁴ with a shaping time of $1\text{ }\mu\text{s}$. The analog signal was then forwarded to a peak-sensing VME analog-to-digital converter (ADC)¹⁵. An event-based data acquisition was performed using the MARaBOU software [172], which is based on the data analysis framework ROOT [173] and MBS [174]. In order to avoid pile-up, the event rate was kept below 1000 s^{-1} by attenuating of the neutron flux, as discussed in Sec. 3.1.2.

¹²MHV-4, Mesytec

¹³WA1422H090F2, CAEN

¹⁴MSCF-16, Mesytec

¹⁵V785, CAEN

3.2 Additional NDP Setups

In this section, two other NDP setups used for some measurements discussed in the following chapters are presented: first, the N4DP demonstrator experiment is shown, which was used at the PGAA facility before the upgrade to the N4DP setup discussed in the previous section. Due to a reactor brake of the FRM II, some NDP measurements discussed in this work were carried out at the cold neutron depth profiling instrument at the NIST Center of Neutron Research using their setup, which is described in the later section.

3.2.1 The N4DP Demonstrator Setup

In the frame of this work, a vacuum chamber donated from R. G. Downing from the National Institute of Standards and Technology (NIST) was installed at the PGAA facility of the MLZ and used as demonstrator experiment (Setup II). This chamber allowed to measure and gain experience on NDP on a very early stage of the N4DP project and had major influence on the later N4DP chamber design (Setup I). Its top-view is schematically shown in Fig. 3.7 [118]. It is a cylindrical chamber with an inner diameter of 21.4 cm. The neutron beam enters and exits the chamber through 100- μm -thick aluminum windows. Additional boron-containing tube collimators inside the chamber reduce the geometrical angle of neutron scattering from the windows to the charged-particle detectors. A 300- μm -thick surface barrier detector¹⁶ was installed at a SDD of 53 mm on a rotatable holder. As shown in the photograph in Fig. 3.8 a, two stages on mechanically-driven planetary gears mounted on the lid of the chamber allowed for manual angular adjustment for up to two detectors. In the center of the lid a sample holder was located,

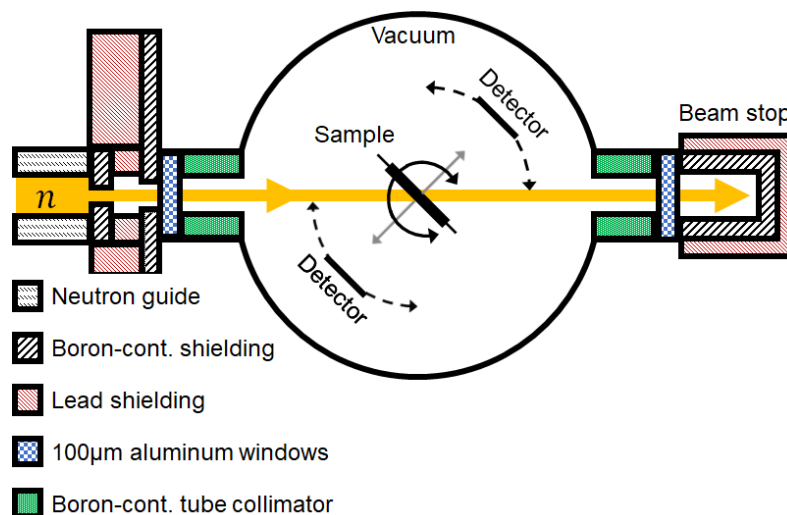


Figure 3.7: Top-view scheme of the NDP demonstrator setup installed at the PGAA facility, as published in [118]. The neutron beam hits the sample at an angle adjustable by a mechanic feed-through. Both detectors are at a fixed SDD of 53 mm and can be individually rotated around the sample position.

¹⁶Model Nr. BE-19-450-300, Ortec

where up to four different samples could be mounted (c.f. Fig. 3.8 b). The sample holder could be rotated and vertically moved using a manual vacuum feed-through. During this work, the sample holder was fixed at an angle of 45° with respect to the neutron beam with the detectors parallel to the sample surface, if not stated otherwise.

On the lid of the chamber a KF flange allowed the connection of the vacuum system consisting of a roughing and a molecular pump. In the demonstrating experiment, a vacuum of only 10^{-3} mbar was achieved. This can be attributed to leakage in the vacuum-sealing of the mechanical feed-throughs of the detectors and the sample holder which could not be repaired. In comparison to the later N4DP setup (Setup I), the worse vacuum induces energy losses of less than 10 eV for both ^3H and α particles produced in the $^6\text{Li}(n,\alpha)^3\text{H}$ reaction. However, this is again negligible compared to the particle energy as well as the detector resolution (keV range). Energies of charged particles were recorded using the VME-/NIM-based electronics and data acquisition system, as discussed in Sec. 3.1.3 with some minor differences: The signals from the detectors were amplified using a MMPR1 preamplifier¹⁷ and shaped with a STM 16+ shaping amplifier¹⁸.

The N4DP demonstrator setup was used for testing, defining specifications, and optimization of the later N4DP setup (Setup I). In the demonstrator experiment, detectors, sample stage and pumping equipment were connected to the chamber lid, which had to be moved and opened after measuring every four samples. This can be harmful for the electric connection of the detectors,

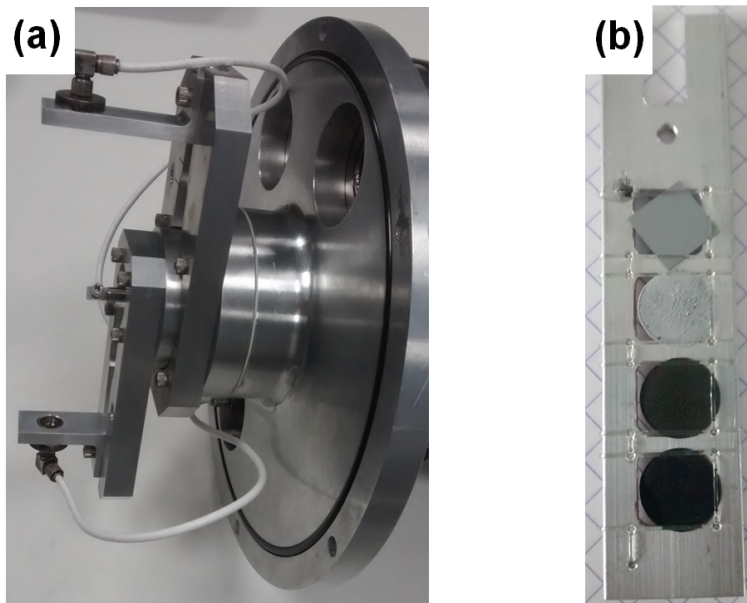


Figure 3.8: (a) Photograph of the chamber lid used in the N4DP demonstration experiment. Charged-particle detectors can be mounted on two stages connected to the planetary gears. The sample stage can be mounted on a rotatable stage in the center. (b) Photograph of the sample stage. Up to four samples could be mounted simultaneously.

¹⁷MMPR1, Mesytec

¹⁸STM 16+, Mesytec

which was sensitive for mechanic changes. In the later design (Setup I), the lid, target stage and detectors are mechanically separated and all electric connections are fixed. The chamber diameter is increased from 21.4 cm to 35 cm to keep the detectors outside of the halo of the neutron beam and provide more flexibility on the SDD. The originally 300- μm -thick particle detectors were replaced by 100- μm -thick ones in transmission geometry. This significantly reduced the low-energy background caused by energy deposition of β and γ radiation passing through the active volume of the detector. As shown, the dimension of the target stage was increased and up to 36 samples can now be measured before sample change, which reduces evacuation times and increases the duty cycle of efficient use of the beam.

3.2.2 The Cold Neutron Depth Profiling Instrument at the NCNR

The neutron-beam split core reactor (NBSCR) is operated by the National Institute of Standards and Technology (NIST) Center for Neutron Research (NCNR) situated at the NIST site in Gaithersburg, Maryland, USA. It became first critical in 1967 and was operated at 10 MW until 1985 and at 20 MW since then, which gives rise to a peak flux of $3.5 \times 10^{14} \text{ cm}^{-2} \text{ s}^{-1}$ [175, 176]. It contains 30 highly enriched fuel elements interchanged in cycles of 38 days [176]. In 2019 the reactor operated for 212 days with a duty factor greater than 98 % [177]. The NBSCR provides thermal and cold neutrons using graphite and D_2O moderators and D_2O and liquid hydrogen cold sources [176]. The NCNR offers 30 experimental stations, where a major part, i.e. 18, are beam facilities used for neutron scattering research [177].

Based of a beamtime proposal within the NCNR user program, several NDP measurements were performed in 2019 at the cold neutron depth profiling (CNDP) instrument of NCNR in the frame of this work. At the CNDP instrument, NDP measurements are performed on various applications, like boron implantation profiles in silicon, lithium distributions in shielding glasses and in lithium-ion batteries [178–180]. The CNDP setup (Setup III) is situated at the end of the Neutron Guide-5 (NG-5), where a cold neutron beam ($\approx 4 \text{ meV}$) with a thermal equivalent neutron flux density of $1.22 \times 10^9 \text{ cm}^{-2} \text{ s}^{-1}$ is achieved using a combination of a cryogenic-cooled hydrogen moderator and Be-Bi crystal filters [68, 177, 181].

NDP measurements were performed in a stainless-steel vacuum chamber with a diameter of 61 cm [182]. A photograph showing the view inside the measurement chamber is shown in Fig. 3.9 a. The neutron beam enters the vacuum chamber on the right through a 100- μm -thick, hardened aluminum window. Due to a spin-polarized triple axis spectrometer (SPINS) located upstream, the neutron spectrum might vary on a percentage level. Therefore, the neutron flux is monitored using a combination of a boron-containing sample and a charged-particle detector directly behind the entry window [65]. The beam then illuminates the sample placed in the center of the chamber at an angle of 45° (c.f. Fig. 3.9 a). Charged particles emanating from the samples are detected using a silicon surface-barrier detector¹⁹ at a sample-to-detector distance (SDD) of $\approx 22 \text{ cm}$ parallel to the sample surface.

¹⁹ORTEC AMETEC, Model no. AB-018-150-150, active area 150 mm^2

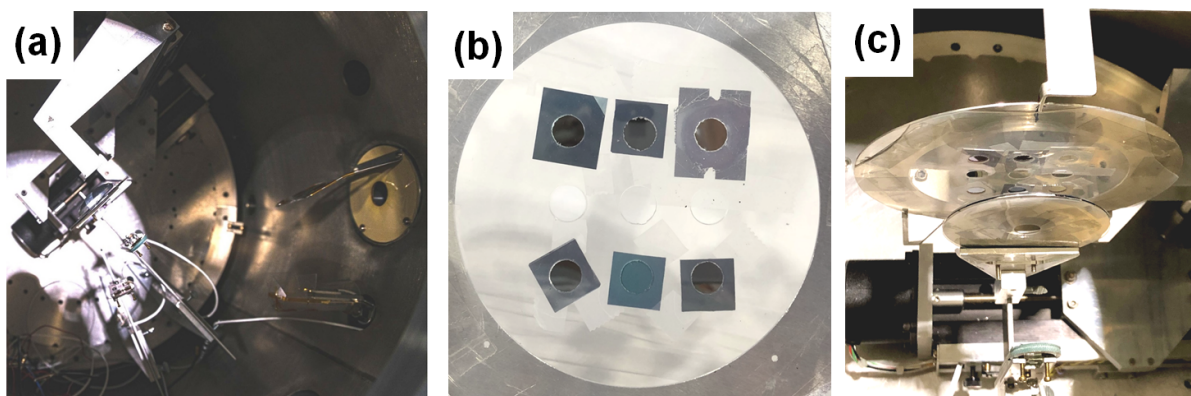


Figure 3.9: (a) Photograph from the top of the inside of the CNDP target chamber at the NCNR. The neutron beam enters the vacuum chamber through an entry window on the right-hand side and is monitored using a boron-containing sample and a SSD. In the center of the chamber, a sample holder is positioned. (b) Photograph of the plastic sample holder, where up to 9 different samples could be taped behind custom-made holes to define the area from where charged particles can emanate. (c) An aperture between sample holder and detector prevents charged-particle signals from samples other than the investigated sample. All photographs were recorded at the NIST Center for Neutron Research²⁰ and are courtesy of Philip Rapp (TUM).

The design of the gauge volume, i.e. the volume defined by the overlap of neutron beam, sample volume and charged-particle pathway towards the detectors, is conceptionally different from the previously discussed N4DP setups (Setup I and II), where the neutron beam area was reduced using a collimator before entering the measurement chamber. At CNDP, the neutron beam size was not reduced before entering the measurement chamber and thus it illuminates a major part of the sample holder with diameter of 12 cm shown in Fig. 3.9 b. Here, the area from where charged particles can emanate towards the detector, was restricted by using a plastic sample holder, which is impermeable for the charged particles, containing custom-made holes (diameters of 8–11 mm). As shown in Fig. 3.9 b, up to 9 different samples could be taped behind the holes, which can be moved in the neutron beam using a 2-axis stage motor. As shown in Fig. 3.9 c an additional aperture was placed between sample and detector to avoid charged particle signals from neighboring samples also illuminated by the large neutron beam.

In terms of signal-to-background the beam collimation with subsequent secondary radiation suppression outside of the chamber (Setup I and II) seems favorable: Guiding the full beam cross section inside the NDP chamber causes additional neutron activation and scattering, which increases background signals. However, the design at CNDP is highly flexible and can be adjusted to various sample sizes by a simple exchange of the plastic sample holder and the aperture. Since the neutron beam is larger than the holes, the hole areas define the area from where charged particles can emanate towards the detector. Since their diameters are varying, the NDP-active areas were individually calibrated using a reference sample behind each hole. This increased

²⁰We acknowledge the support of the National Institute of Standards and Technology, U.S. Department of Commerce, NIST Center for Neutron Research and Material Measurement Laboratory in providing the neutron research facilities used in this work.

the systematic uncertainties by about 2.2% compared to the measurements performed with a reduced beam area (Setup I and II), where the illuminated area from where charged particles can emanate to the detector, i.e. the surface projection of the gauge volume, was constant for all samples.

Data Analysis of Neutron Depth Profiling

CHAPTER 4

As discussed in Chap. 2, the detected count rate scales with the nuclide concentration in the sample while the spectral shape reveals its depth distribution by measuring residual particle energies. Therefore, a qualitative interpretation of the concentration profiles can often be derived from the measured energy spectra. For a quantitative interpretation, absolute energy and quantity calibrations are necessary. Reference samples emitting particles with well-defined energies are used for the energy calibration. The count rate scales with the reaction rate in the sample (or even the activity for α sources) by the detection efficiency and is determined using a reference standard with well-known nuclide content. Both calibrations are presented in this chapter. Concentration profiles can then be obtained taking into account the non-linear energy loss. In order to compare the measured spectra with a modeled nuclide concentration, a forward mapping method is presented.

4.1 Calibration

NDP spectra are measured in digitized channels, apriori being arbitrarily chosen, from the analog-to-digital converter (ADC). An energy calibration is needed to convert the ADC channels to an absolute energy scale. Furthermore, the count rate is normalized to an absolute quantity using a reference sample.

4.1.1 Energy Calibration

When converting ADC channels to an absolute energy scale, charged particles with well-defined energies are used. In order to generate the production energies of the particles listed in Tab. 2.2, thin surface layers of these elements are placed in the neutron beam. This minimizes the particle energy loss in the sample. Since the reaction rate scales with the film thickness, nuclides undergoing (n,p) or (n, α) reactions with a high thermal capture cross section are required. As listed in Tab.2.2, ^3H (5316 b), ^{10}B (3842 b) and ^6Li (938 b) are the stable nuclides exhibiting by far the highest partial thermal capture cross sections branch for particle decay. Thin surface

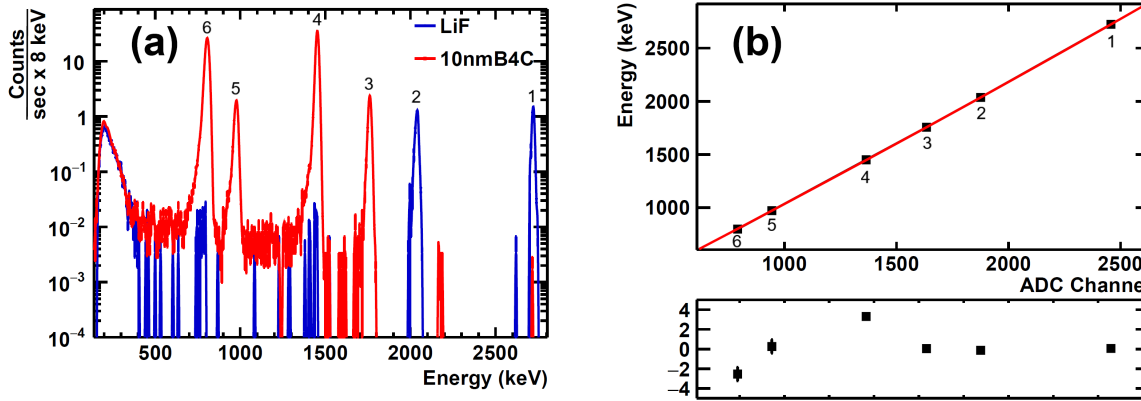


Figure 4.1: (a) Spectra of thin surface layers containing lithium (${}^6\text{LiF}$, blue line) and boron (${}^{10}\text{B}_4\text{C}$, red line). The spectra show well-defined peaks in the range of 0.8 MeV to 2.7 MeV. (b) An absolute energy scale is obtained by describing the six reference signals using a quadratic fit. The residuum below shows that the fit function describes the signals well within ± 2 keV.

layers containing enriched ${}^{10}\text{B}$ and ${}^6\text{Li}$ were used as reference samples for energy calibration: A nominally 10-nm-thick ${}^{10}\text{B}_4\text{C}$ film sputtered on a silicon substrate and a $\approx 6\text{-}\mu\text{g}/\text{cm}^2$ -thick (≈ 23 nm) ${}^6\text{LiF}$ deposited on a 2- μm -thick Mylar[®] foil provide particles over a wide energy range. As shown in Fig. 4.1 a, neutron capture in these two samples gives rise to six reference signals at well-defined energies between 0.8 MeV and 2.7 MeV originating from the ${}^{10}\text{B}(n,\alpha){}^7\text{Li}^*$ (red line) and ${}^6\text{Li}(n,\alpha){}^3\text{H}$ (blue line) reactions. At low energies (< 500 keV) background originating from β and γ radiation induced by neutron capture in the experimental setup and the sample is observed, which rises exponentially towards lower energies [119]. A trigger threshold at ≈ 200 keV limits the total rate for the data acquisition. As shown in Fig. 4.1 b, the positions of the six energy peaks in the ADC spectrum are then determined and plotted against the absolute energies expected for each signal while taking into account the energy loss caused by the so-called detector “dead layer” (typ. equivalent to 80 nm silicon). It refers for a surface layer on top of the signal producing volume in the detector, where charged particles undergo an energy loss before entering the active detector volume. Although an almost linear relation is found, we account for possible remaining non-linearities by including a second order polynomial. The minor non-linearity ($\approx 10^{-5}$) is probably induced by the pulse-height defect (PHD), which describes the detector response depending on the particle type [119, 183–185].

4.1.2 Normalization of Concentrations

While the measured particle energies correlate to the depth where the nuclides are situated in the sample, the measured signal rate reveals the nuclide concentration at a certain depth. When a th. eq. neutron flux Φ illuminates the sample, the signal rate R of charged particles is $R = n \cdot \Phi \cdot \sigma \cdot \varepsilon$, similar to Eq. (2.4). Here, $n = \rho_{\text{nuclide}} \cdot \Delta d_{\text{tot}} \cdot A$ is the total number of nuclides, ρ_{nuclide} is the concentration of nuclides, d_{tot} is the total implantation thickness from where the

charged particles can emanate, A describes the illuminated sample area and σ is the thermal neutron capture cross section of the nuclides (c.f. Tab. 2.2). Therefore, the signal rate can be rewritten as

$$R = \rho_{\text{nuclide}} \cdot d_{\text{tot}} \cdot \sigma \cdot A \cdot \Phi \cdot \varepsilon \quad . \quad (4.1)$$

Here, a precise knowledge about the illuminated area, the absolute neutron flux and the detector efficiency dominated by the detector efficiency is necessary. While the illuminated area is $A \approx 12.56 \text{ mm}^2$ (circle with a diameter of 4 mm), $\Phi \approx 2 \times 10^9 \text{ cm}^{-2} \text{ s}^{-1}$, the detector efficiency mainly given by the geometrical acceptance is $\varepsilon \approx 10^{-3}$ while taking into account the active detector area (150 mm^2) and the SDD (96.1 mm). In contrast to detectors for γ radiation, where the intrinsic detector efficiency is dependent on the energy of the γ , the intrinsic efficiency of charged-particle detectors can be assumed to be close to unity and independent of the charged particle energy, since their thickness is sufficient to stop charged particles at even higher energies than typically emitted using NDP (c.f. Sec. 3.1.3). A variation of the SDD changes the solid angle covered by the detector area and thus the measured signal intensity. For sample holders where the top surface of the sample is at fixed position (c.f. Sec. 3.1.3), the SDD to the front detector is constant. However, when the backside of a sample (massive sample holder) or its center (string holder) is fixed, the SDD changes with the sample thickness. From this, correction factors $\Delta(d)$ for the measured signal rates can be derived: $\Delta(d) = \frac{(r(d))^2}{(r_0)^2}$, assuming a point-like source [118]. Here, r_0 is the original distance and $r(d)$ the SDD altered by the sample thickness d . This correction is non-negligible: Using the massive sample holder in the N4DP experiment (Setup I) the SDD is 96.1 mm and therefore the correction factor is $\Delta(1 \text{ mm}) \approx 2\%$ [118].

The major systematic uncertainties for the determination of the absolute nuclide concentration ρ_{nuclide} from the signal rate R originate from $A \cdot \Phi \cdot \varepsilon$. Since the neutron flux at the NL4b at the FRMII is extremely stable and the experiment geometry is kept constant during the whole beamtime, the measured signal rates are compared to that of a reference standard with a known quantity and normalized to it [119]. This method results in a high quantitative accuracy of the NDP technique mainly limited by the uncertainty of the standard itself, which needs to be added as a systematic uncertainty to all our results. Here, the SRM2137 NIST standard is used as a reference sample, which consists of a single-crystal silicon substrate with a disordered Si implantation avoiding channeling effects for the subsequent ^{10}B implantation [186]. The ^{10}B implantation profile is shown in Fig. 4.2 a. It exhibits a concentration maximum at a depth of $d = 188 \text{ nm}$ and contains $(1.018 \pm 0.035) \times 10^{15} \text{ }^{10}\text{B}/\text{cm}^2$ in total [186]. As shown in Fig. 4.2 a, the boron implantation is completely contained within the first $0.4 \text{ }\mu\text{m}$. The maximum penetration depth of ^7Li and α nuclei in silicon is $2.4 \text{ }\mu\text{m}$ and $5.2 \text{ }\mu\text{m}$, respectively, and thus, particles from the whole implantation profile can be detected using NDP [168].

Based on Eq. (4.1), taking into account the total of $n = (1.28 \pm 0.04) \times 10^{14} \text{ }^{10}\text{B}$ atoms in the vicinity of the illuminated area, the thermal capture cross-section of $\sigma_{^{10}\text{B}} = 3.8 \text{ kb}$ and neutron flux and geometrical acceptance as previously discussed, the signal rate R is estimated to $R \approx 1.26 \text{ s}^{-1}$. Since this result strongly depends on the exact measurement setup, it can only be used as a rough estimation and is compared to the measured signal rate in the following.

The energy spectrum from the SRM2137 sample is shown in Fig. 4.2 b, where four signals stemming from both $^{10}\text{B}(n,\alpha)^7\text{Li}^{(*)}$ reactions are observed. The peak areas are proportional to the total amount of ^{10}B . Due to increasing background at low energies, only the two α signals were integrated, resulting in a signal rate of $(1.136 \pm 0.012) \text{ s}^{-1}$. This value agrees with the geometrical estimation within 10 %, but is only limited by counting statistics. The scaling factor S relating the signal rate R to the total ^{10}B content via $\rho_{\text{nuclide}} \cdot d_{\text{tot}} = S \cdot R$ is determined to $S_{10\text{B}} = (8.96 \pm 0.32) \times 10^{14} \text{ cm}^{-2} \text{ s}^{-1}$, where the systematic uncertainty of the reference standard contributes to the uncertainty of the signal rate. The scaling factor determined using signal integration strongly depends on the exact experimental setup, i.e. $A \cdot \Phi \cdot \varepsilon$ given by the illuminated sample area, the neutron beam flux and the geometrical detector efficiency and needs to be calibrated for each beamtime again.

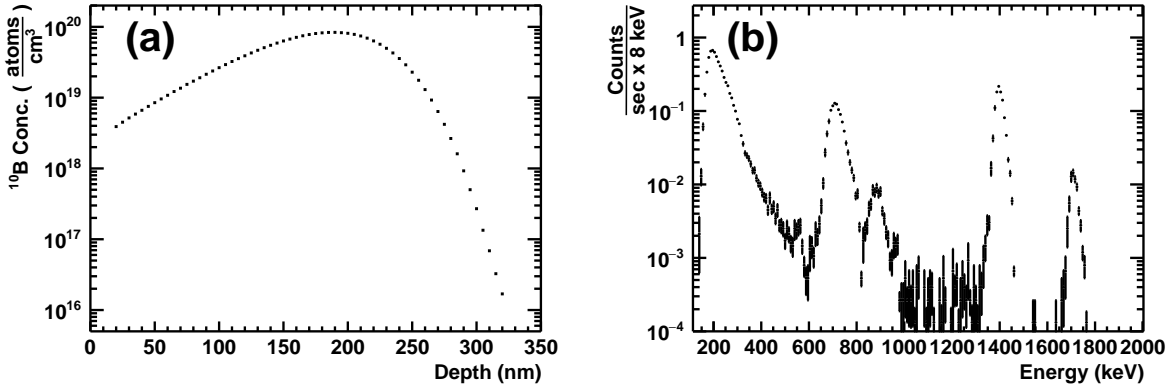


Figure 4.2: (a) ^{10}B depth profile in the SRM2137 standard reference material [186]. (b) Measurement of the SRM2137 NIST standard. Apart from the low-energetic background, four charged particle signals from the two branches of the $^{10}\text{B}(n,\alpha)^7\text{Li}^{(*)}$ reactions resemble the ^{10}B depth distribution. Due to its high penetration, the resulting γ radiation is not observed using the 100- μm -thick silicon surface barrier detectors.

When determining the distribution of the element boron, the natural abundance of ^{10}B ($\approx 19.9\%$) needs to be taken into account, as NDP is only sensitive to ^{10}B nuclides. When detecting elements Z other than boron, the scaling factor S needs to be corrected for both, the (natural or artificially modified) abundances NA_{AZ} and the thermal neutron capture cross sections σ_{AZ} of the isotope AZ (c.f. Tab. 2.2):

$$S_{\text{nat}Z} = S_{10\text{B}} \cdot \frac{\sigma_{10\text{B}} + \sigma_{10\text{B}^*}}{\sigma_{AZ} \cdot \text{NA}_{AZ}}, \quad (4.2)$$

where $\sigma_{10\text{B}} = 241.31 \text{ b}$ and $\sigma_{10\text{B}^*} = 3600.48 \text{ b}$ are the thermal capture cross sections of the two decay channels of the $^{10}\text{B}(n,\alpha)^7\text{Li}^{(*)}$ reaction, as discussed in Sec. 2.2.2. For example, the scaling factor S for detecting natural lithium is then $S_{\text{natLi}} = S_{10\text{B}} \cdot \frac{\sigma_{10\text{B}} + \sigma_{10\text{B}^*}}{\sigma_{6\text{Li}} \cdot 0.0759}$, where 7.59% is the natural abundance of ^6Li [77]. Taking into account the previously determined $S_{10\text{B}} = (8.96 \pm 0.32) \times 10^{14} \text{ cm}^{-2} \text{ s}^{-1}$, then for natural lithium the scaling factor is $S_{\text{natLi}} = (4.83 \pm 0.17) \times 10^{16} \text{ cm}^{-2} \text{ s}^{-1}$.

4.2 Particle Energy Spectra and Concentration Profiles

After energy calibration and signal rate normalization, the measured residual energy of the particles is correlated to their travel distance before detection, i.e. particle energies close to their production energy (c.f. Tab. 2.2) originate from regions close to the sample surface, while particles with lower energies correlate to larger depths. In order to obtain a concentration distribution from the energy spectra, the stopping powers (c.f. Sec. 2.3) of the sample material and of any layers between it and the detector need to be taken into account. Here, the SRIM¹ software and the WebAtima² tool were used [117, 168]. Both are empirical models based on a large set of experimental data covering the full parameters space of projectile-target combinations and energies. We use a kind of back-tracking algorithm starting at the measured energy in the active volume of the Si detector and calculate then all the particle energy losses induced by the materials between the detector and the sample, i.e. the typically 80 nm Si equivalent dead layer of the detector (c.f. Sec. 3.1.3). Depending on the application, a combination of different layers like a 100-nm-thick copper current collector, a nominally 7.5- μm -thick Kapton[®] foil, as well as a helium atmosphere with different pressures were considered. The whole energy spectrum is treated accordingly, which then reflects the particle energy distribution directly after emanating from the sample surface. In this way, also the spectrum distortion induced by the energy-dependent energy loss of particles passing the different layers is corrected for.

The sample often consists of a compound mixture. For example, anodes for lithium-ion batteries studied in this work consist of a dried mixture of electrochemically-active particles, additives, binder material and solvent. In order to model the stopping power of these mixtures, a mean and homogeneous elemental composition is assumed [118]. The resulting stopping power is then calculated using Bragg's rule of additivity by assuming thin layers of pure elements in the given ratio:

$$\frac{dE}{dm_A} = \sum_j w_j \left. \frac{dE}{dm_A} \right|_j, \quad (4.3)$$

where $w_j = \frac{m_j}{M}$ and $\left. \frac{dE}{dx} \right|_j$ are the mass fraction and stopping power of the j -th element, respectively [108, 111, 187, 188]. In a well-defined sample, i.e. where the bulk density ρ and the individual elemental densities ρ_i are known, the mean stopping power can be calculated based on the volume fractions $v_j = \frac{V_j}{V}$ [62]:

$$\frac{dE}{dx} = \rho \cdot \frac{dE}{dm_A} = \rho \cdot \sum_j \frac{w_j}{\rho_j} \left. \frac{dE}{dx} \right|_j = \frac{M}{V} \cdot \sum_j \frac{m_j}{M} \frac{V_j}{m_j} \left. \frac{dE}{dx} \right|_j = \sum_j v_j \left. \frac{dE}{dx} \right|_j. \quad (4.4)$$

Typically, Bragg's rule of additivity describes the stopping power reasonably well with a deviation below 20 % [188–190]. The largest deviations ($\approx 20\%$), occurring at low particle energies in several pure compounds containing mainly light elements, could be reduced to an average of 1.1 %, if core and bound corrections are taken into account [188].

¹Stopping and Range of Ions in Matter, developed by J. Ziegler

²WebAtima, developed by the GSI

Based on these calculations, the maximum penetration range d_{\max} of charged particles in the modeled sample matrix is extracted from the SRIM software as a function of energy, i.e. in the range between 10 keV and 4 MeV, and the data are interpolated [117]. Even though the charged particles lose energy almost linearly for a wide energy range (c.f. Fig. 2.2 b), a ROOT-based cubic spline interpolation is used here to ensure continuous transitions at the boundaries and to sufficiently describe the curvature of the energy loss function, visible in Fig. 2.2 b [191–193]. Together with the particle production energy E_0 , the maximum penetration range d_{\max} can be used to calculate the depth d from which the particle with residual energy E emanated:

$$d(E) = d_{\max}(E_0) - d_{\max}(E) \quad . \quad (4.5)$$

The count rate R within a given energy interval ΔE can be ascribed to a certain depth interval Δd . As shown in Fig. 4.3 a for the energy loss of ${}^3\text{H}$ ($E_0 = 2.7$ MeV) in carbon, the energy widths ΔE correspond to different depths intervals Δd_i , since the stopping power is not constant but depends on the particle velocity. When the charged particles carry a rather high energy they need to pass through more material to lose the energy ΔE than at lower energies. As shown in Fig. 4.3 a, at low residual energies (< 200 keV) the curvature inverts again. For example for ${}^3\text{H}$ and α particles in carbon matrix the inverted slopes are listed in Tab. 4.1 for different residual energies. Due to its higher energy loss, the α particles undergo a greater energy loss resulting in a better depth resolution.

Energy (MeV)	$\frac{\Delta d}{\Delta E}$ (nm/keV) ${}^3\text{H}$	$\frac{\Delta d}{\Delta E}$ (nm/keV) α
2.7	18.0	3.7
2.0	14.9	3.2
1.0	9.9	2.5
0.2 MeV	6.0	2.5
0.1 MeV	7.4	3.6

Table 4.1: Inverted slope of the energy loss of ${}^3\text{H}$ and α particles in a carbon matrix as a function of energy. The stopping power depends on the velocity of the particle. Over a wide range, $\frac{\Delta d}{\Delta E}$ decreases, resulting in a slope in the measured energy spectra. At low energies in the range of the trigger threshold the slope inverts. The α particles lose their energy on a shorter travel path than the ${}^3\text{H}$ particles.

Similar to Eq. (4.1), the signal rate stored in each energy bin reflects the total number of nuclides $I = \rho_{\text{nuclide}} \cdot \Delta d(E)$ in the depth interval $\Delta d(E)$, which is a function of E for constant ΔE intervals (c.f. Tab. 4.1). Over a wide range the energy intervals ΔE integrate over a larger thickness $\Delta d(E)$, which increases the number of nuclides I measured in this interval. As schematically shown in Fig. 4.3 b, this intrinsic effect originating from probing the concentration not in depth but in energy space leads to a gradient in the energy spectra. This gradient is present in all NDP spectra and is even present for samples with a homogeneous element distribution. It is to note that over most of the energy range accessible in NDP (> 200 keV, c.f. Sec. 3.1.3), a decreasing slope towards lower energies is observed, as it is schematically indicated in Fig. 4.3 b

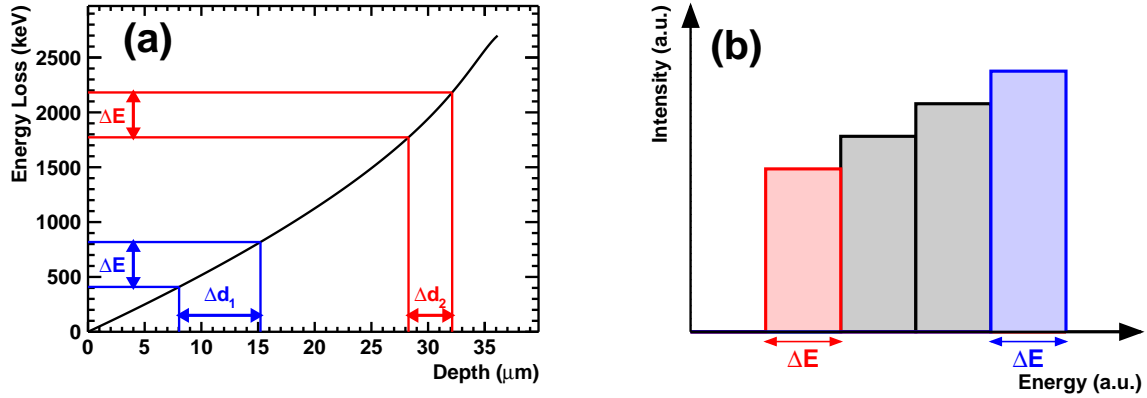


Figure 4.3: (a) The energy loss of ${}^3\text{H}$ nuclei from the ${}^6\text{Li}(n,\alpha){}^3\text{H}$ reaction in a carbon matrix is shown in black [118, 168]. NDP spectra are recorded in energy space in defined ΔE channels, which are shown as blue and red arrows. Due to the non-linear energy loss these channels translate into different depth widths Δd_i . Even if a uniform lithium density is present in a sample, the different integration volumes in real space induce a slope when measuring in energy space, as indicated in sketch (b).

and listed in Tab. 4.1, and only in the low energy regime this trend is inverted, depending on the curvature in Fig. 4.3 a.

In order to calculate the concentration c (atoms/g), the individual depth intervals $\Delta d(E)$ of each energy bin need to be taken into account:

$$c = \frac{I}{\rho \cdot A \cdot \Delta d(E)} \quad , \quad (4.6)$$

where A is the area illuminated by the neutron beam and ρ is the bulk density of the material. This procedure corrects for the intrinsic gradient observed in the energy spectra and flattens the profile for a homogeneous distribution of the measured nuclide.

4.3 Signal Broadening and Depth Mapping

In NDP, an element concentration at the depth x is measured at an energy $E(x)$, but the signal is smeared within an energy interval ΔE around $E(x)$ caused by the statistical nature of the energy loss (c.f. Sec. 2.3) as well as uncertainties from the setup and the sample itself. Upon knowledge of the response function $F(E)$, the original concentration profile can be obtained using various approaches presented in literature [70, 169, 194–198]. Since the statistical smearing of the signal is a non-injective operation, the so-called spectra “deconvolution” is a non-unique function and possible artifacts induced by the individual deconvolution method need to be considered, too. Therefore, a forward mapping method is used in this work. An assumed concentration profile can be tested by smearing it with the known response function and comparing it to the measured signal. This approach is utilized in Chap. 7 where the lithium concentration is measured in such a thick sample that the signals of the two charged particles from the ${}^6\text{Li}(n,\alpha){}^3\text{H}$ reaction overlap and a quantitative analysis is hampered. Due to energy and momentum conservation,

the released binding energy upon neutron capture is split between the two particles produced upon neutron capture (c.f. Tab. 2.2) in such a way that always the lighter particle exhibits the higher kinetic energy. Since its atomic number is also smaller, it is deeper penetrating than the heavier particle, as discussed in Sec. 2.3. A near-surface concentration profile can be approximated from the region between the high-energetic signal onset, e.g. when detecting lithium ≈ 2.7 MeV for ${}^3\text{H}$, and the signal overlap of the heavier charged particle, e.g. ≈ 2 MeV for α . From the obtained lithium concentration the energy signal of the particle with higher atomic number can be derived and both signals are separated allowing a quantitative analysis. The broadening can be described by the response function $F(E)$ for an atomic monolayer of emission at a depth x of a homogeneous target material as a normalized Gaussian distribution:

$$F(E) = \frac{1}{\sqrt{2\pi}\sigma_{E(x)}} \exp\left(-\frac{1}{2}\left(\frac{E - E(x)}{\sigma_{E(x)}}\right)^2\right) , \quad (4.7)$$

where E is the detected energy of particles emanating from the depth x with an expected mean energy $E(x)$ [194]. It is to note that the response function is area conserving, i.e. it does not affect the total signal rate representing the element concentration. Therefore, the total element amount obtained by signal integration is independent of the signal broadening, as it is e.g. used for the total quantity calibration described in Sec. 4.1.2. Assuming a straight travel path (c.f. Sec 3.1.3), the signal broadening

$$\sigma_{E(x)} = \sqrt{\sum_i (\sigma_i)^2} \quad (4.8)$$

consists of the independent broadenings σ_i originating from intrinsic noise of the detector σ_{det} , electronic noise of the read-out chain σ_{elec} , particle-dependent broadening σ_{ion} caused by statistical processes in the detector upon particle detection, particle straggling σ_{stragg} , and multiple small-angle scattering σ_{scatt} [118, 194]. Inhomogeneous materials, like porous electrodes for lithium-ion batteries, broaden the path length distribution of the charged particles and therefore the energy loss distribution and depth information [118]. Due to the geometry of the N4DP experimental setup the contribution of the geometrical acceptance is small compared to the other signal broadenings observed in Chap. 6–8 and an upper limit of the particle path length elongation was estimated in Sec. 3.1.3 to be $\approx 0.5\%$ [199].

The signal broadening from the intrinsic noise of the detector and the electronics read-out chain was determined from the width of the electronic-noise-charge (ENC):

$$\sigma_{\text{ENC}}^2 = \sigma_{\text{elec}}^2 + \sigma_{\text{det}}^2 \quad (4.9)$$

and was measured to be $\sigma_{\text{ENC}} \approx 5$ keV. Measuring the signal width originating from charged particles produced in a thin ${}^6\text{LiF}$ surface layer, the system noise (SN) is measured:

$$\sigma_{\text{SN}}^2 = \sigma_{\text{elec}}^2 + \sigma_{\text{det}}^2 + \sigma_{\text{ion}}^2 , \quad (4.10)$$

from which σ_{ion} was determined to be 5 keV for ${}^3\text{H}$ (2.7 MeV) and 7 keV for ${}^4\text{He}$ (2 MeV) [118]. The energy-/depth-dependent particle straggling σ_{stragg} and multiple small-angle scattering σ_{scatt} were determined using the SRIM software for the individual sample material [117].

When using a forward mapping method, a known concentration profile is assumed, e.g. a rectangular distribution is expected (c.f. Sec. 4.4) or a concentration profile is approximated from the signal shape of the lighter particle (c.f. Chap. 7), and is subdivided into depth intervals and corresponding energy bins. Each interval gives rise to a signal broadening described by the response function $F(E)$ being a normalized Gaussian distribution (c.f. Eq. (4.7)) and is weighted with the nuclide concentration of the individual layer. The final signal is then the superposition of the broadened signals of the individual layers.

4.4 Experimental Verification

In the following, the concentration profile calculation and the forward mapping method is exemplarily shown for a well-defined reference material with a homogeneous lithium concentration and an extremely precise layer thickness. Here, the lithium distribution within a nominally 403.1-nm-thick (determined by the company using non-contact optical measurements) single crystal lithium niobate thin film (natural ${}^6\text{Li}$ abundance is assumed) deposited on an insulating SiO_2 layer (LNOI) on a 2 cm \times 2 cm silicon wafer³ was measured using NDP (Setup II) at two distinct spots 1 cm apart of each other [118]. The optical properties of lithium niobate can be used for photonic waveguides and resonator applications and has also been previously studied using NDP [200, 201]. The energy spectrum is shown in Fig. 4.4 a. Two distinct signals of the ${}^3\text{H}$ and α particles from the ${}^6\text{Li}(n,\alpha){}^3\text{H}$ reaction (c.f. Tab. 2.2) are observed. Within the measurement accuracy the integrals are equal, indicating that the detector efficiency is the same for both particles. Due to the higher stopping power of the α particles, the α particles undergo a larger energy loss in the thin film resulting in a broadened signal with higher depth resolution (c.f. Chap. 2).

The mass layer thickness m_A of the lithium niobate layer is calculated using the energy loss derived from the width of the α particle signal assuming a homogeneous film density and LiNbO_3 composition. The mass layer thicknesses are found to be $(173 \pm 4) \mu\text{g}/\text{cm}^2$ and $(172 \pm 4) \mu\text{g}/\text{cm}^2$ for the two measurement spots. These values indicate a homogeneous layer thickness of the lithium niobate and the average mass thickness can be determined with an uncertainty of $\approx 3\%$ to be $(172.5 \pm 5) \mu\text{g}/\text{cm}^2$. In order to validate this energy loss calculation, the mass loading was determined using a second approach: Integration of the α signals results in a lithium loading of $(6.90 \pm 0.25) \times 10^{17} \text{ Li}/\text{cm}^2$, with 3.6% being the uncertainty composed of the systematic uncertainty of the SRM2137 reference standard and counting statistics. Considering the molar mass of LiNbO_3 being 147.85 g/mol, a mass layer thickness of $(169 \pm 8) \mu\text{g}/\text{cm}^2$ is derived. This value corroborates well with the previously found averaged mass layer thickness of $(172.5 \pm 5) \mu\text{g}/\text{cm}^2$ thus validating the depth calculation based on the energy loss. Furthermore, no channeling

³NanoLN Jinan Jingzheng Electronics Co. Ltd.

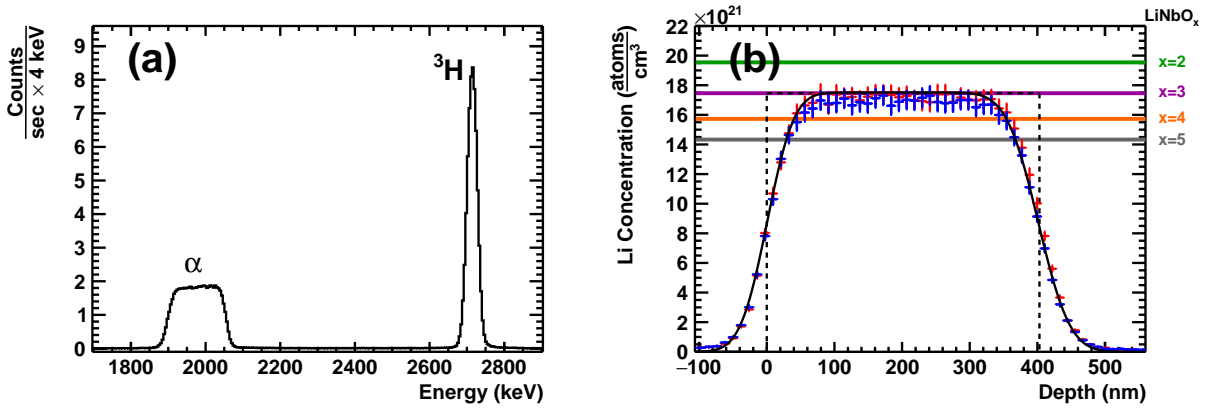


Figure 4.4: (a) Energy spectrum of a nominal 403.1-nm-thick LiNbO_3 film. (b) Concentration profile obtained from the α signal, as published in [118]. On the right side, lithium concentrations for different LiNbO_x compositions with integer x from $x = 2$ to $x = 5$ are shown. The measured concentration profile shows a LiNbO_3 composition.

effects could be observed in this measurement, which can possibly occur in highly-oriented single-crystal films [115].

Taking into account the optically measured film thickness of 403.1 nm and the previously found mass thickness (172.5 ± 5) $\mu\text{g}/\text{cm}^2$, a material density of (4.28 ± 0.17) $\mu\text{g}/\text{cm}^3$ can be derived. Although this finding is in good agreement with previous NDP measurements on lithium niobate thin films, this value deviates $\approx 7.5\%$ from the reported density of $\rho_{\text{soil}} = 4.63 \text{ g}/\text{cm}^3$ for lithium niobate [117, 202, 203]. This deviation might originate from the preparation of the thin film, measurement uncertainties or uncertainties in the stopping power calculated using SRIM [117, 118].

In Fig. 4.4 b, the depth profiles obtained from the α signals are shown for both measurement spots (blue and red dots) assuming a homogeneous material density of $4.28 \text{ g}/\text{cm}^3$ across the film thickness, as previously determined. The error bars consist of the systematic uncertainty of the reference sample and statistical uncertainties of the measurement. A 403.1-nm-thick LiNbO_3 layer is indicated as black dashed line showing the nominal lithium profile. Due to the well-defined properties of the lithium niobate thin film, NDP furthermore allows for the validation of the composition of the a priori LiNbO_x thin film. In Fig. 4.4 b, lithium concentrations originating from LiNbO_x layers with $x = 2$ to $x = 5$ are shown as horizontal lines. Within insignificant uncertainties $< 3\%$ the formation of $x = 3$ is observed.

Taking into account the depth-dependent response function, the expected signal is obtained using forward mapping (drawn through black line). It agrees well with the measured signals thus validating the forward mapping method and indicating that the previously assumed rectangularly-shaped lithium distribution is correct. Due to the statistical nature of the energy loss, the intrinsic signal resolution degrades from $\sigma = 10.6 \text{ keV}$ at the surface to $\sigma = 13.2 \text{ keV}$ at the bottom of the lithium niobate layer. Taking into account the stopping power of α particles in the lithium niobate layer and assuming a constant density of $4.28 \text{ g}/\text{cm}^3$, these values translate to

depth resolutions of 28 nm and 34 nm for single particles, respectively. It is to note that the mass thickness of the total layer, which is defined by the position of the inflection point, can be determined with a greater precision ($\approx 3\%$) than the intrinsic uncertainty of the signal broadening ($\approx 8\%$) [118].

Battery Research Using Neutron Depth Profiling

CHAPTER 5

In the frame of this work, NDP is applied on different materials for lithium-ion batteries. Therefore, the basic working principle of lithium-ion batteries is discussed in this chapter first. Afterwards, the application of NDP on lithium-ion batteries is discussed. The short range of the charged particles utilized in NDP defines the application of *ex situ* electrode layer thicknesses and limits the use of conventional lithium-ion battery casings for *operando* measurements. A novel battery cell casing adapted for measuring NDP is presented in Sec. 5.3.

5.1 Working Principle of Lithium-Ion Batteries

In contrast to aqueous-based battery systems like lead-acid batteries still being used as starter batteries in cars, lithium-ion batteries exhibit a relatively high volumetric and gravimetric energy density [43, 204]. Due to these properties, they are increasingly used in mobile applications like cell phones, notebooks, or power tools, as well as automotive applications like electric bicycles, cars, or scooters [43]. The lithium-ion battery technology revolutionized the energy storage enabling mobile applications and has a great impact on daily life. John B. Goodenough, M. Stanley Whittingham and Akira Yoshino were in 2019 awarded with the Nobel Prize in chemistry for their discoveries in this field [204].

In contrast to single-use (“primary”) lithium batteries, “secondary” lithium-ion batteries are rechargeable. Commercial battery cells appear in various shapes like cylindrical, prismatic, coin, or pouch cells [43]. Typically, several electrochemical cells are interconnected to one battery module parallel and/or serial depending on the application [205]. In this thesis, the focus of discussion and research is on the electrochemical cell, which is the elemental building block for the lithium-ion battery pack.

A schematic overview of the working principle of an electrochemical cell is shown in Fig. 5.1 a. First, the charging process is discussed. In state-of-the-art lithium-ion batteries electric power is stored via lithium intercalation. In earlier days, metallic lithium was used as negative electrode (anode) material, but due to lithium dendrite formation resulting in a short circuit and a po-

tential fire hazard, lithium intercalating materials were developed as electrodes [207–211]. Typically, the cell is charged using a CC-CV (constant current, constant voltage) procedure. First, an external electric voltage is applied to achieve a constant current (CC) and subsequently the applied voltage is kept constant (CV) until the electric current has fallen below a certain value and the battery is fully charged [43]. The electrochemical cell, as shown in Fig. 5.1 a, consists out of four main components: positive electrode (cathode), electrolyte, separator and negative electrode (anode). The cathode is often composed of lithium-containing transition metal compounds. Typically, layered structures of the chemical form LiMO_2 ($M=\text{Co}, \text{Ni}, \text{Mn}, \text{Al}$), spinel structures like LiM_2O_4 ($M=\text{Mn}, \text{Ni}$), or phosphates with the composition LiMPO_4 ($M=\text{Fe}, \text{Mn}, \text{Co}, \text{Ni}$) are used [43]. During charging, electrons are extracted via an external electric circuit connected to both anode and cathode by metallic contacts (so-called “current collectors”). At the cathode (anode) typically aluminum (copper) is used as a current collector. Upon charging, electrons are transferred through an external load from the cathode (oxidation) to the anode (reduction). The electric charge is counterbalanced by Faradaic reactions leading to lithium deintercalation from the cathode material thus releasing positively-charged lithium ions into the (liquid) electrolyte [212].

Carbonated organic solvents are used as liquid electrolytes to avoid chemical reactions of lithium, which is highly reactive when brought into contact with aqueous-based solvents [204]. Lithium-containing additives like lithium hexafluorophosphate (LiPF_6) provide a good lithium-ion transfer and the whole electrolyte is insulating for electrons [204, 212]. A plastic-based and highly porous separator material prevents mechanical contact of both electrodes, which would lead to a short circuit. Due to the externally applied electric field, positively-charged lithium ions are transported within the electrolyte through the separator towards the anode. Two distinct lithium transport mechanisms are possible: first, positively-charged lithium ions can directly be

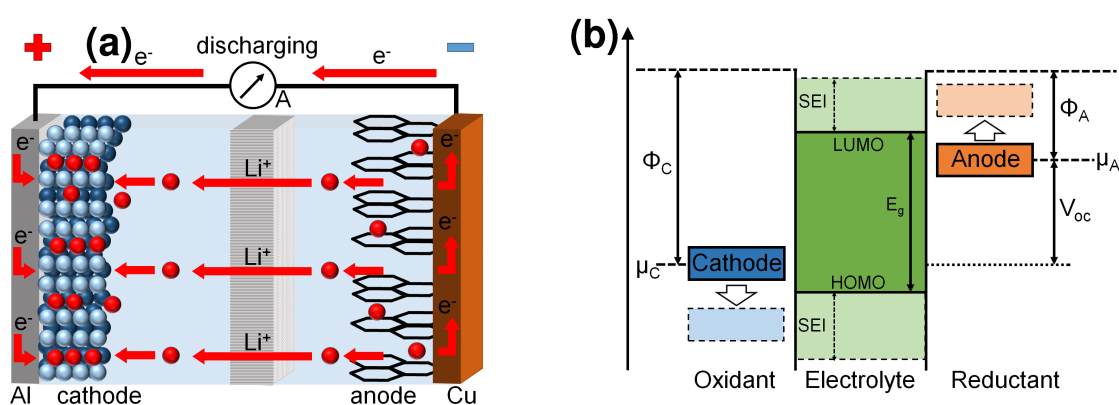


Figure 5.1: (a) Scheme of an electrochemical cell used for lithium-ion batteries. Here, the discharging process is shown: Lithium-ions are deintercalated from the graphite anode and moving to the cathode, while electrons generate an external electric current [43]. (b) Schematic overview of the energy potentials of cathode, electrolyte, and anode in the electrochemical cell. The difference of the electrochemical potentials of anode and cathode $\mu_{C,A}$ define the maximum output voltage V_{oc} [206].

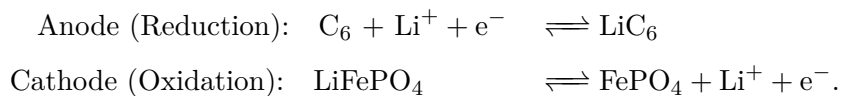
transported through the electrolyte. Due to its charge and small size, a solvent shell is formed around the lithium ion or it can be bound to the polymer electrolyte backbone thus hampering its mobility ν_+ defined by $\vec{v}_D = \nu_+ \vec{E}$, where \vec{v}_D is the ion drift velocity and \vec{E} is the applied electric field [213, 214]. The second transport process is based on the Li^+ release of LiPF_6 molecules at the electrolyte/anode interface and subsequent diffusion of PF_6^- ions towards the cathode. In contrast to the lithium ions, where a solvent shell can form thus hampering the mobility, the PF_6^- ions can be transported unhampered and so its mobility ν_- is larger than ν_+ of the lithium ions. The transport number, which represents the fraction of the total current carried by the individual processes, is then given by [213, 214]:

$$t_{+/-} = \frac{\nu_{+/-}}{\nu_+ + \nu_-} \quad . \quad (5.1)$$

Typically, $t_+ \approx 0.3$ and thus the lithium transport is dominated by the migration of PF_6^- [213, 214]. Since a major part of the current originates from lithium consumption at the interface of the electrode, a salinity gradient can form in the electrolyte limiting the maximum (dis-)charge rate [213, 214].

Eventually, the lithium-ions are transported to the anode and charge neutrality is achieved with the externally transported electrons. For secondary lithium-ion batteries mostly graphite is used as active material in the anode [43]. Typically, binder material and conducting additives are mixed with the active graphite particles to allow for mechanical adhesion on the current collector and a good electronic contact within the anode, respectively [43, 204]. In graphite, the carbon atoms are sp^2 -hybridized and ordered in a hexagonal lattice with a layered ABAB structure and a layer distance of $\approx 3.35 \text{ \AA}$ [43, 215–218]. The layered structure of graphite allows for a well-defined lithium intercalation, which can spatially be followed by a visible color transition from the pristine gray color of pure graphite over dark blue (LiC_{18}) and red (LiC_{12}) to a golden color when the graphite is fully lithiated and LiC_6 has formed (AA-layer structure) [219]. Assuming the molar mass of carbon of $M_C = 12.01 \text{ g/mol}$ and full LiC_6 formation, 13.88 mmol/g_C lithium ions can be intercalated into the graphite. Taking into account that each lithium ion could transfer a single charge, the maximum theoretical capacity for graphite is 372 mAh/g_C . During operation the graphite anode is expanded and contracted by $\Delta V \approx 10 \%$ [43]. Typically, ethylene carbonate (EC) is added to the liquid electrolyte, as it was found to prevent exfoliation, i.e. the peeling of active material from the electrode, and an ongoing decomposition of carbonaceous anode materials [220, 221].

In summary, the electrochemical processes at the cathode and anode during battery charging can be described by the following equations for anode/cathode components graphite and LiFePO_4 (LFP) typically used [43, 222]:



Upon battery discharging, these reactions are inverted. When externally connecting the electrodes with a load R_L , as shown in Fig. 5.1 a, electrons spontaneously move from the anode through the load to the cathode and lithium-ions are transported within the cell in the same direction, thus converting chemically stored energy in electrical energy [205, 212]. By the electric current I and voltage V an electrical power of $P = IV$ can be achieved. Hereby, the voltage $V = V_{oc} - IR_b$ is theoretically limited by the open-circuit voltage V_{oc} , but it is in reality reduced by the (assumed ohmic) internal battery resistance R_b caused by ionic transport resistances in the electrolyte, surface resistances at the electrode/electrolyte interfaces, and internal resistances within the electrodes and current collectors [205].

The open-circuit voltage V_{oc} is defined by the electrochemical potentials $\mu_{C,A}$ of the chosen electrode materials:

$$V_{oc} = \frac{\mu_A - \mu_C}{-nF} \quad , \quad (5.2)$$

where n is the number of charges carried per working ion (e.g. $n = 1$ lithium ions) and $F \approx 96.5 \times 10^3$ As/mol is the Faraday constant [205]. The work function $\chi_{C,A} = e\Phi_{C,A}$ defines the energy needed to raise a bound electron to the vacuum level ($\Phi_{vac} = 0$). Hereby $\Phi_{C,A}$ are the electric potentials of the electrodes below the vacuum level and thus define the energetic position of the electrochemical potentials $\mu_{C,A}$, as shown in Fig. 5.1 b [206]. However, in practice the electrochemical potentials are measured relative to a given standard, which is either the standard hydrogen electrode potential (vs. S.H.E.) at $\Phi_{H^+/H_2, 25^\circ C} = (4.44 \pm 0.02)$ V below vacuum potential, or typically for lithium-ion batteries it is measured with respect to the deposition of metallic lithium (vs. Li^+/Li), which is $\Phi_{Li^+/Li} \approx 1.46$ V below the vacuum level [223, 224]. Therefore, the electrochemical potentials $\mu_{C,A}$ vs. Li^+/Li correlates with the electric potentials $\Phi_{C,A}$ by $\mu_{C,A} = \Phi_{C,A} - \Phi_{Li^+/Li}$.

In order to maximize V_{oc} , materials with low electrochemical potentials are used as anodes, like graphite which exhibits a potential of 0.1–0.2 V vs. Li^+/Li , and a cathode compound with a high electrochemical potential is utilized, like $LiFePO_4$ with a potential of 3.45 V vs. Li^+/Li [43, 222]. Both potentials can not be tuned arbitrarily, but have to be located within the energy gap E_g defined by the highest occupied molecular orbital (HOMO) and the lowest unoccupied molecular orbital (LUMO) of the organic electrolyte, which is typically in the range of 0–5 V vs. Li^+/Li [43, 205]. Here, the electrochemical potential μ_A of the anode needs to be situated below the LUMO level of the electrolyte, otherwise electrons can be transported from the anode into the electrolyte and the electrolyte is reduced. The situation is similar for the cathode, where its electrochemical potential μ_C must be above the HOMO level of the electrolyte, otherwise the electrolyte will be oxidized. It is to note that metallic lithium would be an ideal anode material, since its electrochemical potential is defined by 0 V vs. Li^+/Li and it exhibits a high capacity of 3860 mAh/g [43]. As mentioned above, the usage of metallic lithium gives rise to potential fire hazards and a short battery lifetime [43].

When using carbonaceous anode materials, the anode potential typically increases above the LUMO during battery charging and thus the electrolyte near the anode is electrochemically reduced. It forms the so-called “Solid Electrolyte Interphase” (SEI) on the interface between

the anode and the electrolyte. Similarly, electrolyte can locally be oxidized at the cathode when its potential drops below the HOMO level, forming a passivation layer, too. Both passivation layers protect the active material from direct contact with the electrolyte and further decomposition of the electrolyte [206, 220, 221]. Typically, the formation of the passivation layers consumes previously active lithium ions, which reduces the reversible capacity. As discussed in Chap. 6–8, a major part of the electrochemically observed capacity loss originates from lithium ions irreversibly attached to the SEI in the anode.

5.2 NDP on Anodes for Lithium-Ion Batteries

The sensitivity of NDP on the ${}^6\text{Li}$ nucleus makes it possible to probe intercalation of active lithium in the electrode and furthermore to quantify the irreversible loss of active lithium consumed in the passivation layer. In previous works at MLZ the lithium intercalation in graphite as well as the formation of metallic lithium and the subsequent relaxation has been followed using Neutron Diffraction [53, 55, 225–227]. Neutron Diffraction probes the overall atomic structure and so a partial change of the lattice distances can be precisely quantified during (de-)lithiation but no spatial information within the measured Gauge volume is obtained. Here, NDP acts as a complementary method mapping the lithium density with respect to depth from which again conclusions can be drawn about the sample composition. However, while Neutron Diffraction can be applied on commercial lithium-ion batteries, the short penetration range of the investigated charged particles restricts the NDP method to thin film applications. Two technical approaches for NDP measurements are discussed in the following: first, anodes can be removed *post mortem* from the lithium-ion battery and measured *ex situ*, second, the non-destructive and non-invasive NDP method enables to perform *operando* measurements on a working cell.

5.2.1 *Ex situ* NDP Measurements

For some measurements it is extremely important to study the electrode surface with the highest resolution or to look as deep as possible into the bulk material of the electrode. In order to minimize the charged-particle energy loss and maximizing the viewing depth of NDP into the investigated anodes, they need to be removed *post mortem* from the lithium-ion battery. The electrochemical cells are operated to well-defined (dis-)charging states and opened under a protective atmosphere in a glovebox. The anodes are carefully rinsed using organic solvents also used in the electrolyte in order to remove electrolyte residuals. They are then sealed within a dry atmosphere, transported to the NDP experiment and subsequently measured.

When measuring *post mortem* a graphite anode, the energy loss of the ${}^3\text{H}$ particle enables to study anode mass thicknesses of up to $\approx 6.9 \text{ mg/cm}^2$, which is $\approx 45 \text{ }\mu\text{m}$ when assuming a typical anode porosity of $\phi = \frac{V_{\text{V}}}{V_{\text{tot}}} \approx 30\%$ [168, 170]. Here, V_{V} is the volume of the void and V_{tot} is the total anode volume. Previous *ex situ* NDP studies made it possible to quantify the formation of SEI in graphite anodes at different ageing processes [228, 229]. In this work, the influence

of a lamination technique of graphite anodes on the SEI formation is studied, as discussed in Chap. 6 [230]. Furthermore, both active lithium and lithium irreversibly attached to the SEI of silicon-graphite based anodes are studied *ex situ* and presented in Chap. 7 [118, 231, 232].

Due to their higher stopping power, the α particles from the ${}^6\text{Li}(n,\alpha){}^3\text{H}$ reaction can be used to study *ex situ* near-surface phenomena in the electrode (c.f. Chap. 2). The deeper penetrating ${}^3\text{H}$ particles reveal the lithium distribution in thicker electrodes. In thick electrodes, however, the α signals beginning at 2 MeV to lower energies might overlap with the ${}^3\text{H}$ signal, hampering the quantitative analysis from it. To simplify the analysis for these experiments, particle-filter foils are used to block the α particles [180]. However, the use of these foils limits the maximum penetration range for the ${}^3\text{H}$ particle, too: for example when using a nominally 7.5- μm -thick Kapton[®] foil, as presented in Chap. 6, the viewing depth for NDP is reduced to $\approx 5.7\text{ mg/cm}^2$ ($\approx 37\text{ }\mu\text{m}$ at a porosity of $\approx 30\%$) [168]. Since e.g. Tesla uses anodes with thicknesses of $\approx 100\text{ }\mu\text{m}$ for automotive applications, NDP is suitable to study thin-film anodes or the upper bulk of thicker anodes [233].

5.2.2 *Operando* NDP Experiments

When studying anodes *ex situ*, unwanted lithium losses can not be completely excluded, which might occur during cell opening, anode rinsing or transportation. This can be avoided when measuring the lithium distribution in closed cells during operation. However, energy losses induced by the battery packaging can not be avoided, which limits the near-surface resolution of the investigated particles. *Operando* NDP experiments reveal new and direct insights into the battery during (dis-)charging thus complementing conventional electrochemical measurements. In the framework of this thesis, *operando* NDP measurements were performed on lithium-ion batteries with graphite-based anodes. Here, NDP allows to directly study the lithium (de-)intercalation during the first (dis-)charging process, where initial passivation layers start to form. Furthermore, the lithium transport during fast charging could be investigated, which reveals novel insights into the build-up and equilibration of lithium accumulations in the anode.

5.3 Coin Cell Battery Development for *operando* NDP

Conventional battery casings are non-transparent for the charged particles exhibiting penetration ranges in the μm range. Therefore, a special battery cell casing was developed to measure lithium accumulations in the anode *operando* and is presented in this section. The *operando* coin cell concept was developed in cooperation with F. Linsenmann and P. Rapp from the Lehrstuhl für Technische Elektrochemie (TEC) group of the Chemistry Department at TUM, who also prepared, operated and electrochemically analyzed all *operando* batteries investigated in this work.

5.3.1 NDP Battery Cell Concept

The battery cell for *operando* NDP experiments needs to fulfill several requirements: (i) a low material budget is necessary using materials with low activation in the neutron beam to minimize neutron scattering and activation of the samples. Here, stainless steel parts, i.e. spacers in the cell, were replaced with aluminum which exhibits a short half life of a few minutes. (ii) The battery cell should be based on commercial standards, which allows for mass production and a large series of measurements. Typically lithium-ion battery cells are embedded in a T-, pouch-, cylindrical- or coin-cell to avoid electrolyte leakage or any contact with the atmosphere. These casings are all impermeable for the charged particles and therefore (iii) a thin (μm -thick) window transparent for the charged particles is essential. However, since also a (iv) vacuum or low pressure atmosphere had to be applied for NDP measurements, vaporization or leakage of the liquid electrolyte needs to be prevented by the thin window. (v) Even though the window is thin it needs to be stiff enough assuring good electric contact over the whole anode. All these requirements need to be fulfilled in a way, that (vi) anodes as close as possible to the industrial standard can be measured.

In previous studies, the lithiation in various thin film applications was followed *operando* using pouch cells either with thin Kapton[®] or a thin ($\approx 10\ \mu\text{m}$) copper or aluminum ($\approx 10\text{--}16\ \mu\text{m}$) current collector [62, 234–237]. However, previous works focus on a variety of thin-film electrode compositions e.g. Sn, LiFePO₄ and Li₄Ti₅O₁₂ or directly probe the lithiation in and on different metals like aluminum and copper, but until now, no *operando* NDP measurements on typical graphite anodes are presented in literature, as they are commonly used in the industry nowadays [62, 170, 234–237]. A novel cell design based on commercial coin cells was developed, which allows for measuring *operando* on graphite anodes as close as possible to the commercial standard, while making it possible to probe the complete anode thickness.

5.3.2 Charged-Particle Window

First, the three possible candidates acting as charged-particle window will be discussed, which were mentioned before. Aluminum has a density of $\approx 2.7\ \text{g}/\text{cm}^3$, which might be reasonable for a charged-particle window. However, it is known to electrochemically alloy with lithium at low electric potentials and it thus is only used as cathode current collector [238, 239]. Therefore, copper is commonly used as current collector for the anode in lithium-ion batteries. However, its high density of $\approx 8.96\ \text{g}/\text{cm}^3$ induces also a high energy loss of the ³H charged particles even in μm -thick foils, e.g. a $10\ \mu\text{m}$ -thick copper foil would induce an energy loss of $\approx 1.3\ \text{MeV}$ on the ³H at $2.7\ \text{MeV}$ (c.f. Tab.2.2) [168]. Therefore, similarly to previous studies, a nominally $7.5\ \mu\text{m}$ -thick Kapton^{®1} foil was purchased and used as charged-particle window. Its low density of $\approx 1.42\ \text{g}/\text{cm}^3$ reduces the energy loss of the charged particles passing through it. From previous

¹DuPont, USA

measurements, the energy loss of the nominally 7.5- μm -thick Kapton[®] foil was determined to be (301.0 ± 0.6) keV for the ^3H (at 2.7 MeV), whereby it is impermeable for α particles. However, a copper current collector is still needed to electrically contact the graphite anode. In order to minimize the additional energy loss induced in this layer, a thin (nominal 100 nm) copper film was sputtered² on the Kapton[®] foil (shown in Fig. 5.2 a). The energy loss of ^3H charged particles in this thin layer can be estimated to $\Delta E \approx 11$ keV [168, 170].

5.3.3 Graphite Anode

Energy loss of the charged particles in the battery cell casing limit the viewing range into the investigated anode. In this section, the maximum viewing range is estimated and the anode preparation is outlined. The influence of anode compression on the viewing range for *operando* NDP is discussed.

NDP Viewing Range in Working Graphite Anodes

The NDP viewing range into a graphite anode installed in a battery cell depends on several parameters discussed here. First, the composition of the anodes with pores completely filled with liquid electrolyte needs to be taken into account. Similar to the composition of commercial graphite anodes, the graphite anodes consist of 91:9 wt % graphite and PVDF binder [170]. The volume within the pores (≈ 47 % porosity) is filled by the liquid electrolyte consisting of 3:7 wt % ethylene carbonate (EC):ethyl methyl carbonate (EMC) in which either 1 mol/l or 0.31 mol/l (c.f. Tab. 5.1) of conductive LiPF_6 salt³ was dissolved.

The charged particles need to travel through the window which reduces their maximum penetration range in the anode. Furthermore, as discussed in Chap. 3, the measurement chamber was filled with helium to keep the coin cell above the vaporization pressure $p > 100$ mbar at 25°C of the liquid electrolyte to prevent gas formation [169]. For the *operando* formation (plating) studies, a nominal pressure of $p_{\text{He}} \approx 400$ mbar ($p_{\text{He}} \approx 150$ mbar) was applied. Taking into account the composition of the anode filled with electrolyte and the additional energy losses induced by the Kapton[®] foil and a 400 mbar helium atmosphere in the N4DP measurement chamber (Setup I, SDD = 96.1 mm), the maximum viewing depth of ^3H particles can be estimated at ≈ 4.4 mg/cm² (≈ 26 μm assuming a bulk density of 1.7 g/cm³) [170].

²Movatec, Eching

³LP57, BASF, Germany

Graphite Anode Preparation

Comparing the estimated NDP viewing range and thus the aimed anode thickness to the typical graphite particle size of $d_{50} = 19\ \mu\text{m}$, i.e. the diameter of 50% of all particles is smaller than $19\ \mu\text{m}$, shows that the prepared anode would only mostly consist of a single layer of these particles. Since this structure would not be representative to a commercial graphite anode ($\approx 100\ \mu\text{m}$ thickness), where several layers of graphite particles form the anode, the graphite particles were sieved leading to a particle size distribution of $d_{50} = 5.8\ \mu\text{m}$. This particle size is sufficient to form a homogeneous anode layer with the desired thickness. Even though the increased surface area per graphite mass alters the electrochemical performance compared to commercial graphite anodes, fundamental processes in this setup can already be studied.

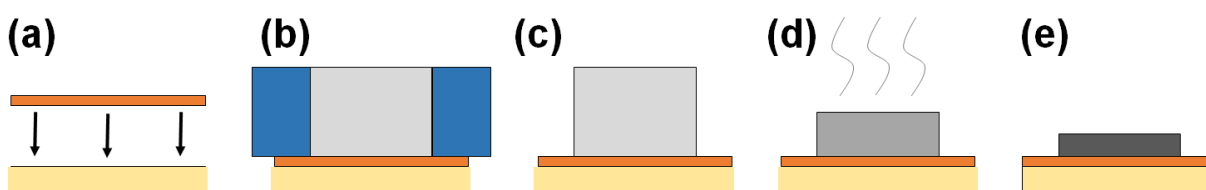


Figure 5.2: Schematic overview of the anode preparation for *operando* measurements. A 100-nm-thick copper layer serving as current collector is deposited on the nominally 7.5- μm -thick Kapton[®] foil, as shown in (a). The liquid anode ink is doctor-blade-coated on the current collector using a 80- μm -thick PTFE-coated spacer shown in (b). After removal of the spacer (c), the anodes are dried for 3 h at 50°C (d), before they were compressed to their final porosity (e).

The graphite anodes were prepared by the TEC group at the chemistry department of TUM. After sieving the graphite particles, the anode material (91:9 wt% graphite and PVDF) was mixed with N-methyl-pyrrolidone (NMP)⁴, reaching a solid content of 28 wt% in a planetary mixer⁵, and stirred for 15 min [170]. As shown in Fig. 5.2 b and on the photograph in Fig. 5.3 a, the resulting ink was then doctor-blade coated onto the Cu-sputtered Kapton[®] foil using a 80- μm -thick PTFE coated fiberglass gasket⁶ mask containing circular holes with 12 mm diameter and subsequent annealing at 50°C for 10 min in a convection oven. After removing the mask (Fig. 5.2 c) several graphite-anode coatings could be obtained from a Cu-sputtered Kapton[®] foil, as shown in the photograph in Fig. 5.3 b. Then, the ink was dried for another 3 h at 50°C (Fig. 5.2 d) and excess of anode material was removed leading to well-defined graphite anodes with a diameter of 12 mm coated on the Cu-sputtered Kapton[®] foil later serving as charged particle window. The thin substrate foils were punched out into discs of a diameter of 15 mm centered around the 12 mm-thick graphite anode, as shown in the photograph in Fig. 5.3 c. The exposed 3-mm-thick free copper ring-shaped area is later used to electrically contact the thin current collector coating. Eventually, the anodes were compressed using a KBr press (PE-011, Mauthe, Germany). This compression leads to a reduction of pores between the graphite

⁴NMP, anhydrous, 99.5%, Sigma-Aldrich, Germany

⁵Thinky, USA

⁶Fiberflon GmbH & Co. KG, Germany

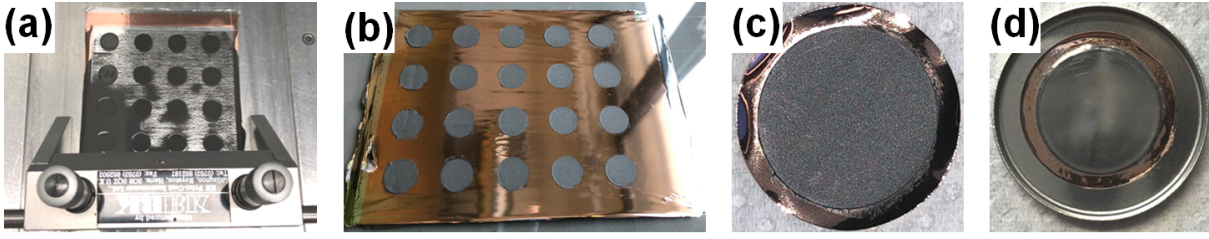


Figure 5.3: Photographs of the anode preparation procedure, as published in [170]. Courtesy of P. Rapp. (a) First, the anode ink is doctor-blade coated on the sputtered Kapton[®] foil. (b) After removal and subsequent drying, up to 20 anodes could be prepared per foil. (c) The anodes (12 mm diameter) were punched out at a diameter of 15 mm, which allows to later electrically contact the copper layer from the 3-mm-thick exposed ring outside of the anode. (d) Eventually, the anodes were compressed to their final porosity and glued into the coin cell cap thus sealing the laser-cut hole grid.

particles and subsequently to a reduction of the porosity and anode film thickness, as indicated in Fig. 5.2 e.

Influence of Anode Compression on NDP Viewing Depth

In industry, e.g. automotive applications, the increase of battery energy density, power density and a reduction of costs are of great interest [240, 241]. In order to achieve a high packing density, the electrodes are compressed, which was performed here using a KBr press. However, anode compression also influences the range accessible using NDP: as shown in Sec. 2.4, the range of NDP depends on the mass thickness $m_A = \rho \times d$. The volumetric mass distribution plays a minor role, i.e. a 10 μm -thick graphite anode with a porosity $\phi = 0.5$ is equivalent to an artificially 5 μm -thick and dense graphite anode (porosity $\phi = 0$). For *ex situ* measurements the elemental composition and areal mass thickness of the anode therefore defines the NDP range, and it is a priori independent of ϕ or the bulk density defined by $\rho_{\text{bulk}} = (1 - \phi)\rho_{\text{soil}}$, where ρ_{soil} is the density of the pure anode material. While this is true for *ex situ* measurements, this relation changes for *operando* measurements. Here, a liquid electrolyte fills the pores of the anode and it adds to the anode mass thickness m_A depending on the anode porosity ϕ . During the anode preparation, the mass m_{Anode} is coated on the substrate and the final anode thickness after compression is given then by

$$d_{\text{Anode}} = \frac{m_{\text{Anode}}}{A(1 - \phi)\rho_{\text{soil}}} \quad , \quad (5.3)$$

where A is the area covered by the circular anode. However, the range d_{NDP} accessible by NDP does not increase in the same manner when going to higher porosities, but is affected by the additional mass from the liquid electrolyte filling the pores. For the following estimation, any minor changes in the energy loss due to a porosity-induced modification of the elemental composition is neglected. Finally, d_{NDP} can be estimated by

$$d_{\text{NDP}} = \frac{m_A}{\rho_{\text{soil}} - \phi(\rho_{\text{soil}} - \rho_{\text{El}})} \quad , \quad (5.4)$$

where m_A is the maximum mass thickness accessible using NDP and ρ_{El} is the density of the liquid electrolyte. In Fig. 5.4, the ratio of $d_{\text{NDP}}/d_{\text{Anode}}$ is shown as a function of the anode porosity, normalized to the starting value. Here, it can be understood that a perfect compression (porosity $\phi = 0$) leads to the maximum NDP range, which was previously accessible for *ex situ* samples, too. As shown in Fig. 5.4, the accessible NDP range is reduced when going towards higher porosities ϕ , i.e. lower anode compression. Here, additional electrolyte mass located in the pores of the anode reduces the NDP range, i.e. at $\phi = 0.8$ only $\approx 30\%$ of the maximum depth are accessible, while anode compression to $\phi = 0.5$ leads to $\approx 64\%$. The anodes investigated *operando* were compressed to porosities of $\approx 47\%$. It is to note that a sufficient wetting, i.e. an increased surface area of the electrode in contact with the liquid electrolyte, is essential for the battery performance [241]. Therefore, the ideal case for NDP resulting in a maximum viewing depth, i.e. a non-porous anode ($\phi = 0$), is not favorable for the battery performance.

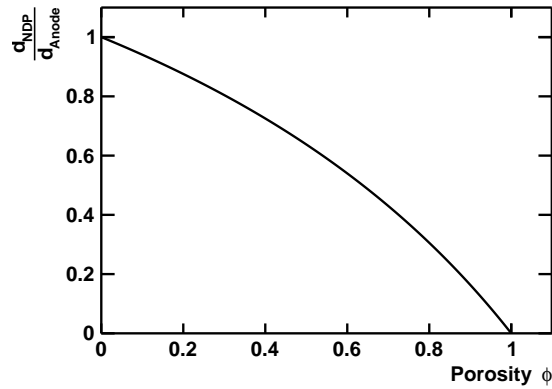


Figure 5.4: Estimation on the influence of the anode compression (porosity reduction) on the accessible range in NDP. Here, the composition of the soil anode material and the EC/EMC liquid electrolyte mixture was taken into account.

5.3.4 Coin Cell Assembly

After processing the graphite anodes on the Cu-sputtered Kapton[®] substrate, the foils were inserted into a lithium-ion-battery cell casing. First testings with pouch cells showed a mechanical instability of its flexible lamination foils at low ambient pressures as they are used in NDP. Therefore, a coin cell battery design was modified. In order to allow transmission of charged particles through the impermeable 0.25 μm -thick CR2032⁷ stainless-steel cap, holes with various diameters were processed into the cap by an external company⁸ and the different hole designs (8 mm, 4 mm diameter single holes, and grids of 0.5 mm and 0.3 mm holes) later tested upon operation. The prepared Kapton[®] foils with graphite anodes were glued⁹ into the caps thus

⁷Hohsen Corp., Japan

⁸Halder Schneidtechnik, Eching, Germany

⁹2 K Epoxy UHU Endfest

sealing the processed holes and subsequently annealed at 80°C, as shown in the photograph in Fig. 5.3 d. A schematic overview of the full *operando* coin cell is shown in Fig. 5.5.

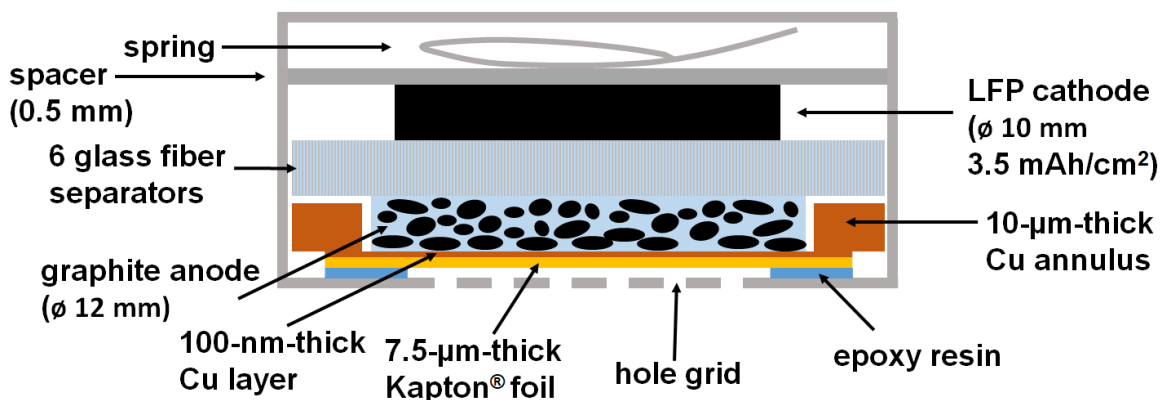


Figure 5.5: Schematic overview of the whole *operando* coin cell, as published in [170]. A laser-cut hole grid in the stainless-steel coin cell cap allows transmission of charged particles. A 7.5- μm -thick Kapton[®] foil with a 100-nm-thick copper current collector on it was glued on the coin cell cap using epoxy resin, thus preventing leakage of the liquid electrolyte through the processed hole grid. A copper annulus enables to contact the anode current collector. The graphite anode was processed to a diameter of 12 mm and 6 glass fiber separators were used as separator material. A LFP electrode with a diameter of 10 mm was used as cathode.

A 20- μm -thick copper annulus ($d_i = 13 \text{ mm}$, $d_a = 19 \text{ mm}$) was used to electrically connect the coin cell cap with the exposed copper current collector around the graphite anode. Six glass-fiber separators with uncompressed thicknesses of 250 μm were used to electrically isolate the graphite anode from the LiFePO_4 (LFP) counter electrode. The separators were then soaked with 270 μl of 1 mol/l (or 0.31 mol/l) LiPF_6 in a mixture of ethylene carbonate and ethyl methyl carbonate (EC:EMC = 30 : 70 wt %; LP57, BASF, Germany) serving as ion-conductive electrolyte. The LFP counter electrode was punched out smaller than the graphite anode (10 mm diameter), in order to avoid edge effects caused by a slight off-centered misalignment of the electrodes during fabrication [170]. Aluminum spacers were used to replace the original stainless-steel spacers behind the cathode thus reducing neutron-capture-induced material activation which causes additional β and γ signals in the spectral background.

For *operando* studies presented in Chap. 8, graphite anodes (91:9 wt % graphite and PVDF binder) with comparable thicknesses and similar porosities were prepared, as listed in Tab. 5.1 [68, 170]. While for the formation study 1 mol/l of conducting LiPF_6 salt was dissolved in the electrolyte, a lowered LiPF_6 content of 0.31 mol/l (c.f. Table 5.1) was used for the latter study. The lowered LiPF_6 content reduced the lithium transport in the electrochemical cell, resulting in lithium plating already at charging rates of $\approx 2\text{C}$, which could be followed using NDP with a time resolution of 2 min.

Study	Anode Thickness	Anode Porosity	LiPF ₆ Content	Hole Grid
Formation	(17±2) μm	(47±6) %	(1.00±0.01) mol/l	17×0.5 mm
Fast Charging	(23±2) μm	(47±5) %	(0.31±0.01) mol/l	139×0.3 mm

Table 5.1: Overview of the samples measured using *operando* NDP presented in Chap. 8. The anodes for both studies (formation study, fast charging study) are of similar thickness and comparable porosity. In order to enforce lithium plating at charging rates of $\approx 2C$, the LiPF₆ content was lowered to 0.31 mol/l compared to the standard used for the formation study (1 mol/l). A hole grid containing 17 holes with a diameter of 0.5 mm was processed in the coin cell cap for the formation study. For the latter fast charging study, an improved hole grid of 139 holes with diameters of 0.3 mm was used to increase the anode area accessible using NDP.

5.3.5 Optical Performance of the *Operando* Coin Cell

In the next step, the performance of the graphite anodes was electrochemically tested in the coin-cell batteries. Therefore, coin-cell batteries with different caps were operated and they were opened in their fully charged state, i.e. when the graphite anodes should be in their fully lithiated state. Photographs of the extracted anodes are shown in Fig. 5.6. It shows a graphite anode lithiated in a coin-cell with a standard cap in Fig. 5.6 a, i.e. no perforated holes in the cap. It has a golden color which is typical for a pure LiC₆ phase [242]. For both, the 8 mm and 4-mm-thick hole (Fig. 5.6 b, c) a dark red color can be seen in the center of the processed hole, indicating a preliminary lithiation phase where a pure LiC₆ phase could not be formed. It shows a completely inhomogeneous electrochemical behavior depending on the position on the current collector probably caused by a lack of contact pressure in the center of the holes. Therefore any NDP measurements, which measure only charged particles emanating from the processed hole, would not be representative for the whole anode. However, in both cases a ≈ 0.5 -mm-thick and fully lithiated ring is observed to form at the edges of the processed holes, indicating that the contact pressure is still sufficient in this small region at the edges of the processed holes. Therefore, the hole diameter size was reduced to 500 μm, in order to ensure

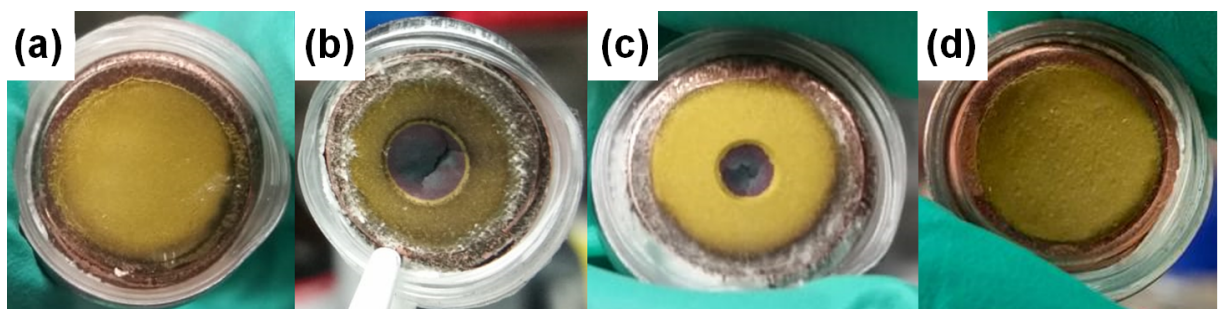


Figure 5.6: Photographs, as published in [170], of the inside of graphite electrodes lithiated at $C/20$ in a) standard coin-cell casing with b) 8 mm diameter, c) 4 mm diameter holes and d) a grid of 0.5 mm holes. In the standard casing, the full formation of LiC₆ is optically observed. In both cells with large holes, different lithiation states can be distinguished. In the cell with the grid consisting of 0.5 mm holes, the image indicates complete LiC₆ formation.

sufficient contact pressure also within the hole. In order to increase the signal obtained from the charged particles, a grid of 17 holes with diameter of 500 μm were processed in a circular area of 8 mm in the coin-cell cap. In this way, a total area of 3.3 mm^2 could be probed with NDP, which is about 3.0% of the whole graphite anode area. As shown in Fig. 5.6 d after opening the battery where the hole grid was processed into the cap the whole anode surface displays a homogeneous golden color. This indicates that the lithiation process is not altered by the grid of holes and thus any NDP measurements obtained through them probe the undisturbed electrochemical process in the graphite anode. The presented grid design was for the later fast charging study (c.f. Sec. 8.2) improved to increase the accessible area using a grid of 139 holes with diameter of 300 μm , as shown in Tab. 5.1. Here, about 8.7% (9.8 mm^2) of the graphite anode area could be probed while ensuring a good contact compression.

5.3.6 Influence of the Coin Cell Design on the NDP Signal

Two distinct hole grids were used for the two *operando* studies presented in Chap. 8 (c.f. Tab. 5.1). As discussed before, they allow for the measurement of charged particles emanating from the anode while maintaining sufficient electronic contact between the copper current collector and the anode. In contrast to *ex situ* studies, they reduce the effective area of the measurement. Therefore, the NDP signal rate can not directly be compared to that of the reference standard for a quantitative analysis (c.f. Chap. 4). The reduced area needs to be taken into account, increasing the systematic uncertainty of the measurement. In the formation study (c.f. Sec. 8.1) performed at N4DP (Setup I), the reduction of the area is calculated based on the geometry of the hole grid (17 \times 0.5 mm) within the neutron beam (beam diameter of 4 mm) at an angle of 45°. The sample holder allowed for a lateral displacement of 1 mm of the cell, and it could arbitrarily be rotated. Furthermore, a maximum angular misalignment of 3° was assumed, induced by a 1 mm misalignment over the 20-mm-thick coin cell diameter. These displacements result in the geometric uncertainty of max. 9.1%, which adds to the uncertainties from the SRM2137 reference standard (3.4%) and the calibration procedure (0.9%) to 9.8% using Gaussian error propagation [170]. In the fast charging study presented in Sec. 8.2, which was performed at the NIST Center for Neutron Research in Gaithersburg, a ^6LiF reference sample on a Mylar foil was placed behind the 139 \times 0.3 mm hole grid and so the geometric uncertainty could experimentally be determined with a higher precision of 1.9%. Together with the uncertainty of 2.2% arising from the custom-made sample holder (c.f. Chap. 3), the uncertainty of 1.4% of the in-house NIST calibration standard RR8B16, the calibration uncertainty of 0.4% and an observed neutron flux variation of 2.3% (c.f. Chap. 3), a total systematic uncertainty of 4.0% was obtained using Gaussian error propagation.

Passivated Lithium

Accumulations in Graphite Anodes

CHAPTER 6

In this chapter, *ex situ* Neutron Depth Profiling is presented quantifying lithium accumulations in graphite anodes for lithium-ion batteries. First, a novel electrode lamination technique is introduced, followed by the sample preparation. In order to study the effect of this lamination technique on the lithium accumulation, XRD measurements on the *ex situ* anodes are presented. They give insight into the anode crystal structure thus complementing the NDP measurements discussed afterwards.

All findings presented here are results of a collaboration of the Physics Department of TUM, the Technologiezentrum Energie at Hochschule Landshut and the MLZ. M. Frankenberger from Hochschule Landshut prepared all investigated samples and performed the electrochemical measurements and S. Seidlmayer from MLZ obtained the XRD data. The NDP results performed and presented here are also part of the Bachelor Thesis of J. Dittloff supervised in the frame of this work and they are published in [230].

6.1 Electrode Lamination in Li-Ion Batteries

Currently graphite is one of the most frequently used anode materials for lithium-ion batteries [243]. It reaches a theoretical specific capacity of 372 mAh/g_C when LiC₆ formation is completed, while providing reasonably good aging and safety properties [244, 245]. In order to further improve the lifetime of a lithium-ion battery especially for fast charging/discharging procedures, Frankenberger *et al.* (2019) recently proposed a lamination process which can be individually applied on the electrodes or on both [246]. The capacity aging of the battery is reduced by the lamination technique, as shown in Fig. 6.1, where the discharge capacities of fully laminated Li-ion battery cells are shown. At a charge/discharge speed of 1C, the battery capacities age for both the laminated and non-laminated cells in a similar way. However, at an elevated cycling rate of 2C the non-laminated cells show faster aging than the laminated cells during the first 500 charge/discharge cycles. This indicates that during the first 500 cycles the lamination process is beneficial for the electrochemical cell aging especially at higher charge/dis-

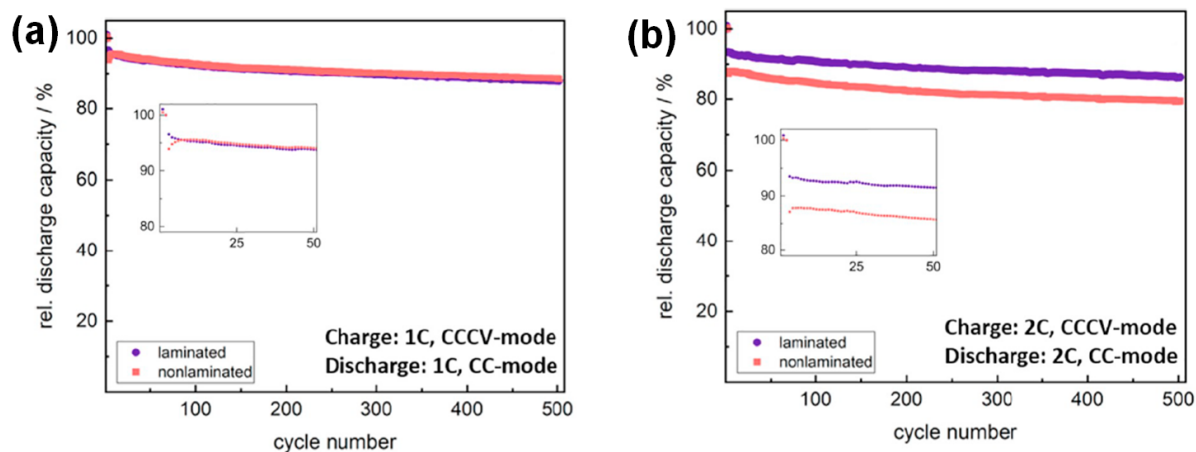


Figure 6.1: Relative discharge capacities of fully laminated (blue) and non-laminated (red) lithium-ion batteries at (a) 1C and (b) 2C cycling rate¹ [246]. At 2C, the laminated cells show a better stability over aging within the first 500 cycles.

charge rates.

Battery aging can be driven by many mechanisms, the three main causes are 1) consumption of active lithium ions, 2) insulation of active material and 3) an increased ohmic resistance due to contact degradations in the electrodes (which affects only the OCV) [247]. Especially in the first charge/discharge cycles, the consumption of active lithium caused by side reactions at the anode surface is known to form a solid-electrolyte-interphase (SEI). Impedance measurements indicate that the lamination process could reduce reductive side reactions of the active lithium [246].

6.2 Sample Preparation

In order to probe the accumulation of immobilized lithium in aged anodes, 50 differently aged anodes (laminated/non-laminated) were prepared by our collaboration partner M. Frankenberger from the Technologiezentrum Energie at the Hochschule Landshut [230, 246]. The graphite anodes consist of 90 %wt active graphite particles (particle size of 22 μm), 2 %wt carbon black², 1 %wt conductive graphite³, and 7 %wt PVDF (CH_2CF_2) binder. They were blade coated on a 10- μm -thick copper current collector foil. A capacitively limited NMC cathode (93 %wt NMC111, 3 %wt conductive carbon, 1 %wt conductive graphite, 3 %wt PVDF binder) was used as counter electrode (using an aluminum current collector) to avoid any deposition of metallic lithium on the anode surface. A $\approx 31\text{-}\mu\text{m}$ -thick and 55 % porous separator (67 % Al_2O_3 , 33 % PVDF) was either mounted loosely in between the electrodes (non-laminated anodes) or it was laminated with both of the electrodes at elevated temperatures (fully-laminated cells [246]).

¹Reprinted from “Laminated Lithium Ion Batteries with improved fast charging capability”, M. Frankenberger *et al.*, Journal of Electroanalytical Chemistry, 2019, 837, 151–158, with permission from Elsevier, license no. 4917530977255.

²Carbon Black, Super C65

³Conductive Graphite, SFG6L

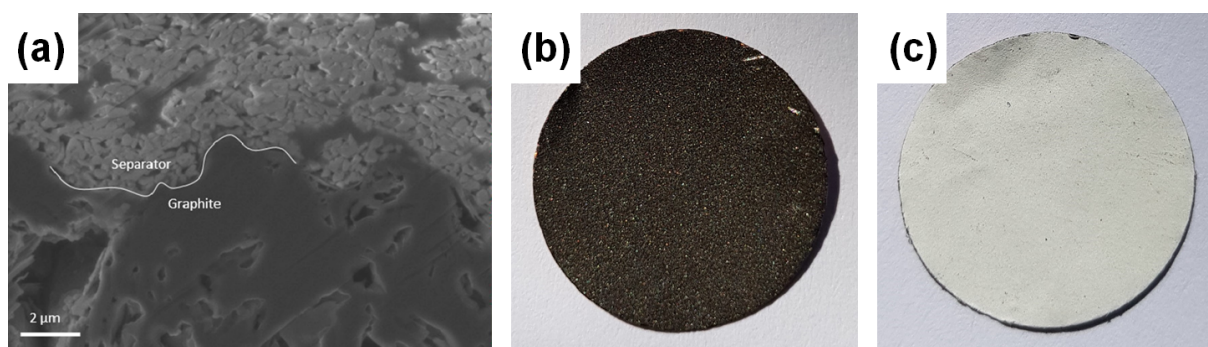


Figure 6.2: (a) Cross-section SEM image of a laminated anode-separator interface. The flexible separator mimics the rough surface of the anode thus filling the anode pores and increasing the contact area⁴ [246]. Photographs of a non-laminated (b) and laminated (c) anode prepared for *ex situ* measurements. The black graphite layer can be seen for the non-laminated anode, which is hidden by the white separator for the laminated anode.

As shown in the SEM cross-section image in Fig. 6.2 a, the flexible separator material mimics the rough graphite surface by filling the pores of the anode, which enhances its contact area. Ionic conductivity was assured using a liquid electrolyte consisting of 98 %wt of 1M LiPF₆ in EC/EMC 3/7 w/w and 2% vinylene carbonate (VC).

The batteries were then cycled for several times using a CTSD-LAB BaSyTec battery tester [230, 246]. For charging, a constant current (CC) mode was used from 3.0 V to 4.2 V, followed by a constant voltage (CV) phase until a cutoff current meaning that the C/20 was reached. Due to the capacitive cathode limitation, the anodes were only charged up to 80 % of their theoretical capacity. Discharging was always performed at the same rate as charging and a CC mode was used from 4.2 V to 3.0 V until the cells were fully discharged (100 %). In order to study effects of the initial formation process, all anodes were (dis-)charged during the first two cycles using rates of 0.1 C, 1 C or 2 C. The three groups of anodes with different formation history were then aged using cycling rates of either 1 C or 2 C.

All anodes were then extracted from the battery cells in their fully discharged state and rinsed using pure EMC to remove lithium residuals. Therefore, all remaining lithium in the anodes could be assigned to lithium situated irreversibly in the anode. Eventually, the anodes were cut into discs with a diameter of 14 mm. As shown in the photographs in Fig. 6.2 b, c, the graphite layer of the non-laminated anode can be seen, which is hidden for the laminated anodes, where the white separator is permanently merged with the anode surface.

⁴Reprinted from “Laminated Lithium Ion Batteries with improved fast charging capability”, M. Frankenberger *et al.*, Journal of Electroanalytical Chemistry, 2019, 837, 151–158, with permission from Elsevier, license no. 4914250963651.

6.3 Characterization of Immobilized Lithium in Graphite Anodes

6.3.1 XRD Measurements

X-ray Diffraction (XRD) was used to measure *ex situ* the crystal structure of the anodes with a high statistical significance. Details of the XRD technique are presented in Appendix A. The XRD spectra of the non-laminated pristine, at 0.1 C formed and at 1 C 500× cycled anodes are shown over the full measurement range in Fig. 6.3 a. The spectra exhibit signals corresponding to a pure graphite phase, indicated with gray markers, and copper from the current collector, marked in orange. Depending on the individual anode thicknesses, the heights of the graphite signals slightly vary. Residuals of Al_2O_3 from the separator were detected and their signals are marked in blue. In Fig. 6.3 b the 2θ -region between $(10.5\text{--}12.5)^\circ$ is shown as magnification. The signal at $2\theta \approx 12.2^\circ$ could be assigned to pure graphite with a layer distance of $\approx 3.35 \text{ \AA}$ [43, 215–218]. The double-peak-shaped signal originates from individual positive interference of the two emitted characteristic wavelengths ($K_{\alpha 1}/K_{\alpha 2} = 0.5$) on the sample lattice structure (c.f. App. A). If lithium would be intercalated into graphite, its inter-layer distance would be increased and

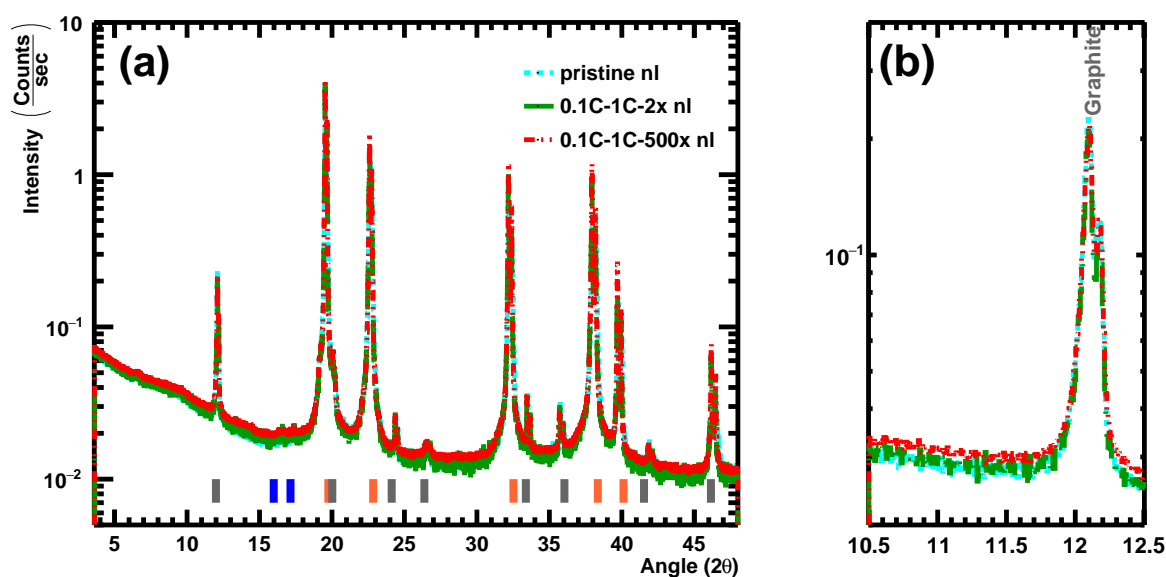


Figure 6.3: (a) XRD measurements of three representative non-laminated anodes upon greater cycle number. Signals from graphite (gray) and from the copper current collector (orange) are observed. Only residuals of Al_2O_3 (blue) from the removal of the separator were detected. (b) In the magnified range only a pure graphite signal and no signals at lower 2θ angles are observed, which could be assigned lithium intercalation. Therefore, all lithium later measured using NDP is irreversibly situated outside of the graphite crystal structure.

a significant shifting of the graphite signals towards lower 2θ angles would be observed [53, 225, 226]. For a complete lithium intercalation, i.e. LiC_6 formation, the inter-layer distance is increased from originally $\approx 3.35 \text{ \AA}$ to $\approx 3.70 \text{ \AA}$ and a signal at $2\theta \approx 11.1^\circ$ would be expected following Bragg's law of diffraction (c.f. App. A) [225]. In Fig. 6.3 b no signals other than graphite were found indicating that independent of their cycle number all reversibly intercalated lithium was extracted during the final discharge of the anodes. Thus, any immobilized lithium later detected using NDP has to be 1) in a non-crystalline phase and 2) not situated within the crystal structure of the graphite material.

Accordingly to the non-laminated anode spectra, the spectra of three representative laminated anodes are shown in Fig. 6.4 a. Additionally to peaks originating from graphite (gray markers) and the copper current collector (orange markers) signals were found which could be assigned to Al_2O_3 (blue marker) and semi-crystalline PVDF (green marker) originating from the separator. In the magnified 2θ region shown in Fig. 6.4 b also signals from Al_2O_3 are observed close to the signals assigned to graphite. Apart from these signals no further peaks indicating a lithium intercalation are found. Therefore, also for the laminated anodes all lithium later measured using NDP originates from non-crystalline lithium outside of the graphite lattice.

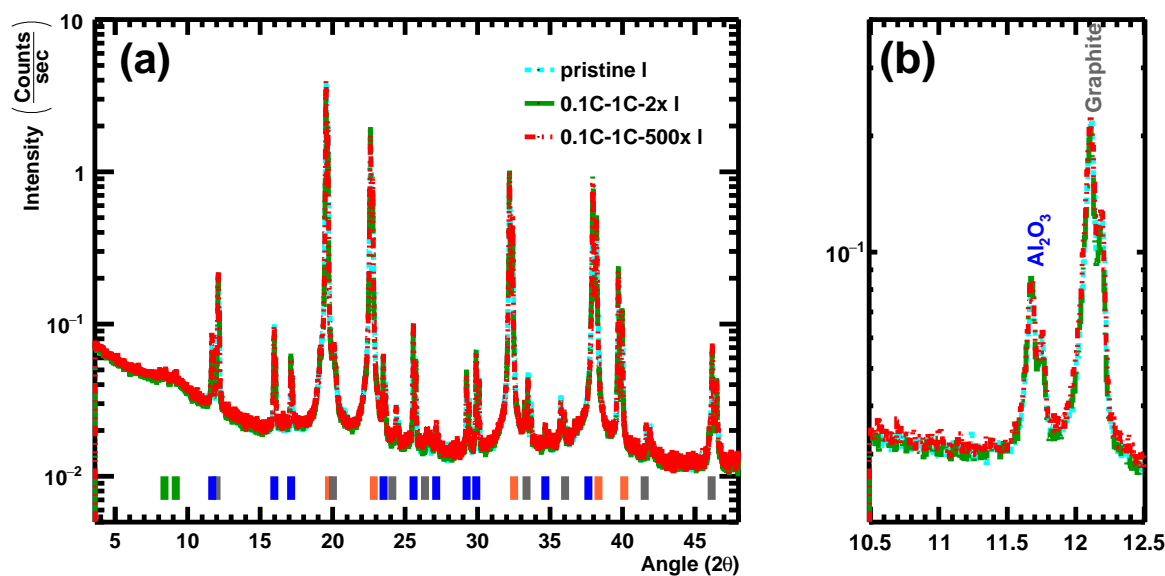


Figure 6.4: (a) XRD measurements of three representative non-laminated anodes upon greater cycle number. Signals from graphite (gray) and the copper current collector (orange) are observed. Also dominant signals from Al_2O_3 (blue) and semi-crystalline PVDF binder (green) are found originating from the laminated separator. (b) In the magnified range only an Al_2O_3 and a pure graphite signal are observed. No signals at lower 2θ angles are observed, which can be attributed to lithium intercalation. Therefore, also for the laminated anodes all lithium later measured using NDP is irreversibly situated outside of the graphite crystal structure.

6.3.2 NDP Measurements

Shape of Anode Spectra

The NDP measurements presented in this study were conducted using Setup 1 with the massive sample holder (c.f. Sec. 3.1.3). In order to suppress any overlap of α and ${}^3\text{H}$ signals, a nominal 7.5- μm -thick Kapton[®] foil was placed in front of the detector (c.f. Sec. 3.1.3). In Fig. 6.5, NDP spectra of (non-)laminated pristine anodes measured directly after fabrication are shown as (blue) red line. The spectra are dominated at low energies by the β - and γ -induced background (c.f. Chap. 4). Although no nominal lithium is present in the reference samples, signals corresponding to a lithium depth distribution are observed in the region 0.8–2.4 MeV. This can be rationalized by neutron scattering into samples mounted in close vicinity of the investigated reference anode [119]. The scattered neutron intensity is higher for the laminated reference where an additional $\approx 31\text{-}\mu\text{m}$ -thick separator material is located on the graphite anode [230]. The reference measurements were subtracted from the anode spectra, as it is shown in Fig. 6.6 for the (non-)laminated anodes formed and aged to 50 cycles at 1C (i.e. 1C-1C-50x). Therefore, the remaining signals entirely stem from lithium situated in the anodes. Due to the use of a Kapton[®] separation foil, the signals purely originate from ${}^3\text{H}$ particles from the ${}^6\text{Li}(n,\alpha){}^3\text{H}$ reaction and the signals are shifted to 2.4 MeV, which corresponds to the surface of the samples, i.e. the separator surface for the laminated and the graphite anode surface for the non-laminated samples (c.f. Fig. 6.2 b, c).

The non-laminated-anode spectrum can be subdivided into three distinct regimes: 1) A peak at 2.4 MeV–2.3 MeV, corresponding to the anode surface, 2) a region with shallow gradient from $\approx 2.3\text{ MeV}$ –1.5 MeV and 3) a region with a steep gradient down to the trigger threshold (200 keV). The peak at the surface might originate from a true lithium enrichment at the surface, but it is indistinguishable from a lithium aggregation morphologically situated on the

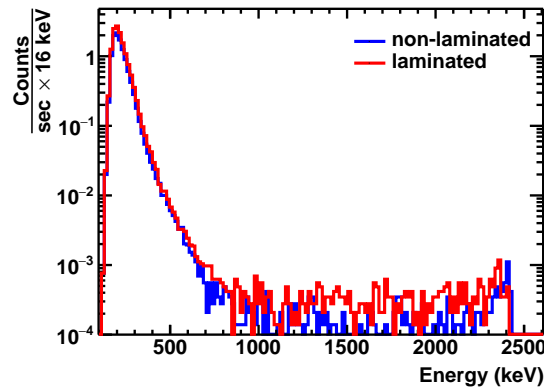


Figure 6.5: NDP spectra of the pristine non-laminated (blue) and laminated (red) anodes. Apart from the exponential low-energy background signal, neutron scattering into neighboring anodes mounted on the sample holder is observed, resulting in low-intensity signals up to 2.4 MeV.

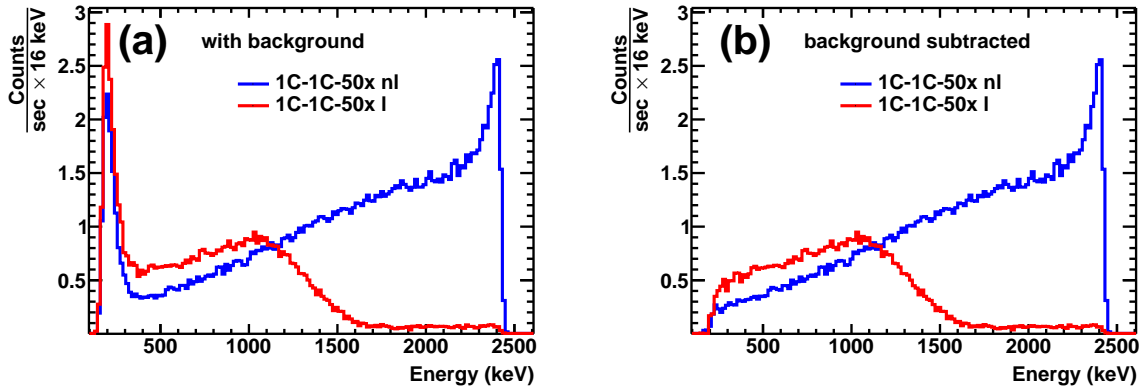


Figure 6.6: (a) NDP spectra of non-laminated (blue) and laminated (red) anodes from the 1C-1C series extracted after 50 cycles. The energy spectra after pristine background subtraction are shown in (b). The separator on top of the anode shifts the laminated-anode spectra to lower energies, thus reducing the viewing depth.

graphite particles giving rise to volumes with lower lithium content within the particles [118]. This morphological lithium distribution would corroborate well with the findings of the XRD measurements (c.f. section 6.3.1), indicating that the immobilized lithium is situated on the surface of the graphite particles, i.e. the graphite active-material/electrolyte interface, thus forming a non-crystalline solid-electrolyte-interface (SEI). As discussed in Sec. 4.2, a shallow slope (region 2) originates from the NDP measurement principle and it indicates a homogeneous lithium distribution within the bulk of the anode. The inflection point of the intensity decrease at lower energies (region 3) indicates the end of the anode (anode/current collector interface) [118]. It is measured with a broadened energy resolution and is much larger than the broadening of $\sigma_E \approx 30$ keV expected for pure energy straggling [168]. This deviation might originate from the porous material distribution of the anode (c.f. SEM cross-section in Fig. 6.2 a), which gives rise to various path lengths of the ^3H particles in the anode material [118].

For the laminated-anode spectra the lithium distribution of the graphite anode is shifted to even lower energies (1.3 MeV), since the charged particles lose additional energy on their way passing through the nominal 31- μm -thick separator before reaching the detector. Therefore, the viewing depth in the laminated anodes is reduced from previously ≈ 5.7 mg/cm² (c.f. Chap. 5) to 2.3 mg/cm² [168]. Furthermore, the resolution at the anode surface being in the range (1.0–1.7) MeV is worsened in comparison to the spectra of the non-laminated samples. This energy broadening can not be ascribed to energy straggling of the ^3H particles in the separator, which can be estimated to $\sigma_{\Delta E} \approx 15$ keV, but it probably originates from the filling of the separator material within the rough graphite anode surface, which is shown in Fig. 6.2 a. As it can be seen in Fig. 6.6, lithium residuals which could not be removed via rinsing are present within the separator material. In the region, where both materials are blended (≈ 1.0 MeV to ≈ 1.7 MeV), this signal can not be distinguished from signals originating from lithium in the anode. Since the viewing depth of the non-laminated anodes differs vastly from the laminated

samples, first all non-laminated anodes will be discussed, followed then by a comparison to the laminated samples.

Lithium Immobilization in Non-Laminated Anodes

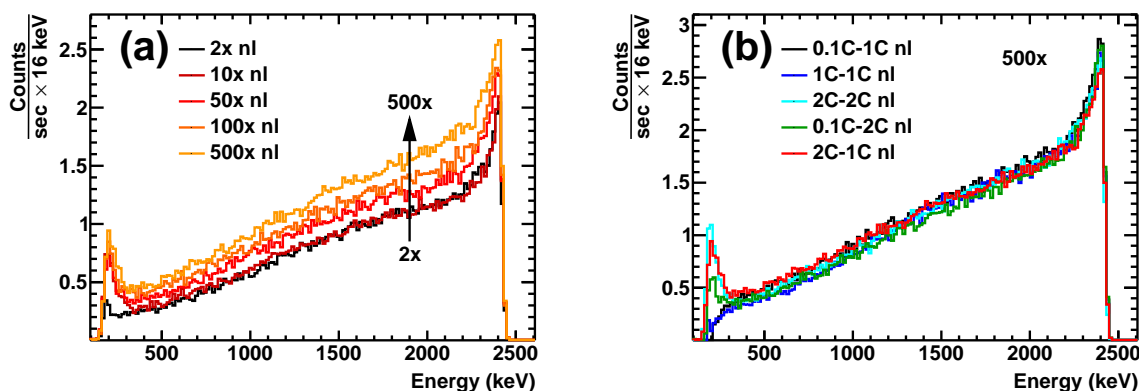


Figure 6.7: All spectra are background subtracted. (a) Spectra of the 2C-1C-series, measured after different cycle number. An increase of immobilized lithium upon higher cycle number is observed, thus indicating that the formation of the passivated layer is not fully completed after two cycles. (b) Comparison of all measured aging series extracted after 500 cycles. Small fluctuations can be observed, which arise from the statistic nature of the sample production process. Different cycling histories do not indicate a systematic effect on the lithium immobilization in the graphite anodes. At low energies artefacts from the background subtraction can be observed for both images.

Representative for all aging series, the immobilized lithium accumulation within the anodes up to 500 cycles is shown in Fig. 6.7 a by the spectra of the anodes formed at 2 C and aged at 1 C (2C-1C-series). Measurements of the other series are listed in Appendix C. Most of the immobilized lithium is formed during the formation phase in the first two cycles. However, upon extended cycling the immobilized lithium in the anode still increases, indicating that the reduction process of active lithium is even at 500 cycles not fully completed. This may be caused by the formation and exposure of new anode surfaces and subsequent SEI formation upon extended cycling. It is to note that the shape of the spectra remains similar, indicating that during all cycles the distribution of the immobilized lithium stays constant.

In Fig. 6.7 b the spectra of all non-laminated anodes with different cycling histories are exemplarily shown after 500 cycles of aging. The spectra indicate small variations in their lithium profiles, which are mainly caused by minor uncertainties during sample preparation [230]. The spectra of anodes acquired after different number of cycles are shown the Appendix C. Similar to Fig. 6.7 b, no systematic evolution of the lithium distribution could be observed with respect to the cycling rates.

In Fig. 6.8 a, the concentration profiles of the 2C-1C-series are shown assuming the anode sample composition described in Sec. 6.2. The previously shallow gradient (c.f. Fig. 6.7 a) shows a constant depth distribution indicating that the measured gradient of region 2 originates from the

NDP measurement principle. Thus, the lithium distribution within the anode was immobilized homogeneously with respect to depth, independent of the aging history. The depth profiles of all non-laminated anodes extracted after 500 cycles are shown in Fig. 6.8 b. Here, layer thickness variations due to sample preparation are visible, which are displayed by the varying mass thicknesses. Within the anodes, no systematic influence of the cycle history on the immobilized lithium distribution was found. The other depth profiles are shown in the Appendix C.

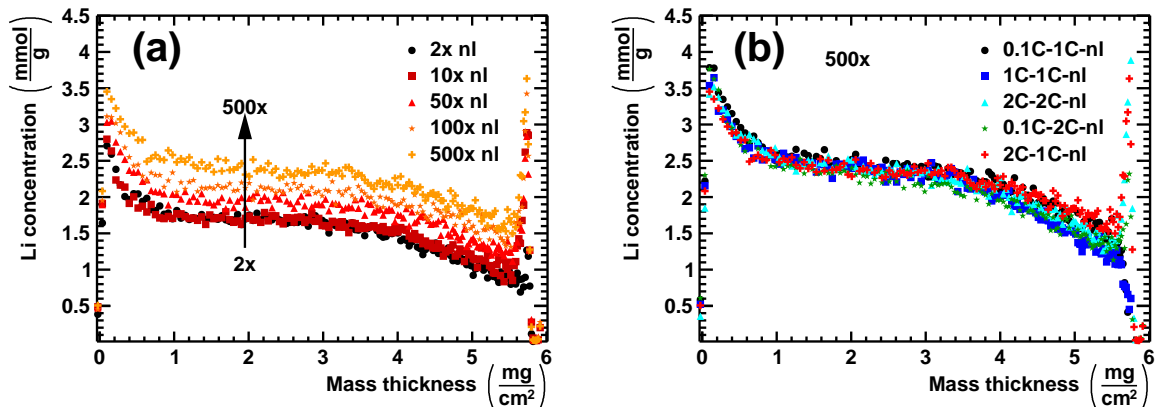


Figure 6.8: (a) Lithium concentration profiles of the anodes from the 2C-1C-series calculated from the NDP energy spectra. (b) Comparison of the lithium concentration profiles of the different series after 500 cycles.

The inflection point of the decreasing slope marks the end of the lithium distribution, i.e. the anode/current collector interface when assuming that lithium is immobilized throughout the whole depth of the anode [118]. Since the inflection point is below the trigger threshold, the decreasing slope was extrapolated using a Gaussian as the signal response function (c.f. Chap. 4). The determined inflection points are shown in Fig. 6.9 a. Here, the anode material thickness variation within the samples is observed. In order to validate the obtained anode mass loadings obtained from NDP, the anodes were weighed and their areal mass thicknesses are shown in Fig. 6.9 b. Both measurements agree well within $\pm 6\%$, as shown in the mass thickness ratios in Fig. 6.9 c. These findings support the previous assumption that the anodes are filled with immobilized lithium and the inflection point of the lithium depth profile depicts the anode/current collector interface.

The integral of the spectra represents the total lithium amount in the anodes and it was corrected by Gaussian extrapolation of the signals detected in Fig. 6.7. Assuming a single charge transport per lithium ion, the total lithium amount obtained from the NDP spectra was then interpreted as the capacity which was immobilized throughout the whole anode depth. The capacities corresponding to immobilized lithium in the anodes are shown in Fig. 6.10 a as drawn-through lines. As previously discussed, most of the immobilized lithium is observed to be formed during the first two cycles. However, a systematic irreversible capacity increase is observed upon greater cycle numbers. The dashed lines in Fig. 6.10 a illustrate the irreversible capacity observed during (dis-)charging of the batteries. The irreversible capacities measured using NDP are systemati-

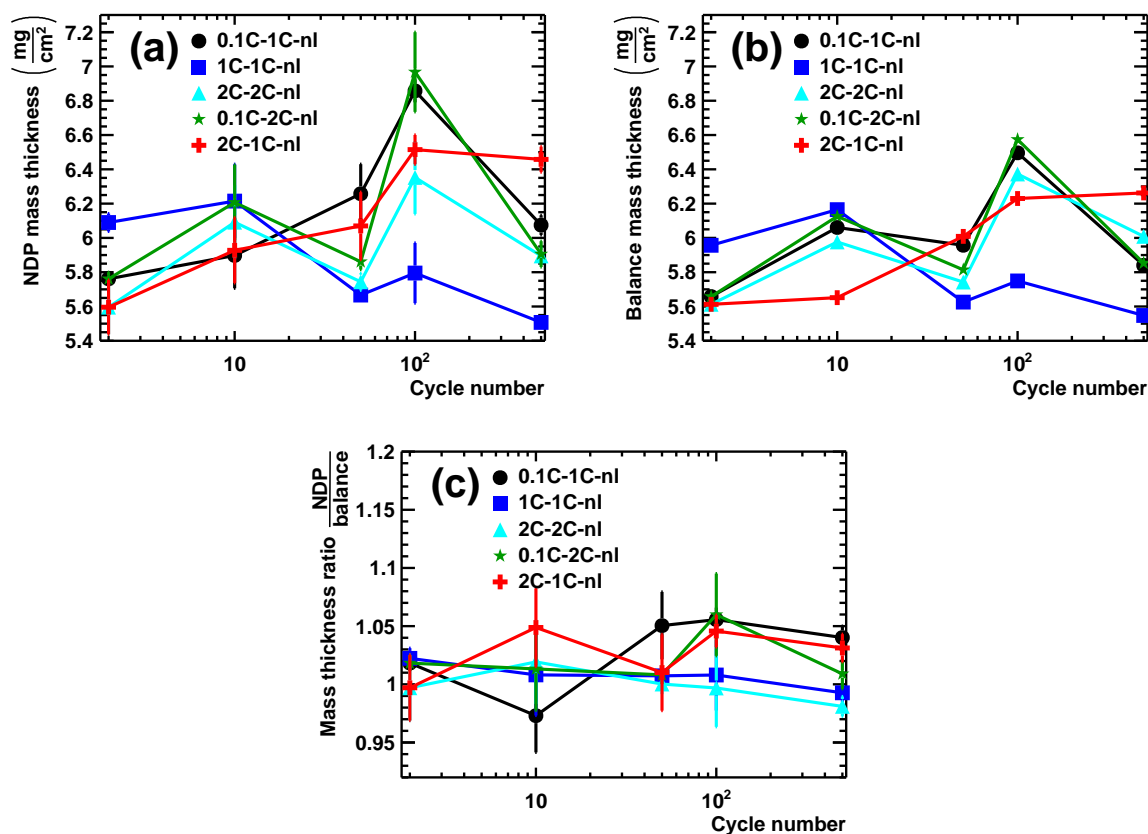


Figure 6.9: (a) Mass thicknesses determined from the lithium concentration profiles. (b) Mass thicknesses determined by weighing of the anode discs. (c) Ratio of the mass thicknesses determined from the lithium depth profiles and the weighed mass thicknesses. It shows a good agreement of both data sets within $\pm 3\%$.

cally smaller than the measured irreversible capacities of the whole batteries. Only for the anode formed at 0.1 C an irregularly low capacity was measured during battery cycling, which probably arises from differences in ohmic overpotentials from the lowered C-rate in the 1st two cycles, what apparently reduces the calculated capacity losses compared to subsequent cycles [230]. As shown in Fig. 6.10 b, between 55% and 80% of the irreversible capacities could be detected as immobilized lithium in the anodes. This confirms that the main part of the irreversible capacity is caused by lithium immobilization in the anode forming SEI. However, deviations could be caused by lithium losses occurring during anode extraction, separator removal or during washing the anodes before measured *ex situ*. Also electronic or mechanic contact losses of the active material might cause a capacity fading without forming an SEI [248]. Further capacity losses outside the anode, like structural and phase changes in the cathode, could be possible [248].

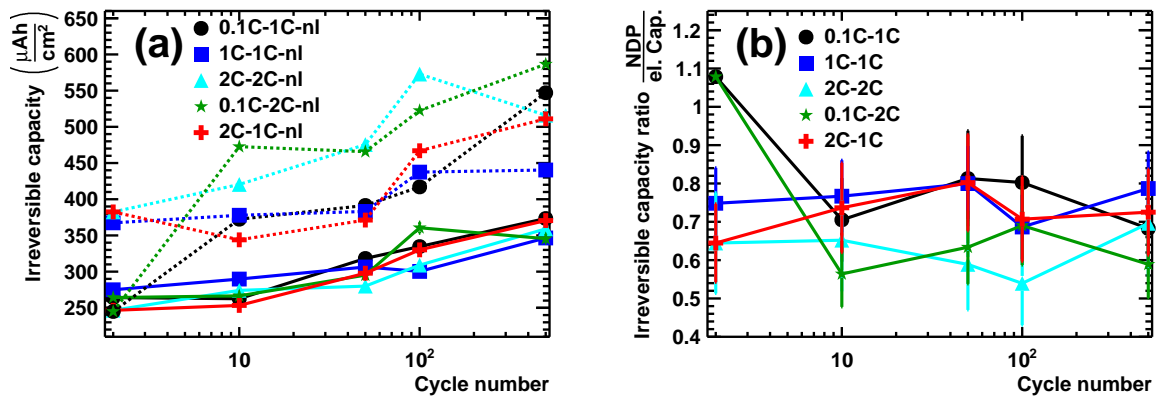


Figure 6.10: (a) Comparison of the irreversible capacities observed during battery operation (dashed lines) plotted together with the capacity directly detected as immobilized lithium in the anodes (drawn-through lines). The irreversible capacity stored within the anodes is systematically lower than the observed capacity loss. (b) Ratio of the irreversible capacities detected in NDP and the measured irreversible capacity indicates that about 55 % to 80 % of the irreversible capacity originates from immobilized lithium in the anodes.

Lithium Immobilization in Laminated Anodes

The viewing depth for the laminated anode spectra is limited by the additional separator material to $\approx 2.3 \text{ mg}/\text{cm}^2$ and thus the lithium immobilization in this accessible region can be compared between laminated and non-laminated anodes [168]. In order to exclude lithium residuals from the separator near the graphite anode surface, only the interval between (1000–400) keV of the laminated-anode spectra (c.f. Fig. 6.6 b) was integrated for the immobilized lithium amount in this region. The corresponding irreversible capacities are shown in Fig. 6.11 a. The chosen energy interval corresponds to a depth region of (0.96–2.06) mg/cm^2 carbon equivalent, which corresponds to the energy range (2160–1830) keV for the non-laminated anode spectra [168]. The

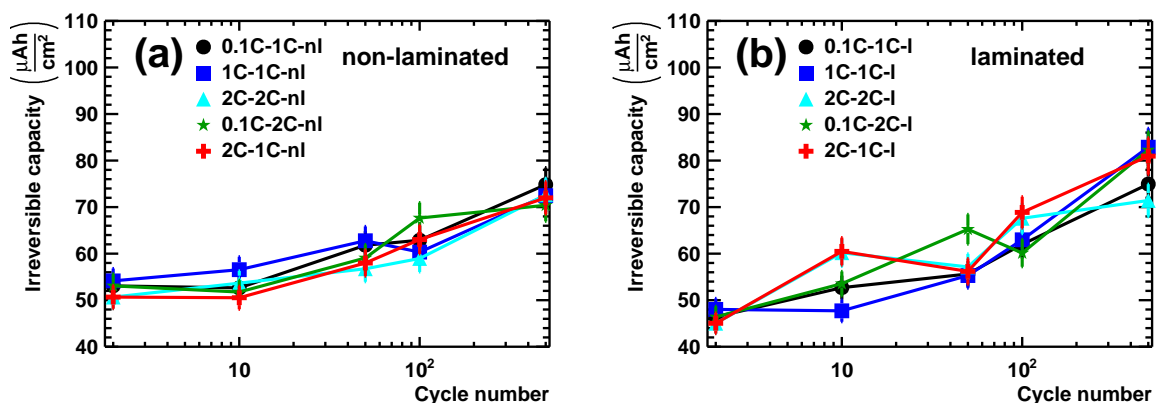


Figure 6.11: Irreversible capacity in form of immobilized lithium within non-laminated (a) and laminated (b) anodes. For a direct comparison the energy spectra were integrated over an energy region corresponding to the same depth interval.

amount of immobilized lithium in this interval is shown in Fig. 6.11 b. The increasing lithium immobilization upon extended cycling is visible for both cases.

The differences of both irreversible capacities are shown in Fig. 6.12, taking into account the varying sample preparation fluctuations and statistical uncertainties. It shows no clear dependence of the capacity difference to the cycle number or series. Assuming a constant capacity difference with respect to the cycle number, an average capacity difference of $(-0.3 \pm 4.2) \mu\text{Ah}/\text{cm}^2$ is obtained and therefore no variation from zero is observed within the uncertainties of the measurement. Based on these findings, the lamination procedure shows no systematic effect on the development of immobilized lithium at different cycling rates in the investigated depth interval, as it was observed previously for the capacity aging [246].

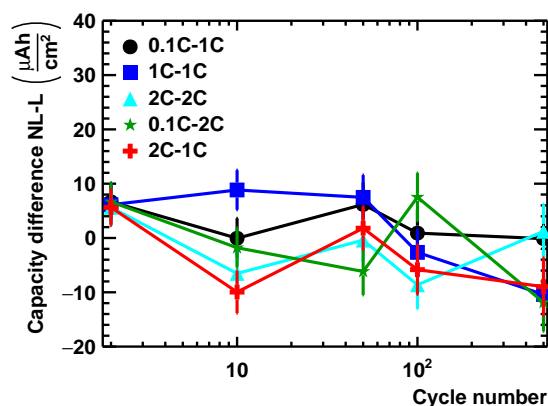


Figure 6.12: Difference of lithium immobilized in the same depth interval in non-laminated and laminated anodes (c.f. Fig. 6.11)

6.4 Conclusion

Electrode lamination was previously shown to be beneficial for the capacity aging of lithium-ion batteries [246]. Since the reason for this aging phenomenon is yet not fully understood, the effect of lamination on the accumulation of immobilized lithium was studied. Here, previous active lithium is known to be immobilized at the anode via forming a SEI, which is one major aging mechanism in lithium-ion batteries [247, 248].

Independent of their cycling history or lamination, XRD measurements indicated neither a crystalline lithium phase nor remaining lithium-graphite intercalation in the fully discharged anodes. On the macroscopic level, NDP measurements on the non-laminated anodes showed a homogeneous lithium immobilization with respect to depth, while indicating that the immobilized lithium is situated on the surface of the graphite particles, thus forming a non-crystalline SEI. NDP measurements showed that $\approx 80\%$ of the lithium immobilized over 500 cycles is formed during the first two charge-discharge cycles and about (55–80)% of the total electrochemically observed irreversible capacity could be assigned to immobilized lithium in the anode.

For the non-laminated cells, the viewing depth for NDP was sufficient to probe the complete

anode layer, whereas for the laminated anodes the viewing depth was reduced by the additional separator material. Therefore, only depth regions accessible for both, laminated and non-laminated anodes, could be compared. Here, no systematic effect of the lamination on the amount of immobilized lithium was observed, which indicates that the beneficial lamination effect on the battery capacity aging might originate from other effects than the lithium immobilization in the upper bulk layers of the anode, but could originate from an improved contact area directly at the anode/separator interface [230].

Silicon-Graphite Anodes for Li-Ion Batteries

CHAPTER 7

In this chapter, the lithium accumulation in silicon-containing anodes during the first cycle (c.f. Sec. 7.1) and during extended (dis-)charge cycling (c.f. Sec. 7.2) probed by NDP is presented. NDP reveals the anode swelling as well as the homogeneity of the (ir-)reversibly accumulated lithium concentration profile. While this work focuses on the analysis of the NDP measurements, the investigated SiG electrodes were prepared and operated by our cooperation partner M. Wetjen from the Lehrstuhl für Technische Elektrochemie (TEC) group of the Chemistry Department at TUM. Based on the results presented in this chapter, three articles are published [118, 231, 232].

7.1 Lithium Accumulation During the First (Dis-)Charge Cycle

Silicon is one of the most promising candidates for lithium-ion battery anode materials for the near future [48, 249]. In contrast to graphite, where upon charging lithium is physically intercalated into the layered graphite structures forming LiC_6 , silicon is undergoing an amorphous Li_xSi phase until a crystalline $\text{Li}_{15}\text{Si}_4$ or $\text{Li}_{22}\text{Si}_5$ compound alloy has formed [249–251]. Hence, also the theoretical capacity of silicon, exceeding $4000 \text{ mAh/g}_{\text{Si}}$, vastly outperforms the theoretical capacity of conventional graphite of $372 \text{ mAh/g}_{\text{C}}$ [48]. However, silicon anodes show volumetric changes during cycling and a rapid capacity fade over a few (dis-)charge cycles, which hampers their applicability in secondary lithium-ion batteries [249].

Here, an established composite silicon-graphite (SiG) system was examined, which had previously been investigated in several studies [252–256]. They consist of a porous mixture of 35 wt.% silicon nanoparticles ($\approx 200 \text{ nm}$ length), 45 wt.% graphite particles ($\approx 20 \mu\text{m}$ length), 10 wt.% carbon fibers, and 10 wt.% lithium poly(acrylate) binder (LiPAA) doctor-blade coated onto a $20\text{-}\mu\text{m}$ -thick copper current collector.

A major contribution to the irreversible capacity loss at the anode is caused by chemical reduction of previously active lithium at the anode/electrolyte surface. This SEI formation plays a dominant role during the first (dis-)charge cycles in order to form the initial passivation layer

covering the graphite particle surface. Here, the lithium accumulation within SiG-based anodes was studied during the first (dis-)charge cycle. Twelve identically coated SiG anodes with an average mass loading of $(1.41 \pm 0.02) \text{ mg/cm}^2$ were assembled in CR2032 coin-cells¹ and cycled versus lithium metal serving as lithium donor at a symmetric (dis-)charging rate of C/10, i.e. one complete (dis-)charge within 10 hours. The SiG anodes were then extracted after defined state-of-charges (SOC) and depth-of-discharges (DOD) of 20, 40, 60, 80, and 100 %, respectively. After subsequent disassembling in an argon-filled glovebox, the anodes were rinsed using dimethyl carbonate (DMC) to remove residues of the liquid electrolyte. Hereby also the relaxation of possible concentration gradients was slowed down. The disassembled anodes were then *ex situ* examined using the N4DP demonstration experiment (Setup II). In total, 12 different anodes were investigated.

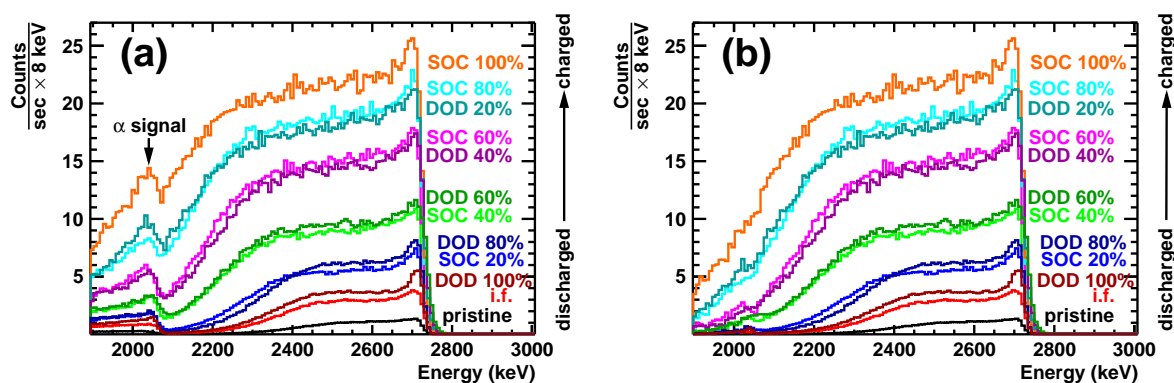


Figure 7.1: (a) *Ex situ* measured energy spectra obtained from SiG anodes during the first (dis-)charge cycle, as published in [232]. (b) Spectra of separated ^3H signals, which were then used to obtain the lithium concentration profile in the SiG anodes [232].

In Fig. 7.1 a, the energy spectra obtained from the SiG anodes at different SOC (DOD) are shown. A pristine anode was measured (black line), also to quantify the lithium content from the LiPAA binder only. After the initial formation stopped at 0.25 V vs. Li/Li⁺ a higher ^3H signal intensity is observed (i.f., red line) to that of the pristine anode (black line), indicating a lithium accumulation in the formed SEI layer. Towards greater SOC the signal intensity further increases, indicating an ongoing lithium accumulation in the anode. Upon battery operation, three sources of lithium are present in the anode: 1) lithium from the LiPAA binder, 2) active lithium ions reversibly incorporated into the anode, and 3) lithium irreversibly immobilized via electrochemical reduction on the SiG particle surface forming a SEI. Since NDP is not sensitive to the chemical state of the detected lithium, these sources are indistinguishable [232].

After fully charging (100 % SOC), the batteries were discharged (towards greater DOD), leading to a depletion of active lithium in the anode: the signal intensity decreases again towards greater DOD, where more and more reversibly attached lithium ions are transferred back from the anode to the counter electrode. Eventually, the fully discharged state (100 % DOD, brown

¹CR2032, Hohen, Japan

line) is reached, where all active lithium ions were extracted and the measured signal originates only from the LiPAA binder and the immobilized lithium.

Furthermore, the ^3H signal width broadens to lower energies upon charging (greater SOC) and returns upon discharging (greater DOD). This indicates that the anode mass loading increases (decreases) upon greater SOC (DOD). This is caused by the additional material accumulation (depletion) on the anode upon charging (discharging). Starting from ≈ 2 MeV to lower energies, the α charged-particle signals from the $^6\text{Li}(n,\alpha)^3\text{H}$ reaction partially overlap with some of the ^3H signals at greater SOC, where the anodes show an increased mass loading. In contrast to the previous study (c.f. Chap. 6), the charged-particle signals could not be separated during the measurement using a separation foil: A holder for the reproducible use of a separation foil at a fixed position was only implemented later in the N4DP setup and was not available in this preliminary demonstration experiment.

Due to their higher penetration depth, the ^3H particles probe the whole SiG anodes, whereas the α particles only arise from their near-surface volume. Therefore, the ^3H distribution was used as a measure for the lithium concentration profile in the SiG anodes. Integration of the ^3H signals was used to quantify and compare the total amount of lithium accumulated in the anodes. Since the integration is biased by the overlap with the α signals, a mathematical separation method was derived, which is based on the well-known difference of the energy losses of the ^3H and α particles. This method is discussed and verified on a measurement with a separation foil in more detail in the next section. The mathematically separated ^3H signals are shown in Fig. 7.1 b.

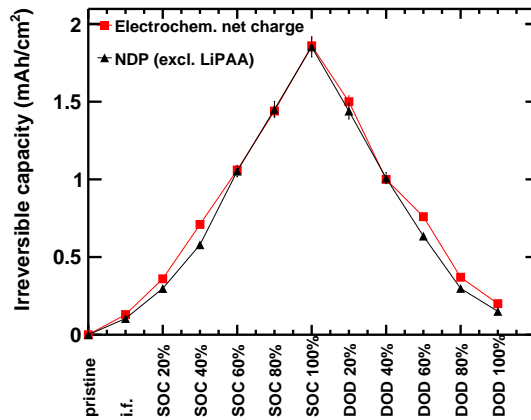


Figure 7.2: Capacity stored in the SiG anodes measured using NDP (black triangles) compared to the capacity measured during cell operation (red squares). The two measurements are in good agreement [232].

Integrating the signals yields the total amount of lithium accumulated in the anodes. Assuming a single electric charge for the lithium ions during operation, the capacity in the form of lithium ions within the SiG anode was compared to the electrochemical capacities observed during (dis-)charging. The contribution from the LiPAA binder was subtracted from the results, since the lithium in the binder carries no electric charge during battery operation. As shown in Fig. 7.2, the capacity observed in the lithium distribution within the SiG anodes agrees quantitatively

with the capacity measured during battery cycling and only a few data points are outside of the measurement uncertainties probably originating from variations during sample preparation. Therefore, the major part of the electric charges is transferred as lithium ions to the SiG anode, and no other parasitic reactions could be observed. The integrated capacities accumulated in the anodes show that $(76.6 \pm 0.4)\%$ of the SEI accumulated after the first (dis-)charge cycle at 100 % DOD was already formed after the initial formation (i.f.) step.

Eventually, the separated ^3H signals were used to determine the lithium concentration profiles of the SiG anodes. The composition of the SiG anodes varies over a wide range due to the different SOC and DOD states, which influences the specific energy loss of the ^3H charged particles as described in Sec. 4.2. In order to take into account this variation of the material stopping power, the SiG anode compositions were modeled based on three different mass contributions: (i) the well-known composition of the pristine SiG anode (35 wt.% Si, 55 wt.% C, 10 wt.% LiPAA), (ii) the mass of the observed lithium accumulated in the anodes at different SOC/DOD states, and (iii) the mass of the decomposition products (SEI) formed in the anodes determined by weighing each anode and subtracting the masses of the previous contributions. Previous studies on SiG anodes revealed the elemental composition of the SEI [252]. The modeled elemental anode compositions are listed in Tab. 7.1. Based on the SRIM software, the variation in the stopping power due to the composition change was estimated to be $< 1\%$ in the investigated region [117]. Due to its lower elemental mass, the influence of lithium on the stopping power is small, even though its contribution to the material composition changes by more than an order of magnitude, as shown in Tab. 7.1.

Anode	H (mol%)	Li (mol%)	C (mol%)	O (mol%)	F (mol%)	Si (mol%)
pristine	5.5	1.8	71.1	3.7	0.0	17.9
i.f.	6.6	6.0	65.7	5.0	0.6	16.1
20 % SOC	7.0	12.5	59.7	5.6	0.9	14.3
40 % SOC	6.7	20.8	53.5	5.4	0.9	12.7
60 % SOC	6.1	27.9	48.8	4.9	0.8	11.6
80 % SOC	5.8	33.5	44.7	4.7	0.8	10.6
100 % SOC	7.3	35.9	40.0	6.4	1.5	8.9
20 % DOD	5.9	33.6	44.3	4.9	0.9	10.4
40 % DOD	6.5	25.7	49.7	5.3	1.0	11.8
60 % DOD	6.8	21.5	52.7	5.6	1.0	12.5
80 % DOD	7.5	12.4	59.0	6.0	1.0	14.0
100 % DOD	7.1	7.8	63.5	5.5	0.8	15.3

Table 7.1: Elemental composition change of the SiG anodes induced by battery operation. In the pristine state, the anode composition is known. The composition was modeled for the different (dis-)charge states by taking into account the accumulated lithium as well as additional decomposition products of the SEI formation.

Assuming a homogeneous material composition with respect to depth, the lithium concentration profiles were calculated using the SRIM software and they are shown in Fig. 7.3 [117, 232]. Like in the previous study (c.f. Chap. 6), the concentration profiles can qualitatively be divided into three parts: (i) a peak near the surface, which could indicate a lithium formation around the investigated particles, but in NDP this effect would be indistinguishable from a true lithium enrichment (c.f. Chap. 6). The peak is already present for the pristine SiG anode, i.e. where lithium can only originate from the LiPAA binder interconnecting the SiG particles, which supports the peak formation based on the morphology when assuming a homogeneous binder distribution with respect to depth. The surface peak grows significantly after the initial formation (i.f.) procedure, indicating that the first SEI layer has formed around the particles within this step. It grows only slightly throughout the subsequent (dis-)charging cycle until eventually 100% DOD is reached and only irreversibly attached lithium is present within the anode. These findings indicate that the major part of the SEI has formed at the anode surface during the initial formation (i.f.) step, which matches the previous observation that after formation, $(76.6 \pm 0.4)\%$ of the lithium irreversibly attached at 100% DOD is present. (ii) For all SOC/DOD states a homogeneous lithium concentration is observed throughout the depth of the anodes. Therefore, the accumulation of active lithium as well as immobilized lithium in the SEI are both formed uniformly across the anodes with respect to depth. (iii) The end of the signals reveal the decreasing depth resolution due to the statistical nature of the energy loss of the charged particles. Here, the mass swelling of the anodes upon charging becomes visible with the inflection point at the end of the signal indicating the anode/current-collector interface. The mass thickness of the SiG anodes is observed to increase ≈ 2 -times from pristine to 100% SOC before it decreases again until at the fully discharged state (100% DOD) a mass thickness $\approx 18\%$ larger than the pristine is reached.

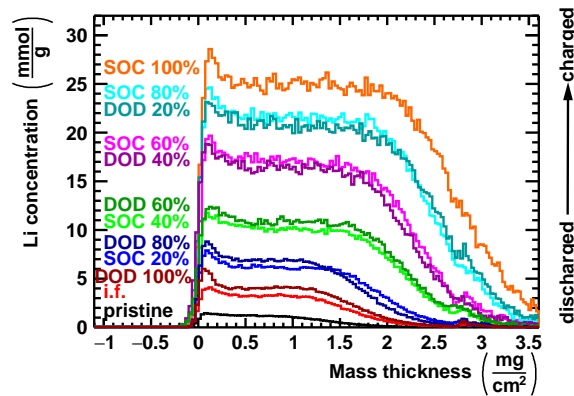


Figure 7.3: Lithium concentration profiles measured in SiG anodes during the first (dis-)charge cycle. Upon charging, lithium is accumulated in the anodes until 100% SOC is reached. During discharging, active lithium is removed from the anodes, while irreversibly attached lithium remains even in the fully discharged state (0% SOC). Independent of the SOC states, a homogeneous lithium distribution with respect to the depth is observed. Reproduced from [232].

7.2 Lithium Immobilization During Extended Cycling

In a next step, the development of the lithium immobilization during extended (dis-)charge cycling was studied. First, the SiG anodes were operated at two formation cycles at a C-rate of 1/10 ($\approx 0.2 \text{ mAh/cm}^2$) between $\approx 0.01 \text{ V}$ and $\approx 1.25 \text{ V}$ vs. Li^+/Li to form an initial SEI layer [231]. In order to study the passivation layers formed upon extended cycling, the anodes were then symmetrically cycled at a C-rate of 1/2 ($\approx 1.0 \text{ mAh/cm}^2$) with respect to their theoretical capacity of $\approx 2.0 \text{ mAh/cm}^2$. Using a final lithiation to 0.01 V vs. Li^+/Li and full delithiation to $\approx 2.0 \text{ V}$ vs. Li^+/Li at a C-rate of 1/50 all active lithium was extracted from the SiG anodes. The anodes were then harvested after 1, 5, 20, 40, 60, 80, 100, 120 and 140 completed number of (dis-)charge cycles in an argon-filled glovebox² (H_2O and O_2 concentration $< 0.1 \text{ ppm}$) and rinsed using $50 \mu\text{l}$ of dimethyl carbonate (DMC) to remove residuals of the lithium salt from the liquid electrolyte. Therefore, the remaining lithium in the SiG anodes could be ascribed to originate from the LiPAA binder or the lithium-containing electrolyte decomposition products (SEI), observed as irreversible capacity loss. After sealing the anodes in argon-filled boxes, the anodes were transported to the PGAA facility and were measured using the N4DP demonstrator experiment (Setup II).

The NDP energy spectra of the SiG anodes are shown in Fig. 7.4. For the pristine anode (0 cycles, black line), the ^3H and α signals are separated. Upon charging, immobilized lithium accumulates in the anodes, thus increasing the signal intensity. Furthermore, the ^3H signal broadens towards lower energies for greater cycling, indicating a mass thickness growth induced by the immobilized lithium in the anode. Starting from 20 cycles, the onset of the α signal starts superimposing with the low-energy tail of the ^3H signal. Even at greater cycle numbers, an additional signal arising at 1.47 MeV is observed, which superimposes with the two signals from lithium detection. This signal was ascribed to α particles from boron stemming from glass fiber residuals from the separator located on top of the anodes. Both α particle contributions (1.47 MeV , 2 MeV) superimpose with the ^3H signal and affect a quantitative concentration analysis.

Therefore, a mathematical signal-separation approach is presented and exemplarily shown for the SiG anode which was (dis-)charged 60 times. The measured signal is shown as black line in Fig. 7.4 b. Both ^3H and α signals from the $^6\text{Li}(n,\alpha)^3\text{H}$ reaction arise from the same lithium profile within the SiG anodes. Only the specific energy losses of the charged particles is different which probe this lithium distribution. The differences of the two energy losses originate from the well-known particle properties and were used to calculate one signal shape from the other. Therefore, the lithium concentration distribution in the upper layers of the SiG anode was determined from the high-energy part of the ^3H signal, as shown as red-line in Fig. 7.4 b. This layer represents the whole region from which also the α particles can reach the detector before losing their kinetic energy. Since the actual concentration profile at the near surface is

²MBraun

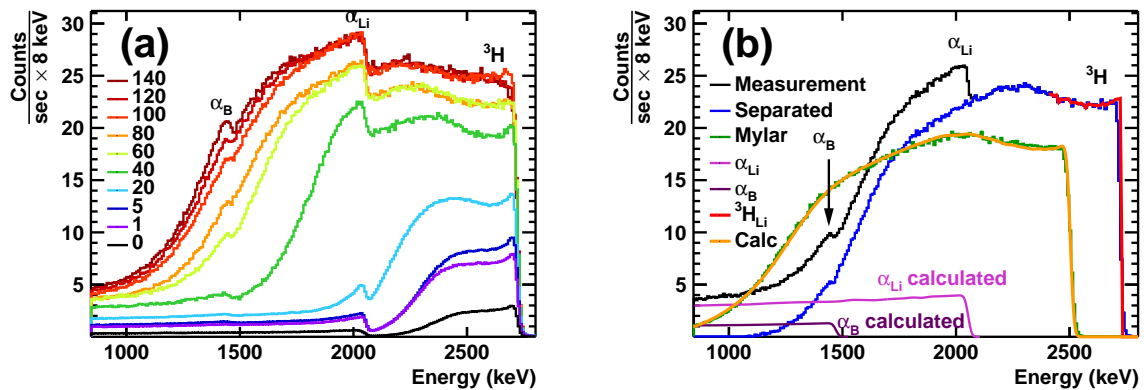


Figure 7.4: (a) Energy spectra *ex situ* obtained from extended SiG anodes. Upon greater cycles the signal intensity increases, which indicates an ongoing lithium immobilization in these anodes. Furthermore, the 3H signals broaden to lower energies, until they eventually overlap with two α contributions. Reproduced from [118]. (b) Mathematical separation method showed on the 60 cycles anode (black). From the onset of the 3H signal (red) the α contribution is calculated (pink). For boron a homogeneous distribution was assumed (purple). A measurement of the anode using a separation foil (green) proves the shape of the separated 3H signal (blue) taking into account the influence of the separation foil (yellow). Reproduced from [118].

measured by the detector resolution, the 3H signal was extrapolated to the surface and an ideal step-function was assumed. This assumed lithium distribution was then forward mapped using the response function of α particles in the SiG matrix (c.f. Chap. 4). The expected α signal is shown as pink line in Fig. 7.4 b. The signal height difference arises from the different stopping powers of α and 3H particles. It was then subtracted from the measured curve (black line). Even though the α signal superposition from lithium accounts for the main part of the 3H signal distortion, also a small correction was performed taking into account the boron contribution from the glass fibers. A homogeneous boron distribution was assumed within the glass fibers. The respective α signal of a homogeneous boron distribution is shown as a purple line. The height of the signal reflects the amount of glass fiber residuals on top, which was different for each sample. The signal height was chosen such that the resulting 3H signal was continuous in the region of overlap. The resulting 3H signal after subtracting both α contributions (pink, purple) is shown as blue line.

In order to verify the mathematically separated 3H signal, the 60 cycled SiG anode was additionally measured using a nominally 6- μm -thick Mylar separation foil between sample and detector. In the NDP demonstrator setup (Setup II) no standard holder was present for the separation foil and thus the foil was placed between the sample and the detector on a provisional frame. The measured signal is shown in Fig. 7.4 b as green line. Contributions by charged particles with atomic numbers $Z > 1$ are moved outside of the 3H signal. The energy loss and broadening induced by the separation foil was then calculated based on the SRIM software and applied to the previously mathematically separated signal (blue line) [117]. Since the separation foil could not be placed directly on sample or detector, additional scattering and straggling effects might

have lowered the signal rate of the green curve and so the height of the calculated profile (yellow line) was reduced to match that of the green curve. Hereby, the shape of the calculated (yellow line) and measured signal using a separation foil (green line) was found to match, which confirms the shape of the ^3H signal (blue line) previously obtained by the mentioned mathematical separation method.

The ^3H signals after subtracting α contributions from boron and lithium are shown for all SiG

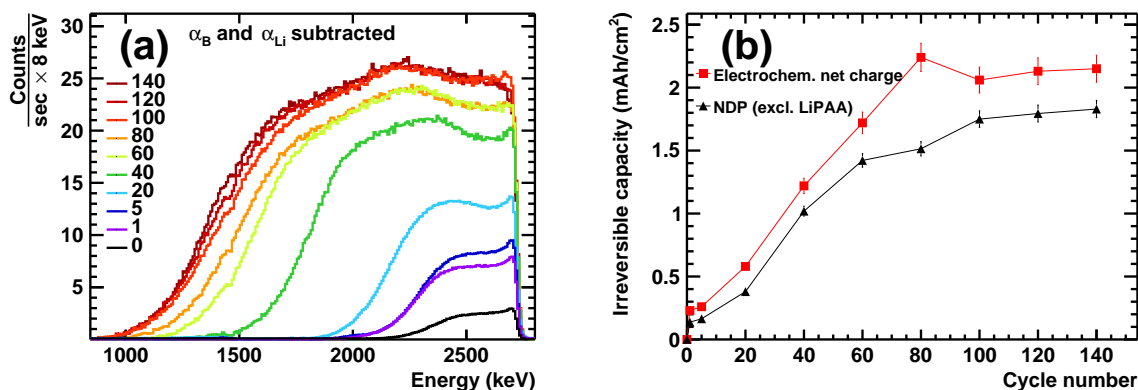


Figure 7.5: (a) Mathematically separated ^3H signals of the SiG anodes upon extended cycling. Reproduced from [118]. (b) The total lithium accumulated in the SiG anodes (black triangles, obtained by integrating the energy spectra) are compared to the irreversible capacity obtained during battery operation (red squares). The main driving mechanism for the capacity fade was identified as the lithium immobilized in the anode. Reproduced from [231].

anodes in Fig. 7.5 a. The spectra were then integrated to calculate the total lithium amount irreversibly attached throughout the whole SiG anode. Assuming a single charge, the irreversibly attached lithium in the anodes was compared to the irreversible capacity loss observed during battery operation and it is shown in Fig. 7.5 b. Hereby the lithium amount stemming from the LiPAA binder was subtracted by taking into account the lithium amount in the pristine SiG anode. Both curves show the same trend, i.e. a growth with subsequent saturation of irreversible capacity and irreversibly attached lithium in the anode. On average, $(75.2 \pm 9.8)\%$ of the electrochemically measured irreversible capacity is observed using NDP as inactive lithium in the SiG anodes, showing that the loss of active lithium on the anodes is the main driving process of the electrochemical capacity fade. The difference might arise from the rinsing procedure of the SiG anodes after dismounting them, but further side reactions during operation can not be excluded, either. The 80-times cycled anode showed a slightly different (dis-)charging behavior during operation probably caused by a difference in the manufacturing of the lithium-ion battery and thus an unusually high irreversible capacity was observed. At the same time, a lithium depletion in the anode was seen using NDP. This hints to lithium-consuming side reactions in the lithium-ion battery outside of the SiG anode, which might be dominant for this sample due to an unwanted variation in the fabrication process.

In order to later calculate the concentration profiles from the separated ^3H signals shown in

Fig. 7.5 a, first the SiG anode composition change upon operation was taken into account, since it influences the specific energy loss for the charged particles. Not only the irreversibly attached lithium contributes to the composition change, but also the electrolyte is reduced when the SEI is formed. Jung *et al.* reported that for the SEI formation in SiG-based anodes 4 lithium ions are consumed to chemically reduce one $C_3H_3FO_3$ molecule from the electrolyte, and it forms different reduction products like CO_2 , LiF , Li_2O , Li_2CO_3 , and H_2 , which can then be further reduced at the anode [252]. Even though the exact ratio of the reduction products are unknown, the elemental ratio stays constant, which means four lithium ions are consumed for one $C_3H_3FO_3$ molecule and the anode composition was corrected for the elemental composition of this reaction. The entire irreversibly attached lithium in the anode, obtained from the integrals shown in Fig. 7.5 b, were assumed to be consumed in this reduction reaction. The resulting compositions are listed in Tab. 7.2.

Anode	H (mol%)	Li (mol%)	C (mol%)	O (mol%)	F (mol%)	Si (mol%)
pristine	5.5	1.8	71.1	3.7	0.0	17.9
1 cycle	7.6	5.4	64.5	6.0	0.9	15.5
5 cycles	8.0	6.0	63.5	6.4	1.1	15.1
20 cycles	10.2	9.8	56.3	9.0	2.1	12.5
40 cycles	14.0	16.1	44.7	13.1	3.8	8.4
60 cycles	15.3	18.2	40.6	14.6	4.4	6.9
80 cycles	15.5	18.6	39.9	14.8	4.5	6.6
100 cycles	16.0	19.5	38.2	15.4	4.7	6.0
120 cycles	16.1	19.7	38.0	15.5	4.8	5.9
140 cycles	16.2	19.8	37.8	15.6	4.8	5.9

Table 7.2: Elemental composition of the SiG anodes. The elemental composition changes during battery operation due to reduction reactions occurring in the SiG anodes. In the pristine state, the anode composition is known. The composition was modeled for the different (dis-)charge states by taking into account the accumulated lithium as well as additional decomposition products of the SEI formation.

The SiG anode composition change affects the specific energy loss of the 3H particles in the investigated energy regime up to $\frac{\text{pristine}}{140 \text{ cycles}} \approx 4\%$ [117]. Assuming homogeneous compositions throughout the depth of the anodes, the 3H signals were then translated to lithium concentration profiles, which are shown in Fig. 7.6 a. Here, the mass thicknesses of the SiG anodes are swelling over 100 (dis-)charge cycles to ≈ 3 -times of that of the pristine anode [118]. At the same time, complementary cross-section SEM images, shown in Fig. 7.6 b, reveal a swelling of the previously $(18.7 \pm 0.3)\text{-}\mu\text{m}$ -thick pristine anode to $(57.7 \pm 1.2)\text{ }\mu\text{m}$ when cycled 100 times, which is $(309 \pm 11)\%$ [118]. Both observations agree well, and so the mass thickness $m_A = d\rho$ probed with NDP is almost completely based on a thickness increase, while the bulk anode density stays fairly constant for all (dis-)charging states.

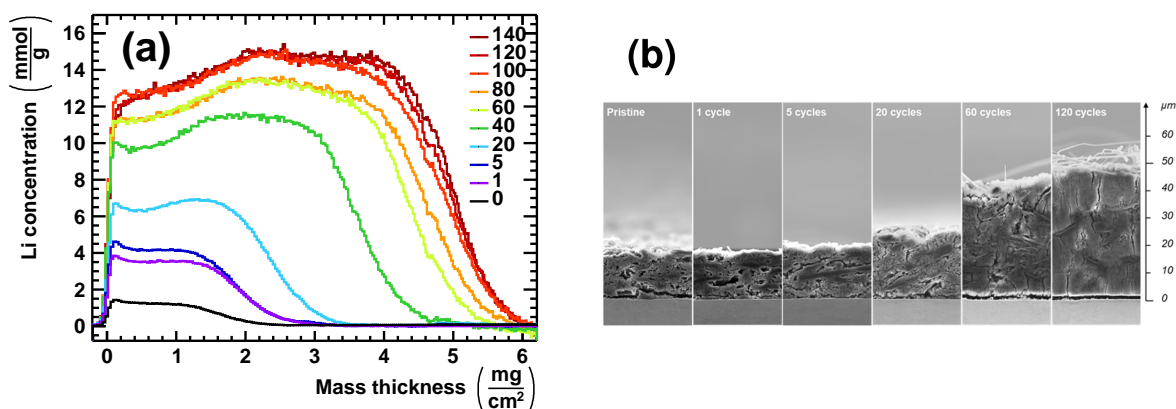


Figure 7.6: (a) Lithium concentration profiles obtained from the ^3H particle signals assuming the individual SiG anode compositions [118]. (b) Cross-section SEM images showing the thickness change of the SiG anodes upon extended (dis-)charge cycling, as published in [231]. On top of the anodes, residuals from the boron-containing glass fiber separator are observed.

Until the first five (dis-)charge cycles, the shape of the concentration profiles of the immobilized lithium shown in Fig. 7.6a stays constant while the intensity increases, indicating that during each cycle more lithium is immobilized homogeneously over the depth of the SiG anode. From 20 cycles on, a small lithium enrichment at the backside of the SiG electrodes (i.e. the electrode-current collector interface) starts growing, which extends for further cycle numbers. This might indicate a slightly improved active material utilization close to the electrode-current collector interface. The risk of the electrical isolation of silicon particles may be higher in the outermost electrode layers compared to the electrode bulk. In contrast, no ionic transport limitation can be observed which would favor the active material utilization in layers near the anode/electrolyte surface. Overall, an almost homogeneous active material utilization across the electrode depth is observed upon further cycling.

The peak at the anode surface, which might originate from the morphological formation of lithium on the surface of the SiG particles, decreases during the first 60 cycles and eventually vanishes up to 140 cycles. This might indicate a morphological change of SiG particles on which the lithium is irreversibly attached. First, lithium could only accumulate on the surface of the SiG particles, giving rise to volumes with lower lithium content within the SiG particles. This might not be the case for greater cycle numbers where the NDP signals indicate a lithium incorporation into the volumes previously protected from the electrolyte, resulting in an ongoing depletion of the peak at the surface. This morphological change has previously been observed by Wetjen *et al.* using transmission-electron-microscopy (TEM) on SiG anodes [254]. The SiG particles were observed to form at first closed volumes, which swell up at larger cycle numbers allowing for electrolyte reduction within volumes which were previously not in contact with the electrolyte. This clogging of the particles was later also confirmed in a different study based on Small-Angle Neutron Scattering (SANS) [56].

7.3 Conclusion

Here, the lithium accumulation in silicon-graphite-based (SiG) anodes was studied using NDP. Due to its high theoretical capacity, silicon is a promising material to substitute common graphite-based anodes. However, SiG anodes undergo a huge volumetric change upon operation, which was directly observed using NDP. Here, a mass thickness swelling of ≈ 2 -times upon the first charging and subsequent decrease to $\approx 118\%$ of the pristine mass thickness was observed during discharging. Upon extended cycling, also the mass thickness in the fully discharged anode increases to ≈ 3 -times during 100 (dis-)charge cycles. Furthermore, a large lithium immobilization in the SiG anodes was observed, leading to a fade of the initial capacity of $\approx 50\%$ after 140 complete (dis-)charge cycles. Here, $\approx 75\%$ of the irreversible capacity was observed to be present as immobilized lithium in the anodes, leading to particle clogging. This lithium immobilization in the anodes is hence the main driving process of the capacity loss.

Operando Investigation of Lithium Transport in Graphite Anodes

CHAPTER 8

In order to avoid possible lithium losses induced by harvesting anodes *post mortem* for *ex situ* NDP measurements, *operando* NDP measurements on commercially relevant graphite anodes were performed here for the first time. Two *operando* studies are presented in this chapter. In Sec. 8.1, the lithium accumulation during the first (dis-)charge cycle at a low symmetric (dis-)charging rate (C/16) is probed (formation study). In Sec. 8.2, the lithium accumulation at elevated charging rates up to 2C is followed and lithium plating could be observed for the first time in graphite-based anodes using NDP (fast charging study). While this work focuses on the analysis of the NDP spectra, all findings presented in this chapter result from a cooperation with F. Linsenmann and P. Rapp from the Lehrstuhl für Technische Elektrochemie (TEC) group of the Chemistry Department at TUM, who prepared and operated the electrochemical cells. These results of the formation study are published in [170] and an article based on the findings of the fast charging study is in preparation [68].

8.1 *Operando* Lithium Intercalation During Formation

First, the lithium accumulation in a graphite anode during the first (dis-)charge cycle of battery operation was followed using the N4DP Setup I. The lithium-ion battery was symmetrically (dis-)charged at C/16 ($\approx 39 \mu\text{A}$) for three half cycles. The voltage profiles of the investigated graphite/LFP cell is shown in Fig. 8.1 a. The (dis-)charging processes are indicated with arrows. A reversible capacity of $\approx 348 \text{ mAh/g}_{\text{graphite}}$ was observed, which is close to that of $\approx 355 \text{ mAh/g}_{\text{graphite}}$ of a conventional coin cell, showing a good performance of the *operando* coin cell [170]. A rather high irreversible capacity of $\approx 98 \text{ mAh/g}_{\text{graphite}}$ was observed, probably originating from the increased surface area (BET area) of the sieved graphite particles (c.f. Chap 5) [170].

The continuous NDP spectra were divided into 1 h intervals and are shown in Fig. 8.1 b for

seven distinct SOC states. The first three profiles (black lines) show the profiles during the first half cycle (charging) in the pristine state (1), at $\approx 50\%$ SOC (2) and at 100% SOC (3), the blue lines indicate the profiles during the second half cycle (discharging) at $\approx 50\%$ DOD (4) and 100% DOD (5) and the spectra of the last half cycle (charging) is shown as red lines at $\approx 50\%$ SOC (6) and 100% SOC (7). The positions of the different SOC are also indicated in Fig. 8.1 a. The high-energy onset of the spectra are at (2163 ± 10) keV, which depicts the anode/charged-particle window interface. No signal shift to greater energies was observed during the experiment indicating that the Kapton[®] foil was indeed impermeable for the lithium-containing electrolyte. The signal onset can be used as a precise measure of the gas pressure within the NDP chamber: taking into account the experimentally determined energy loss to (301 ± 0.6) keV for the Kapton[®] foil and the calculated energy loss to ≈ 11 keV for the 100-nm-thick copper current collector, about (248 ± 10) keV can be ascribed to ^3H energy loss in the helium atmosphere [168]. It corresponds to a helium mass thickness of (0.72 ± 0.03) mg/cm² [168]. Assuming a sample to detector distance of 96.1 mm (c.f. Sec. 3.1.3), this translates to a helium gas pressure of (420 ± 18) mbar.

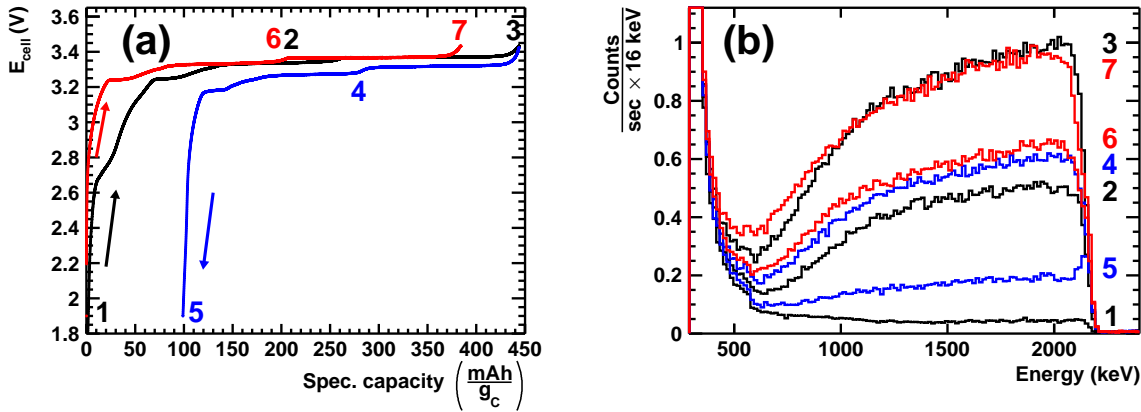


Figure 8.1: (a) The cell potential profiles for the *operando* formation study over three half cycles at C/16. A good reasonable capacity (≈ 348 mAh/g_{graphite}) is observed [170]. (b) NDP spectra recorded over the course of 1 h for distinct states of (dis-)charges also indicated in a. Upon (dis-)charging, the signal intensity increases (decreases) indicating lithium enrichment (depletion) within the anode. At low energies the exponential background dominates the spectra.

At low energies (< 500 keV), the spectrum is dominated by the exponential background induced by β and γ radiation (c.f. Chap. 4). During cell operation, the lithium content in the graphite anode represented by the ^3H signal intensity rises from the pristine state (1) upon charging (2, 3), decreases (4, 5) in the second half cycle until the fully discharged state (5), and increases during the third half cycle upon charging again (6, 7). In the pristine state, the only source of lithium is the LiPF_6 salt in the liquid electrolyte. This contribution is still present in all following SOC, while both the reversibly and irreversibly attached lithium accumulates in the graphite anode. Since NDP is not sensitive to the chemical state of the lithium, they are indis-

tinguishable. Only in the fully discharged state (5) no reversibly intercalated lithium is present and the main lithium contribution is the lithium irreversibly attached in the SEI.

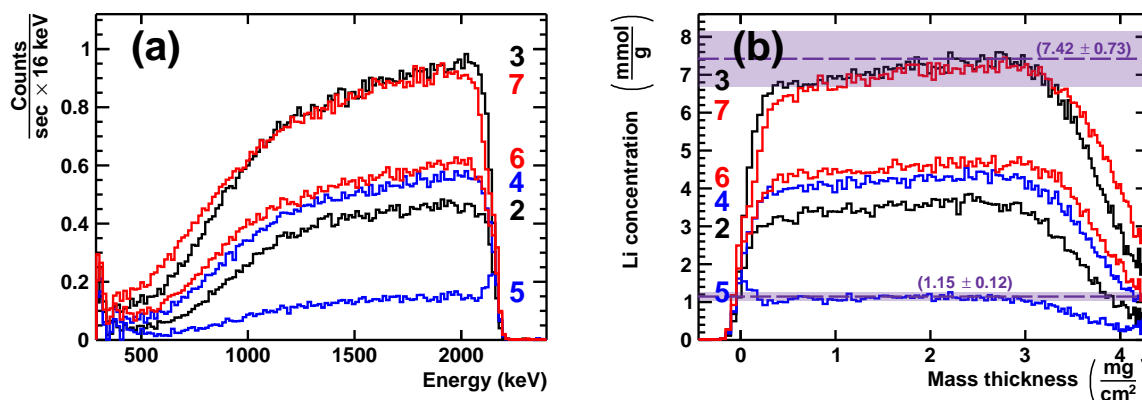


Figure 8.2: (a) Energy spectra of the *operando* graphite anode at distinct SOC states. In order to remove the low-energy background and to distinguish the accumulated lithium from that in the electrolyte, the spectrum of the pristine graphite anode was subtracted, where lithium entirely originated from LiPF_6 in the electrolyte [170]. (b) Lithium concentration profiles obtained from the background-subtracted energy spectra (c.f. Fig. 8.2 a). While during operation reversibly and irreversibly attached lithium are indistinguishable, the concentration profile in the fully discharged state (5) consists only of irreversibly attached lithium in the SEI.

In order to remove the low-energy background and to probe the change in lithium concentration upon battery operation, the pristine signal (1) was subtracted from all other signals, as shown in Fig. 8.2 a. For the calculation of the stopping power, the elemental composition of the pristine anode, based on its preparation procedure (c.f. Chap. 5), was used together with the composition of the liquid electrolyte (containing 1 M LiPF_6) assuming a complete filling of the $\approx 47\%$ porous graphite anode. The composition change of the filled electrode upon operation was determined with integrating the subtracted energy spectra (Fig. 8.2 a). The electrode compositions at different SOC were then corrected for the additional lithium amount observed in the anode and they are listed in Tab. 8.1.

During battery operation, the liquid electrolyte (EC/EMC with 1 M LiPF_6) is electrochemically reduced at the anode surface and thus forming various reduction products mainly given by LiF, lithium ethylene dicarbonate (LEDC), lithium methyl carbonate (LMC), and lithium ethyl carbonate (LEC) [257]. Therefore, upon harvesting the anodes, additional SEI material would be observed on the anode for an *ex situ* measurement. However, for *operando* anodes, the elements of the liquid electrolyte then being electrochemically reduced at the anode surface are already present around the graphite particles and were therefore previously considered for the calculation of the pristine composition within the anode pores.

This is shown in Fig. 8.3 for greater clarification. In the pristine state (Fig. 8.3 a), the liquid electrolyte surrounds the graphite particle and thus all elements later forming the SEI other than lithium are already present within the graphite anode. Lithium in the SEI stemming from

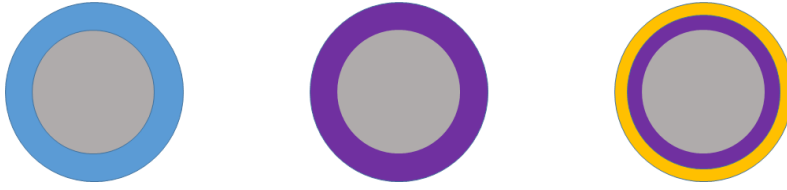


Figure 8.3: Composition change of the electrolyte-filled anode. First, the graphite particles (gray) are surrounded by liquid electrolyte (blue), as shown in (a). Upon electrochemical reduction, the liquid electrolyte is forming an SEI around the particles, as shown in (b). As a good approximation, the density of the nm-thick SEI layer is considered to be similar to that of the electrolyte and the elemental composition remains constant. In reality, the SEI forms a thin layer around the particles with a slightly higher density, thus allowing for electrolyte afterflow (yellow) into the anode, as shown in (c).

lithium ions electrochemically transferred from the LFP cathode into the graphite anode and will be separately considered. At an elevated anode potential, electrochemical reduction of the liquid electrolyte occurs, as shown in Fig. 8.3b. Hereby, the reduced elements are still located surrounding the graphite particle and therefore the elemental composition of the whole system is not altered. It is to state that in reality also more complex reduction processes like gas formation might occur which can also be further reduced at the anode surface. However, due to the liquid-solid phase transition of the electrolyte, the material density might slightly increase from that of the liquid electrolyte ($\approx 1.2 \text{ g/cm}^3$). The reduced electrolyte volume would then allow a consecutive afterflow of fresh liquid electrolyte (orange volume in Fig. 8.3c) which would then change the total elemental composition. Even though to the best of our knowledge the exact molecular SEI composition as well as the resulting SEI density are unknown, the graphite density of $\rho_{\text{graphite}} \approx 2.2 \text{ g/cm}^3$ may serve as a realistic upper limit. Assuming a maximum SEI density equivalent to that of graphite ($\rho_{\text{graphite}} \approx 2.2 \text{ g/cm}^3$), the previous liquid electrolyte would be electrochemically reduced to $V = \frac{\rho_{\text{EI}}}{\rho_{\text{graphite}}} V_0 \approx 55\%$ of its liquid volume and thus $\approx 45\%$ could be refilled with fresh electrolyte. Taking into account that over 50% of the graphite particles

Anode SOC	H (mol%)	Li (mol%)	C (mol%)	O (mol%)	F (mol%)	P (mol%)
Pristine (1)	22.0	0.3	64.8	9.1	3.6	0.3
50 % (2)	21.3	3.5	62.7	8.8	3.5	0.3
100 % (3)	20.5	6.9	60.5	8.5	3.3	0.3
50 % (4)	21.1	4.3	62.2	8.7	3.4	0.3
0 % (5)	21.8	1.4	64.1	9.0	3.5	0.3
50 % (6)	21.0	4.6	62.0	8.7	3.4	0.3
100 % (7)	20.5	6.9	60.5	8.4	3.3	0.3

Table 8.1: Elemental composition of the graphite anode upon operation, as published in [170]. The pristine anode composition was obtained from the composition of the graphite anode upon operation, while assuming complete pore filling with the liquid electrolyte. Upon operation, lithium accumulating in the electrode was determined with integrating the NDP spectra across their depths.

exhibit a diameter of $d_{50} \approx 6 \mu\text{m}$ and assuming a final SEI formed around the particle with a typical thickness in the (10–100) nm range, then $\approx (0.8\text{--}8) \%$ of the graphite volume could be refilled with fresh electrolyte around the particle [258]. Furthermore, the graphite anode exhibits a porosity of $\approx 47 \%$, meaning that 53% of the anode volume consists of a graphite/PVDF mixture. Thus, $\approx (0.4\text{--}4) \%$ of the total anode volume could be refilled with fresh electrolyte, which is only (0.9–9)% of the total electrolyte volume previously present within the pores of the graphite anode. As a good approximation, the electrochemical reduction itself does not significantly influence the elemental composition of the pristine anode filled with electrolyte. However, the major part of the composition change given by lithium ions electrochemically transferred from the LFP cathode into the graphite anode was determined with integrating the NDP spectra (c.f. Tab. 8.1).

The elemental compositions listed in Tab. 8.1 were used to calculate the combined stopping power of the graphite anode assuming a constant composition with respect to depth. The lithium concentration profiles of the separated SOC signals (c.f. Fig. 8.2 a) are shown in Fig. 8.2 b. The previously discussed uncertainty of the NDP measurement (9.8%) is indicated, mainly (9.1%) originating from the geometrical uncertainty of the coin cell grid placed in the neutron beam. It is to note that this is a systematic uncertainty being constant for all SOC and thus the ratio of the different SOC can be determined with higher precision. After translating the energy spectra to depth profiles, a rather flat lithium concentration profile is observed indicating that a rather homogeneous lithium accumulation takes place within the graphite anode. However, a slight linear gradient towards greater depths is still visible. Although an uncertainty of the SRIM-based energy loss calculation can not be excluded, it might originate from partial scattering of the ^3H particles into the edges of the stainless-steel cap. This would artificially lower the signal near the surface and it would be driven by the geometrical aspect ratio of the 500 μm holes in the 250- μm -thick coin cell cap.

The observed lithium concentrations at 100% SOC after the first half cycle (spectrum 3) and after the third half cycle (spectrum 7) show an almost identical profile. This indicates that the SEI formation was completed prior to the first fully charged state (first half cycle) and in the later charging process no significant amount of SEI layers have formed. Therefore, the difference of the lithium concentration observed in the fully charged state (spectra 3, 7), being $(7.42 \pm 0.73) \text{ mmol}_{\text{Li}}/\text{g}_{\text{electrode}}$ and the lithium concentration $(1.15 \pm 0.12) \text{ mmol}_{\text{Li}}/\text{g}_{\text{electrode}}$ observed as irreversibly attached lithium in the SEI (spectrum 5) reflects the reversibly intercalated lithium concentration of $(6.28 \pm 0.61) \text{ mmol}_{\text{Li}}/\text{g}_{\text{electrode}}$ in the anode. Based on the electrochemically observed reversible capacity of $\approx 348 \text{ mAh}/\text{g}_{\text{graphite}}$, the mass of the charged electrode of $(4.04 \pm 0.23) \text{ mg}$, a LiPF_6 concentration in the electrolyte of $(1.00 \pm 0.01) \text{ mol}/\text{l}$ and a ratio of $1 \text{ Li}/\text{e}^-$, a lithium concentration of $(6.41 \pm 0.48) \text{ mmol}_{\text{Li}}/\text{g}_{\text{electrode}}$ is obtained. This value agrees well with the intercalated lithium concentration of $(6.28 \pm 0.61) \text{ mmol}_{\text{Li}}/\text{g}_{\text{electrode}}$ previously derived from the NDP measurements thus confirming these calculations [170].

In the next step, the concentration of the SEI of $(1.15 \pm 0.12) \text{ mmol}_{\text{Li}}/\text{g}_{\text{electrode}}$ obtained from the NDP measurements is considered. Based on the irreversible capacity of $\approx 98 \text{ mAh}/\text{g}_{\text{graphite}}$

observed for the electrochemical cell and the electrode mass of (3.86 ± 0.23) mg for the fully discharged electrode, a lithium concentration of (1.89 ± 0.15) mmol_{Li}/g_{electrode} would be expected, when assuming a ratio 1 Li/e⁻. A lithium consumption of one lithium atom per electric irreversible charge would be a reasonable assumption, since the major decomposition of EC was previously found in literature to form lithium ethylene dicarbonate (LEDC) and ethylene (C₂H₄) [170, 259]. In contrast to the reversible lithium concentration, a significant difference of the lithium concentration in the SEI expected based on the irreversible capacity of (1.89 ± 0.15) mmol_{Li}/g_{electrode} is observed compared to that of (1.15 ± 0.12) mmol_{Li}/g_{electrode} based on the NDP measurements. This indicates that the Li/e⁻ ratio of the lithium immobilizing in the SEI is (0.61 ± 0.08) being significantly lower than unity. To our knowledge, this difference was observed in this *operando* study for the first time. This value was independently verified by measuring the irreversibly attached lithium in identically fabricated *operando* cells using *ex situ* inductively coupled plasma optical emission spectroscopy (ICP-OES) performed by an external company¹ [260]. Here, (62 ± 4) % of the irreversible capacity could be detected as lithium in the electrode, which agrees well with the results of the NDP measurements.

A possible explanation would be that the intrinsic Li/e⁻ ratio is indeed smaller than 1, but the solubility of the SEI products within the liquid electrolyte might be sufficient to result in a partial dissolution of SEI products thus reducing the amount of irreversibly attached lithium remaining in the electrode [170, 260]. It is to note, that in the electrochemical single cell the mass ratio of the liquid electrolyte compared to graphite is $\approx 160/1$, which is ≈ 200 -times higher than in the large-scale lithium-ion batteries [260–262]. Therefore, a potential SEI dissolution might be favored in the investigated single cell but might be restricted by the SEI solubility within the electrolyte for large-scale lithium-ion batteries.

Apart from the lithium concentration within the graphite anode upon cycling, a lithium enrichment near the surface (the anode/Kapton[®] charged-particle window) is formed during operation, which stays present even in fully discharged state. This lithium accumulation probably originates from a lithium accumulation within the copper current collector, as it has previously been observed using NDP [237, 263]. In order to validate this assumption and exclude a lithium enrichment in the anode itself, two additional cells were measured *in situ*. Here, an uncoated (pure) copper current collector sputtered on the charged-particle window were directly brought into contact with the liquid electrolyte, i.e. the same electrochemical cell but without the graphite anode. One of the cells was then scanned to 20 mV vs. Li/Li⁺, while the other was kept at open circuit voltage (OCV) at 25°C, i.e. without an external electric contact between the electrodes. The *in situ* spectra of the two electrodes are shown in Fig. 8.4 a. While for the reference cell kept at OCV (black line) only lithium in the electrolyte is observed, a lithium enrichment on the inside of the Kapton[®] foil is visible for the cell operated to 20 mV vs. Li/Li⁺. When subtracting the reference measurement from it, the lithium peak is separated, as shown in Fig. 8.4 b. Though the resolution is ≈ 25 keV, which means ≈ 200 nm in copper, the total amount of lithium in copper was found to be $(1.77 \pm 0.17) \times 10^{16}$ Li atoms/cm² by integrating

¹Mikroanalytisches Labor Pascher, Remagen

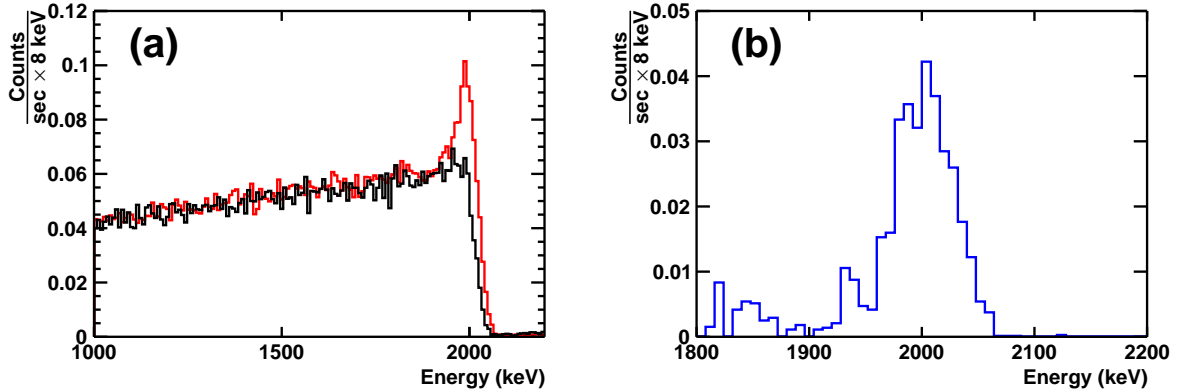


Figure 8.4: (a) *In situ* NDP spectra of a pure 100- μm -thick copper current collector within the electrochemical cell used for *operando* NDP. In contrast to the reference cell kept at open circuit voltage (OCV, black line), where only lithium within the liquid electrolyte is detected, a lithium accumulation within the copper is observed when scanning the cell potential to 20 mV vs. Li/Li^+ . (b) Difference of the spectra reveals the lithium amount intercalated into the copper current collector to be $(1.77 \pm 0.17) \times 10^{16}$ Li atoms/ cm^2 . Pictures taken from [170].

the signal and taking into account the previously discussed uncertainties. Since this amount equals $\approx 0.1\%$ of the reversible capacity, it is hardly visible using electrochemical (dis-)charge measurements. This lithium amount agrees well with previous findings on 10- μm -thick copper current collectors and was also verified using an *ex situ* XPS study [170, 237].

8.2 Lithium Transport Process During Fast Charging

After studying the fundamental process of lithium accumulation during the first (dis-)charge cycle and the ongoing SEI formation, the lithium transport at elevated charging rates was also studied. Here, the cold neutron depth profiling instrument at the NIST Center for Neutron Research (Setup III) was used. The spectra were recorded in intervals of 2 min. In order to increase counting statistics, all lithium sources were enriched in ^6Li to an abundance of $\approx 95\%$ using ^6Li -enriched LFP cathodes from the TEC group of TUM Chemistry Department and a commercial $^6\text{LiPF}_6$ conductive salt [68]. As discussed earlier, a low LiPF_6 salt content of 0.31 mol/l was dissolved in the liquid EC/EMC (3/7 wt.%) electrolyte to allow lithium plating already at low charging rates of $\approx 2\text{C}$ (c.f. Tab. 5.1). After preparation, the cell was formed using three cycles at constant current using a C-rate of C/10, followed by a constant voltage step until the cutoff current of C/40 was reached. It was then sealed under a protective argon atmosphere in an air-tight pouch foil and inertly transported to NIST. Ten days after the preparation, the cell was measured using *operando* NDP.

In order to probe the influence of different charging rates on the lithium accumulation within the graphite anode, the cell was charged at increasing rates of C/4, C/2, 1C, and 2C, while the anodes were always discharged at a rate of C/4 to ensure a complete delithiation of the graphite

electrode. The voltage profile during the *operando* experiment is shown in Fig. 8.5. Here, the end of charge was defined by the cell potential cutoff voltage of 3.41 V_{cell}, followed by a constant voltage phase until the cutoff current of C/20 was reached. For faster charging rates, i.e. C/2, 1C, and 2C, charging was stopped when the theoretical capacity limit of 355 mAh/g_{graphite} was reached [68]. The anode potential may drop below 0 V vs. Li/Li⁺ to maintain sufficient currents for the elevated charging rates, thus allowing for lithium plating to occur.

The spectra of the anode prior to charging (pristine, 0% SOC) and at 100% SOC are shown in Fig. 8.6 a. These signals mainly originate from ³H signals which are dominated at low energies by an exponential background from β and γ radiation (c.f. Chap. 4). At the beginning of the experiment (pristine, 0% SOC), the signal in the anode consists of lithium signal from the electrolyte and irreversible lithium accumulated during the three previous formation cycles. At ≈ 1 MeV, a step-like increase was observed. It does not originate from the NDP setup since it was not observed in the exponential-shaped reference spectrum (gray line Fig. 8.6 a) of an identical reference cell without lithium. It shows ⁶Li enrichment rising at the end of the electrode and might stem from an unusually high lithium content in the volume where the electrolyte is situated. However, a possible formation of an additional SEI at the top surface of the electrode is currently investigated further [68]. Although the origin of the higher lithium concentration outside of the electrode, the lithium accumulation within the electrode can be studied independently with time intervals of 2 min. During charging, the signal intensity from the anode increases, indicating a lithium enrichment in the anode. Here, the previously observed step-like signal was not observed, indicating a shift of the end of the anode to lower energies, i.e. an increase of the electrode mass thickness. This is even better visible in Fig. 8.6 b, where the background was subtracted from the anode spectra. Background was subtracted from all spectra for further

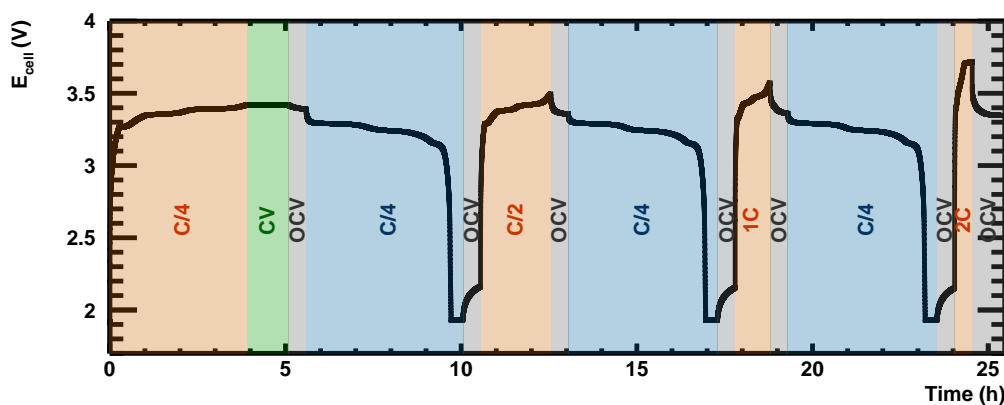


Figure 8.5: Cell voltage profile during the *operando* measurement. While the cell was always discharged (blue areas) at C/4 to ensure complete lithium deintercalation, the charging rate (red areas) was increased from C/4, C/2, 1C up to 2C. While for C/4 a constant voltage phase (CV, green area) was applied until the cutoff current of C/20 was reached, faster charging rates were stopped when the theoretical capacity limit of 355 mAh/g_{graphite} was reached. The cell was held for 30 min at open circuit voltage (OCV) after each half cycle (gray areas).

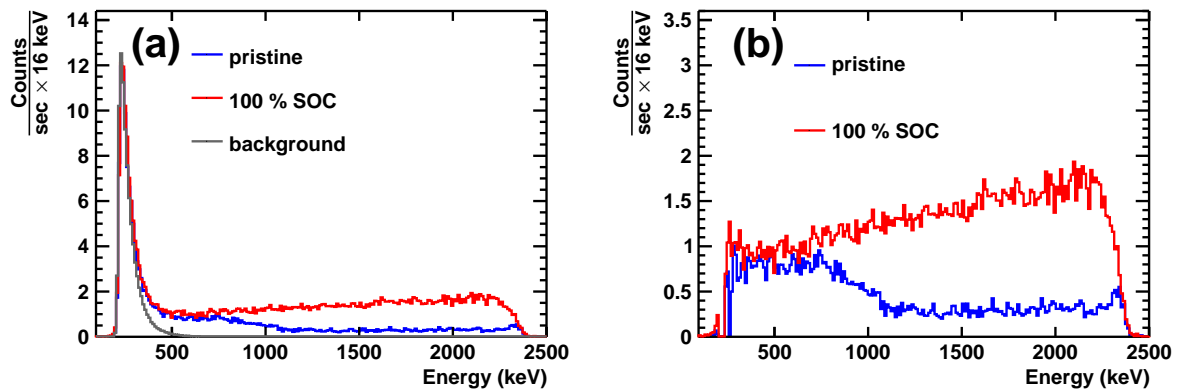


Figure 8.6: (a) Spectra of the graphite anode at the beginning (blue line) and end (red line) of the first operando charging process at $C/4$. The cell has previously been cycled for three formation cycles at $C/10$. Lithium in the pristine electrode originates from ${}^6\text{LiPF}_6$ in the electrolyte and irreversible lithium formed as SEI during the formation cycles. The lithium content in the fully charged anode (100 % SOC) increases due to reversibly intercalated lithium. Due to the mass swelling of the anode the end of the anode is shifted to smaller energies. The gray spectrum is a background using an identical reference sample without lithium. (b) Background-subtracted anode spectra at the beginning (blue line) and end (red line) of the first operando charging process at $C/4$.

evaluation.

Analog to the concentration profile calculation of the previous formation study, the change of the lithium content was taken into account for the different SOC states, while $\approx 62\%$ of the electrochemically observed irreversible capacity during the formation cycles was assumed to be present within the anode (c.f. Sec. 8.1). Hereby, the lithium content in the uncharged anode (0 % SOC) of the SEI is expected to be 20.5-times higher than that of the pure electrolyte (0.31 M LiPF_6). All other lithium contributions were obtained by integrating the NDP spectra, therefore only the lithium truly present in the anodes was taken into account for the composition, independent of the electrochemical data. The assumed elemental compositions at the different SOC are listed in Tab. 8.2.

Taking into account the compositions listed in Tab. 8.2, as well as the energy losses of the copper current collector (≈ 11 keV), the Kapton[®] particle window ((301 ± 0.6) keV) and the nominal ≈ 150 mbar helium atmosphere (≈ 51 keV), the lithium concentration profiles were determined from the energy spectra. They are shown as 2D graph in Fig. 8.7. During discharging at $C/4$ a homogeneous lithium delithiation is observed for all half cycles and a homogeneous lithiation is observed for charging rates up to $1C$. A step-like lithium distribution is formed at a charging rate of $2C$, indicating lithium plating on the top of the graphite anode. The concentration profiles at the beginning and end of each half cycle are shown in Fig. 8.8 a–d for greater understanding. Similar to the formation study, a minor slope remains in the concentration profiles, probably originating from additional energy loss within the stainless-steel casing in which the hole grid was processed (c.f. Sec. 8.1). The lithium concentrations expected from the electrochemical measurements are shown, assuming that $\approx 62\%$ of the irreversible capacity is present as irreversibly

Anode SOC	H (mol%)	Li (mol%)	C (mol%)	O (mol%)	F (mol%)	P (mol%)
Pristine	22.3	0.1	65.8	9.2	2.5	0.1
0 % (1)	22.0	1.7	64.7	9.0	2.4	0.1
100 % (2)	20.5	8.5	60.3	8.4	2.3	0.1
0 % (3)	21.9	2.1	64.5	9.0	2.4	0.1
100 % (4)	20.4	8.7	60.1	8.4	2.3	0.1
0 % (5)	21.9	2.2	64.4	9.0	2.4	0.1
100 % (6)	20.4	8.9	60.0	8.4	2.3	0.1
0 % (7)	21.9	2.2	64.4	9.0	2.4	0.1
100 % (8)	20.6	7.7	60.8	8.5	2.3	0.1

Table 8.2: Elemental compositions of the graphite anode at different SOC states. While the composition of the electrolyte-filled pristine anode is well-known, the contribution of the SEI formation was calculated based on previous results, i.e. $\approx 62\%$ of the irreversible capacity was present as SEI in the anode after formation. All further lithium contributions were obtained by integrating the signals.

attached lithium after the formation cycles (c.f. Sec. 8.1). The uncertainty bands are composed of the systematic uncertainty of the NDP measurement ($\pm 4.0\%$) and the uncertainty of the concentration calculation based on preparation uncertainties (c.f. Tab. 5.1) and uncertainties of the electrochemical data ($\pm 4\%$) [68].

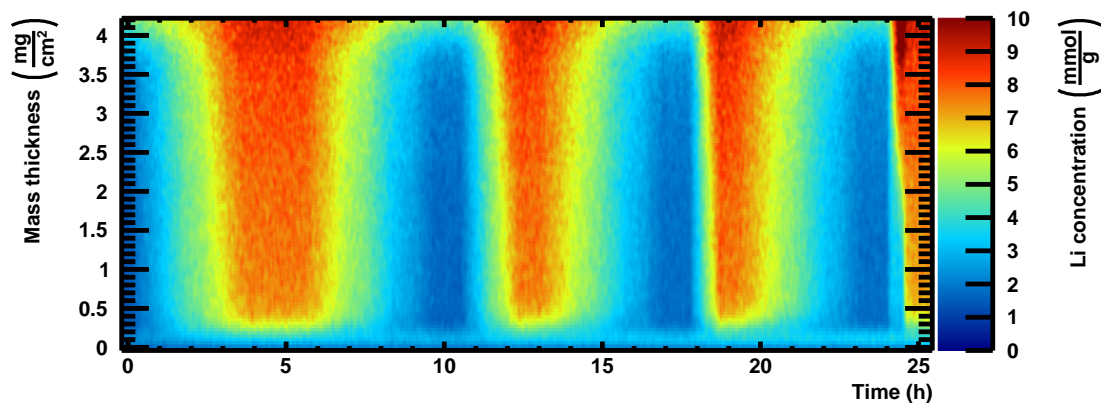


Figure 8.7: 2D plot of the lithium concentration profiles obtained during the *operando* experiment. While the discharging rate was kept at $C/4$, the charging rate is increased from $C/4$ to $C/2$, $1C$ and $2C$. During discharging, as well as for low charging rates, lithium is homogeneously (de-)intercalated within the graphite anode. At a charging rate of $2C$, an inhomogeneous lithium transport is observed in the graphite anode.

For all discharged states (blue lines in Fig. 8.8 a–d), the original lithium concentration was obtained indicating that (i) during the experiment no further SEI has formed, (ii) the discharging rate of $C/4$, which was kept constant for all cycles, is sufficient to homogeneously remove reversibly attached lithium from the anode, and (iii) the cell exhibits a good cycling repeatability. This is also true for the first three charging rates of $C/4$ (Fig. 8.8 a), $C/2$ (Fig. 8.8 b), and $1C$

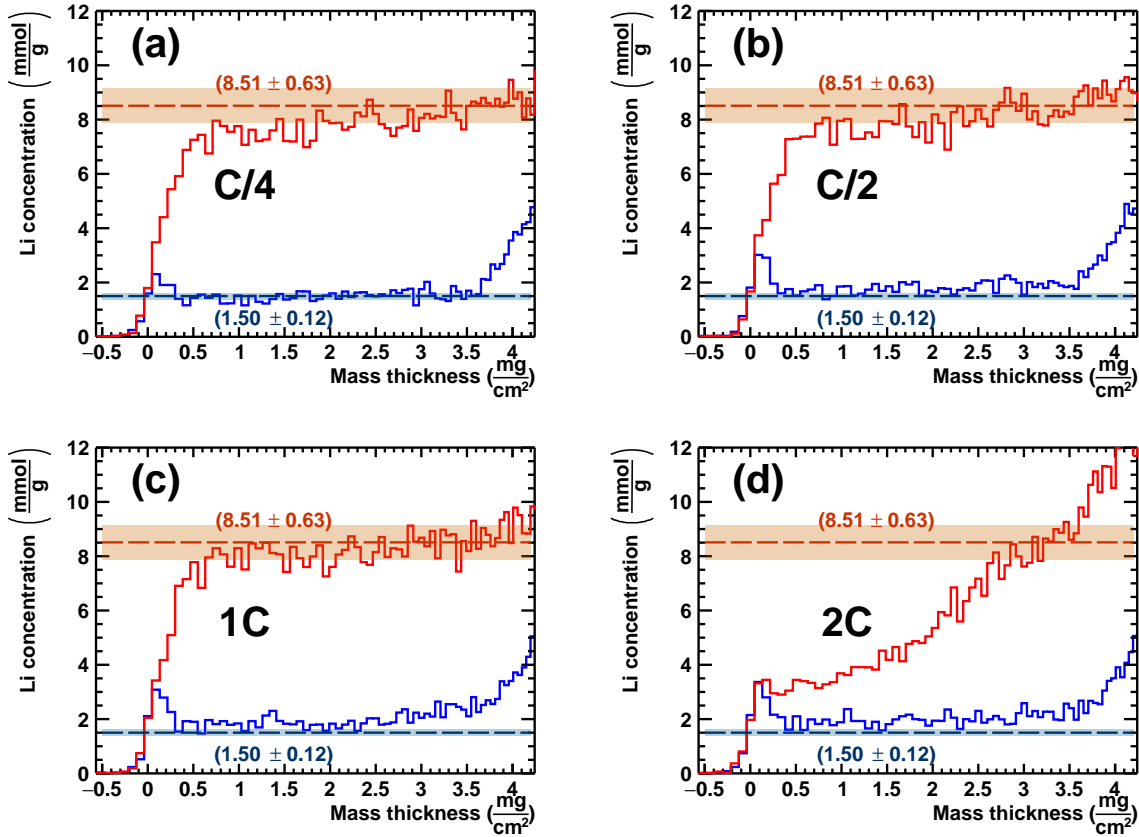


Figure 8.8: Lithium concentration profiles within the graphite anode at 0% SOC (blue line) and 100% SOC (red line) after charging at rates of C/4, C/2, 1C and 2C are respectively shown in a, b, c and d. For charging rates of C/4, C/2 and 1C the obtained concentration profiles agree well with the expected concentrations obtained from electrochemical data assuming an SEI formation of $\approx 62\%$ of the irreversible capacity (c.f. Sec. 8.1), which are shown as dashed lines. Combined concentration uncertainties originating from the sample preparation and the NDP measurement are highlighted. For all discharge states, the same concentration profile is obtained. Furthermore, at 100% SOC after C/4, C/2 and 1C the same concentration profile is obtained, indicating a good cycling repeatability of the *operando* NDP cell. At 2C, lithium plating occurs and a highly inhomogeneous concentration profile is observed directly after complete charge (100% SOC).

(Fig. 8.8 c), where a rather homogeneous lithium distribution was observed meaning that these charging speeds are well suited to a homogeneous lithiation of the graphite anode. This changes for the charging rate of 2C (red line in Fig. 8.8 d), where a highly inhomogeneous lithium concentration profile is obtained directly after charging. The measured lithium concentration at the anode/electrolyte interface exceeds the highest lithium concentration possible assigned to complete LiC_6 formation (horizontal red band), suggesting an accumulation of pure lithium, i.e. deposition of metallic lithium (lithium plating) on the anode surface. The formation of metallic lithium has previously been detected using Neutron Diffraction and now also its spatial distribution is revealed using NDP [53, 226].

In order to study the build-up of this inhomogeneous profile in more detail, as well as the

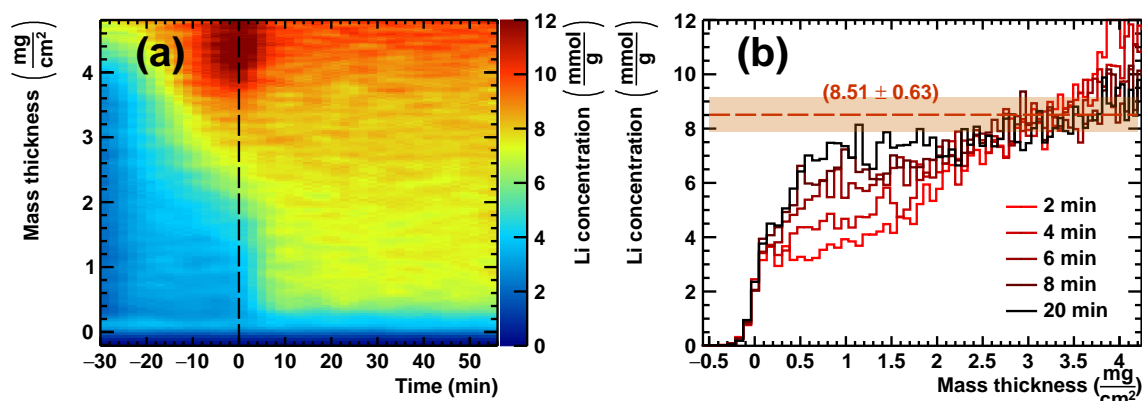


Figure 8.9: (a) 2D graph of the concentration profiles with time resolution of 2 min. The lithiation with respect to depth is observed during the charging process, until lithium plating starts at the anode surface (yellow area). After charging, the cell is held at OCV and the lithium concentration starts to balance within the anode. (b) Lithium concentration profiles for distinct times after charging at 2C. Three distinct regions ($0\text{--}2\text{ mg/cm}^2$, $2\text{--}3.5\text{ mg/cm}^2$, $> 3\text{ mg/cm}^2$) are observed directly after charging (red line), with a high lithium concentration at the anode/separators interface indicating lithium plating. The lithium equilibration across the anode is followed with a time resolution of 2 min, until equilibrium is reached after $\approx 8\text{ min}$ [68].

lithium transport ongoing in the anode in the subsequent OCV phase, the process is more shown in Fig. 8.9. Fig. 8.9a shows a 2D map of the lithium concentration with respect to depth (mass thickness) over time. The time interval splits into charging and relaxation time, while 0 depicts the transition between these two. During the first $\approx 5\text{ min}$, a rather homogeneous lithium concentration level is obtained in the anode. At $\approx 10\text{ min}$, lithium enriches in the upper layers of the graphite anode ($> 3\text{ mg/cm}^2$), while its concentration in the lower layers of the electrode remains at a low level. Starting from $\approx 10\text{ min}$, until the end of the charging, a linear lithium transport across the anode is observed expanding towards the lower anode domain until it eventually reaches the $\approx 1.5\text{ mg/cm}^2$. Furthermore, starting at 20 min, a local lithium enrichment is built up at the outermost anode layer, i.e. the anode/electrolyte interface at $\approx 4\text{ mg/cm}^2$, which clearly shows the formation of metallic lithium, i.e. lithium plating. After charging was completed (0 min), the cell was kept at OCV to follow the lithium redistribution within the anode during this relaxation phase. As shown in Fig. 8.9a, the highly inhomogeneous lithium distribution levels out within minutes until a final homogeneous profile is reached. This relaxation can be better followed in Fig. 8.9b, where the concentration profiles are shown at distinct time intervals. At the beginning of this relaxation (first 2 min), the lithium profile is highly inhomogeneous. It consists of three distinct regions: at $0\text{--}2\text{ mg/cm}^2$ (near the anode/current collector interface) lithium is depleted. At $2\text{--}3.5\text{ mg/cm}^2$, a lithium concentration close to the expected value of fully lithiated LiC_6 (100% SOC) is seen. Towards greater depths at the end of the anode ($> 3.5\text{ mg/cm}^2$), a lithium enrichment assigned to lithium plating is observed, which vastly exceeds the concentration expected from LiC_6 (100% SOC, horizontal line). The inhomogeneous concentration profile starts leveling out with increasing relaxation time and

lithium is transported to the depletion region ($0\text{--}2\text{ mg/cm}^2$) while the amount of plated lithium decreases. At $\approx 3\text{ mg/cm}^2$, i.e. where the LiC_6 (100% SOC) phase was already reached at the beginning of the relaxation, the lithium concentration stays constant during the relaxation process. Here, lithium is constantly transported from the upper region ($> 3\text{ mg/cm}^2$) towards the anode/current collector region and thus this inflection point is solenoidal, i.e. the divergence of the concentration gradient ∇c_{Li} is $\nabla(\nabla c_{\text{Li}}) = 0$. Until 8 min almost the whole relaxation is complete and the concentration profile after 8 min is close to that of the reference signal chosen at 20 min after charging was completed.

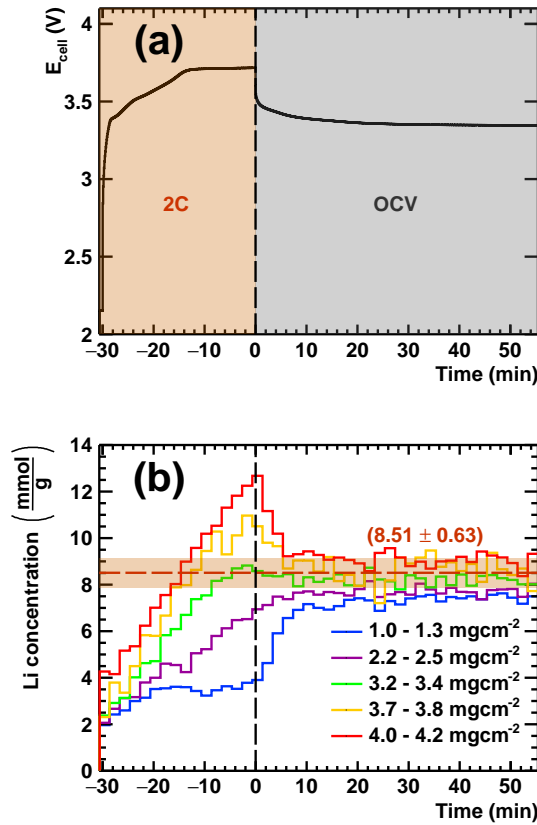


Figure 8.10: (a) Magnified region of the voltage profile (c.f. Fig. 8.5) showing the charging at 2C (orange area) At 0 min (vertical dashed line) the charging process is stopped and the cell is held at OCV and relaxation occurs. (b) Measured lithium concentrations for distinct depth intervals between 1 mg/cm^2 and 4.2 mg/cm^2 within the anode during charging at 2C and subsequent relaxation. The horizontal orange line indicates the lithium concentration for fully lithiated graphite (100% SOC) [68].

The time-dependent relaxation is better understood when separately considering the concentration levels at distinct depth intervals during the charging at 2C and the subsequent OCV phase (c.f. Fig. 8.10 a). As shown in Fig. 8.10 b, the previous findings are also observed but in greater detail: during the first 10 min, the lithium concentration in the anode rises in the same manner and stays at a constant level for the uppermost layer ($1.0\text{--}1.3\text{ mg/cm}^2$). While for the intermediate layer ($2.2\text{--}2.5\text{ mg/cm}^2$) an almost linear lithium increase is seen, the con-

concentrations in the outer layers rapidly increase until finally in the two outermost layers lithium concentrations become higher than that of lithiated graphite (100% SOC). During relaxation, this trend is reversed: In the uppermost layer (1.0–1.3 mg/cm²), far from equilibrium, a fast accumulation of lithium is observed, simultaneously to a depletion of metallic lithium at the outer layers (4.0–4.2 mg/cm²).

8.3 Conclusion

In this chapter, graphite anodes for lithium-ion batteries were measured using *operando* NDP. In contrast to *ex situ* measurements, where the anodes need to be harvested from the battery in a *post mortem* state, subsequently washed and measured after a certain time delay, the lithium concentration profiles could be directly measured during battery operation. A coin-cell-based *operando* cell design was developed to overcome the limited range of the NDP technique and furthermore to extend the viewing depth into the graphite anode. Hereby, the electrochemical performance of the cell was shown to be undisturbed and thus the measured spectra are representative for common cells. In order to probe throughout the complete anode, its thickness was reduced to $\approx 20\ \mu\text{m}$ via using commercial graphite particles with reduced particle sizes. Therefore, the effective surface area of the graphite anode was increased, which influences their performance compared to commercial anodes. However, fundamental processes could still be studied.

It was observed that during the first (dis-)charge cycle, most of the irreversible solid-electrolyte-interphase (SEI) was formed. However, only $\approx 62\%$ of the electrochemically measured irreversible capacity was found to be irreversibly attached to the graphite anode. Although the exact origin of this is unknown, a partial dissolution of SEI into the electrolyte might be the reason [260]. A lithium accumulation within the copper current collector is also seen, which is in accordance with previous studies [170, 237, 263]. At a low charging rate of C/16 the formation of LiC₆ is found, like it was also previously observed using Neutron Diffraction [53, 55, 225–227]. For the first time, the formation of metallic lithium (lithium plating) on graphite-based anode could be observed using NDP and was resolved with a time resolution of 2 min. Due to a reactor brake of the FRM II, these measurements were performed at the NIST Center for Neutron Research (c.f. Sec. 3.2.2). When comparing the absolute count rates from *operando* measurements of both facilities (c.f. Fig. 8.1 b and Fig. 8.6 a) in the range of (300–400) keV, i.e. in a region where the exponentially-shaped background signal dominates the measurement signal while being above the trigger threshold, the N4DP instrument shows a (28–67) % lowered background intensity compared to the Cold Neutron Depth Profiling Instrument at the NCNR. Additionally, the N4DP instrument exhibits a ≈ 1.6 -times higher cold neutron flux density (c.f. Tab. 1.1) which is planned to be increased further to $5 \times 10^{10}\ \text{cm}^{-2}\text{s}^{-1}$ (c.f. Sec. 3.1.2). Based on these numbers a $\approx (1.3\text{--}6.4)$ -times shorter time resolution would be expected at the N4DP instrument while the statistical significance of the measurement is maintained.

In order to favor lithium plating, a low LiPF₆ concentration of 0.31 M was dissolved in the

liquid electrolyte. Different charging rates of C/4, C/2, 1C, and 2C were applied. While for the slower rates a homogeneous graphite lithiation was observed, a highly inhomogeneous lithium accumulation was found for the 2C charging rate resulting in the formation of metallic lithium at the surface of the anode. The lithiation process in the anode could be studied *operando* showing distinct depth regions in which the lithiation progresses. During a subsequent OCV phase, the relaxation towards the equilibrium was studied. Hereby, the lithium profile was observed to homogenize within ≈ 8 min. This is much faster than findings from previous Neutron Diffraction measurements on commercial lithium-ion batteries with graphite anodes [53, 226]. These batteries were cooled to low temperatures of -2°C and -20°C so that lithium plating occurred already at charging rates of C/2 and C/5, respectively. Relaxation times of ≈ 2 h and (17–20) h were found [53, 226]. Since the electrochemical cells which were investigated in this NDP study were cycled at room temperature and the porous graphite anode thicknesses were kept thin allowing for charged-particle penetration, faster kinetics and transport mechanisms would be expected compared to measurements obtained at low temperatures, which eventually resulted in this study in a shorter relaxation time of ≈ 8 min [53, 68, 226].

The major findings of this work are first summarized in Sec. 9.1. In the framework of this thesis, a total of six articles are published and two are in preparation: findings on irreversible lithium accumulations in graphite anodes discussed in Chap. 6 are published in [230]. *Ex situ* NDP measurements on silicon-graphite composite anodes presented in Chap. 7 are published in [118, 231, 232]. Results on *operando* NDP, presented in Chap. 8, during the initial formation cycle for graphite anodes are published in [170]. A publication based on the findings on fast charging is in preparation [68]. In Sec. 9.2, near-future developments and applications for the N4DP instrument are presented. Many of the technical developments are under development.

9.1 Conclusion

In the scope of this work, essential contributions to the development of the N4DP instrument at the Heinz Maier-Leibnitz Zentrum were performed and several samples from different material science applications were investigated. Thanks to the high sensitivity of NDP in particular to ^6Li nuclei, concentration profiles of lithium can non-destructively be probed with highest precision. This is of special interest for lithium-ion batteries, which play an increasingly important role on the daily life.

In order to translate the obtained spectra to concentration profiles, a software tool was developed, which is based on the experimental stopping range tables provided by the SRIM software [117]. A signal forward mapping method was also presented, which substitutes the use of particle filter foils in special applications.

Here, two different anode materials (graphite-based and silicon-graphite-based) for lithium-ion batteries were investigated. In a cooperation with the Hochschule Landshut, the influence of a special lamination technique on the SEI formation within the graphite anodes was probed. The laminated separator was irreversibly attached to the *post mortem* anodes harvested from the battery, limiting the NDP viewing depth. Therefore, the SEI formation could only be followed in the upper bulk layers. Here, during 500 cycles no significant influence of the lamination technique on the SEI formation was observed for C-rates between 0.1 C and 2 C. For the non-laminated anodes, the NDP viewing range was sufficient to probe the concentration profile across the whole thickness. A surface-near peak was observed for the first time, which could possibly be ascribed

to a lithium formation at the surface of the particles, indicating that an SEI has formed on the particles, i.e. at the contact surface of the active graphite with the electrolyte. Furthermore, NDP revealed that (55–80) % of the electrochemically observed irreversible capacity was present as irreversibly attached lithium in the anodes. Therefore, lithium immobilization due to SEI formation in the anode is the main driving mechanism for capacity fading. Lithium loss induced by harvesting the *post mortem* anodes could not be excluded.

In contrast to commercial graphite anodes, silicon-based anodes offer a higher theoretical capacity, but they induce a faster capacity aging upon operation. Within a cooperation with the TEC group of the chemistry department of TUM, anodes with a silicon-graphite mixture as active material were investigated *ex situ*. Here, NDP enabled to follow the accumulation of the active lithium and the formation of passivated lithium forming an SEI during the first (dis-)charging process. Furthermore, a mass swelling of the anodes of ≈ 2 -times of that of the pristine could be directly followed. After the first completed cycle, the anodes gained ≈ 18 % in mass caused by irreversible SEI formation in the anodes. The SEI formation was then followed for extended battery operation up to 140 cycles. After 100 cycles, the anodes reached a ≈ 3 -times mass thickness compared to their pristine state due to SEI formation. The irreversibly attached lithium in the SEI accounts for ≈ 75 % of the irreversible capacity observed. Using NDP, a shrinking of the surface-near lithium peak is observed for larger (dis-)charge cycle numbers, indicating a morphological change within the anode, as it was observed in an earlier TEM study and later verified at MLZ using GISANS [56, 254].

Lithium losses could not be excluded for both *ex situ* studies during anode harvesting or subsequent washing. Therefore, *operando* NDP measurements were conducted to directly measure the lithium concentration in the operating cell. Due to the depth limitation of the NDP technique and the mechanical and electrical demands of a lithium-ion battery, a novel cell design was developed together with the TEC group. It prevents a leakage of the liquid electrolyte and was shown to ensure a good electrochemical performance of the cell. Here, electrochemical cells containing graphite anodes could be measured, which were as close as possible to the commercial standard while enabling to probe their complete depth. NDP was used to quantify *operando* the lithium accumulation during the first (dis-)charge cycle, i.e. during formation, and at elevated charging speeds where lithium plating was induced. During formation, the accumulation of the active lithium could be quantified showing a good agreement with the electrochemically observed reversible capacity. On the other hand, similar to the previous *ex situ* studies, only $\approx 2/3$ of the irreversible capacity was observed as irreversibly attached lithium in the anodes. This was verified by an independent commercial *ex situ* ICP-OES study on identically constructed graphite anodes, which showed that indeed ≈ 62 % of the irreversible capacity is present as irreversible lithium within the anode [260]. Although the mechanism of this SEI reduction is still unknown in literature, a possible explanation could be the partial dissolution of SEI into the electrolyte during battery operation [260]. The direct lithium measurement during *operando* NDP made it also possible to study non-destructively the lithium accumulation at higher charging speeds. Here, for the first time lithium plating in graphite anodes at a charging rate of 2C could be di-

rectly measured using NDP with a time resolution of 2 min complementing earlier findings using Neutron Diffraction [53, 226]. In a subsequent relaxation phase, the diffusion of the previously plated lithium into the graphite anode could be directly studied and was observed to take place within ≈ 8 min.

9.2 Outlook

The N4DP project was funded by the Federal Ministry of Education and Research (BMBF) no. 05K16WO1. During this time, 17 proposals were accepted and measured at the N4DP instrument. While 6 proposals deal with test measurements and instrument development, a broad range of materials used for different applications were measured based on the 11 proposals submitted by our collaboration partners. This high demand from users even in the early stage of the project reflects the great impact of the N4DP instrument on the materials science community. Recently, a follow-up BMBF project (no. 05K19WO8) was successfully approved. It aims to transfer the N4DP instrument to a complete user facility. In order to meet the increasing demand of the users, numerous technical improvements are planned and the major developments are presented here. An overview of possible future applications is also shown.

9.2.1 Technical Developments

Segmented 2D Detectors

The use of segmented double-sided silicon strip detectors allows for the reconstruction of the lateral distribution of ions in the sample. The detectors could measure not only static lateral reconstructions, but also to study directly a 3D concentration evolution also with a good time resolution in the minute range. Here, we aim for a two-dimensional particle mapping with a good lateral resolution of $\approx 100 \mu\text{m}$, while maintaining the energy resolution of the current setup [66]. Therefore, highly homogeneous and thin dead layers are required for the charged-particle detectors [66]. The segmented detectors with 64×128 strips, 150 nm implantation depth and thin dead layers close to the physical limit are under development as part of the work of L. Werner and first prototypes have been produced by the company CiS [66]. Within the work of L. Werner and C. Berner, a custom readout system is developed, based on the TRB-readout including the SKIROC¹ readout chips and a custom GEAR frontend [66, 264]. The detector prototypes and the novel readout system could already be tested using a triple- α radioactive source. Here, the α signals could be resolved with a FWHM of 24 keV, which is comparable to the resolution of 21 keV (FWHM) achieved using the current N4DP setup [66].

¹SKIROC 2A and SKIROC CMS

Elliptical Guide Extension

In order to achieve a reasonable time resolution when mapping the evolution of 3D concentration profiles using segmented detectors, a high neutron flux is needed to maximize the signal originating from the small probing volumes being in the $\approx 100\ \mu\text{m} \times 100\ \mu\text{m} \times 20\ \mu\text{m}$ range. An elliptical guide extension increases the neutron beam to a maximum of $5 \times 10^{10}\ \text{n cm}^{-2}\ \text{s}^{-1}$ thermal neutron equivalent, but at a position of $\approx 7.5\ \text{cm}$ behind the guide exit [67, 166]. It also shows a highly inhomogeneous beam profile [166]. When going towards time-resolved 3D measurements, a homogeneous beam profile with a high intensity close to the sample position at $\approx 26\ \text{cm}$ is needed. Here, E. Kluge could already compare various guide geometries based on simulations using McStas, which is a software used for simulating neutron scattering in materials with defined geometries [265–268].

Coincident γ -Detection

The N4DP instrument is situated at the PGAA facility. This could be further exploited when measuring concentration profiles of ^{10}B . As discussed in Chap. 2, the $^{10}\text{B}(n,\alpha)^7\text{Li}$ reaction undergoes a γ -ray emission with a probability of 93.7% upon cold neutron capture. The high-purity germanium detectors of the PGAA facility placed at an angle of 90° with respect to the neutron beam could be used to coincidentally detect this γ radiation. It could be used to trigger the NDP electronic and thus to isolate boron signals from background radiation. While this approach seems rather straight-forward, it is currently limited by the detection efficiency for coincidence. The high purity germanium detectors alone give rise to a efficiency in the 10^{-4} range [144]. Combined with the geometrical acceptance of the NDP detectors being in the 10^{-3} range, the total detection efficiency for coincidence is estimated to be 10^{-7} . The geometrical acceptance of both detectors can be increased by reducing the distance from the sample to the detectors, while keeping detector damage induced by radiation on a minimum level.

Determination of the Matrix Composition

In this work, the material stopping power was calculated based on the knowledge of the preparation procedure. However, non-coincident PGAA could be used to probe the bulk composition of the investigated material simultaneously to NDP. This would make it possible to detect even impurities and correct for their stopping power. The N4DP chamber allows for the simultaneous PGAA measurement through the aluminum windows connecting the sample position with the germanium detectors, thus optimizing the beamtime. However, this approach is only of interest for static, isolated, samples and not for e.g. anodes in *operando* batteries. Here, the bulk composition of the whole battery (anode/separator/electrolyte/cathode) and its casing would be measured using PGAA, which is constant throughout operation. On the other hand the composition at the anode side, which solely defines the local stopping power for the charged

particles there, might change during operation. The isotope-specific detection limits of PGAA should be considered when measuring the sample matrices, too [67].

Sample Environment

Apart from technical developments of the N4DP instrument itself, also different sample environments are of high interest. In this work, an exchangeable gas atmosphere was applied which enabled to measure *operando* lithium-ion batteries. As a next step, sample cooling ($\approx -20^\circ\text{C}$) and heating ($\approx 80^\circ\text{C}$) could be implemented in the current setup using a cooling fluid circulator² and electric heaters with additional thermocouples for temperature control, respectively. Here, the previously used sample holders could be adjusted for these applications. However, a thermal contact of the heated sample with the N4DP chamber should be avoided, which might be achieved using temperature-resistant plastic connectors. Furthermore, a glovebox with controlled atmosphere might be favorable to be installed in connection with the N4DP chamber. It would enable an inert sample transfer into the measurement position which is of special interest for air-sensitive samples like e.g. lithium metal.

N4DP User Facility at MLZ

The main goal of the follow-up BMBF project (no. 05K19WO8) is the development of the current setup to an instrument open to users. Here, several components (hard- and software) need to be installed to enable an independent and easy user handling of the measurement and the evaluation. In this context a crane has already been installed in the PGAA bunker for a simple mounting of the instrument.

9.2.2 Future Applications

The developed *operando* coin-cell design as well as the above discussed sample environment allow for further applications of the NDP method. Low temperature ($\approx -20^\circ\text{C}$) *operando* studies on lithium-ion batteries might reveal insight into the slowed-down kinetics occurring at reduced temperatures. On the other hand, sample heating is also of special interest for lithium-containing light-emitting diodes (LED). First *ex situ* NDP test measurements were performed within devices produced by cooperation partners at the Linköping University, Sweden. Here, an elevated temperature of $\approx 70^\circ\text{C}$ is typically applied for operation.

Furthermore, our *operando* coin-cell design can be adjusted for many “wet” applications containing a liquid beyond lithium-ion battery research and as protection for atmosphere-sensitive samples.

²Julabo, Germany

Complementary Characterization Methods



The experimental setups of characterization methods complementary utilized to NDP are presented in this section. First, X-ray diffraction is discussed, followed by microscopy methods.

A.1 X-Ray Diffraction

X-rays are well-suited to complement neutron-based methods, since they allow for probing the sample in a non-invasive and non-destructive way, while providing on a large sample volume with high-statistical information [269]. X-rays can be treated as electromagnetic waves at energies in the keV range and can be described as a plane wave [270]:

$$\Psi(\vec{r}) = \Psi_0 \exp(i\vec{k} \cdot \vec{r}) \quad , \quad (\text{A.1})$$

where Ψ_0 is the wave amplitude, \vec{k} is the wave vector, and $\Psi(\vec{r})$ is the excitation at position \vec{r} . Energies between 1 keV and 20 keV respectively correspond to wavelengths λ of 12.4 Å and 0.62 Å. This is in the regime of the sample morphology (nm regime) and the atomic lattice structure (Å regime) and therefore X-rays are a suitable tool to resolve both structures.

In X-ray diffraction (XRD) the electromagnetic waves impinge the sample at an angle θ with a wavelength of λ of atomic scales, and they scatter on variations of the electron density in the periodic crystal lattice giving rise to the propagation of spherical waves emanating from the scattering centers [270]. In poly-crystalline samples, where the crystal layers are randomly oriented, interference of the waves leads to the evolution of Debye-Scherrer rings and their intensity maxima are measured in XRD at an angle of 2θ with respect to the incoming beam [270]. The scattering of the impinging wave on the local electron density of a single atom is described by the form factor f_j , which is the Fourier transform of the electron density:

$$f_j(\vec{G}) = \int_{atom} \rho_e^j(\vec{r}) e^{-i\vec{G} \cdot \vec{r}} d^3\vec{r} \quad . \quad (\text{A.2})$$

Here, \vec{r} is the space vector from the center of atom j to a volume element of its electron shell. The structure factor S_G describes the local arrangement of atoms in an elementary unit cell and is given by:

$$S_G = \sum_j f_j e^{-i\vec{G}\cdot\vec{r}_j} \quad . \quad (\text{A.3})$$

The position of the center of atom j is given by \vec{r}_j . \vec{G} depicts the reciprocal lattice vector defined by the Miller indices (h, k, l) [270]. The intensity maxima are described by the Laue condition

$$\Delta\vec{k} = \vec{k}' - \vec{k} = \vec{G} \quad , \quad (\text{A.4})$$

where the momentum transfer $\Delta\vec{k}$ of the incident plane and the scattered spherical waves need to match the reciprocal lattice vector. Considering only elastic scattering, where $|\vec{k}'| = |\vec{k}|$, the Laue condition gives rise to the construction of the Ewald sphere, which defines the momentum transfers possible.

The Laue condition is also often referred to as the Bragg's law of diffraction:

$$2d_{hkl} \sin(\theta) = n\lambda \quad , \quad (\text{A.5})$$

where d_{hkl} is the lattice spacing in the given direction [270].

X-ray diffraction (XRD) measurements were conducted at the Materials Science Lab of the MLZ. A molybdenum-based PANalytical Empyrean X-ray diffractometer at an acceleration voltage of 55 kV and a current of 40 mA was used to generate X-ray radiation with characteristic wavelengths of $K_{\alpha 1} = 0.709319 \text{ \AA}$, $K_{\alpha 2} = 0.713609 \text{ \AA}$, $K_{\beta} = 0.632305 \text{ \AA}$ [271, 272]. Hereby, the intensities had the relations of $K_{\alpha 1}/K_{\alpha 2} = 0.5$, $K_{\beta}/K_{\alpha 1} = 0.011$ [273]. All measurements were performed by Stefan Seidlmayer and Armin Kriele of the Materials Science Lab. XRD spectra were then evaluated using the freeware software VESTA [274]. Spectral lines were identified using the Crystallography Open Database [275].

A.2 Optical Microscopy

Surface textures of samples, i.e. their lateral structure and homogeneity, were optically characterized using a Leitz Ergolux AMC optical microscope at the Central Technology Lab (ZTL) of the Physics Department of TUM. The microscope provided magnifications up to $1000\times$ using a lens. A CCD-camera connected to a remote computer enabled a digitization of the images. Depending on the size of the structure, magnifications between $100\times$ and $500\times$ were chosen, which respectively correspond to lateral areas of $1144\times 858 \mu\text{m}^2$ and $229\times 172 \mu\text{m}^2$.

A.3 Atomic Force Microscopy

Atomic Force Microscopy (AFM) was used in the tapping-mode to mechanically probe the height profile of a sample surface. Here, an atomic force microscope MFP-3D by Asylum Research at the Center for Nanotechnology and Nanomaterials (ZNN) of TUM was used and controlled using a remote computer. A cantilever with a spring constant of 2 N/m (Asylum Research) was oscillated below its resonance frequency (50 kHz) while its 14 μm -high tip (tip radius was 7 nm) was approaching the sample. Close to the surface Van-der-Waals forces and Lennard Jones Potentials alter the oscillation of the tip caused by sample deformation and the spring force of the cantilever. Changes of the oscillation frequency were recorded using a laser beam adjusted to the backside of the cantilever, which reflected signal was detected by a photo diode. The beam was previously aligned to the center of the photodiode via adjusting the deflection signal. Depending on the hardness of the material, the AFM provided a nearly damage-free surface height profiling down to a precision of several \AA . The recorded data were treated and analyzed using the freeware software Gwyddion [276].

Beam Profile Images

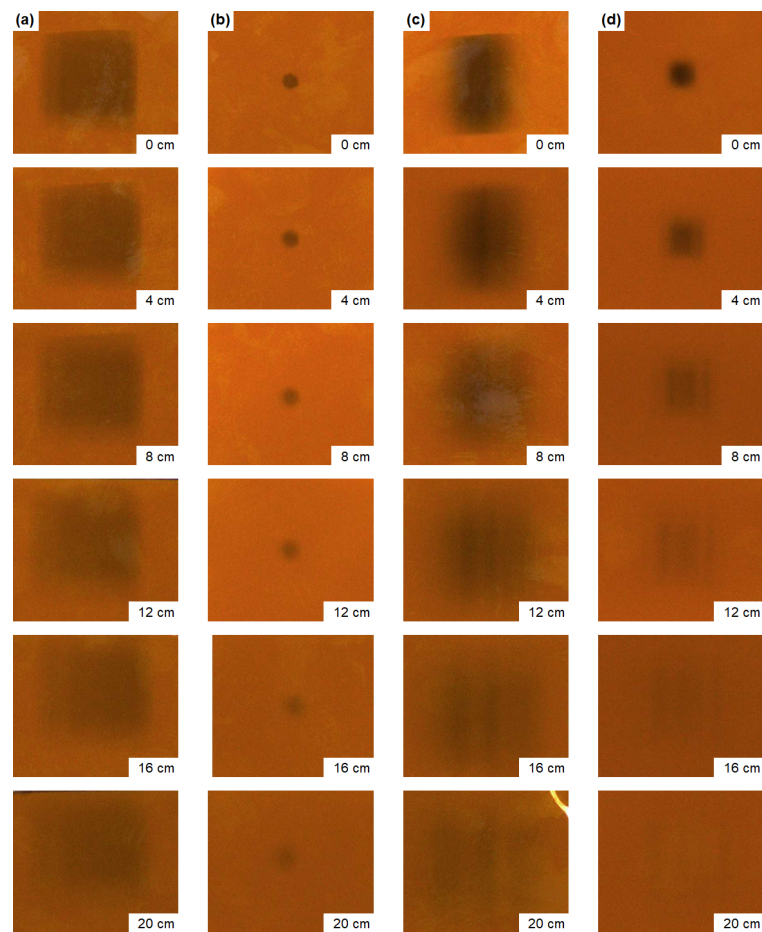


Figure B.1: (a) Column showing the evolution of the collimated neutron beam at distances of up to 20 cm after the neutron guide exit. (b) Column showing the evolution of the collimated neutron beam when using an additional circular collimator. (c) Column showing the evolution of the focused neutron beam profile after the guide exit. (d) Column showing the evolution of the focused neutron beam when using an additional circular collimation. For the focused neutron beam a divergence is observed inducing a broadening of the beam profile. Furthermore, several beam maxima are observed probably caused by inhomogeneities of the supermirror and subsequent reflection at the curvature of the neutron guide [166]. Photographs were taken using a radiation-sensitive film.

Ex Situ Graphite Anode Spectra

Energy Spectra of Non-Laminated Anodes

Anode Spectra for Different Cycling Rates

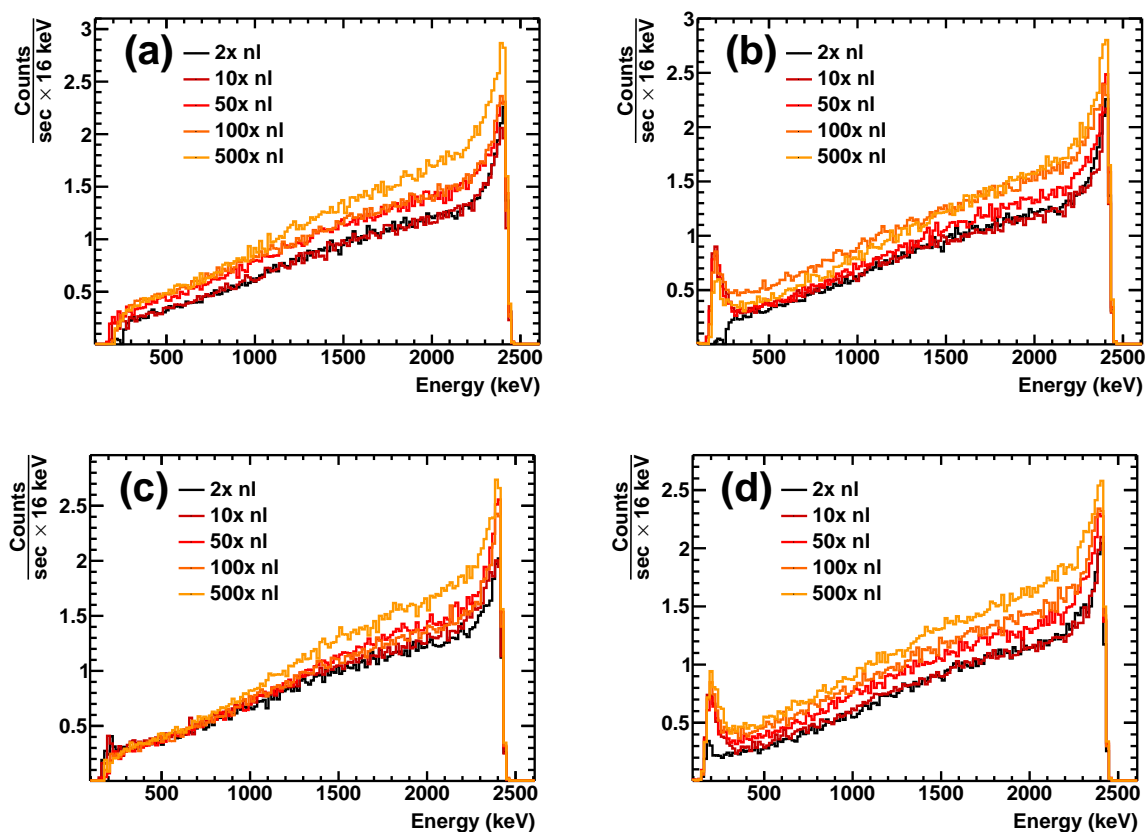


Figure C.1: (a) Anode spectra of the non-laminated 0.1C-1C series after background subtraction. (b) Anode spectra of the non-laminated 0.1C-2C series after background subtraction. (c) Anode spectra of the non-laminated 1C-1C series after background subtraction. (d) Anode spectra of the non-laminated 2C-1C series after background subtraction.

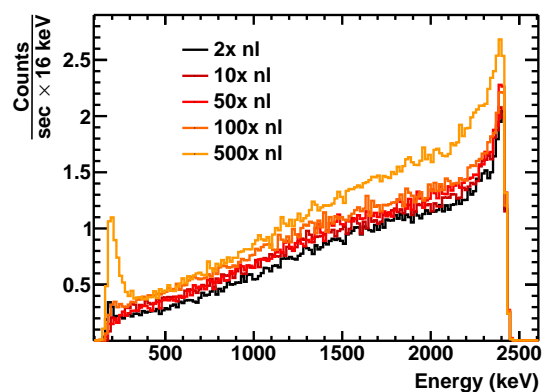


Figure C.2: Anode spectra of the non-laminated 2C-2C series after background subtraction.

Anode Spectra for Different Numbers of Cycles

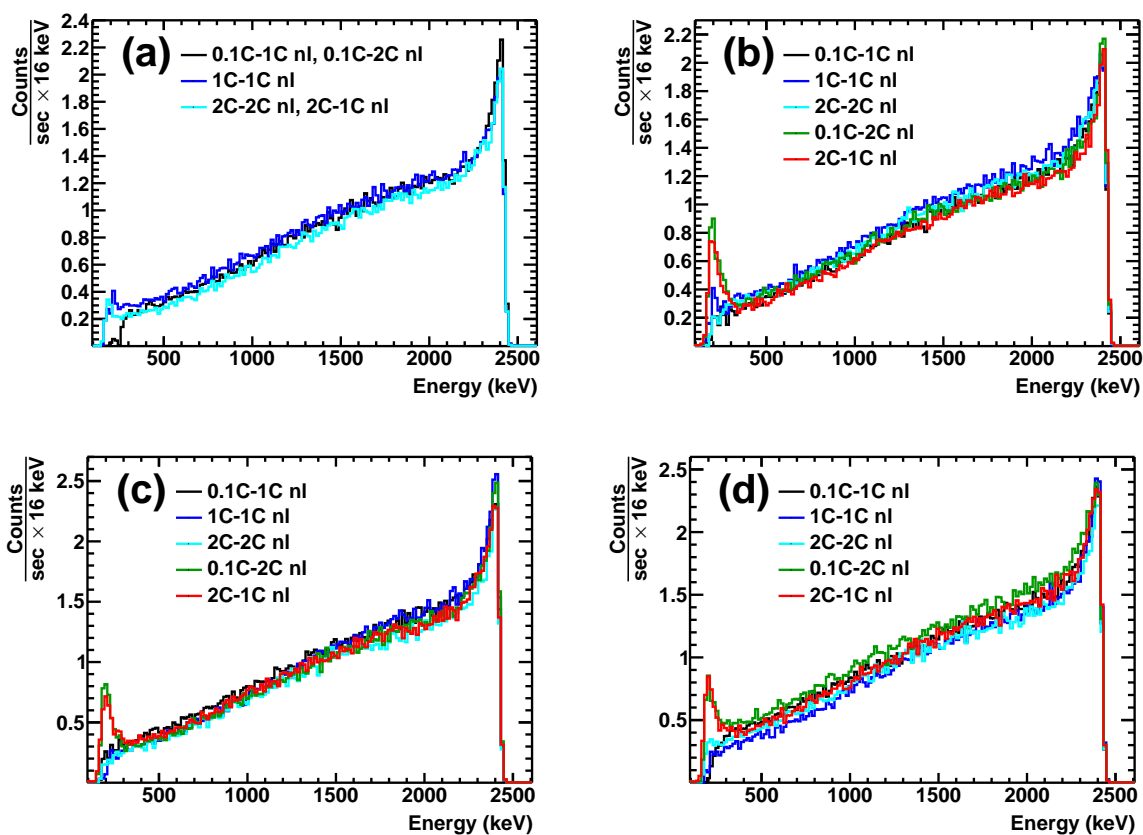


Figure C.3: (a) Background subtracted spectra of the non-laminated anodes after 2 cycles. (b) Background subtracted spectra of the non-laminated anodes after 10 cycles. (c) Background subtracted spectra of the non-laminated anodes after 50 cycles. (d) Background subtracted spectra of the non-laminated anodes after 100 cycles.

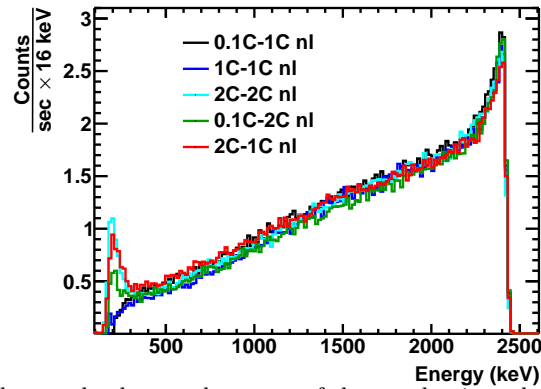


Figure C.4: Background subtracted spectra of the non-laminated anodes after 500 cycles.

Energy Spectra of Laminated Anodes

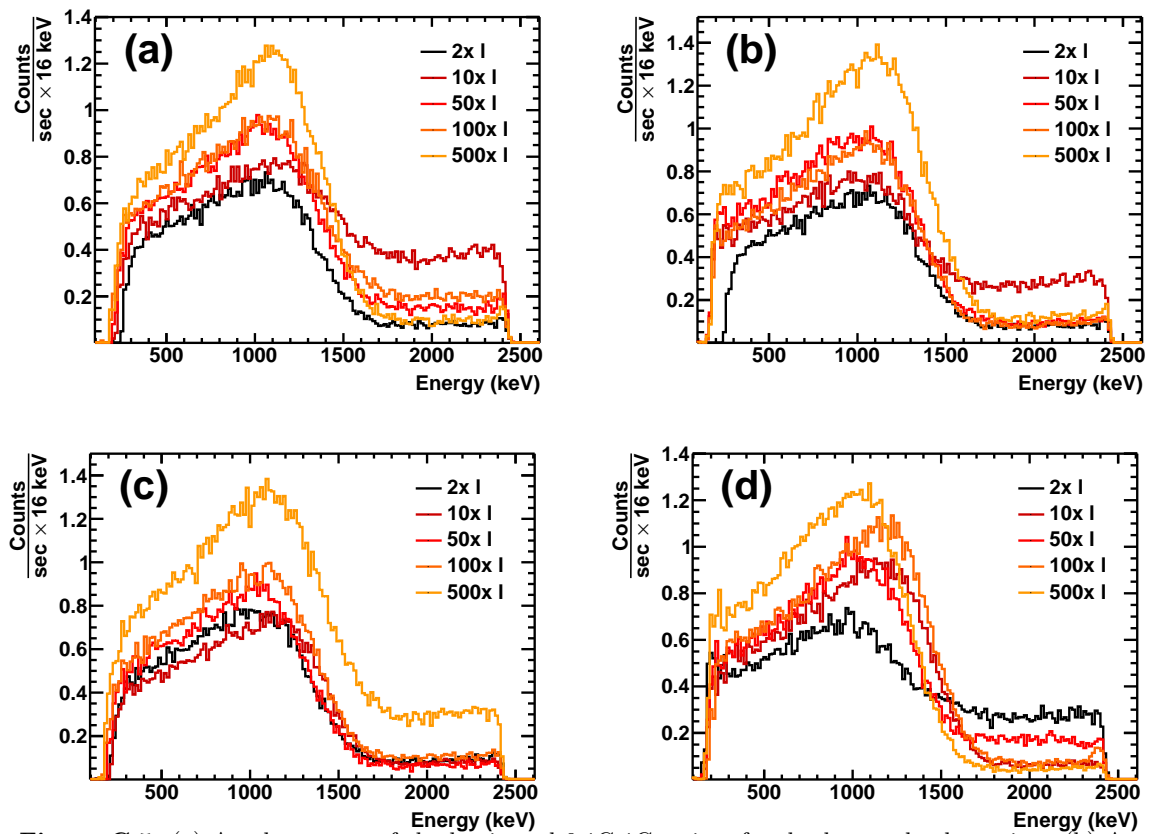


Figure C.5: (a) Anode spectra of the laminated 0.1C-1C series after background subtraction. (b) Anode spectra of the laminated 0.1C-2C series after background subtraction. (c) Anode spectra of the laminated 1C-1C series after background subtraction. (d) Anode spectra of the laminated 2C-1C series after background subtraction.

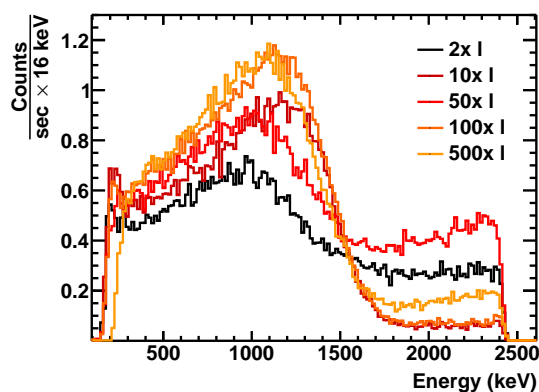


Figure C.6: Anode spectra of the laminated 2C-2C series after background subtraction.

Concentration Profiles

Concentration Profiles for Different Cycling Rates

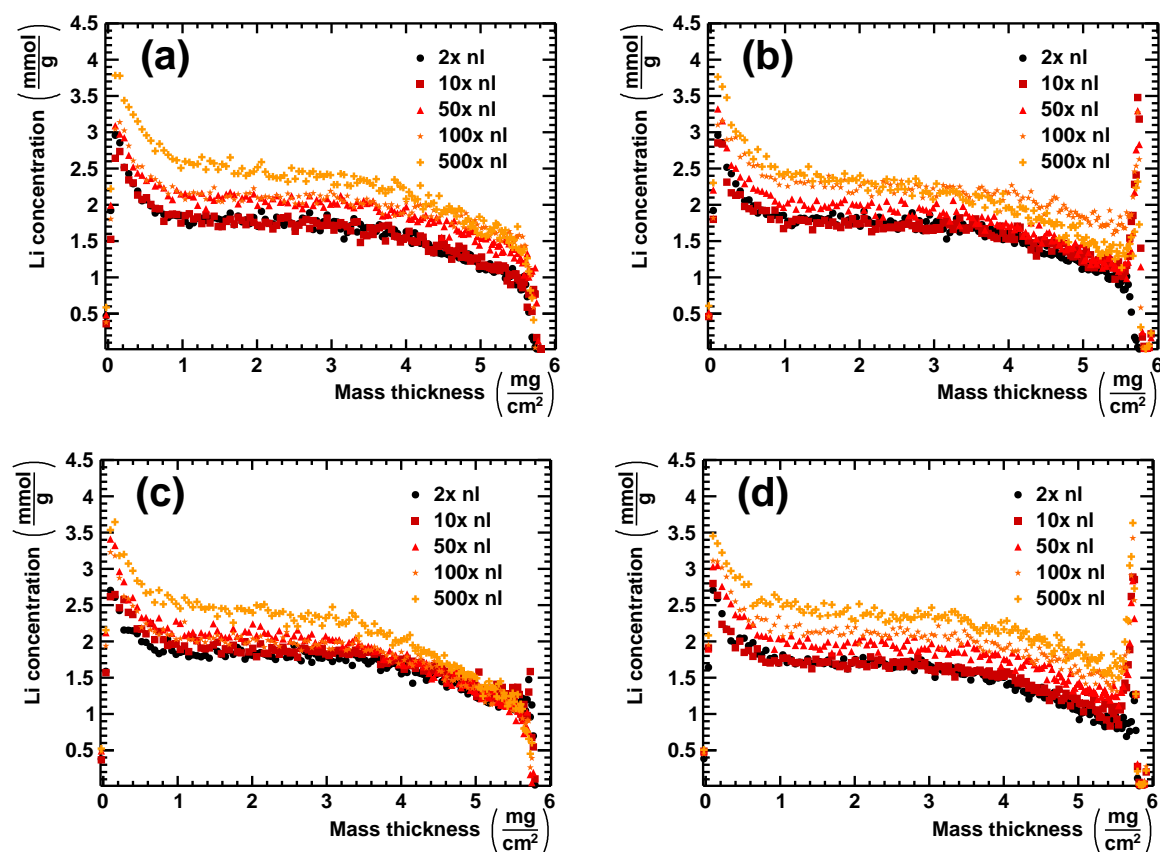


Figure C.7: (a) Concentration profiles of non-laminated anodes of the 0.1C-1C series. (b) Concentration profiles of non-laminated anodes of the 0.1C-2C series. (c) Concentration profiles of non-laminated anodes of the 1C-1C series. (d) Concentration profiles of non-laminated anodes of the 2C-1C series.

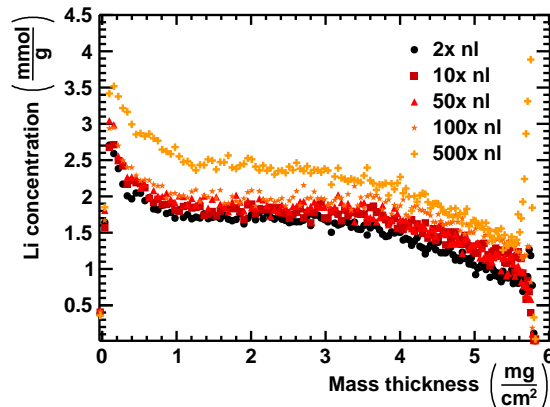


Figure C.8: Concentration profiles of non-laminated anodes of the 2C-2C series.

Concentration Profiles for Different Numbers of Cycles

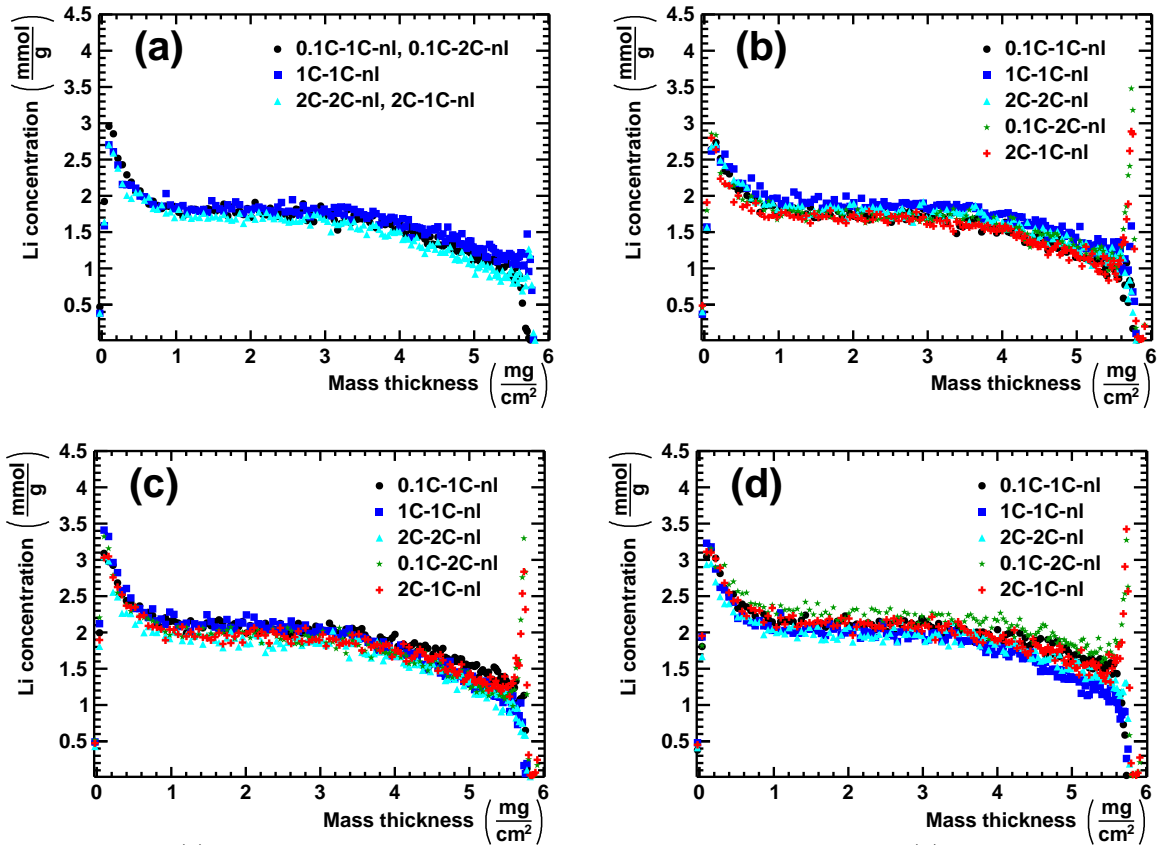


Figure C.9: (a) Concentration profiles of non-laminated anodes of after 2 cycles. (b) Concentration profiles of non-laminated anodes of after 10 cycles. (c) Concentration profiles of non-laminated anodes of after 50 cycles. (d) Concentration profiles of non-laminated anodes of after 100 cycles.

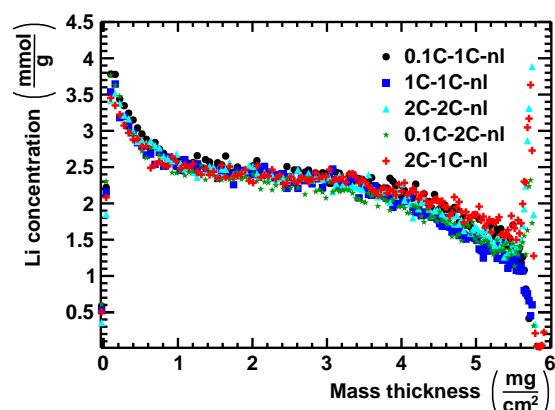


Figure C.10: Concentration profiles of non-laminated anodes of after 500 cycles.

Mass Thickness Fits

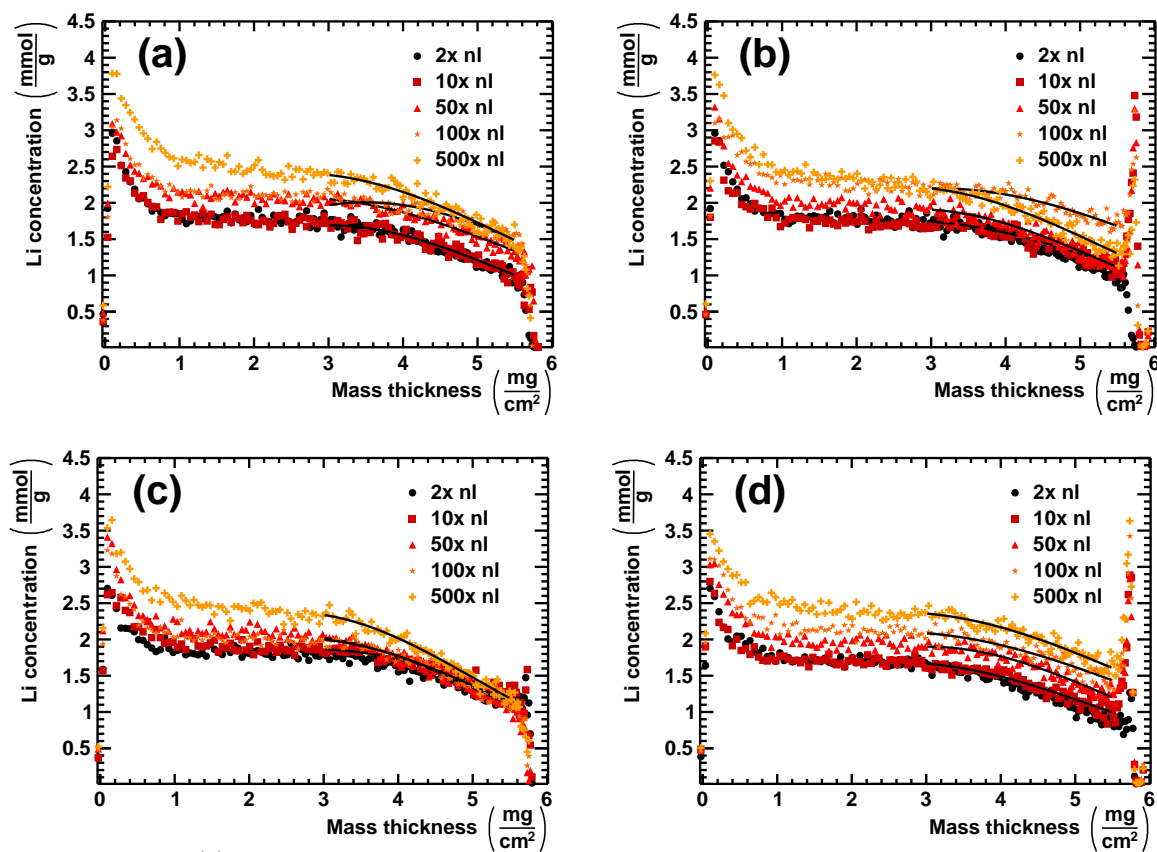


Figure C.11: (a) Gaussian fit to determine the inflection point of the concentration profiles of the 0.1C-1C series. (b) Gaussian fit to determine the inflection point of the concentration profiles of the 0.1C-2C series. (c) Gaussian fit to determine the inflection point of the concentration profiles of the 1C-1C series. (d) Gaussian fit to determine the inflection point of the concentration profiles of the 2C-1C series.

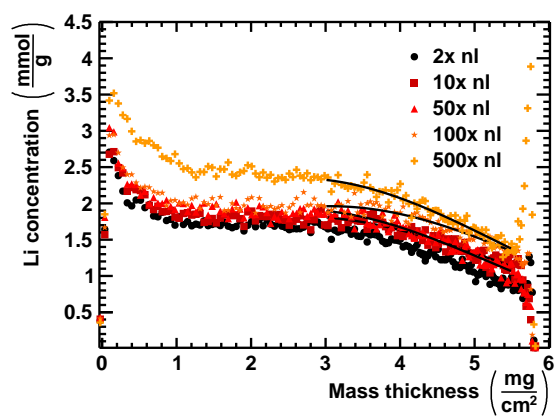


Figure C.12: Gaussian fit to determine the inflection point of the concentration profiles of the 2C-2C series.

Bibliography

- [1] United Nations. (Oct. 2020). About the Sustainable Development Goals – United Nations Sustainable Development, [Online]. Available: <https://www.un.org/sustainabledevelopment/sustainable-development-goals/> (visited on 10/21/2020).
- [2] United Nations. (Nov. 2016). Climate Change - United Nations, [Online]. Available: <https://www.un.org/en/sections/issues-depth/climate-change/> (visited on 10/21/2020).
- [3] United Nations. (Mar. 2020). Kyoto Protocol to the United Nations Framework Convention on Climate Change, [Online]. Available: <https://unfccc.int/resource/docs/convkp/kpeng.pdf> (visited on 10/21/2020).
- [4] United Nations. (Mar. 2020). Report of the Conference of the Parties on Its Twenty-First Session, Held in Paris from 30 November to 13 December 2015, [Online]. Available: <https://unfccc.int/resource/docs/2015/cop21/eng/10a01.pdf> (visited on 10/22/2020).
- [5] United Nations. (Jul. 2019). Global Warming of 1.5°C, [Online]. Available: https://www.ipcc.ch/site/assets/uploads/sites/2/2019/06/SR15_Full_Report_High_Res.pdf (visited on 10/22/2020).
- [6] T. S. Ledley, E. T. Sundquist, S. E. Schwartz, D. K. Hall, J. D. Fellows, and T. L. Killeen, “Climate Change and Greenhouse Gases”, *Eos, Transactions American Geophysical Union*, vol. 80, no. 39, pp. 453–458, 1999.
- [7] S. A. Montzka, E. J. Dlugokencky, and J. H. Butler, “Non-CO₂ Greenhouse Gases and Climate Change”, *Nature*, vol. 476, no. 7358, pp. 43–50, 2011.
- [8] NASA. (Jan. 2019). Causes, Facts – Climate Change: Vital Signs of the Planet, [Online]. Available: <https://climate.nasa.gov/causes/> (visited on 10/22/2020).
- [9] The World Bank, *World Development Report 2010: Development and Climate Change*. 2010, ISBN: 978-0-8213-7989-5.
- [10] Deutsches Atomforum e.V. (Jan. 2021). Kernenergie: Klimaschutz “Vom Anfang bis zum Ende”, [Online]. Available: https://www.kernd.de/kernd/presse/pressemitteilungen/2007/2007-03-21_kernenergie_klimaschutz.php (visited on 03/21/2007).
- [11] Oxford Martin School, University of Oxford. (Mar. 2014). Energy - Our World in Data, [Online]. Available: <https://ourworldindata.org/energy> (visited on 10/22/2020).

- [12] I. Dincer, “Renewable Energy and Sustainable Development: A Crucial Review”, *Renewable and Sustainable Energy Reviews*, vol. 4, no. 2, pp. 157–175, 2000.
- [13] X. Luo, J. Wang, M. Dooner, and J. Clarke, “Overview of Current Development in Electrical Energy Storage Technologies and the Application Potential in Power System Operation”, *Applied Energy*, vol. 137, pp. 511–536, 2015.
- [14] S. O. Amrouche, D. Rekioua, T. Rekioua, and S. Bacha, “Overview of Energy Storage in Renewable Energy Systems”, *International Journal of Hydrogen Energy*, vol. 41, no. 45, pp. 20 914–20 927, 2016.
- [15] H. C. Hesse, M. Schimpe, D. Kucevic, and A. Jossen, “Lithium-ion Battery Storage for the Grid—A Review of Stationary Battery Storage System Design Tailored for Applications in Modern Power Grids”, *Energies*, vol. 10, no. 12, p. 2107, 2017.
- [16] H. Chen, T. N. Cong, W. Yang, C. Tan, Y. Li, and Y. Ding, “Progress in Electrical Energy Storage System: A Critical Review”, *Progress in Natural Science*, vol. 19, no. 3, pp. 291–312, 2009.
- [17] K. Jayaramulu, M. Horn, A. Schneemann, H. Saini, A. Bakandritsos, V. Ranc, M. Petr, V. Stavila, C. Narayana, B. Scheibe, *et al.*, “Covalent Graphene-MOF Hybrids for High-Performance Asymmetric Supercapacitors”, *Advanced Materials*, p. 2004560, 2020.
- [18] A. Contreras, S. Yiğit, K. Özyay, and T. Veziroğlu, “Hydrogen as Aviation Fuel: A Comparison with Hydrocarbon Fuels”, *International Journal of Hydrogen Energy*, vol. 22, no. 10-11, pp. 1053–1060, 1997.
- [19] G. Karim, I. Wierzba, and Y. Al-Alousi, “Methane-Hydrogen Mixtures as Fuels”, *International Journal of Hydrogen Energy*, vol. 21, no. 7, pp. 625–631, 1996.
- [20] Bundesministerium der Justiz und für Verbraucherschutz. (Jan. 2021). Gesetz für den Vorrang Erneuerbarer Energien (Erneuerbare-Energien-Gesetz-EEG) sowie zur Änderung des Energiewirtschaftsgesetzes und des Mineralölsteuergesetzes, [Online]. Available: https://www.bgb1.de/xaver/bgb1/start.xav?startbk=Bundesanzeiger_BGB1&jumpTo=bgb1100s0305.pdf (visited on 03/29/2000).
- [21] Bundesministerium der Justiz und für Verbraucherschutz. (Jan. 2021). International Market for Green Electricity. Overview on German Policy and Opinions Among German Market Actors, [Online]. Available: <http://ftp.zew.de/pub/zew-docs/umwelt/EnergiDag2.pdf> (visited on 10/31/1999).
- [22] Strom Report. (Jan. 2021). Electricity Prices in Europe - Who pays the most? 2010 - 2020, [Online]. Available: <https://strom-report.de/electricity-prices-europe/> (visited on 01/2020).
- [23] Bundesnetzagentur. (Jan. 2021). Presse EEG Umlage 2020, [Online]. Available: https://www.bundesnetzagentur.de/SharedDocs/Pressemitteilungen/DE/2019/20191015_EEG.html (visited on 10/15/2019).

- [24] Bundesnetzagentur. (Jan. 2021). Presse EEG Umlage 2021, [Online]. Available: https://www.bundesnetzagentur.de/SharedDocs/Pressemitteilungen/DE/2020/20201015_EEGUmlage.html (visited on 10/15/2020).
- [25] Bundesministerium für Umwelt, Naturschutz und nukleare Sicherheit. (Jun. 2020). Klimaschutzplan 2050, [Online]. Available: https://www.bmu.de/fileadmin/Daten_BMU/Download_PDF/Klimaschutz/klimaschutzplan_2050_bf.pdf (visited on 02/18/2019).
- [26] Bundesministerium für Wirtschaft und Energie. (Jun. 2020). Die Energie der Zukunft, [Online]. Available: https://www.bmwi.de/Redaktion/DE/Publikationen/Energie/vierter-monitoring-bericht-energie-der-zukunft.pdf%3F__blob%3DpublicationFile%26v%3D24 (visited on 06/27/2018).
- [27] E. Umbach and H.-M. Henning, “Ist die Energiewende noch zu retten?”, *Physik Journal*, vol. 3, pp. 34–39, 2019.
- [28] Arbeitsgemeinschaft Energiebilanzen e.V. (Jan. 2021). Stromerzeugung nach Energieträgern (Strommix) von 1990 bis 2020 (in TWh) Deutschland insgesamt, [Online]. Available: <https://www.ag-energiebilanzen.de/28-0-Zusatzinformationen.html> (visited on 12/16/2020).
- [29] T. Ohnishi, “The Disaster at Japan’s Fukushima-Daiichi Nuclear Power Plant after the March 11, 2011 Earthquake and Tsunami, and the Resulting Spread of Radioisotope Contamination”, *Radiation Research*, vol. 177, no. 1, pp. 1–14, 2012.
- [30] International Atomic Energy Agency. (Jan. 2021). The Fukushima Daiichi Accident, [Online]. Available: <https://www-pub.iaea.org/MTCD/Publications/PDF/Pub1710-ReportByTheDG-Web.pdf> (visited on 08/31/2015).
- [31] International Atomic Energy Agency. (Jan. 2021). Fukushima Nuclear Accident Update Log, [Online]. Available: <https://www.iaea.org/newscenter/news/fukushima-nuclear-accident-update-log-15> (visited on 07/26/2017).
- [32] International Atomic Energy Agency. (Jan. 2021). The International Nuclear and Radiological Event Scale, [Online]. Available: <https://www-pub.iaea.org/MTCD/Publications/PDF/INES2013web.pdf> (visited on 09/09/2014).
- [33] Deutscher Bundestag. (Aug. 2011). Dreizehntes Gesetz zur Änderung des Atomgesetzes (13. AtGÄndG), [Online]. Available: <http://www.buzer.de/gesetz/9848/a172688.htm> (visited on 10/22/2020).
- [34] F. Wagner, “Zwischenbilanz der Energiewende”, *Physik Journal*, vol. 10, pp. 43–49, 2019.
- [35] Umweltbundesamt. (Jan. 2021). Bilanz 2019: CO₂ Emissionen pro Kilowattstunde Strom sinken weiter, [Online]. Available: <https://www.umweltbundesamt.de/presse/pressemitteilungen/bilanz-2019-co2-emissionen-pro-kilowattstunde-strom> (visited on 04/08/2020).

- [36] Climate Transparency. (Jan. 2021). Climate Transparency Report: Comparing G20 Climate Action and Responses to the COVID-19 Crisis, [Online]. Available: <https://www.climate-transparency.org/wp-content/uploads/2020/11/France-CT-2020.pdf> (visited on 11/23/2020).
- [37] Statista. (Jan. 2021). Production of Electricity in France in 2019, by Energy Source, [Online]. Available: <https://www.statista.com/statistics/768066/electricity-production-france-source/#statisticContainer> (visited on 05/26/2020).
- [38] International Energy Agency. (Jan. 2021). Nuclear Power in a Clean Energy System, [Online]. Available: <https://www.iea.org/reports/nuclear-power-in-a-clean-energy-system> (visited on 2021).
- [39] Umweltbundesamt. (Dec. 2020). Greenhouse Gas Emissions, [Online]. Available: <https://www.umweltbundesamt.de/en/indicator-greenhouse-gas-emissions#assessing-the-development> (visited on 12/14/2020).
- [40] P. Jochem, S. Babrowski, and W. Fichtner, “Assessing CO₂ Emissions of Electric Vehicles in Germany in 2030”, *Transportation Research Part A: Policy and Practice*, vol. 78, pp. 68–83, 2015.
- [41] European Environment Agency. (Jan. 2021). Monitoring CO₂ Emissions from Passenger Cars and Vans in 2018, [Online]. Available: <https://www.eea.europa.eu/publications/co2-emissions-from-cars-and-vans-2018> (visited on 06/08/2020).
- [42] J. Tarascon, “The Li-Ion Battery: 25 Years of Exciting and Enriching Experiences”, *Electrochemical Society Interface*, vol. 25, no. 3, p. 79, 2016.
- [43] R. Korthauer, *Lithium-Ion Batteries: Basics and Applications*. Springer, 2018, ISBN: 978-3-662-53071-9.
- [44] D. C. Bock, A. C. Marschlok, K. J. Takeuchi, and E. S. Takeuchi, “Batteries Used to Power Implantable Biomedical Devices”, *Electrochimica Acta*, vol. 84, pp. 155–164, 2012.
- [45] M. C. Smart, B. V. Ratnakumar, R. C. Ewell, S. Surampudi, F. J. Puglia, and R. Gitzen-danner, “The Use of Lithium-Ion Batteries for JPL’s Mars Missions”, *Electrochimica Acta*, vol. 268, pp. 27–40, 2018.
- [46] European Environment Agency. (Jun. 2020). EEA Report: Monitoring CO₂ Emissions from Passenger Cars and Vans in 2018, [Online]. Available: <https://www.eea.europa.eu/publications/co2-emissions-from-cars-and-vans-2018> (visited on 12/14/2020).
- [47] K. G. Gallagher, S. E. Trask, C. Bauer, T. Woehrl, S. F. Lux, M. Tschech, P. Lamp, B. J. Polzin, S. Ha, B. Long, *et al.*, “Optimizing Areal Capacities Through Understanding the Limitations of Lithium-Ion Electrodes”, *Journal of the Electrochemical Society*, vol. 163, no. 2, A138, 2015.
- [48] J. W. Choi and D. Aurbach, “Promise and Reality of Post-Lithium-Ion Batteries with High Energy Densities”, *Nature Reviews Materials*, vol. 1, no. 4, pp. 1–16, 2016.

- [49] M. A. Pope and I. A. Aksay, “Structural Design of Cathodes for Li-S Batteries”, *Advanced Energy Materials*, vol. 5, no. 16, p. 1500124, 2015.
- [50] Q. Liu, C. Du, B. Shen, P. Zuo, X. Cheng, Y. Ma, G. Yin, and Y. Gao, “Understanding Undesirable Anode Lithium Plating Issues in Lithium-Ion Batteries”, *RSC Advances*, vol. 6, no. 91, pp. 88683–88700, 2016.
- [51] S. J. An, J. Li, C. Daniel, D. Mohanty, S. Nagpure, and D. L. Wood III, “The State of Understanding of the Lithium-Ion-Battery Graphite Solid Electrolyte Interphase (SEI) and Its Relationship to Formation Cycling”, *Carbon*, vol. 105, pp. 52–76, 2016.
- [52] G. J. Kearley and V. K. Peterson, *Neutron Applications in Materials for Energy*. 2015, ISBN: 978-3-319-06655-4.
- [53] V. Zinth, C. von Lüders, M. Hofmann, J. Hattendorff, I. Buchberger, S. Erhard, J. Rebelo-Kornmeier, A. Jossen, and R. Gilles, “Lithium Plating in Lithium-Ion Batteries at Sub-Ambient Temperatures Investigated by In Situ Neutron Diffraction”, *Journal of Power Sources*, vol. 271, pp. 152–159, 2014.
- [54] A. Senyshyn, M. Mühlbauer, K. Nikolowski, T. Pirling, and H. Ehrenberg, ““In-Operando” Neutron Scattering Studies on Li-Ion Batteries”, *Journal of Power Sources*, vol. 203, pp. 126–129, 2012.
- [55] D. R. Sørensen, M. Heere, J. Zhu, M. S. Darma, S. M. Zimmik, M. J. Mühlbauer, L. Mereacre, V. Baran, A. Senyshyn, M. Knapp, *et al.*, “Fatigue in High-Energy Commercial Li Batteries while Cycling at Standard Conditions: An In Situ Neutron Powder Diffraction Study”, *ACS Applied Energy Materials*, vol. 3, no. 7, pp. 6611–6622, 2020.
- [56] N. Paul, M. Wetjen, S. Busch, H. Gasteiger, and R. Gilles, “Contrast Matched SANS for Observing SEI and Pore Clogging in Silicon-Graphite Anodes”, *Journal of the Electrochemical Society*, vol. 166, no. 6, pp. A1051–A1054, 2019.
- [57] B. Jerliu, L. Dörrer, E. Hüger, G. Borchardt, R. Steitz, U. Geckle, V. Oberst, M. Bruns, O. Schneider, and H. Schmidt, “Neutron Reflectometry Studies on the Lithiation of Amorphous Silicon Electrodes in Lithium-Ion Batteries”, *Physical Chemistry Chemical Physics*, vol. 15, no. 20, pp. 7777–7784, 2013.
- [58] B. Jerliu, E. Huüger, L. Dörrer, B.-K. Seidlhofer, R. Steitz, V. Oberst, U. Geckle, M. Bruns, and H. Schmidt, “Volume Expansion during Lithiation of Amorphous Silicon Thin Film Electrodes Studied by In-Operando Neutron Reflectometry”, *The Journal of Physical Chemistry C*, vol. 118, no. 18, pp. 9395–9399, 2014.
- [59] W. Weydanz, H. Reisenweber, A. Gottschalk, M. Schulz, T. Knoche, G. Reinhart, M. Masuch, J. Franke, and R. Gilles, “Visualization of Electrolyte Filling Process and Influence of Vacuum during Filling for Hard Case Prismatic Lithium Ion Cells by Neutron Imaging to Optimize the Production Process”, *Journal of Power Sources*, vol. 380, pp. 126–134, 2018.

- [60] J. B. Habedank, F. J. Günter, N. Billot, R. Gilles, T. Neuwirth, G. Reinhart, and M. F. Zaeh, “Rapid Electrolyte Wetting of Lithium-Ion Batteries Containing Laser Structured Electrodes: In Situ Visualization by Neutron Radiography”, *The International Journal of Advanced Manufacturing Technology*, vol. 102, no. 9-12, pp. 2769–2778, 2019.
- [61] H. Wang, R. G. Downing, J. A. Dura, and D. S. Hussey, “In Situ Neutron Techniques for Studying Lithium Ion Batteries”, in *Polymers for Energy Storage and Delivery: Polyelectrolytes for Batteries and Fuel Cells*, ACS Publications, 2012, pp. 91–106.
- [62] T. W. Verhallen, S. Lv, and M. Wagemaker, “Operando Neutron Depth Profiling to Determine the Spatial Distribution of Li in Li-ion Batteries”, *Frontiers in Energy Research*, vol. 6, p. 62, 2018.
- [63] J. Ziegler, B. Crowder, G. Cole, J. Baglin, and B. Masters, “Boron Atom Distributions in Ion-Implanted Silicon by the (n,⁴He) Nuclear Reaction”, *Applied Physics Letters*, vol. 21, no. 1, pp. 16–17, 1972.
- [64] J. F. Ziegler, G. W. Cole, and J. E. E. Baglin, “Technique for Determining Concentration Profiles of Boron Impurities in Substrates”, *Journal of Applied Physics*, vol. 43, no. 9, pp. 3809–3815, 1972.
- [65] R. Downing, G. Lamaze, J. Langland, and S. Hwang, “Neutron Depth Profiling: Overview and Description of NIST Facilities”, *Journal of Research of the National Institute of Standards and Technology*, vol. 98, no. 1, p. 109, 1993.
- [66] L. Werner, “The N4DP Instrument”, Dissertation, Technische Universität München, 2020.
- [67] Heinz Maier-Leibnitz Zentrum. (Jun. 2020). PGAA - Bildgebende Verfahren & Analyse - Instrumente & Labore - MLZ - Heinz Maier-Leibnitz Zentrum, [Online]. Available: <https://mlz-garching.de/pgaa/de> (visited on 10/22/2020).
- [68] F. Linsenmann, P. Rapp, M. Trunk, J. Weaver, B. Märkisch, H. Gasteiger, *et al.*, “Spatially- and Time-Resolved Detection of Lithium Plating during Fast-Charging of a Graphite-Based Lithium-Ion Battery”, *in preparation*,
- [69] E. Vezhlev, A. Ioffe, S. Mattauch, S. Staringer, V. Ossovyi, C. Felder, E. Hüger, J. Vacik, I. Tomandl, V. Hnatowicz, *et al.*, “A New Neutron Depth Profiling Spectrometer at the JCNS for a Focused Neutron Beam”, *Radiation Effects and Defects in Solids*, vol. 175, no. 3-4, pp. 342–355, 2020.
- [70] T. Chanjuan, X. Caijin, Y. Yonggang, S. Cong, J. Xiangchun, Y. Weixu, L. Xudong, N. Bangfa, and W. Pingsheng, “Neutron Depth Profiling System at CARR”, *Applied Radiation and Isotopes*, vol. 148, pp. 102–107, 2019.
- [71] R. Li, X. Yang, G. Wang, H. Dou, D. Qian, and S. Wang, “Development of Neutron Depth Profiling at CMRR”, *Nuclear Instruments and Methods in Physics Research Section A: Accelerators, Spectrometers, Detectors and Associated Equipment*, vol. 788, pp. 1–4, 2015.

- [72] B. Park, G. Sun, and H. Choi, “Development of Cold Neutron Depth Profiling System at HANARO”, *Nuclear Instruments and Methods in Physics Research Section A: Accelerators, Spectrometers, Detectors and Associated Equipment*, vol. 752, pp. 20–26, 2014.
- [73] S. Çetiner, K. Ünlü, and R. G. Downing, “Development of Time-of-Flight Neutron Depth Profiling at Penn State University”, *Journal of Radioanalytical and Nuclear Chemistry*, vol. 271, no. 2, pp. 275–281, 2007.
- [74] P. Mulligan, L. Cao, and D. Turkoglu, “A Multi-Detector, Digitizer Based Neutron Depth Profiling Device for Characterizing Thin Film Materials”, *Review of Scientific Instruments*, vol. 83, no. 7, p. 073303, 2012.
- [75] G. Ceccio, J. Vacik, P. Horák, A. Cannavò, and V. Hnatowicz, “Measurement of Lithium Diffusion Coefficient in Thin Metallic Multilayer by Neutron Depth Profiling”, *Surface and Interface Analysis*, pp. 1–4, 2020.
- [76] R. G. Downing and G. P. Lamaze, “Near-Surface Profiling of Semiconductor Materials Using Neutron Depth Profiling”, *Semiconductor Science and Technology*, vol. 10, no. 11, p. 1423, 1995.
- [77] R. G. Downing. (Nov. 2009). NIST NDP, [Online]. Available: <https://sites.google.com/site/nistndp/home> (visited on 10/22/2020).
- [78] H. Börner, J. Brown, and C. J. Carlile, *Neutron Data Booklet*. 2003, ISBN: 0-9704143-7-4.
- [79] B. Märkisch, H. Mest, H. Saul, X. Wang, H. Abele, D. Dubbers, M. Klopff, A. Petoukhov, C. Roick, T. Soldner, *et al.*, “Measurement of the Weak Axial-Vector Coupling Constant in the Decay of Free Neutrons Using a Pulsed Cold Neutron Beam”, *Physical Review Letters*, vol. 122, no. 24, p. 242501, 2019.
- [80] P. C. H. Mitchell, *Vibrational Spectroscopy with Neutrons: With Applications in Chemistry, Biology, Materials Science and Catalysis*. World Scientific, 2005, vol. 3, ISBN: 978-981-256-013-1.
- [81] R. Levicky, T. M. Herne, M. J. Tarlov, and S. K. Satija, “Using Self-Assembly to Control the Structure of DNA Monolayers on Gold: A Neutron Reflectivity Study”, *Journal of the American Chemical Society*, vol. 120, no. 38, pp. 9787–9792, 1998.
- [82] R. F. Barth, A. H. Soloway, and R. G. Fairchild, “Boron Neutron Capture Therapy for Cancer”, *Scientific American*, vol. 263, no. 4, pp. 100–107, 1990.
- [83] A. H. Soloway, W. Tjarks, B. A. Barnum, F.-G. Rong, R. F. Barth, I. M. Codogni, and J. G. Wilson, “The Chemistry of Neutron Capture Therapy”, *Chemical Reviews*, vol. 98, no. 4, pp. 1515–1562, 1998.
- [84] E. Kluge, C. Stieghorst, F. Wagner, R. Gebhard, Z. Révay, and J. Jolie, “Archaeometry at the PGAA Facility of MLZ—Prompt Gamma-Ray Neutron Activation Analysis and Neutron Tomography”, *Journal of Archaeological Science: Reports*, vol. 20, pp. 303–306, 2018.

- [85] C. Stieghorst, G. Hampel, B. Karches, P. Krenckel, P. Kudějová, C. Plonka, Z. Révay, S. Riepe, K. Welter, and N. Wiehl, “Determination of Boron and Hydrogen in Materials for Multicrystalline Solar Cell Production with Prompt Gamma Activation Analysis”, *Journal of Radioanalytical and Nuclear Chemistry*, vol. 317, no. 1, pp. 307–313, 2018.
- [86] X.-L. Wang, K. An, L. Cai, Z. Feng, S. E. Nagler, C. Daniel, K. J. Rhodes, A. D. Stoica, H. D. Skorpenske, C. Liang, *et al.*, “Visualizing the Chemistry and Structure Dynamics in Lithium-Ion Batteries by In-Situ Neutron Diffraction”, *Scientific Reports*, vol. 2, p. 747, 2012.
- [87] Particle Data Group, P. Zyla, R. Barnett, J. Beringer, O. Dahl, D. Dwyer, D. Groom, C.-J. Lin, K. Lugovsky, E. Pianori, *et al.*, “Review of Particle Physics”, *Progress of Theoretical and Experimental Physics*, vol. 2020, no. 8, p. 083C01, 2020.
- [88] Heinz Maier-Leibnitz Zentrum. (Oct. 2020). TUM FRMII: Sekundäre Quellen für Neutronen & Positronen, [Online]. Available: <https://www.frm2.tum.de/sekund%C3%A4rquellen/> (visited on 10/22/2020).
- [89] N. Buitrago, J. Santisteban, A. Tartaglione, J. Marín, L. Barrow, M. Daymond, M. Schulz, M. Grosse, A. Tremsin, E. Lehmann, *et al.*, “Determination of Very Low Concentrations of Hydrogen in Zirconium Alloys by Neutron Imaging”, *Journal of Nuclear Materials*, vol. 503, pp. 98–109, 2018.
- [90] S. Ishiwata, T. Nakajima, J.-H. Kim, D. Inosov, N. Kanazawa, J. White, J. Gavilano, R. Georgii, K. Seemann, G. Brandl, *et al.*, “Emergent Topological Spin Structures in the Centrosymmetric Cubic Perovskite SrFeO_3 ”, *Physical Review B*, vol. 101, no. 13, p. 134406, 2020.
- [91] N. van Well, S. Ramakrishnan, K. Beauvois, N. Qureshi, E. Ressouche, M. Skoulatos, R. Georgii, O. Zaharko, and S. van Smaalen, “Magnetic-Field-Controlled Quantum Critical Points in the Triangular Antiferromagnetic $\text{Cs}_2\text{CuCl}_{4-x}\text{Br}_x$ Mixed System”, *Annalen der Physik*, vol. 532, p. 2000147, 2020.
- [92] S. Grigoriev, E. Altynbaev, S.-A. Siegfried, K. Pshenichnyi, D. Honnecker, A. Heinemann, and A. Tsvyashchenko, “Spin-Wave Dynamics in Mn-doped FeGe Helimagnet: Small-Angle Neutron Scattering Study”, *Journal of Magnetism and Magnetic Materials*, vol. 459, pp. 159–164, 2018.
- [93] S. V. Grigoriev, K. A. Pshenichnyi, E. V. Altynbaev, S.-A. Siegfried, A. Heinemann, D. Honnecker, and D. Menzel, “On the Measurement of the Stiffness of Spin Waves in the $\text{Fe}_{0.75}\text{Co}_{0.25}\text{Si}$ Helimagnet by the Small-Angle Neutron Scattering Method”, *JETP Letters*, vol. 107, no. 10, pp. 640–645, 2018.
- [94] S. Mühlbauer, B. Binz, F. Jonietz, C. Pfleiderer, A. Rosch, A. Neubauer, R. Georgii, and P. Böni, “Skyrmion Lattice in a Chiral Magnet”, *Science*, vol. 323, no. 5916, pp. 915–919, 2009.

- [95] V. F. Sears, “Neutron Scattering Lengths and Cross Sections”, *Neutron News*, vol. 3, no. 3, pp. 26–37, 1992.
- [96] J. Lichtinger, “Quantitative Untersuchungen der lokalen Lithiumkonzentration im menschlichen Gehirn und ihr Bezug zu affektiven Störungen”, Dissertation, Technische Universität München, 2015.
- [97] G. Molnar, Z. Révay, R. M. Lindstrom, T. Belgya, C. Yonezawa, and D. L. Anderson, *Handbook of Prompt Gamma Activation Analysis with Neutron Beams*. 2004, ISBN: 978-0-387-23359-8.
- [98] Element Collection, Inc. (Nov. 2017). Neutron Cross Section for all the Elements in the Periodic Table, [Online]. Available: <https://periodictable.com/Properties/A/NeutronCrossSection.sp.log.html> (visited on 10/22/2020).
- [99] P. Kudejova, “Two New Installations for Non-Destructive Sample Analysis: PIXE and PGAA”, Dissertation, Universität zu Köln, 2005.
- [100] R. F. Fleming, “Neutron Self-Shielding Factors for Simple Geometries”, *International Journal of Applied Radiation and Isotopes*, vol. 33, no. 11, pp. 1263–1268, 1982.
- [101] International Atomic Energy Agency. (Oct. 2020). IAEA Nuclear Data Services, [Online]. Available: <https://www-nds.iaea.org/> (visited on 10/22/2020).
- [102] B. Povh, K. Rith, C. Scholz, F. Zetsche, and W. Rodejohann, *Teilchen und Kerne: Eine Einführung in die physikalischen Konzepte*. Springer-Verlag, 2014, ISBN: 978-3-642-37822-5.
- [103] M. Nastasi, J. W. Mayer, and J. K. Hirvonen, *Ion-Solid Interactions: Fundamentals and Applications*. Cambridge University Press, 1996, ISBN: 978-0-511-56500-7.
- [104] M. K. Kubo and Y. Sakai, “A Simple Derivation of the Formula of the Doppler Broadened 478 keV γ -Ray Lineshape from ${}^7\text{Li}$ and Its Analytical Application”, *Journal of Nuclear and Radiochemical Sciences*, vol. 1, no. 2, pp. 83–85, 2000.
- [105] L. Szentmiklósi, K. Gmélíng, and Z. Révay, “Fitting the Boron Peak and Resolving Interferences in the 450–490 keV Region of PGAA Spectra”, *Journal of Radioanalytical and Nuclear Chemistry*, vol. 271, no. 2, pp. 447–453, 2007.
- [106] Y. Sakai, C. Yonezawa, M. Magara, H. Sawahata, and Y. Ito, “Measurement and Analysis of the Line Shape of Prompt γ -Rays from Recoiling ${}^7\text{Li}$ produced in the ${}^{10}\text{B}(n, \alpha){}^7\text{Li}$ Reaction”, *Nuclear Instruments and Methods in Physics Research Section A: Accelerators, Spectrometers, Detectors and Associated Equipment*, vol. 353, no. 1-3, pp. 699–701, 1994.
- [107] M. Magara and C. Yonezawa, “Decomposition of Prompt Gamma-Ray Spectra Including the Doppler-Broadened Peak for Boron Determination”, *Nuclear Instruments and Methods in Physics Research Section A: Accelerators, Spectrometers, Detectors and Associated Equipment*, vol. 411, no. 1, pp. 130–136, 1998.

- [108] M. Tanabashi, K. Hagiwara, K. Hikasa, K. Nakamura, Y. Sumino, F. Takahashi, J. Tanaka, K. Agashe, G. Aielli, C. AMSler, *et al.*, “Review of Particle Physics”, *Physical Review D*, vol. 98, no. 3, p. 030 001, 2018.
- [109] H. Gümüş and F. Köksal, “Effective Stopping Charges and Stopping Power Calculations for Heavy Ions”, *Radiation Effects and Defects in Solids*, vol. 157, no. 5, pp. 445–458, 2002.
- [110] H. Bethe, “Bremsformel für Elektronen relativistischer Geschwindigkeit”, *Zeitschrift für Physik*, vol. 76, no. 5-6, pp. 293–299, 1932.
- [111] J. Ziegler, “Stopping of Energetic Light Ions in Elemental Matter”, *Journal of Applied Physics*, vol. 85, no. 3, pp. 1249–1272, 1999.
- [112] National Institute of Standards and Technology. (Oct. 2020). CODATA Value: Molar Mass Constant, [Online]. Available: <https://physics.nist.gov/cgi-bin/cuu/Value?mu> (visited on 10/22/2020).
- [113] H. Sugiyama, “Modification of Lindhard-Scharff-Schi φ_{tt} Formula for Electronic Stopping Power”, *Journal of the Physical Society of Japan*, vol. 50, no. 3, pp. 929–932, 1981.
- [114] J. Lindhard, M. Scharff, and H. E. Schiøtt. (1963). Range Concepts and Heavy Ion Ranges, [Online]. Available: <http://gymarkiv.sdu.dk/MFM/kdvs/mfn%2030-39/mfm-33-14.pdf> (visited on 10/22/2020).
- [115] D. Fink, “Die Verwendung von (n, p)-und (n, α)-Reaktionen für die Messung von Reichweite- und Diffusionsprofilen und Channeling- und Blocking-Effekten”, Dissertation, Freie Universität Berlin, 1974.
- [116] H. H. Andersen and J. F. Ziegler, *Hydrogen Stopping Powers and Ranges in all Elements*. 1977, ISBN: 978-0-080-21605-8.
- [117] J. Ziegler. (Aug. 2017). SRIM & TRIM, [Online]. Available: <http://www.srim.org/> (visited on 10/22/2020).
- [118] M. Trunk, M. Wetjen, L. Werner, R. Gernhäuser, B. Märkisch, Z. Révay, H. Gasteiger, and R. Gilles, “Materials Science Applications of Neutron Depth Profiling at the PGAA Facility of Heinz Maier-Leibnitz Zentrum”, *Materials Characterization*, vol. 146, pp. 127–134, 2018.
- [119] L. Werner, M. Trunk, R. Gernhäuser, R. Gilles, B. Märkisch, and Z. Révay, “The New Neutron Depth Profiling Instrument N4DP at the Heinz Maier-Leibnitz Zentrum”, *Nuclear Instruments and Methods in Physics Research Section A: Accelerators, Spectrometers, Detectors and Associated Equipment*, vol. 911, pp. 30–36, 2018.
- [120] Heinz Maier-Leibnitz Zentrum. (Oct. 2020). MLZ - Heinz Maier-Leibnitz Zentrum, [Online]. Available: <https://www.mlz-garching.de/> (visited on 10/22/2020).

- [121] Nuclear Power. (Oct. 2020). Uranium-235 Fission, [Online]. Available: <https://www.nuclear-power.net/nuclear-power-plant/nuclear-fuel/uranium/uranium-235/uranium-235-fission/> (visited on 10/22/2020).
- [122] Heinz Maier-Leibnitz Zentrum. (Nov. 2020). Neutronenquelle MLZ, [Online]. Available: <https://mlz-garching.de/neutronenforschung/neutronenquelle.html> (visited on 11/10/2020).
- [123] Heinz Maier-Leibnitz Zentrum. (Oct. 2010). Experimental Facilities Forschungsneutronenquelle Heinz Maier-Leibnitz (FRM II), [Online]. Available: http://cdn.frm2.tum.de/fileadmin/stuff/instruments/BlueBook/exp-fac_weboptimiert-2p.pdf (visited on 10/22/2020).
- [124] Heinz Maier-Leibnitz Zentrum. (2020). MLZ Annual Report 2019, [Online]. Available: <https://mlz-garching.de/media/20200423-jb-2019-online.pdf> (visited on 10/22/2020).
- [125] Heinz Maier-Leibnitz Zentrum. (Nov. 2020). Das Atom-Ei feiert 60. Geburtstag, [Online]. Available: https://mlz-garching.de/aktuelles-und-presse/newsartikel/das-atom-ei-feiert-60-geburtstag.html?search_highlighter=forschungsreaktor+m%C3%BCnchen (visited on 11/10/2020).
- [126] Stadt Garching b. München. (Sep. 2020). Wappen und Fahne, [Online]. Available: <https://www.garching.de/mobile/Leben+in+Garching/Garching+stellt+sich+vor/Wappen+und+Fahne.html> (visited on 11/10/2020).
- [127] Heinz Maier-Leibnitz Zentrum. (Oct. 2020). Positronen - Instrumente & Labore - MLZ - Heinz Maier-Leibnitz Zentrum, [Online]. Available: <https://www.mlz-garching.de/instrumente-und-labore/positronen.html> (visited on 10/22/2020).
- [128] M. Meven, V. Hutanu, and G. Heger, “Scientific Review: HEiDi: Single Crystal Diffractometer at the Hot Source of the FRM II”, *Neutron News*, vol. 18, no. 2, pp. 19–21, 2007.
- [129] V. Hutanu, M. Meven, S. Masalovich, G. Heger, and G. Roth, “ ^3He Spin Filters for Spherical Neutron Polarimetry at the Hot Neutrons Single Crystal Diffractometer POLI-HEiDi”, in *Journal of Physics: Conference Series*, IOP Publishing, vol. 294, 2011, p. 012012.
- [130] A. Chao and W. Chou, *Reviews of Accelerator Science and Technology*. World Scientific, 2008, vol. 1, ISBN: 978-9-814-38398-1.
- [131] K. Zeitelhack, C. Schanzer, A. Kastenmüller, A. Röhrmoser, C. Daniel, J. Franke, E. Gutmiedl, V. Kudryashov, D. Maier, D. Pätke, *et al.*, “Measurement of Neutron Flux and Beam Divergence at the Cold Neutron Guide System of the New Munich Research Reactor FRM-II”, *Nuclear Instruments and Methods in Physics Research Section A: Accelerators, Spectrometers, Detectors and Associated Equipment*, vol. 560, no. 2, pp. 444–453, 2006.
- [132] C. Franz and T. Schröder, “RESEDA: Resonance Spin Echo Spectrometer”, *Journal of Large-Scale Research Facilities JLSRF*, vol. 1, p. 14, 2015.

- [133] B. Pedersen, F. Frey, W. Scherer, P. Gille, and G. Meisterernst, “The New Single Crystal Diffractometer RESI at FRM-II”, *Physica B: Condensed Matter*, vol. 385, pp. 1046–1048, 2006.
- [134] M. Hoelzel, A. Senyshyn, N. Juenke, H. Boysen, W. Schmahl, and H. Fuess, “High-Resolution Neutron Powder Diffractometer SPODI at Research Reactor FRM II”, *Nuclear Instruments and Methods in Physics Research Section A: Accelerators, Spectrometers, Detectors and Associated Equipment*, vol. 667, pp. 32–37, 2012.
- [135] M. Hofmann, G. A. Seidl, J. Rebelo-Kornmeier, U. Garbe, R. Schneider, R. C. Wimpory, U. Wasmuth, and U. Noster, “The New Materials Science Diffractometer STRESS-SPEC at FRM-II”, in *Materials Science Forum*, Trans Tech Publ, vol. 524, 2006, pp. 211–216.
- [136] A. Houben, W. Schweika, T. Brückel, and R. Dronskowski, “New Neutron-Guide Concepts and Simulation Results for the POWTEX Instrument”, *Nuclear Instruments and Methods in Physics Research Section A: Accelerators, Spectrometers, Detectors and Associated Equipment*, vol. 680, pp. 124–133, 2012.
- [137] E. Germani, H. Lelouard, and M. Fallet, “SAPHIR: A Shiny Application to Analyze Tissue Section Images”, *F1000Research*, vol. 9, no. 1276, p. 1276, 2020.
- [138] P. Link, G. Eckold, and J. Neuhaus, “The New Thermal Triple-Axis Spectrometer PUMA at the Munich Neutron-Source”, *Physica B: Condensed Matter*, vol. 276, pp. 122–123, 2000.
- [139] T. Keller, P. Aynajian, S. Bayrakci, K. Buchner, K. Habicht, H. Klann, M. Ohl, and B. Keimer, “Scientific Review: The Triple Axis Spin-Echo Spectrometer TRISP at the FRM II”, *Neutron News*, vol. 18, no. 2, pp. 16–18, 2007.
- [140] J. Voigt, E. Babcock, and T. Brückel, “Beam Transport and Polarization at TOPAS, the Thermal Time-Of-Flight Spectrometer with Polarization Analysis”, in *Journal of Physics: Conference Series*, IOP Publishing, vol. 211, 2010, p. 012032.
- [141] T. Bücherl and S. Söllradl, “NECTAR: Radiography and Tomography Station Using Fission Neutrons”, *Journal of Large-Scale Research Facilities JLSRF*, vol. 1, p. 19, 2015.
- [142] F. M. Wagner, P. Kneschaurek, A. Kastenmüller, B. Loeper-Kabasakal, S. Kampfer, H. Breitzkreutz, W. Waschkowski, M. Molls, and W. Petry, “The Munich Fission Neutron Therapy Facility MEDAPP at the Research Reactor FRM II”, *Strahlentherapie und Onkologie*, vol. 184, no. 12, pp. 643–646, 2008.
- [143] A. Ostermann and T. Schrader, “BIODIFF: Diffractometer for Large Unit Cells”, *Journal of Large-Scale Research Facilities JLSRF*, vol. 1, p. 2, 2015.
- [144] Z. Révay, P. Kudějová, K. Kleszcz, S. Söllradl, and C. Genreith, “In-Beam Activation Analysis Facility at MLZ, Garching”, *Nuclear Instruments and Methods in Physics Research Section A: Accelerators, Spectrometers, Detectors and Associated Equipment*, vol. 799, pp. 114–123, 2015.

- [145] A. V. Feoktystov, H. Frielinghaus, Z. Di, S. Jaksch, V. Pipich, M.-S. Appavou, E. Babcock, R. Hanslik, R. Engels, G. Kemmerling, *et al.*, “KWS-1 High-Resolution Small-Angle Neutron Scattering Instrument at JCNS: Current State”, *Journal of Applied Crystallography*, vol. 48, no. 1, pp. 61–70, 2015.
- [146] A. Radulescu, N. K. Szekely, and M.-S. Appavou, “KWS-2: Small Angle Scattering Diffractometer”, *Journal of Large-Scale Research Facilities JLSRF*, vol. 1, p. 29, 2015.
- [147] G. Goerigk and Z. Varga, “Comprehensive Upgrade of the High-Resolution Small-Angle Neutron Scattering Instrument KWS-3 at FRM II”, *Journal of Applied Crystallography*, vol. 44, no. 2, pp. 337–342, 2011.
- [148] A. Heinemann and S. Mühlbauer, “SANS-1: Small Angle Neutron Scattering”, *Journal of Large-Scale Research Facilities JLSRF*, vol. 1, p. 10, 2015.
- [149] E. Calzada, F. Gruenauer, M. Mühlbauer, B. Schillinger, and M. Schulz, “New Design for the ANTARES-II Facility for Neutron Imaging at FRM II”, *Nuclear Instruments and Methods in Physics Research Section A: Accelerators, Spectrometers, Detectors and Associated Equipment*, vol. 605, no. 1-2, pp. 50–53, 2009.
- [150] W. Schweika and P. Böni, “The Instrument DNS: Polarization Analysis for Diffuse Neutron Scattering”, *Physica B: Condensed Matter*, vol. 297, no. 1-4, pp. 155–159, 2001.
- [151] O. Holderer, M. Monkenbusch, R. Schätzler, H. Kleines, W. Westerhausen, and D. Richter, “The JCNS Neutron Spin-Echo Spectrometer J-NSE at the FRM II”, *Measurement Science and Technology*, vol. 19, no. 3, p. 034 022, 2008.
- [152] S. Pasini, O. Holderer, T. Kozielski, D. Richter, and M. Monkenbusch, “J-NSE-Phoenix, a Neutron Spin-Echo Spectrometer With Optimized Superconducting Precession Coils at the MLZ in Garching”, *Review of Scientific Instruments*, vol. 90, no. 4, p. 043 107, 2019.
- [153] M. Janoschek, P. Böni, and M. Braden, “Optimization of Elliptic Neutron Guides for Triple-Axis Spectroscopy”, *Nuclear Instruments and Methods in Physics Research Section A: Accelerators, Spectrometers, Detectors and Associated Equipment*, vol. 613, no. 1, pp. 119–126, 2010.
- [154] A. Schneidewind, P. Link, D. Etdorf, R. Schedler, M. Rotter, and M. Loewenhaupt, “PANDA—First Results from the Cold Three-Axes Spectrometer at FRM-II”, *Physica B: Condensed Matter*, vol. 385, pp. 1089–1091, 2006.
- [155] J. Wuttke, A. Budwig, M. Drochner, H. Kämmerling, F.-J. Kayser, H. Kleines, V. Ossovyi, L. C. Pardo, M. Prager, D. Richter, *et al.*, “SPHERES, Jülich’s High-Flux Neutron Backscattering Spectrometer at FRM II”, *Review of Scientific Instruments*, vol. 83, no. 7, p. 075 109, 2012.
- [156] T. Unruh, J. Neuhaus, and W. Petry, “The High-Resolution Time-Of-Flight Spectrometer TOFTOF”, *Nuclear Instruments and Methods in Physics Research Section A: Accelerators, Spectrometers, Detectors and Associated Equipment*, vol. 580, no. 3, pp. 1414–1422, 2007.

- [157] S. Mattauich, A. Koutsioubas, and S. Pütter, “MARIA: Magnetic Reflectometer with High Incident Angle”, *Journal of Large-Scale Research Facilities JLSRF*, vol. 1, p. 8, 2015.
- [158] Y. Khaydukov, O. Soltwedel, and T. Keller, “NREX: Neutron Reflectometer with X-Ray Option”, *Journal of Large-Scale Research Facilities JLSRF*, vol. 1, p. 38, 2015.
- [159] R. Kampmann, M. Haese-Seiller, V. Kudryashov, B. Nickel, C. Daniel, W. Fenzl, A. Schreyer, E. Sackmann, and J. Rädler, “Horizontal TOF-Neutron Reflectometer REF-SANS at FRM-II Munich/Germany: First Tests and Status”, *Physica B: Condensed Matter*, vol. 385, pp. 1161–1163, 2006.
- [160] R. Georgii, T. Weber, G. Brandl, M. Skoulatos, M. Janoschek, S. Muehlbauer, C. Pfeiderer, and P. Boeni, “The Multi-Purpose Three-Axis Spectrometer (TAS) MIRA at FRM II”, *Nuclear Instruments and Methods in Physics Research Section A: Accelerators, Spectrometers, Detectors and Associated Equipment*, vol. 881, pp. 60–64, 2018.
- [161] J. Klenke, “MEPHISTO: Facility for Particle Physics with Cold Neutrons”, *Journal of Large-Scale Research Facilities JLSRF*, vol. 1, p. 21, 2015.
- [162] X. Wang, C. Ziener, H. Abele, S. Bodmaier, D. Dubbers, J. Erhart, A. Hollering, E. Jericha, J. Klenke, H. Fillunger, *et al.*, “Design of the Magnet System of the Neutron Decay Facility PERC”, in *EPJ Web of Conferences*, EDP Sciences, vol. 219, 2019, p. 04 007.
- [163] C. Hugenschmidt, C. Piochacz, M. Reiner, and K. Schreckenbach, “The NEPOMUC Upgrade and Advanced Positron Beam Experiments”, *New Journal of Physics*, vol. 14, no. 5, p. 055 027, 2012.
- [164] C. Hugenschmidt, H. Ceeh, T. Gigl, F. Lippert, C. Piochacz, M. Reiner, K. Schreckenbach, S. Vohburger, J. Weber, and S. Zimnik, “Positron Beam Characteristics at NEPOMUC Upgrade”, in *Journal of Physics: Conference Series*, IOP Publishing, vol. 505, 2014, p. 012 029.
- [165] Heinz Maier-Leibnitz Zentrum. (Nov. 2020). MLZ - Heinz Maier-Leibnitz Zentrum, [Online]. Available: <https://mlz-garching.de/neutronenforschung/experimentelle-methoden.html> (visited on 11/23/2020).
- [166] E. Kluge, C. Stieghorst, Z. Révay, P. Kudějová, and J. Jolie, “Optimization and Characterization of the PGAI-NT Instrument’s Neutron Tomography Set-Up at MLZ”, *Nuclear Instruments and Methods in Physics Research Section A: Accelerators, Spectrometers, Detectors and Associated Equipment*, vol. 932, pp. 1–15, 2019.
- [167] Micronix USA. (Oct. 2020). Linear Motion-Translation Stage VT-50L, [Online]. Available: <http://www.micronixusa.com/motion/product/prodDetail.cfm?firstlevel=1&sublevel=16&prodid=190> (visited on 10/22/2020).
- [168] GSI Helmholtzzentrum für Schwerionenforschung GmbH. (Aug. 2020). WebAtima - Energy Loss Calculator, [Online]. Available: <https://www.isotopea.com/webatima/#/> (visited on 10/22/2020).

- [169] The Good Scents Company. (Oct. 2020). The Good Scents Company Information System, [Online]. Available: <http://www.thegoodscentscopy.com/> (visited on 10/22/2020).
- [170] F. Linsenmann, M. Trunk, P. Rapp, L. Werner, R. Gernhäuser, R. Gilles, B. Märkisch, Z. Revay, and H. Gasteiger, “A Liquid Electrolyte-Based Lithium-Ion Battery Cell Design for Operando Neutron Depth Profiling”, *Journal of the Electrochemical Society*, vol. 167, no. 10, p. 100554, 2020.
- [171] C. Sheehan, W. Lennard, and J. Mitchell, “Measurement of the Efficiency of a Silicon Surface Barrier Detector for Medium Energy Ions Using a Rutherford Backscattering Experiment”, *Measurement Science and Technology*, vol. 11, no. 8, p. L5, 2000.
- [172] R. Lutter, O. Schaile, K. Schoeffel, K. Steinberger, and C. Broude. (May 2019). MARaBOU: MBS and Root Based Online Offline Utility, [Online]. Available: <https://www-old.mll-muenchen.de/marabou/htmldoc/> (visited on 10/22/2020).
- [173] R. Brun and F. Rademakers, “ROOT—An Object Oriented Data Analysis Framework”, *Nuclear Instruments and Methods in Physics Research Section A: Accelerators, Spectrometers, Detectors and Associated Equipment*, vol. 389, no. 1-2, pp. 81–86, 1997.
- [174] J. A.-M. G. Nikolaus Kurz. (Oct. 2020). Multi-Branch-System, MBS, [Online]. Available: <https://www.gsi.de/work/forschung/experimentelektronik/datenverarbeitung/datenerfassung/mbs.htm> (visited on 10/22/2020).
- [175] NIST Center for Neutron Research. (Nov. 2011). The NIST Center for Neutron Research: 40 Years Serving NIST/NBS and the Nation, [Online]. Available: https://www.ncnr.nist.gov/NCNRHistory_Rush_Cappelletti.pdf (visited on 10/22/2020).
- [176] NIST Center for Neutron Research. (Oct. 2020). NIST Center for Neutron Research (NIST), [Online]. Available: <https://www.nist.gov/ncnr> (visited on 10/22/2020).
- [177] NIST Center for Neutron Research. (Apr. 2020). NIST Center for Neutron Research Accomplishments and Opportunities 2019, [Online]. Available: <https://nvlpubs.nist.gov/nistpubs/SpecialPublications/NIST.SP.1242.pdf> (visited on 10/22/2020).
- [178] R. G. Downing, J. Maki, and R. Fleming, “Analytical Applications of Neutron Depth Profiling”, *Journal of Radioanalytical and Nuclear Chemistry*, vol. 112, no. 1, pp. 33–46, 1987.
- [179] J. L. Weaver and D. Turkoglu, “Natural Alteration of ^6Li Alumino-Silicate Glass”, *Journal of Nuclear Materials*, vol. 512, pp. 56–64, 2018.
- [180] Y. He, R. G. Downing, and H. Wang, “3D Mapping of Lithium in Battery Electrodes Using Neutron Activation”, *Journal of Power Sources*, vol. 287, pp. 226–230, 2015.
- [181] R. G. Downing, “NIST Neutron Depth Profiling Facility: 2013”, *Transactions*, vol. 109, no. 1, pp. 527–528, 2013.

- [182] National Institute of Standards and Technology. (Oct. 2020). Material Analysis Using Neutron Depth Profiling — NIST, [Online]. Available: <https://www.nist.gov/laboratories/tools-instruments/material-analysis-using-neutron-depth-profiling> (visited on 10/22/2020).
- [183] W. Lennard, H. Geissel, K. Winterbon, D. Phillips, T. Alexander, and J. Forster, “Non-linear Response of Si Detectors for Low-Z Ions”, *Nuclear Instruments and Methods in Physics Research Section A: Accelerators, Spectrometers, Detectors and Associated Equipment*, vol. 248, no. 2-3, pp. 454–460, 1986.
- [184] W. Lennard and K. Winterbon, “Response of Silicon Detectors to ^1H and ^4He Ions”, *Nuclear Instruments and Methods in Physics Research Section B: Beam Interactions with Materials and Atoms*, vol. 24, pp. 1035–1038, 1987.
- [185] E. Finch and A. Rodgers, “Measurements of the Pulse Height Defect and Its Mass Dependence for Heavy-Ion Silicon Detectors”, *Nuclear Instruments and Methods*, vol. 113, no. 1, pp. 29–40, 1973.
- [186] National Institute of Standards and Technology. (Aug. 2010). Certificate of Analysis Standard Reference Material 2137, [Online]. Available: <https://www-s.nist.gov/srmors/certificates/2137.pdf> (visited on 10/22/2020).
- [187] W. H. Bragg and R. Kleeman, “On the α Particles of Radium, and their Loss of Range in Passing Through Various Atoms and Molecules”, *The London, Edinburgh, and Dublin Philosophical Magazine and Journal of Science*, vol. 10, no. 57, pp. 318–340, 1905.
- [188] J. Ziegler and J. Manoyan, “The Stopping of Ions in Compounds”, *Nuclear Instruments and Methods in Physics Research Section B: Beam Interactions with Materials and Atoms*, vol. 35, no. 3-4, pp. 215–228, 1988.
- [189] Y. Zhang and W. J. Weber, “Validity of Bragg’s Rule for Heavy-Ion Stopping in Silicon Carbide”, *Physical Review B*, vol. 68, no. 23, p. 235 317, 2003.
- [190] E. Bär, P. Andreo, A. Lalonde, G. Royle, and H. Bouchard, “Optimized I-Values for Use with the Bragg Additivity Rule and Their Impact on Proton Stopping Power and Range Uncertainty”, *Physics in Medicine & Biology*, vol. 63, no. 16, p. 165 007, 2018.
- [191] CERN European Research Laboratory. (Oct. 2020). ROOT: A Data Analysis Framework, [Online]. Available: <https://root.cern.ch/> (visited on 10/22/2020).
- [192] CERN European Research Laboratory. (Dec. 2015). ROOT: Interpolation Classes, [Online]. Available: https://root.cern.ch/doc/v606/group__Interpolation.html (visited on 10/22/2020).
- [193] A. Kvarving, Norwegian University of Science and Technology. (Oct. 2008). Natural Cubic Splines, [Online]. Available: <https://www.math.ntnu.no/emner/TMA4215/2008h/cubicsplines.pdf> (visited on 10/22/2020).

- [194] J. T. Maki, R. F. Fleming, and D. H. Vincent, “Deconvolution of Neutron Depth Profiling Spectra”, *Nuclear Instruments and Methods in Physics Research Section B: Beam Interactions with Materials and Atoms*, vol. 17, no. 2, pp. 147–155, 1986.
- [195] K. J. Coakley, “A Cross-Validation Procedure for Stopping the EM Algorithm and Deconvolution of Neutron Depth Profiling Spectra”, *IEEE Transactions on Nuclear Science*, vol. 38, no. 1, pp. 9–15, 1991.
- [196] V. Hnatowicz, J. Vacik, and D. Fink, “Deconvolution of Charged Particle Spectra from Neutron Depth Profiling Using Simplex Method”, *Review of Scientific Instruments*, vol. 81, no. 7, p. 073 906, 2010.
- [197] X. Yang, R. Downing, G. Wang, D. Qian, H. Liu, and K. Wang, “A Monte Carlo Code to Get Response Spectrum of Ions for Neutron Depth Profiling”, *Journal of Radioanalytical and Nuclear Chemistry*, vol. 301, no. 1, pp. 213–220, 2014.
- [198] B. Park and G. Sun, “Analysis of Depth Profiles of ^{10}B and ^6Li in Si Wafers and Lithium Ion Battery Electrodes Using the KAERI-NDP System”, *Journal of Radioanalytical and Nuclear Chemistry*, vol. 307, no. 3, pp. 1749–1756, 2016.
- [199] J. Shultis, “Notes on Neutron Depth Profiling”, *Engineering Experiment Station Report*, vol. 298, 2003.
- [200] C. Wang, M. J. Burek, Z. Lin, H. A. Atikian, V. Venkataraman, I.-C. Huang, P. Stark, and M. Loncar, “Integrated High Quality Factor Lithium Niobate Microdisk Resonators”, *Optics Express*, vol. 22, no. 25, pp. 30 924–30 933, 2014.
- [201] P. Kolarova, J. Vacik, J. Spirkova-Hradilova, and J. Cervena, “Neutron Depth Profiling Study of Lithium Niobate Optical Waveguides”, *Nuclear Instruments and Methods in Physics Research Section B: Beam Interactions with Materials and Atoms*, vol. 141, no. 1–4, pp. 498–500, 1998.
- [202] I. Paulini, W. Heiland, A. Arnau, E. Zarate, and P. Bauer, “Stopping Cross Section of Protons and Deuterons in Lithiumniobate near the Stopping Power Maximum”, *Nuclear Instruments and Methods in Physics Research Section B: Beam Interactions with Materials and Atoms*, vol. 118, no. 1-4, pp. 39–42, 1996.
- [203] R. Weis and T. Gaylord, “Lithium Niobate: Summary of Physical Properties and Crystal Structure”, *Applied Physics A*, vol. 37, no. 4, pp. 191–203, 1985.
- [204] The Royal Swedish Academy of Sciences. (Oct. 2019). Scientific Background on the Nobel Prize in Chemistry 2019: Lithium-Ion Batteries, [Online]. Available: <https://www.nobelprize.org/uploads/2019/10/advanced-chemistryprize2019-2.pdf> (visited on 10/22/2020).
- [205] J. Goodenough, G. Li, H. Ikuta, M. Whittingham, J. Yamaki, M. Winter, J. Besenhard, Y. Nishi, and B. Scrosati, *Lithium Ion Batteries: Fundamentals and Performance*. Wiley-VCH: Weinheim, Germany, 1998, ISBN: 3-527-29569-0.

- [206] A. Wang, S. Kadam, H. Li, S. Shi, and Y. Qi, “Review on Modeling of the Anode Solid Electrolyte Interphase (SEI) for Lithium-Ion Batteries”, *NPJ Computational Materials*, vol. 4, no. 1, pp. 1–26, 2018.
- [207] G. N. Lewis and F. G. Keyes, “The Potential of the Lithium Electrode”, *Journal of the American Chemical Society*, vol. 35, no. 4, pp. 340–344, 1913.
- [208] C. Glaize and S. Genies, *Lithium Batteries and other Electrochemical Storage Systems*. Wiley Online Library, 2013, ISBN: 978-1-118-76112-0.
- [209] M. Armand, “Intercalation Electrodes”, in *Materials for Advanced Batteries*, Springer, 1980, pp. 145–161, ISBN: 978-1-4684-3851-2.
- [210] M. Armand and P. Touzain, “Graphite Intercalation Compounds as Cathode Materials”, *Materials Science and Engineering*, vol. 31, pp. 319–329, 1977.
- [211] W. Rüdorff and U. Hofmann, “Über Graphitsalze”, *Zeitschrift für anorganische und allgemeine Chemie*, vol. 238, no. 1, pp. 1–50, 1938.
- [212] J. Landesfeind, “Determination of Physical and Electrochemical Parameters for Lithium-Ion Batteries and Advanced Electrochemical Impedance Analysis”, Dissertation, Technische Universität München, 2020.
- [213] J. Mindemark, M. J. Lacey, T. Bowden, and D. Brandell, “Beyond PEO—Alternative Host Materials for Li⁺-Conducting Solid Polymer Electrolytes”, *Progress in Polymer Science*, vol. 81, pp. 114–143, 2018.
- [214] M. Lacey. (Oct. 2020). Transport and Transference in Battery Electrolytes, [Online]. Available: <http://lacey.se/science/transference/> (visited on 10/22/2020).
- [215] A. Magerl, H. Zabel, and I. Anderson, “In-Plane Jump Diffusion of Li in LiC₆”, *Physical Review Letters*, vol. 55, no. 2, p. 222, 1985.
- [216] G. Wertheim, P. T. M. Van Attekum, and S. Basu, “Electronic Structure of Lithium Graphite”, *Solid State Communications*, vol. 33, no. 11, pp. 1127–1130, 1980.
- [217] X. Song, K. Kinoshita, and T. Tran, “Microstructural Characterization of Lithiated Graphite”, *Journal of the Electrochemical Society*, vol. 143, no. 6, p. L120, 1996.
- [218] J. Rossat-Mignod, A. Wiedenmann, K. Woo, J. Milliken, and J. Fischer, “First-Order Phase Transition in the Graphite Compound LiC₆”, *Solid State Communications*, vol. 44, no. 8, pp. 1339–1342, 1982.
- [219] Y. Qi and S. J. Harris, “In Situ Observation of Strains During Lithiation of a Graphite Electrode”, *Journal of the Electrochemical Society*, vol. 157, no. 6, A741, 2010.
- [220] R. Fong, U. Von Sacken, and J. R. Dahn, “Studies of Lithium Intercalation into Carbons Using Nonaqueous Electrochemical Cells”, *Journal of the Electrochemical Society*, vol. 137, no. 7, p. 2009, 1990.

- [221] E. Peled, “The Electrochemical Behavior of Alkali and Alkaline Earth Metals in Non-aqueous Battery Systems—The Solid Electrolyte Interphase Model”, *Journal of the Electrochemical Society*, vol. 126, no. 12, p. 2047, 1979.
- [222] H. Berg, *Batteries for Electric Vehicles: Materials and Electrochemistry*. Cambridge University Press, 2015, ISBN: 978-1-316-09097-8.
- [223] International Union of Pure and Applied Chemistry. (Oct. 2020). IUPAC - Standard Hydrogen Electrode (S05917), [Online]. Available: <http://goldbook.iupac.org/terms/view/S05917> (visited on 10/22/2020).
- [224] W. M. Haynes, Ed., *CRC Handbook of Chemistry and Physics*. CRC press, 2016, ISBN: 978-1498754286.
- [225] A. Senyshyn, O. Dolotko, M. Mühlbauer, K. Nikolowski, H. Fuess, and H. Ehrenberg, “Lithium Intercalation into Graphitic Carbons Revisited: Experimental Evidence for Twisted Bilayer Behavior”, *Journal of the Electrochemical Society*, vol. 160, no. 5, A3198, 2013.
- [226] C. von Lüders, V. Zinth, S. V. Erhard, P. J. Osswald, M. Hofmann, R. Gilles, and A. Jossen, “Lithium Plating in Lithium-Ion Batteries Investigated by Voltage Relaxation and In Situ Neutron Diffraction”, *Journal of Power Sources*, vol. 342, pp. 17–23, 2017.
- [227] O. Dolotko, A. Senyshyn, M. Mühlbauer, K. Nikolowski, and H. Ehrenberg, “Understanding Structural Changes in NMC Li-Ion Cells by In Situ Neutron Diffraction”, *Journal of Power Sources*, vol. 255, pp. 197–203, 2014.
- [228] S. C. Nagpure, R. G. Downing, B. Bhushan, S. Babu, and L. Cao, “Neutron Depth Profiling Technique for Studying Aging in Li-Ion Batteries”, *Electrochimica Acta*, vol. 56, no. 13, pp. 4735–4743, 2011.
- [229] S. Whitney, S. R. Biegalski, Y. Huang, and J. B. Goodenough, “Neutron Depth Profiling Applications to Lithium-Ion Cell Research”, *Journal of the Electrochemical Society*, vol. 156, no. 11, pp. A886–A890, 2009.
- [230] M. Frankenberger, M. Trunk, S. Seidlmayer, A. Dinter, J. Dittloff, L. Werner, R. Gernhäuser, Z. Révay, B. Märkisch, R. Gilles, *et al.*, “SEI Growth Impacts of Lamination, Formation and Cycling in Lithium Ion Batteries”, *Batteries*, vol. 6, no. 2, p. 21, 2020.
- [231] M. Wetjen, M. Trunk, L. Werner, R. Gernhäuser, B. Märkisch, Z. Révay, R. Gilles, and H. A. Gasteiger, “Quantifying the Distribution of Electrolyte Decomposition Products in Silicon-Graphite Electrodes by Neutron Depth Profiling”, *Journal of the Electrochemical Society*, vol. 165, no. 10, pp. A2340–A2348, 2018.
- [232] M. Wetjen, M. Trunk, L. Werner, H. A. Gasteiger, R. Gernhäuser, R. Gilles, B. Märkisch, and Z. Révay, “Monitoring the Lithium Concentration across the Thickness of Silicon-Graphite Electrodes during the First (De-) Lithiation”, *Journal of the Electrochemical Society*, vol. 166, no. 8, pp. A1408–A1411, 2019.

- [233] M. Uitz, M. Sternad, S. Breuer, C. Täubert, T. Traußnig, V. Hennige, I. Hanzu, and M. Wilkening, “Aging of Tesla’s 18650 Lithium-Ion Cells: Correlating Solid-Electrolyte-Interphase Evolution with Fading in Capacity and Power”, *Journal of the Electrochemical Society*, vol. 164, no. 14, p. A3503, 2017.
- [234] D. X. Liu, J. Wang, K. Pan, J. Qiu, M. Canova, L. R. Cao, and A. C. Co, “In Situ Quantification and Visualization of Lithium Transport with Neutrons”, *Angewandte Chemie*, vol. 126, no. 36, pp. 9652–9656, 2014.
- [235] X. Zhang, T. W. Verhallen, F. Laboim, and M. Wagemaker, “Direct Observation of Li-Ion Transport in Electrodes under Nonequilibrium Conditions Using Neutron Depth Profiling”, *Advanced Energy Materials*, vol. 5, no. 15, p. 1500498, 2015.
- [236] D. X. Liu, L. R. Cao, and A. C. Co, “Demonstrating the Feasibility of Al as Anode Current Collector in Li-Ion Batteries via In Situ Neutron Depth Profiling”, *Chemistry of Materials*, vol. 28, no. 2, pp. 556–563, 2016.
- [237] S. Lv, T. Verhallen, A. Vasileiadis, F. Ooms, Y. Xu, Z. Li, Z. Li, and M. Wagemaker, “Operando Monitoring the Lithium Spatial Distribution of Lithium Metal Anodes”, *Nature Communications*, vol. 9, no. 1, p. 2152, 2018.
- [238] Y. Hamon, T. Brousse, F. Jousse, P. Topart, P. Buvat, and D. Schleich, “Aluminum Negative Electrode in Lithium Ion Batteries”, *Journal of Power Sources*, vol. 97, pp. 185–187, 2001.
- [239] N. Imanishi, S. Hasegawa, T. Zhang, A. Hirano, Y. Takeda, and O. Yamamoto, “Lithium Anode for Lithium-Air Secondary Batteries”, *Journal of Power Sources*, vol. 185, no. 2, pp. 1392–1397, 2008.
- [240] National Research Council *et al.*, *Effectiveness of the United States Advanced Battery Consortium as a Government-Industry Partnership*. National Academies Press, 1998, ISBN: 978-0-309-17387-2.
- [241] S. G. Lee and D. H. Jeon, “Effect of Electrode Compression on the Wettability of Lithium-Ion Batteries”, *Journal of Power Sources*, vol. 265, pp. 363–369, 2014.
- [242] S. J. Harris, A. Timmons, D. R. Baker, and C. Monroe, “Direct In Situ Measurements of Li Transport in Li-Ion Battery Negative Electrodes”, *Chemical Physics Letters*, vol. 485, no. 4-6, pp. 265–274, 2010.
- [243] A. Barré, B. Deguilhem, S. Grolleau, M. Gérard, F. Suard, and D. Riu, “A Review on Lithium-Ion Battery Ageing Mechanisms and Estimations for Automotive Applications”, *Journal of Power Sources*, vol. 241, pp. 680–689, 2013.
- [244] J.-M. Tarascon and M. Armand, “Issues and Challenges Facing Rechargeable Lithium Batteries”, in *Materials for Sustainable Energy: A Collection of Peer-Reviewed Research and Review Articles from Nature Publishing Group*, World Scientific, 2011, pp. 171–179.

- [245] F. Joho, P. Novák, and M. E. Spahr, “Safety Aspects of Graphite Negative Electrode Materials for Lithium-Ion Batteries”, *Journal of the Electrochemical Society*, vol. 149, no. 8, pp. A1020–A1024, 2002.
- [246] M. Frankenberger, M. Singh, A. Dinter, S. Jankowsky, A. Schmidt, and K.-H. Pettinger, “Laminated Lithium Ion Batteries with Improved Fast Charging Capability”, *Journal of Electroanalytical Chemistry*, vol. 837, pp. 151–158, 2019.
- [247] T. Plattard, N. Barnel, L. Assaud, S. Franger, and J.-M. Duffault, “Combining a Fatigue Model and an Incremental Capacity Analysis on a Commercial NMC/Graphite Cell under Constant Current Cycling with and without Calendar Aging”, *Batteries*, vol. 5, no. 1, p. 36, 2019.
- [248] J. Vetter, P. Novák, M. Wagner, C. Veit, K.-C. Möller, J. Besenhard, M. Winter, M. Wohlfahrt-Mehrens, C. Vogler, and A. Hammouche, “Ageing Mechanisms in Lithium-Ion Batteries”, *Journal of Power Sources*, vol. 147, no. 1-2, pp. 269–281, 2005.
- [249] Y. Kubota, M. C. S. Escaño, H. Nakanishi, and H. Kasai, “Crystal and Electronic Structure of $\text{Li}_{15}\text{Si}_4$ ”, *Journal of Applied Physics*, vol. 102, no. 5, p. 053704, 2007.
- [250] M. Ashuri, Q. He, and L. L. Shaw, “Silicon as a Potential Anode Material for Li-Ion Batteries: Where Size, Geometry and Structure Matter”, *Nanoscale*, vol. 8, no. 1, pp. 74–103, 2016.
- [251] C.-M. Wang, X. Li, Z. Wang, W. Xu, J. Liu, F. Gao, L. Kovarik, J.-G. Zhang, J. Howe, D. J. Burton, *et al.*, “In Situ TEM Investigation of Congruent Phase Transition and Structural Evolution of Nanostructured Silicon/Carbon Anode for Lithium Ion Batteries”, *Nano Letters*, vol. 12, no. 3, pp. 1624–1632, 2012.
- [252] R. Jung, M. Metzger, D. Haering, S. Solchenbach, C. Marino, N. Tsiouvaras, C. Stinner, and H. A. Gasteiger, “Consumption of Fluoroethylene Carbonate (FEC) on Si-C Composite Electrodes for Li-Ion Batteries”, *Journal of the Electrochemical Society*, vol. 163, no. 8, pp. A1705–A1716, 2016.
- [253] M. Wetjen, D. Pritzl, R. Jung, S. Solchenbach, R. Ghadimi, and H. A. Gasteiger, “Differentiating the Degradation Phenomena in Silicon-Graphite Electrodes for Lithium-Ion Batteries”, *Journal of the Electrochemical Society*, vol. 164, no. 12, pp. A2840–A2852, 2017.
- [254] M. Wetjen, S. Solchenbach, D. Pritzl, J. Hou, V. Tileli, and H. A. Gasteiger, “Morphological Changes of Silicon Nanoparticles and the Influence of Cutoff Potentials in Silicon-Graphite Electrodes”, *Journal of the Electrochemical Society*, vol. 165, no. 7, pp. A1503–A1514, 2018.
- [255] M. Wetjen, D. Pritzl, S. Niesen, and H. A. Gasteiger, “Investigation of the Porosity and Tortuosity of Silicon-Graphite Electrodes in Lithium-Ion Batteries”, in *ECS Meeting Abstracts*, The Electrochemical Society, 2017, pp. 2176–2176.

- [256] M. Wetjen, D. Pritzl, S. Solchenbach, J. Hou, V. Tileli, and H. A. Gasteiger, “Less is More—Decreasing Silicon Particle Degradation by Limiting the Delithiation Cut-Off Potential”, in *Meeting Abstracts*, The Electrochemical Society, 2017, pp. 424–424.
- [257] K. U. Schwenke, S. Solchenbach, J. Demeaux, B. L. Lucht, and H. A. Gasteiger, “The Impact of CO₂ Evolved from VC and FEC during Formation of Graphite Anodes in Lithium-Ion Batteries”, *Journal of the Electrochemical Society*, vol. 166, no. 10, p. A2035, 2019.
- [258] M. Nie, D. Chalasani, D. P. Abraham, Y. Chen, A. Bose, and B. L. Lucht, “Lithium Ion Battery Graphite Solid Electrolyte Interphase Revealed by Microscopy and Spectroscopy”, *The Journal of Physical Chemistry C*, vol. 117, no. 3, pp. 1257–1267, 2013.
- [259] B. Zhang, M. Metzger, S. Solchenbach, M. Payne, S. Meini, H. A. Gasteiger, A. Garsuch, and B. L. Lucht, “Role of 1, 3-Propane Sultone and Vinylene Carbonate in Solid Electrolyte Interface Formation and Gas Generation”, *The Journal of Physical Chemistry C*, vol. 119, no. 21, pp. 11 337–11 348, 2015.
- [260] F. Linsenmann, P. Rapp, H. A. Gasteiger, *et al.*, “Dissolution of SEI Products in the Liquid Electrolyte”, *in preparation*,
- [261] F. J. Günter, C. Burgstaller, F. Konwitschny, and G. Reinhart, “Influence of the Electrolyte Quantity on Lithium-Ion Cells”, *Journal of the Electrochemical Society*, vol. 166, no. 10, p. A1709, 2019.
- [262] F. T. Wagner, B. Lakshmanan, and M. F. Mathias, “Electrochemistry and the Future of the Automobile”, *The Journal of Physical Chemistry Letters*, vol. 1, no. 14, pp. 2204–2219, 2010.
- [263] S. C. Nagpure, R. G. Downing, B. Bhushan, and S. Babu, “Discovery of Lithium in Copper Current Collectors Used in Batteries”, *Scripta Materialia*, vol. 67, no. 7-8, pp. 669–672, 2012.
- [264] C. Berner, “Development of the Compact, High Resolution Particle Detection System HI-TREX”, Dissertation, Technische Universität München, 2020.
- [265] K. Lefmann and K. Nielsen, “McStas, A General Software Package for Neutron Ray-Tracing Simulations”, *Neutron News*, vol. 10, no. 3, pp. 20–23, 1999.
- [266] P. Andersen, K. Lefmann, L. T. Kuhn, P. K. Willendrup, and E. Farhi, “Monte Carlo Simulations as a Part of the Configuration for Neutron Instruments”, *Physica B: Condensed Matter*, vol. 350, no. 1-3, pp. E721–E724, 2004.
- [267] P. Willendrup, E. Farhi, E. Knudsen, U. Filges, and K. Lefmann, “McStas: Past, Present and Future”, *Journal of Neutron Research*, vol. 17, no. 1, pp. 35–43, 2014.
- [268] P. K. Willendrup and K. Lefmann, “McStas: Introduction, Use, and Basic Principles for Ray-Tracing Simulations”, *Journal of Neutron Research*, vol. 22, pp. 1–16, 2019.

- [269] P. Müller-Buschbaum, “A Basic Introduction to Grazing Incidence Small-Angle X-Ray Scattering”, in *Applications of Synchrotron Light to Scattering and Diffraction in Materials and Life Sciences*, Springer, 2009, pp. 61–89.
- [270] A. Marx and R. Gross, *Festkörperphysik*. Oldenbourg Wissenschaftsverlag, 2014, ISBN: 978-3-11-035870-4.
- [271] Heinz Maier-Leibnitz Zentrum. (Oct. 2020). Materials Science Lab - Materialwissenschaftliches Labor, [Online]. Available: <https://www.mlz-garching.de/instrumente-und-labore/labore/materialwissenschaftliches-labor.html> (visited on 10/22/2020).
- [272] J. Wilhelm, S. Seidlmayer, P. Keil, J. Schuster, A. Kriele, R. Gilles, and A. Jossen, “Cycling Capacity Recovery Effect: A Coulombic Efficiency and Post-Mortem Study”, *Journal of Power Sources*, vol. 365, pp. 327–338, 2017.
- [273] P. Marzak, J. Yun, A. Dorsel, A. Kriele, R. Gilles, O. Schneider, and A. S. Bandarenka, “Electrodeposited $\text{Na}_2\text{Ni}[\text{Fe}(\text{CN})_6]$ Thin-Film Cathodes Exposed to Simulated Aqueous Na-Ion Battery Conditions”, *The Journal of Physical Chemistry C*, vol. 122, no. 16, pp. 8760–8768, 2018.
- [274] Koichi Momma, National Museum of Nature and Science, Japan. (Sep. 2020). Visualization for Electronic and Structural Analysis (VESTA), [Online]. Available: <http://jp-minerals.org/vesta/> (visited on 10/22/2020).
- [275] D. Chateigner, X. Chen, M. Ciriotti *et al.* (Oct. 2020). Crystallography Open Database, [Online]. Available: <http://www.crystallography.net/cod/> (visited on 10/22/2020).
- [276] Department of Nanometrology, Czech Metrology Institute. (Oct. 2020). Gwyddion – Free SPM (AFM, SNOM/NSOM, STM, MFM, ...) Data Analysis Software, [Online]. Available: <http://gwyddion.net/> (visited on 10/22/2020).

List of Publications

Publications as First/Shared-First Author

- M. Trunk, M. Wetjen, L. Werner, R. Gernhäuser, B. Märkisch, Z. Revay, H. Gasteiger, R. Gilles, “Materials Science Applications of Neutron Depth Profiling at the PGAA Facility of Heinz Maier-Leibnitz Zentrum”, *Materials Characterization*, vol. 146, pp. 127-134, **2018**, doi: 10.1016/j.matchar.2018.09.030
- M. Wetjen, M. Trunk, L. Werner, R. Gernhäuser, B. Märkisch, Z. Revay, R. Gilles, H. Gasteiger, “Quantifying the Distribution of Electrolyte Decomposition Products in Silicon-Graphite Electrodes by Neutron Depth Profiling”, *Journal of the Electrochemical Society*, vol. 165, no. 10, pp. A2340-A2348, **2018**, doi: 10.1149/2.1341810jes
- M. Wetjen, M. Trunk, L. Werner, R. Gernhäuser, B. Märkisch, Z. Revay, R. Gilles, H. Gasteiger, “Monitoring the Lithium Concentration Across the Thickness of Silicon-Graphite Electrodes During the First (De-)Lithiation”, *Journal of the Electrochemical Society*, vol. 166, no. 8, pp. A1408-A1411, **2019**, doi: 10.1149/2.0581908jes
- F. Linsenmann, M. Trunk, P. Rapp, L. Werner, R. Gernhäuser, R. Gilles, B. Märkisch, Z. Revay, H. Gasteiger, “A Liquid Electrolyte-Based Lithium-Ion Battery Cell Design for *Operando* Neutron Depth Profiling”, *Journal of the Electrochemical Society*, vol. 167, no. 10, p. 100554, **2020**, doi: 10.1149/1945-7111/ab9b20

Further Publications as Co-Author

- L. Werner, M. Trunk, R. Gernhäuser, R. Gilles, B. Märkisch, Z. Revay, “The New Neutron Depth Profiling Instrument N4DP at the Heinz Maier-Leibnitz Zentrum”, *Nuclear Instruments and Methods in Physics Research Section A*, vol. 911, pp. 30-36, **2018**, doi: 10.1016/j.nima.2018.09.113
- M. Frankenberger, M. Trunk, S. Seidlmayer, A. Dinter, J. Dittloff, L. Werner, R. Gernhäuser, Z. Revay, B. Märkisch, R. Gilles, K. Pettinger, “SEI Growth Impacts of Lamination, Formation and Cycling in Lithium Ion Batteries”, *Batteries*, vol. 6, no. 2, p. 21, **2020**, doi: 10.3390/batteries6020021
- E. Moyassari, L. Streck, N. Paul, M. Trunk, R. Neagu, C.-C. Chang, S.-C. Hou, B. Märkisch, R. Gilles, A. Jossen, “Impact of Silicon Content within Silicon-Graphite Anodes on Performance and Li Concentration Profiles of Li-Ion Cells Using Neutron Depth

Profiling (NDP)”, *Journal of the Electrochemical Society*, vol. 168, no. 2, p. 020519, **2021**, doi: 10.1149/1945-7111/abe1db

- F. Linsenmann, P. Rapp, M. Trunk, J. Weaver, B. Märkisch, H. Gasteiger, *et al.* “Spatially- and Time-Resolved Detection of Lithium Plating During Fast-Charging of a Graphite-Based Lithium-Ion Battery”, in preparation

Conference Talks

- M. Trunk, R. Gernhäuser, B. Märkisch, Z. Revay, L. Werner, H. Gasteiger, M. Wetjen, R. Gilles, “Non-Destructive Studies Using a New Neutron Depth Profiling Instrument at the Heinz Maier-Leibnitz Zentrum in Garching near Munich”, *DPG Frühjahrstagung, Anwendung kernphysikalischer Methoden*, Bochum (Germany), 26.02.–02.03.**2018**.
- M. Trunk, R. Gernhäuser, B. Märkisch, Z. Revay, L. Werner, H. Gasteiger, M. Wetjen, R. Gilles, “First Material Science Applications At the New Neutron Depth Profiling Instrument at the PGAA Beamline of Heinz Maier-Leibnitz Zentrum, Garching, Germany”, *Methods & Applications of Radioanalytical Chemistry (MARC) XI*, Kailua-Kona (United States), 08.04.–13.04.**2018**.
- M. Trunk, M. Wetjen, L. Werner, R. Gernhäuser, B. Märkisch, Z. Revay, H. Gasteiger, R. Gilles, “Concentration Profiles in Thin Films Obtained From Neutron Depth Profiling at the PGAA Facility”, *German Conference for Research with Synchrotron Radiation, Neutrons and Ion Beams at Large Facilities (SNI 2018)*, Garching (Germany), 17.09.–19.09.**2018**.
- M. Trunk, L. Werner, R. Gernhäuser, R. Gilles, B. Märkisch, Z. Revay, H. Gasteiger, M. Wetjen, F. Linsenmann, “Gaining Insight into Lithium-Ion Battery Electrodes Using Neutron Depth Profiling at the N4DP Instrument at MLZ”, *27th Seminar on Activation Analysis and Gamma Spectrometry (SAAGAS 27)*, Garching (Germany), 24.02.–27.02.**2019**.
- M. Trunk, L. Werner, R. Gernhäuser, R. Gilles, B. Märkisch, Z. Revay, H. Gasteiger, M. Wetjen, F. Linsenmann, “Applications of Neutron Depth Profiling at the N4DP Instrument at the Heinz Maier-Leibnitz Zentrum”, *DPG Frühjahrstagung, Anwendung kernphysikalischer Methoden*, Munich (Germany), 17.03.–22.03.**2019**.

Conference Poster Presentations

- M. Trunk, R. Gernhäuser, R. Gilles, B. Märkisch, Z. Revay, L. Werner, “Neutron Depth Profiling for Materials Science Application”, *3rd Internal Biennial Science Meeting of the MLZ*, Grainau (Germany), 19.06.–22.06.**2017**.
- M. Trunk, L. Werner, R. Gernhäuser, R. Gilles, B. Märkisch, Z. Revay, “The Neutron Depth Profiling Experiment at the PGAA Facility”, *4th Internal Biennial Science Meeting of the MLZ*, Grainau (Germany), 24.06.–27.06.**2019**.

- M. Trunk, L. Werner, R. Gernhäuser, R. Gilles, B. Märkisch, Z. Revay, “The Neutron Depth Profiling Instrument N4DP at the Heinz Maier-Leibnitz Zentrum in Garching, Germany”, *European Conference on Neutron Scattering (ECNS)*, Saint Petersburg (Russia), 30.06.–05.07.**2019**.
- M. Trunk, L. Werner, R. Gernhäuser, R. Gilles, B. Märkisch, Z. Revay, “Cold Neutron Depth Profiling at the PGAA facility”, *MLZ User Meeting*, Munich (Germany), 10.12.–11.12.**2019**.

Award Obtained Related to this Work

- 1st price for the best oral contribution (presentation) awarded by the Gesellschaft deutscher Chemiker (GDCh; engl.: *Society of German Chemists*) at the 27th Seminar on Activation Analysis and Gamma Spectrometry (SAAGAS 27), Garching (Germany), 24.–27.02.**2019**.

Advised Thesis

- Johannes Dittloff, “Bestimmung alterungsabhängiger Tiefenprofile in Elektroden für Lithium-Ionen-Batterien”, *Bachelor Thesis*, **2019**

Acknowledgment

First of all I want to greatly thank Prof. Dr. Bastian Märkisch for his confidence in the N4DP project and in us doctorate candidates. I thank him for taking the time for weekly meetings with us and his professional support for experimental details as well as instructional matters.

I want to greatly thank Lukas Werner, who was the second doctorate candidate of the N4DP project. He is a person to rely on when it counts and I thank him for his patience in introducing me into the technical details of his hardware work. Throughout the years we formed a productive two-headed team based on hardwork, trust and humor, and so we were able to manage day-, night- and weekend-shifts during beamtimes.

With at least as much importance, I want to thank Dr. Roman Gernhäuser, who has always an open door and mind for all us students from the different working groups. He always supported us with highest dedication, no matter if we needed theoretical, political, or even hands-on support in the lab and during beamtimes. Without his effort, our expensive lab equipment would probably still being confiscated at German or American Customs.

I give special thanks to Greg Downing, Ph. D., recently retired from the National Institute of Standards and Technology in Gaithersburg, USA. He is probably one of the top worldwide experts in the NDP section and we are so glad that he visited us at the beginning of our project in 2017, where we got to know him as a very kind and helpful person. Without sharing his many advices, suggestions and experiences, the whole N4DP project would have greatly suffered and would not have been as successful as it was.

I want to thank Prof. Dr. Winfried Petry for accepting to be the second reviewer of this thesis. I thank him for the productive discussion about this topic, too.

I want to thank Christian Berner for always finding time to help us in the N4DP project. Especially, I want to thank him for his time and expertise during beamtimes at the MLZ.

I want to give special thanks to our working students Kerstin Mitterer and Lucinda Schönfeld, who both supported us with technical drawings and mechanical implementation of the N4DP experimental setup and surroundings.

I want to thank my bachelor student Johannes Dittloff, who made an excellent work and surpassed my expectations. He did a very accurate and responsible job, and we hope he might find his way back to this project for a later thesis.

I want to give special thanks to Dr. Zsolt Revay and Dr. Christian Stieghorst from the PGAA group of MLZ. They provided us access to their beamline for the N4DP experiment and a nice working environment. I want to thank both of them for their great and detailed help when writing papers and this thesis.

I want to give special thanks to some members of the TEC group at the chemistry department

at TUM. First of all, I want to thank Prof. Dr. Hubert Gasteiger for the countless meetings and time he spent on this project. I want to thank Morten Wetjen, who was our first contact into the group of Prof. Dr. Hubert Gasteiger. He is an outstanding cooperation partner with fruitful results. I want to thank Fabian Linsenmann and Philip Rapp for their excellent work especially on the *operando* NDP project and their relentless fabrication of countless of test cells. I want to thank Dr. Ralph Gilles for his effort in finding new cooperation partners and making the N4DP project famous all over the world. I want to furthermore thank Dr. Stefan Seidlmayer and Dr. Neelima Paul of Ralph's group for their help and contact between the N4DP project and the users. I want to thank Armin Kriele from the Materials Science Lab of MLZ for his effort in teaching me the XRD machine and providing me sufficient time for the measurements. I want to thank Martin Frankenberger from the Technologiezentrum Energie of the Hochschule Landshut for his effort on preparing, measuring and electrochemically evaluating several graphite anodes.

Very special thanks to Jamie Weaver, Ph. D., who allowed us to visit her on short notice at her CNDP facility at the NIST Center for Neutron Research. She welcomed us very warmly and helped us as much as possible, independent of official working hours or any other restrictions. She shared her very detailed and well-funded knowledge in NDP with us and supported us in any possible way. I thank her especially for continuing some NDP measurements for us, even though our stay at NCNR had ended.

I want to thank Sonja Winkler, Dominik Rechten and Ralf Lang from the physics department of TUM. They respectively supported me in any way concerning the clean room, the introduction to the evaporation machine, and all the help with the technical drawings and their realization. Special thanks to Eschly Kluge for his effort in calculating various neutron focusing geometries for future applications.

I also thank Robert Neagu, who recently started as a doctorate candidate in our project in 2020. He productively continues the work of Lukas and me with great effort and success.

I want to thank the whole ENE group of Prof. Dr. Bastian Märkisch and their guests for the nice working environment and all the supporting around our project. Special thanks go to Karin Frank, who helped us with any contract and organizational details, Alexander Hollering, Dr. Jens Klenke, Kathrin Lehmann, Karina Bernert, Max Lamparth, Christoph Roick and Heiko Saul.

Zum Schluss möchte ich noch all jenen danken, die mich so grundlegend im Privaten unterstützt und so essentiell beigetragen haben, dass sie hier keiner gelisteten Aufzählung mehr bedürfen.